



HAL
open science

Contribution of ultra-wide band and polarization diversity for the non-destructive evaluation of civil engineering structures using the ground penetrating radar (GPR)

Elias Tebchrany

► To cite this version:

Elias Tebchrany. Contribution of ultra-wide band and polarization diversity for the non-destructive evaluation of civil engineering structures using the ground penetrating radar (GPR). Civil Engineering. Université Paris-Est, 2015. English. NNT : 2015PESC1105 . tel-01355938

HAL Id: tel-01355938

<https://theses.hal.science/tel-01355938>

Submitted on 24 Aug 2016

HAL is a multi-disciplinary open access archive for the deposit and dissemination of scientific research documents, whether they are published or not. The documents may come from teaching and research institutions in France or abroad, or from public or private research centers.

L'archive ouverte pluridisciplinaire **HAL**, est destinée au dépôt et à la diffusion de documents scientifiques de niveau recherche, publiés ou non, émanant des établissements d'enseignement et de recherche français ou étrangers, des laboratoires publics ou privés.

Thèse de doctorat de l'université Paris-Est (UPE)

École doctorale Sciences, Ingénierie et Environnement (SIE)

Spécialité: Sciences de l'ingénieur

Préparée à l'Institut Français des Sciences et Technologies des Transports, de
l'Aménagement et des Réseaux (IFSTTAR)
Département COSYS – Laboratoire LISIS

Titre

Apports de l'ultra large bande et de la diversité de polarisation du radar de sol pour l'auscultation des ouvrages du génie civil

Présentée et soutenue publiquement par

Elias TEBCHRANY

Le 8 Octobre 2015
à Champs-sur-Marne

En vue d'obtenir le titre de Docteur de l'Université Paris-Est

Jury

Rapporteurs:	M. Yide Wang	Professeur à l'Université de Nantes
	Mme. Albane Saintenoy	Maître de Conférences à l'Université Paris-Sud, Orsay
Examineurs:	M. Ghais El Zein	Professeur à l'INSA de Rennes
	M. Pascal Xavier	Professeur à l'Université Joseph Fourier de Grenoble
Membre invité:	M. Xavier Dérobert	ITPE, HDR, IFSTTAR-Nantes
Directrice de thèse:	Mme. Florence Sagnard	Chargée de Recherches, HDR, IFSTTAR-MLV
Co-encadrant de thèse:	M. Vincent Baltazart	Chargé de Recherches, IFSTTAR-Nantes

Résumé

La technique de Georadar (GPR) est actuellement largement utilisée comme une technique non-destructive de sondage et d'imagerie dans plusieurs applications du génie civil qui concernent principalement: l'inspection des structures et des matériaux de construction, la cartographie des réseaux enterrés et des cavités, la caractérisation des fondations souterraines et du sol ainsi que l'estimation de la teneur en eau volumique du sous-sol. Le radar GPR est une technique en continuelle évolution en raison de l'intégration toujours plus poussée des équipements électroniques, des performances des calculateurs numériques, et des traitements avancés du signal. La promotion de cette technologie repose sur le développement de nouvelles configurations de systèmes et d'outils de traitement des données en vue de l'interprétation des images du sous-sol. Dans ce contexte, les travaux de cette thèse présentent tout d'abord le système GPR ULB (Ultra large bande) à double polarisation couplé au sol, lequel a été développé récemment au laboratoire. Par la suite, les traitements des données ont été focalisés sur le développement d'outils d'analyse en vue d'obtenir, à partir des images brutes (Bscans), des images plus facilement lisibles par l'utilisateur. Il s'agit d'améliorer l'interprétation des données GPR, en particulier dans le cadre de la détection de canalisations urbaines et la caractérisation des sols. Les moyens de traitement utilisés concernent au cours d'une étape de prétraitement l'élimination du clutter en utilisant des adaptations et des extensions d'algorithmes fondés sur les techniques PCA et ICA. Par la suite, une technique de traitement d'image "template matching" est proposée pour faciliter la détection d'hyperbole dans une image Bscan. La diversité de polarisation est abordée dans le but de fournir des informations supplémentaires pour la détection d'objets diélectriques et des discontinuités du sous-sol. Les performances de nos outils d'analyse sont évaluées sur de données synthétiques (simulations 3D FDTD) et des données de mesures obtenues dans des environnements contrôlés. Pour cela, nous avons considéré différentes configurations de polarisation et des objets à caractéristiques diélectriques variées. Le potentiel de discrimination des cibles a été quantifié en utilisant le critère statistique fondé sur les courbes ROC.

Remerciements

Ce travail de thèse a été mené au sein du laboratoire d'instrumentation, simulation et informatique scientifique (LISIS) du département COSYS de l'IFSTTAR Marne-la-Vallée. Il n'aurait pu aboutir sans la contribution directe ou indirecte de nombreuses personnes, que je remercie toutes chaleureusement.

Mes premiers remerciements s'adressent à ma directrice de thèse Mme. Florence Sagnard et mon co-encadrant M. Vincent Baltazart pour leur accueil et leur encadrement scientifique et linguistique. Je les remercie sincèrement pour l'opportunité et l'expérience qu'ils m'ont offertes.

Je tiens à remercier l'ensemble de la commission d'examen constituée de Mme. Albane Saintenoy et M. Yide Wang pour m'avoir fait l'honneur d'accepter de rapporter ce travail, ainsi que M. Ghais El Zein, M. Pascal Xavier et M. Xavier Dérobert pour avoir accepté les rôles d'examineurs. Merci pour le temps que vous avez consacré à lire et apporter vos remarques à ce manuscrit.

Un grand merci à M. Gonzague Six et M. Jean-Luc Bachelier pour leur aide durant les diverses mesures effectuées et pour leur très agréable compagnie.

Je souhaite particulièrement remercier M. Patrice Chatellier directeur du LISIS et Mme Marion Berbineau directrice Adjointe COSYS pour l'organisation des réunions de suivi qui ont conduit à des discussions très constructives.

Je souhaite exprimer ma gratitude à M. Jean-Philippe Tarel et M. Xavier Dérobert pour m'avoir conseillé et introduit sur certaines techniques conventionnelles et indispensables à ce travail. J'adresse également mes remerciements à M. Fayçal Réjiba et son Docteur Quentin Vitale du laboratoire Matis de l'UPMC qui nous ont prêté occasionnellement leur analyseur de réseau portable.

Je souhaite également exprimer mes remerciements à tous mes collègues du laboratoire LISIS de l'Ifsttar, François, Maddly, Dominique, Erick, Julien, Anne, Stéphane, Aghiad, Fatima, Joelle, Rachida, Bérengère, Nicolas, Emmanuel, Philippe, Pierre, Maria et Omar; ainsi que le directeur du COSYS M. Frédéric Bourquin, le directeur scientifique délégué M. Jean-Luc Clement, la gestionnaire RH Mme Meranh Karounna et tout le reste de l'équipe, avec qui j'ai eu le plaisir de discuter. Et je n'oublie pas l'école doctorale de Paris-Est, notamment Mme Cécile Blanchemanche, pour son aide et sa disponibilité pour toutes questions et démarches.

Plus particulièrement je pense notamment à tous mes collègues du campus Paris-Est/IFSTTAR : Laurent, Leyla, Hani, Filippo, William, Arnaud, Moustaffa, Nader... Et aux futurs docteurs et amis Laura, Fulvio, Janelle, Ha et Léa qui ont tous été d'une très agréable et enrichissante compagnie. Merci également à tous mes amis extérieurs au campus pour l'ambiance exceptionnelle qu'ils ont apportée durant ma période de préparation doctorale.

Enfin, je remercie chaleureusement ma famille pour son soutien et encouragement pendant les moments difficiles, en particulier mes parents qui ont été pour moi une source de motivation, de patience et de persévérance.

Elias Tebchrany

PhD thesis, University of Paris-Est (UPE)

Doctoral School of Science, Engineering and Environment (SIE)

Specialty: Engineering Sciences

Prepared at the French Institute of Science and Technology for Transport,
Development and Networks (IFSTTAR)
Department COSYS - Laboratory LISIS

Title

**Contribution of ultra-wide band and polarization
diversity for the non-destructive evaluation of civil
engineering structures using the ground penetrating
radar (GPR)**

Presented and submitted publicly by

Elias TEBCHRANY

8 October 2015
Champs-sur-Marne

To obtain the degree of Doctor of the University Paris-Est

Jury

Reporters:	Mr. Yide Wang	Professor, University of Nantes
	Mrs. Albane Saintenoy	Associate professor, HDR, Paris-Sud University, Orsay
Reviewers:	Mr. Ghais El Zein	Professor, INSA Rennes
	Mr. Pascal Xavier	Professor, Joseph Fourier University, Grenoble
Invited member:	Mr. Xavier Dérobert	ITPE, HDR, IFSTTAR-Nantes
Thesis director:	Mrs. Florence Sagnard	Senior Researcher, HDR, IFSTTAR-MLV
Thesis Co-supervisor:	Mr. Vincent Baltazart	Senior Researcher, IFSTTAR-Nantes

Abstract

The Ground Penetrating Radar technique (GPR) is now widely used as a non destructive probing and imaging tool in several civil engineering applications mainly concerning the inspection of construction materials and structures, the mapping of underground utilities and voids, the characterization of sub-structures, the foundations and soil and estimation of sub-surface volumetric moisture content. GPR belongs to a continuously innovative field due to electronic integration, high-performance computing, and advanced signal processing. The promotion of this technology relies on the development of new system configurations and data processing tools for the interpretation of sub-surface images. In this context, the work presents first the dual polarization UWB ground coupled GPR system which has been developed recently. Then, the data processing has focalized on the development of analysis tools to transform the raw images in a more user-readable image in order to improve the GPR data interpretation especially within the scope of detection of urban pipes and soil characterization. The data processing concern clutter removal using some adaptation and extension of the PCA and ICA algorithms. Afterwards, a template matching image processing technique is presented to help the detection of hyperbola within GPR raw B-scan images. The dual polarization is finally shown to bring additional information and to improve the detection of buried dielectric objects or any dielectric contrasts within the subsurface. The performance of the tested data processing and the influence of the polarization diversity are illustrated using synthetic data (3D FDTD simulations) and field data in controlled environments. Different polarization configurations and dielectric characteristics of objects have been considered. The potential for target discrimination has been quantified using statistical criteria such as ROC.

Glossary

BSS	Blind source separation
CMP	Common midpoint
ECG	Electrocardiogram scan
EIG	Eigenvalue decomposition
EM	Electromagnetic
FA	Factor analysis
FDTD	Finite Difference Time Domain
FOM	Fixed offset method
FR4	Flame Resistant 4
GPR	Ground Penetrating Radar
ICA	Independent component analysis
ICs	Independent Components
IF	Intermediate Filter
IFFT	Inverse Fast Fourier Transform
ML	Maximum Likelihood
MST	Mean (or median) subtraction technique
PCA	Principal component analysis
PCs	Principal Components
PSCNR	Peak signal to Clutter and Noise Ratio
PSCR	Peak signal to clutter ratio
PVC	Polyvinyl chloride
RCS	Radar cross section
ROC	Receiver operating characteristic
SCNR	Signal to Clutter and Noise Ratio
SCR	Signal to Clutter ratio
SFCW	Stepped-frequency continuous wave
SMA	Sub-Miniature version A
SNR	Signal to noise ratio
SVD	Singular Value Decomposition
SW	Scattering width
TE	Transverse Electric

TM	Transverse Magnetic
UWB	Ultra Wide Band
VNA	Vector Network Analyzers
WARR	Wide-angle reflection and refraction
WGN	White Gaussian Noise

Table of contents

Résumé	2
Remerciements	3
Abstract	6
Glossary	7
Introduction.....	13
Chapter 1: Background of the ground penetrating radar technology and its applications for civil engineering purposes	17
Résumé	17
I. Introduction.....	19
II. Basics of the GPR measurement technique	19
II.1. GPR technologies.....	21
II.2. Bandwidth and depth resolution	21
II.3. Exciting pulse shape	22
II.4. Antennas in GPR.....	23
II.5. The radar range equation	24
III. GPR surveys	25
III.1. Plane reflector.....	27
III.2. Target reflection (Hyperbolic signature)	28
IV. EM wave propagation in civil engineering materials	29
IV.1. Maxwell's equations	29
IV.2. Complex conductivity and permittivity.....	30
IV.3. The wave propagation equation.....	31
IV.4. Dielectric characteristics of materials	32
IV.5. Polarization mechanisms of dielectric materials	34
IV.6. Mixing models.....	35
V. Waves polarization	36
VI. Processing GPR data	37
VII. Applications of GPR surveys in civil engineering	39
VIII. Challenges in the detection and characterization of utilities	39
IX. Conclusion	41
Bibliography	42
List of figures and tables.....	48
Chapter 2: Ground-coupled GPR system and experimental test sites	49
Résumé	49

I. Introduction.....	51
II. GPR SFCW system	51
II.1. Overview.....	51
II.2. Antenna geometry and design.....	52
II.3. Parametric study.....	55
II.4. Tx and Rx Antenna configurations for GPR survey	55
II.5. Acquisition system.....	57
III. Test Sites	58
III.1. Sand boxes.....	58
III.2. Embankment near the IFSTTAR building.....	59
III.3. The urban test-site Sense-City	60
IV. Conclusion	62
Bibliography	63
List of figures and tables.....	64
Chapter 3: Evaluation of statistical-based clutter reduction techniques for the pre-processing of ground-coupled GPR images.....	65
Résumé	65
I. Introduction.....	67
II. Existing clutter reduction techniques.....	68
III. Principal Component Analysis (PCA)	77
III.1. Introduction	77
III.2. Algorithm	78
III.2.1. Matrix Decomposition	78
III.2.2. Clutter reduction using PCA.....	79
III.3. Improved clutter reduction technique using PCA.....	81
III.3.1. Problem overview	81
III.3.2. Principle and illustration for modified PCA	81
III.3.3. Application to the data.....	82
IV. Independent component Analysis (ICA).....	84
IV.1. Introduction	84
IV.2. Application strategies for ICA	84
IV.3. Algorithm	86
IV.3.1. Preprocessing.....	86
IV.3.2. The FastICA algorithm.....	87
IV.3.3. Independence estimation	88
IV.3.4. ICs selection	89
IV.4. ICA applied to GPR data.....	90
V. Performance assessment of the clutter reduction techniques	91
V.1. Introduction	91
V.2. Assessment criteria	92
V.2.1. Qualitative comparison	92
V.2.2. Signal to Clutter plus Noise Ratio (SCNR)	92

V.2.3. ROC curves.....	93
V.3. Results on the simulated data set.....	95
V.3.1. Data set.....	95
V.3.2. Results.....	97
V.4. Results on the field data set.....	108
V.4.1. Data set.....	108
V.4.2. Results.....	108
VI. Conclusion.....	114
Bibliography.....	116
List of figures and tables.....	121
Chapter 4: Hyperbola fitting and template matching for target detection within GPR Bscan images.....	125
Résumé.....	125
I. Introduction.....	127
II. Ray-path model.....	127
III. Template matching.....	129
IV. Hyperbola extraction and fitting.....	130
V. Validation on numerical results.....	131
VI. Conclusion.....	133
Bibliography.....	134
List of figures and tables.....	136
Chapter 5: Contribution of polarization diversity to target detection.....	137
Résumé.....	137
I. Introduction.....	139
II. Previous studies.....	140
III. Multi-configuration for data acquisition.....	142
IV. Analytical scattering model for cylindrical targets.....	143
IV.1. Modeling Techniques.....	143
IV.2. Hypothesis.....	144
IV.3. Parametric study.....	145
IV.4. Scattering width (SW).....	148
V. FDTD simulation results.....	149
V.1. Geometries modeled.....	149
V.2. Results.....	151
VI. Experimental results.....	160
VII. Conclusion.....	165

Bibliography	167
List of figures and tables.....	170
Conclusion and perspectives	173
Appendix	177
Appendix A: Fresnel scattering equations	178
Appendix B: Scattering from a cylindrical infinite pipe	179
I. Case of a TM^Z polarization (E in z direction).....	179
I.1. Case of a perfectly conductive cylinder	180
I.2. Case of a dielectric cylinder	180
II. Case of a TE^Z polarization (H in z direction)	182
II.1. Case of a perfectly conductive cylinder	183
II.2. Case of a dielectric cylinder	183
Appendix C: ICA algorithm.....	185

Introduction¹

I. Background and objectives

The aim of the presented study is to develop measurement methods and data processing tools for the application of ultra wide band (UWB) ([0.3;4] GHz) ground penetrating radar (GPR) to survey civil engineering structures, and more specifically to detect small urban utilities, cracks, damages and discontinuities in civil engineering structures. GPR system is a non-destructive technique used in the measurement of electromagnetic waves that has been scattered by subsurface discontinuities. The use of ultra wide band allows to obtain a trade-off between time resolution and penetration depth. Research studies aim to obtain quantitative information and data interpretation relative to the subsurface of civil engineering structures. GPR is a promising technology being commercialized and constant innovative developments are made by researchers.

The two institutes IFSTTAR and Cerema have been participating for about 20 years to the development and research on the application of GPR systems to geophysical surveys and then, to the survey of civil engineering structures, e.g., X. Dérobert [1], C. Fauchard [2], D. Leparoux [3], F. Sagnard [4], J-M. Simonin [5], F. Liu [6], C. LeBastard [7], M. Adous [8], K. Chahine [9], Among others, past studies have focused on the use of UWB to measure thin pavement thickness, the detection of cracks and pipes, dielectric characterization of civil engineering materials (e.g., Adous [8]), data processing methods for improving the time resolution of GPR (LeBastard, 2007) and their extension to dispersive materials (Chahine, 2010), etc. The most recent work deals with the water content and the water gradient estimations within concrete with specific GPR configuration (Xiaoting, 2015 [10]).

GPR performance for target detection and characterization imposes to overcome several problems such as:

- The degree of heterogeneities and the multi-layer subsurface structure: the multilayered composition of civil structures with a variety of dielectric characteristics such as soils, concrete, asphalt... and the presence of air gaps, small debris, and gravels... , results in complex GPR images with large magnitude echoes overlapping target echo (i.e.: the clutter or horizontal echoes, and discontinuity echoes). The suppression of these echoes appears as a first step before any further data processing for interpretation. In this work, algorithms have been selected to suppress horizontal echoes and have been evaluated on numerical and experimental data in chapter 3.

- The presence of humidity in outdoor ground structures due to weather conditions. The humidity affects in a significant way the effective permittivity of the soil and the attenuation of EM waves, making GPR measurements much more difficult to interpret.

- The EM field scattering from subsurface targets: the difficulty encountered here is that the scattering is mostly related to the low dielectric contrast between the buried dielectric target and the media, and to the incident EM field properties (magnitude, angle of incidence,

¹ References cited in the introduction are included in chapter 1 bibliography

phase, and polarization). A preliminary study has been made on the polarization effect as a solution in the detection of low contrasts (chapter 5). Analyses of experimental and numerical data have been made.

- In this work, we favored the evaluation of a newly developed bowtie antenna described in chapter 2. The antenna was developed by F. Sagnard before the beginning of the thesis. It has the advantage of being compact in size (size of an A4 sheet) compared to other UWB antennas. Also, using such antennas gives the benefits of flexibility (antennas relative orientation) in extracting information related to the polarization diversity.

The final step in GPR processing consists in image processing techniques for the detection of objects (chapter 4), and afterwards their classification using inversion and migration to extract information about the nature, position, depth and shape of each target.

II. Chapter content

This thesis can be divided into three main parts: the first part constitutes chapters 1 and 2. They contain definitions and small portions of work, which contribute directly or indirectly to the developed work in chapters 3 and 5. The second part represented by chapters 3 and 4, focuses on data processing, for the suppression of clutter and unwanted echoes present in the GPR images and obscuring target response, and for later the detection of hyperbolic signatures. As for the third part studied in chapter 5, it is dedicated to extracting the features of applying multi-polarization surveys on GPR cylindrical targets.

For this aim, the first chapter introduces the definition of an UWB GPR system, its operation and functionality, and the technologies required and used by such system. However, the detection of buried targets is a complex and hard process, and much pre-processing and understanding of the media properties and physical phenomenon is needed before any analysis. Thus, the presentation pursued by an explanation of the different surveys used for sweeping the sub-surface; the ground media dielectric properties, especially the materials present in civil engineering structures; EM wave propagation; medium velocity estimation; some signal pre-processing techniques, and the challenges encountered in this application. Much work is done in the field of processing GPR data for civil engineering applications in Europe and published continuously with the COST Action and the EGU community; the work concerns the characterization of subsurface dielectric properties in geophysical applications, the detection of urban utilities in civil structures, the detection of cracks in transportation infrastructures, etc.

Chapter 2 describes the bi-static UWB GPR system used system and its radiation characteristics. GPR system uses ground-coupled radar configuration and is made of two bowtie-slot antennas, developed at Ifsttar by F. Sagnard [11], connected to a Step-Frequency Continuous Wave (SFCW) generator. In addition, the evaluation test sites are described in detail in this chapter: they include two sand box, the clay/silt heterogeneous ground around the Ifsttar building, and the urban controlled test site (mini sense-city). The probed tests have similar natures to civil engineering structures and with different medium dielectric properties, compaction, water content, and degree of heterogeneities (their dimensions and space

distribution). Those characteristics influence in a significant way on GPR signatures and detection and introduce a large diversity for experimental results.

Chapter 3 defines the clutter as an unwanted signal composed of the superposition of the ground surface reflection, antennas coupling signal and reflection of the heterogeneities present in the subsurface. A review of some existing clutter reduction techniques is presented then a detailed description of two statistical clutter reduction techniques (PCA Principal Component Analysis and ICA Independent Component Analysis) is presented for the suppression of shallow and deep targets (with and without clutter overlap). Those techniques are not well compared in literature for shallow and deep objects, however they seems to give good performance and well adapted to the application under scope with no prior knowledge of the sub-surface and target signatures. The performance of each technique is compared to the conventional mean subtraction technique and evaluated on different type of targets and at different depths. The simulation environment is considered homogeneous, however the field test environment is heterogeneous.

Chapter 4 explicates the equations and the geometry of the propagation path of EM waves between the transmitter and the receiver, and then it uses the template matching algorithm developed by F. Sagnard et al. [12], and the linear least-square fitting to detect hyperbolas presented in the Bscan image for later identification according to the ray-path model. The identification allowed us to extract the buried target parameters: position, depth and radius. It is also demonstrated with a numerical example.

Chapter 5 discusses how changes in the orientation of the antennas (transmitter and receiver) could affect the amplitude, the arrival time and the form of collected signatures. The orientation of the antennas relative to each other and relative to the target (explicitly to the direction of movement) is used to define many possible configurations and each configuration of the antennas defines a particular polarization. The chapter begins with a general illustration of the work developed in the literature on polarization diversity effect on the detection of pipes and cracks, and then we study this effect for cylindrical shaped targets with small size compared to the wavelength; the study is made according to an analytical model and through experimental and simulated data. The analytical model used is based on the method of Mie, using an incident plane wave and Maxwell equations to compute the dispersion of waves refracted and reflected on an infinite cylinder. While the measurement data are performed at various sites and in correspondence with the simulation data, they were used to validate the results of the analytical study.

Chapter 1: Background of the ground penetrating radar technology and its applications for civil engineering purposes

Résumé

Ce chapitre introduit les notions nécessaires à la compréhension des différents chapitres de ce travail. Ainsi, sont présentés le principe de fonctionnement du système GPR, des notions de base sur la propagation des ondes électromagnétiques, ainsi que leur interaction avec les propriétés diélectriques des matériaux à ausculter, quelques notions de base sur le rayonnement des antennes utilisées et leurs caractéristiques de polarisation et enfin, la formation des images radar à analyser. Dans le cadre de l'application, les éléments à détecter dans l'image radar correspondent à des hyperboles de réflexions sur des cibles ponctuelles.

Le travail présenté dans ce document se focalise sur la détection de petites cibles urbaines enfouies, en exploitant un nouveau système de radar géophysique ultra large bande (ULB) couplé au sol, et qui est présenté au chapitre 2. Les besoins de l'application nécessitent de détecter des cibles peu profondes et de petites tailles par rapport à la longueur d'onde. Dans l'image radar Bscan, la signature de la cible, i.e. une hyperbole, est masquée partiellement par un signal parasite dominant, i.e. le clutter de sol. Pour améliorer la détection et l'identification des cibles, deux solutions sont explorées dans les chapitres 3 et 5. Une première solution concerne l'élimination du signal de clutter en utilisant des techniques statistiques de traitement du signal; trois techniques de traitement sont sélectionnées et comparées au chapitre 3. Au chapitre 4, la détection des hyperboles des cibles est réalisée en utilisant un algorithme de type "template matching". Enfin, le chapitre 5 propose d'exploiter la diversité de polarisation du système radar pour l'amélioration de la détection du signal cible à travers différentes simulations et les données.

Contents

Résumé	17
I. Introduction.....	19
II. Basics of the GPR measurement technique	19
II.1. GPR technologies.....	21
II.2. Bandwidth and depth resolution	21
II.3. Exciting pulse shape	22
II.4. Antennas in GPR.....	23
II.5. The radar range equation	24
III. GPR surveys	25
III.1. Plane reflector.....	27
III.2. Target reflection (Hyperbolic signature)	28
IV. EM wave propagation in civil engineering materials	29
IV.1. Maxwell's equations	29
IV.2. Complex conductivity and permittivity.....	30
IV.3. The wave propagation equation.....	31
IV.4. Dielectric characteristics of materials	32
IV.5. Polarization mechanisms of dielectric materials	34
IV.6. Mixing models.....	35
V. Waves polarization	36
VI. Processing GPR data	37
VII. Applications of GPR surveys in civil engineering	39
VIII. Challenges in the detection and characterization of utilities	39
IX. Conclusion	41
Bibliography	42
List of figures and tables.....	48

I. Introduction

The Ground Penetrating Radar (GPR) is a non destructive measurement technique which has been developed in the early 20th century. It is based on the propagation, reflection and scattering of electromagnetic waves within a medium containing dielectric discontinuities. The ultra wide frequency band (UWB) of the excitation signal, that has usually the shape of a pulse, positions the GPR as a high time resolution imaging technique of the near subsurface of soils or of man-made structures. The frequency range of the radio waves generally extends from 100 MHz to 4 GHz. The operating principle is simple, but as the subsurface is usually made of several components randomly distributed and of different sizes, the image obtained is hardly directly interpreted by the user without some prior training. Among the main parameters involved in the GPR imaging techniques, the frequency band determines the physical phenomena that sustain the wave propagation within the structure. There exist two fundamental types of characterization associated with GPR imaging: the soil structure, and the buried objects. The range of applications of the GPR technique is very wide: archaeological, geological, environmental, civil engineering, military (mines)...

In order to interpret GPR images of civil engineering structures, that concern the main application of this thesis, we propose in this chapter to detail the electromagnetic physical principles, the operational conditions, the dielectric characteristics of civil engineering materials, and the main signal processing techniques that can be used to extract quantitative information from GPR images.

II. Basics of the GPR measurement technique

GPR technology is a special kind of radar devoted to the detection, and the location of buried objects and structures within subsurface. Data interpretation is not straightforward and requires the supervising of skilled operators.

The primary components of a GPR system are illustrated in Figure 1.1 (a). A GPR device is basically composed of shielded transmitting (Tx) and receiving (Rx) antennas (bistatic system) which are linked to a control unit including a source generator, a data acquisition and a display unit.

GPR antennas are designed for either “air-launched” or “ground-coupled” operation. The “air-launched” radar is designed to be suspended above the probed subsurface with an air gap (~30-50 cm), thus allowing to collect measurements data on large distances at high speed, under the far field assumption. The ground-coupled radar is designed to be in direct contact with the material surface with no air gap. The air-launched radar suffers from a strong amplitude reflection at the medium surface which may reduce the SNR of the deep echoes. For the ground-launched radar, the small air-gap allows a better antenna impedance matching with the probed medium that allows a better power penetration and thus a deeper sounding. As a counterpart, the data interpretation is more complex owing to EM wave interaction at near-field and to likely signals overlapping. Both radars operate in a wide range of central frequencies from 100 MHz to 4 GHz. The central frequency should be matched to the application, and first of all, to the expected depth of the target considering the attenuation

characteristics of the soil. The “ground-coupled” GPR has been selected in this work to obtain lower surface reflection, in the detection of utilities at several depths.

The linear displacement of the radar system allows to collect vertical signal traces (Ascans) at sampled distances as a function of time or frequency, thus jointly producing a Bscan image (or radargram), as shown on Figure 1.1 (b). Thus, GPR insures the imaging of the subsurface without intrusion. A synthetic Bscan issued from 3D FDTD simulations (using the commercial software EMPIRE XPU) is illustrated in Figure 1.1 (b) in the case of a metallic cylindrical pipe buried in a soil with a real permittivity of 3.5 (conductivity 0.01S.m^{-1}) at a depth of 160 mm using a GPR system made of two bowtie slot antennas in the end fire configuration. The excitation signal is the first derivative of the Gaussian function with duration of 0.5 ns, and a spectrum centered at 1 GHz. In the Bscan, three main signal components can be distinguished: the direct air-wave (at 2.5 ns) with a weak amplitude, the ground wave and the reflection at the interface visualized as a horizontal band with a high amplitude (at 3.36 ns), and the hyperbola signature due to the wave scattering over the pipe along the scanning direction (apex at 4.58 ns). By considering a time zero at 1.1 ns calculated according to section VI, the hyperbola arrival time is calculated to 3.4 ns and the surface reflection time is 2.1 ns. These times can be visualized in the Bscan such as: $2.1+1.1=3.2\text{ ns} \sim 3.36\text{ ns}$ and $3.4+1.1=4.5\text{ ns} \sim 4.58\text{ ns}$.

In general, the horizontal band corresponds to wave phenomena at the air-soil interface, (reflection, scattering, and antenna coupling) that is called clutter because it does not contain information about the subsurface; the clutter has to be eliminated to retrieve the target hyperbolic signatures (chapter 2). Hyperbolic signatures are fitted using the least-square criterion; they serve in the extraction of targets information, by comparing observed arrival times with the calculated times and by extracting hyperbolic parameters (see chapter 4).

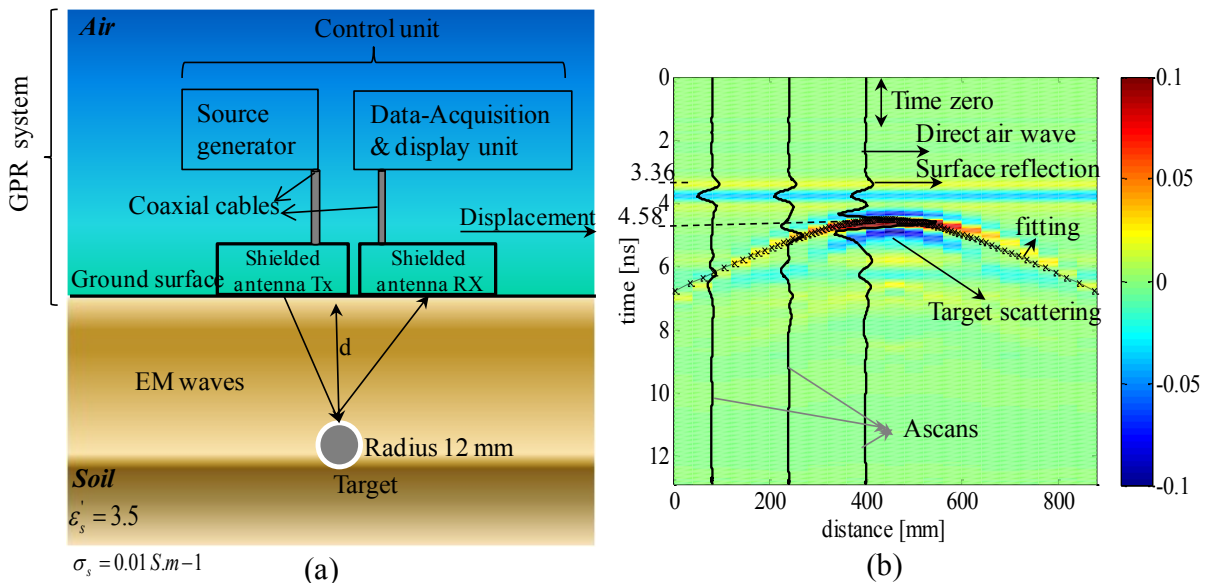


Figure 1.1: GPR principles: a) Scheme of a ground-coupled GPR system on a soil including a buried metallic pipe at a 160 mm depth; b) Synthetic Bscan (FDTD simulations) corresponds to the buried metallic pipe.

II.1. GPR technologies

The two major technologies associated with GPR systems are the short-pulse radar and the stepped-frequency continuous wave (SFCW) radar. Commercial radars are mostly impulse radars and provide data in the time domain. SFCW radars are tailored to provide complex data in the frequency domain, some companies affords the users a specific tool to visualize the SFCW in the time data domain as for the short-pulse radars.

The impulse technique was first manufactured in the mid-70s and keeps to exist in mainly commercial GPR systems because the hardware technology required is simpler and the electronic components were lower-cost. The impulse technique allows a real time visualization of the data in the time domain. The central frequency and the bandwidth of commercial devices have continuously increased in the past, enabling better resolution with depth. However, the dynamic range of the receiver (oscilloscope) rarely exceeds 70 dB. As a comparison, SFCW radar needs a frequency synthesizer with a high stability to step through a range of frequencies equally spaced by an interval Δf . At each frequency, the amplitude and phase of the received signal are compared with the transmitted signal. The inverse Fourier transform enables the visualization of data in the time domain. Nowadays, this technology is more easily affordable and powerful and fast digital signal processing technologies have been introduced.

In this work, the SFCW radar has been preferred because of its higher range resolution (larger bandwidth compared to short-pulse radar), its better sensitivity (narrow instantaneous bandwidth), and the possibility to obtain a higher power per frequency (S/N higher). The novel portable Vector Network Analyzers (VNA) can have a dynamic range reaching 90 dB (for the portable VNA Anritsu MS2026B). The main disadvantage of the SFCW GPR is the acquisition time, because this radar has to step through a large number of frequencies for each trace acquisition. Afterwards, an IFFT (Inverse Fast Fourier Transform) has to be performed to transform the data in the time domain.

II.2. Bandwidth and depth resolution

As, the GPR system used mainly in this work is a SFCW radar made of UWB (Ultra Wide Band) slot bowtie antennas, it appears necessary to define the term UWB in this context. The term UWB is generally used in wireless communications and air radar systems, and there is no specific definition for GPR systems. It is commonly accepted that the following fractional bandwidth f_{BW} is larger than 120% to define UWB system:

$$f_{BW} = \frac{2(f_{\max} - f_{\min})}{f_{\max} + f_{\min}} = \frac{B}{f_c} \text{ where } f_c = \frac{f_{\max} + f_{\min}}{2} \quad (1-1)$$

Where f_{\min} and f_{\max} are the low and high cut frequencies at -10 dB.

Considering the operating frequency band [0.46; 4] GHz of the bowtie slot antenna used the fractional bandwidth is estimated to $f_{BW} = 158\%$, a significative value higher than the one recommended in UWB wireless communications (bandwidth > 20% of the center frequency).

The bandwidth of the antennas plays a critical role in the GPR performance because it influences the vertical depth resolution. The choice of the frequency range is usually a trade-off between the resolution capability (implying large bandwidth and high frequencies) and the penetration of EM waves into the soil (implying low frequencies). The depth (vertical) resolution ΔV [13] is closely related to the radar operational bandwidth BW such as:

$$\Delta V = \frac{v}{2 \times BW} \quad (1-2)$$

Where v is the velocity of the electromagnetic signal in the medium and c the velocity in the air ($c = 3.10^8 \text{ m.s}^{-1}$). ϵ is defined as the relative complex permittivity and μ the relative complex permeability ($\mu = \mu_0 = 1$). Assuming that ϵ' is the real relative permittivity of the soil and that the conductivity $\sigma (\text{S.m}^{-1})$ is negligible, the expression of the velocity in the medium can be simplified to:

$$v = \frac{c}{\sqrt{\epsilon \mu}} \approx \frac{c}{\sqrt{\epsilon'}} \quad (1-3)$$

Considering the operating frequency range of the bowtie antennas, i.e. [0.46, 4] GHz and a conventional dry soil characterized by $\epsilon' = 5$, the vertical resolution is estimated to $\Delta V = 1.89 \text{ cm}$.

II.3. Exciting pulse shape

The basic pulse signal used is the Gaussian monocycle that is the first derivative of the Gaussian function. The advantage of this shape is that it can be generated by electronic equipments and it can be described analytically in both time and frequency domains. Moreover, there exist analytical relations between the frequency peak and the signal bandwidth. This signal has been used as the excitation pulse of the transmitting antenna in the FDTD simulations and also in the data processing of the SFCW measurements. The pulse shows two amplitude oscillations and its deformation or sign inversion can be easily observed in radargrams. The Gaussian pulse $S(t)$ is given by [14] [15]:

$$S(t) = -a^2 A t \exp(-a^2 t^2) \quad (1-4)$$

Where A is the pulse amplitude, and a the shape factor that determines the slope of the Gaussian pulse. In this work, we have considered the constant shape factor $\tau = \frac{1}{\sqrt{2}a}$.

The spectral response of the Gaussian monocycle is given by [16]:

$$S(\omega) = \frac{j \omega A}{a \sqrt{2}} \exp\left(-\frac{\omega^2}{4a^2}\right) \quad (1-5)$$

Where $j^2 = -1$ and $\omega = 2\pi f$ is the frequency pulsation. The pulse spectrum is characterized by its peak frequency and its bandwidth at -3dB such as:

$$\begin{cases} f_0 = \frac{a \sqrt{2}}{2 \pi} \\ \Delta f = 1.155 f_0 = \frac{1.155}{T_0} \end{cases} \quad (1-6)$$

Where T_0 is defined as the pulse duration. It must be noticed that the -3dB bandwidth is roughly equal to 115% of the pulse center frequency f_0 .

As an illustration, two monocycles associated with different central (peak) frequencies f_0 at 500 MHz and 1 GHz have been plotted in Figure 1.2a and b in the temporal and frequency domains, The parameters of these pulses are the following: if $f_0 = 500 \text{ MHz}$: $T_0 = 2 \text{ ns}$; $\tau = 0.32 \text{ ns}$, and if $f_0 = 1 \text{ GHz}$: $T_0 = 1 \text{ ns}$; $\tau = 0.16 \text{ ns}$.

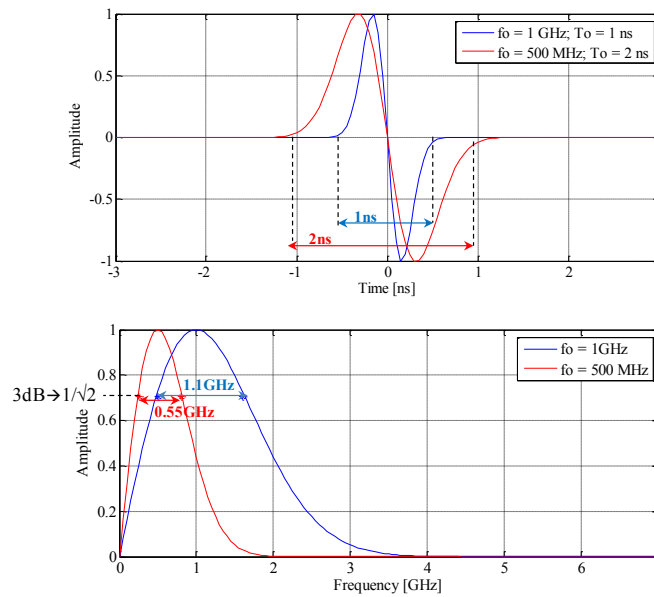


Figure 1.2: GPR wavelet defined as the first derivative of Gaussian pulse in (Top) time domain, and in (Bottom), frequency domain.

II.4. Antennas in GPR

The antennas are designed to radiate and receive an electromagnetic signal. Both antennas are usually identical. In the case of a time domain radar, the emitted pulse is supposed to radiate a reasonable copy of the exciting pulse in section II.3. The antenna and the soil govern the shape of the exciting pulse in both the time and the frequency domains. The principal antenna types used in GPR are the loaded and the folded dipoles, horns, bowtie antennas, logarithmic spiral antennas, Vivaldi antennas, slot antennas.... In general, antennas transmit linear polarized signals such as encountered in most commercial GPR systems.

The antenna geometry depends on the frequency, the physical size, the portability and the application. The impedance and the antenna radiation pattern (i.e. current distribution) become strongly influenced by the dielectric characteristics of the ground as the antenna gets closer to the soil surface i.e. in the near-field zone. The antenna footprint, which indicates the shape and the size of the spot illuminated by the antenna on a plane, has a large influence on the imaging capability of the radar; sensitivity and target localization can be then improved when the size of the antenna footprint is close to those of the targets [17] [18]. The footprint

dimensions (relative to the medium plane Oxy) for a dipole antenna are given by Annan's equation such as [19] (Figure 1.3):

$$\begin{cases} y = \frac{\lambda}{4} + \frac{x}{\sqrt{\epsilon' - 1}} \\ z = \frac{y}{2} \end{cases} \quad (1-7)$$

Where $\lambda = vT = v/f$ is the electromagnetic wavelength.

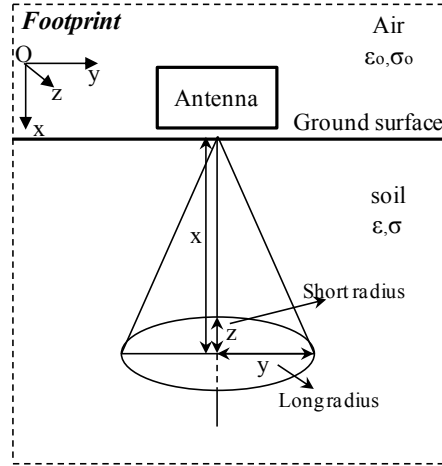


Figure 1.3: Footprint of an elliptical illuminated surface as function of the depth x .

When the footprint is too large it gives rise to a surface clutter as the spot illuminated on the ground is larger than what is really needed (larger footprint for air-launched radars). Thus, an optimal footprint is important to improve target localization. Fortunately, for GPR applications the antenna radiation pattern is preferentially directed into a medium with higher dielectric permittivity ϵ' , thus leading to a narrower beam lobe with the energy focusing in the direction of interest.

II.5. The radar range equation

The magnitude of the signal on the reception antenna (Rx) depends on several parameters. All these parameters are considered in the radar range equation which expresses the power received at the receiving antenna P_R as a function of the power supplied at the transmitting antenna P_T such as [20] (see figure 1.4):

$$P_R = P_T \frac{G_T(\theta_T, \phi_T) A_{eR}(\theta_R, \phi_R)}{(4\pi r_1 r_2)^2} \zeta \quad (1-8)$$

Where $G_T(\theta_T, \phi_T)$ is the transmitting antenna gain, $A_{eR}(\theta_R, \phi_R)$ is the receiving effective surface, r_1 is the distance from transmitter to the reflecting (point) target, r_2 is the distance from the reflecting (point) target to the receiver and ζ is the scattering radar cross section (RCS) of the target. The effective surface depends on the square of the wavelength:

$$A_{eR}(\theta, \phi) = \frac{\lambda^2}{4\pi} G(\theta, \phi) = \frac{\lambda^2}{4\pi} \eta D(\theta, \phi) \quad (1-9)$$

Where $G(\theta, \phi)$ is the antenna gain, $D(\theta, \phi)$ the antenna directivity and η the aperture efficiency.

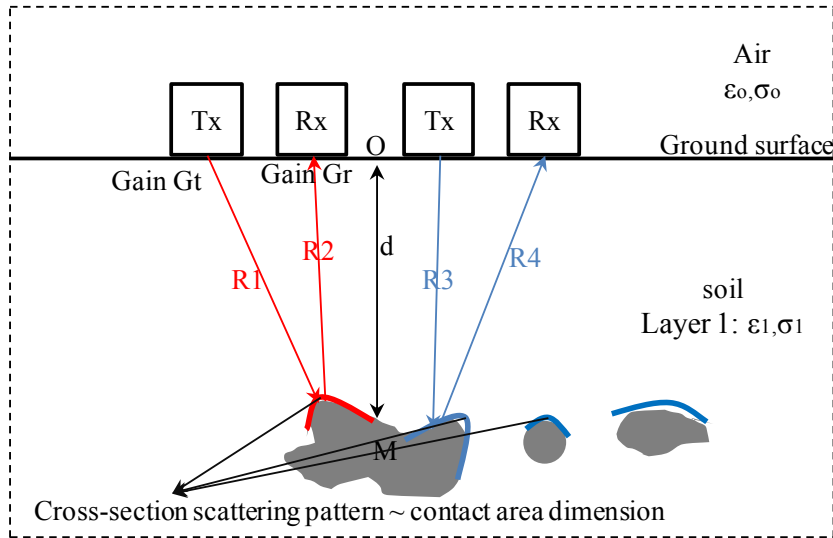


Figure 1.4: Target geometry for the radar range problem in the bi-static configuration.

III. GPR surveys

The ground-coupled GPR is usually moved at a constant speed along the y -axis in a straight line, i.e. the scanning direction as shown on Figure 1.3. Commercial GPR systems use a coded wheel to record time data at regular distance intervals. At each distance sample, a single waveform $s(z_i, y_i, t)$ called an **Ascan** (or a vertical trace) is recorded (see Figure 1.1 (b)). The vertical variable is the time which is related to the depth by the wave velocity along the propagation path. The gather of a set of Ascans forms a 2D amplitude image $b(z_i, y, t)$, called a **Bscan**, that represents a vertical slice in the ground. The time axis or the related depth axis is usually pointed downwards. Because of the large beam radiating patterns in transmission and reception, a dielectric discontinuity of small extent in the ground is viewed as a hyperbola in the image. In the presence of different discontinuities or objects, hyperbolic signatures bring information relative to their dielectric contrast with the ground, their polarization/depolarization relative to their orientation relative to the incident electric field. Afterwards, when moving the GPR system over a regular grid in the z - y plane, a 3D data set $c(z, y, t)$ can be recorded that is called a **Cscan**.

The imaging of the subsurface by the GPR technique relies on three major survey types:

- The first type is called the common midpoint (**CMP**) survey, in which both the transmitter and receiver antennas are moved apart from each other at a constant spatial increment (see Figure 1.5 (a)).

- The second survey type is the wide-angle reflection and refraction (**WARR**) where the transmitting antenna is kept at a fixed location while the receiving antenna is moved away from the transmitter at a constant spatial increment called the antenna offset (see Figure 1.5 (b)). The main difference between both surveys is that in the WARR survey the reflection point moves along the reflector. This is why WARR measurements are conducted over either horizontally reflectors, or slightly sloping reflectors or homogeneous ground material (along the scanning direction).

-The third survey type is conducted by keeping a fixed transmitter–receiver antenna offset and moving both antennas at a constant spatial increment over the survey area that is called profiling (see Figure 1.5 (c)). This survey is also called the fixed offset method (**FOM**).

The CMP and WARR surveys are normally used to estimate the subsurface velocity structure in a multilayered ground by analyzing both the shape and the slope of time-offset curves. This analysis supposes to define a time zero that corresponds to the direct air wave associated with the coupling between both antennas. In the ground, the inverse slope of the time-offset relationship gives the average ground wave velocity between the minimum and maximum antenna offsets.

Since air and ground wave travel directly between the transmitting and the receiving antenna, there exists a linear relationship between the travel time t of each wave and the antennas offset with the constant of proportionality $1/v$ such as $t = A/v$. Where A is a constant of proportionality. $v = c = 3.10^8 \text{ m.s}^{-1}$ for an air wave, and $v = c/\sqrt{\epsilon'}$ ($\epsilon'' \ll \epsilon'$) for the ground wave. The air wave arrival time is usually used as a reference to define the time zero (see time zero correction in section VI).

In the far-field zone, the paths of EM waves at high frequencies can be modeled by rays. This approach allows to obtain first estimates of real permittivities from the arrival times. In GPR, we distinguished two types of reflectors in a soil: a plane layer and a target reflector.

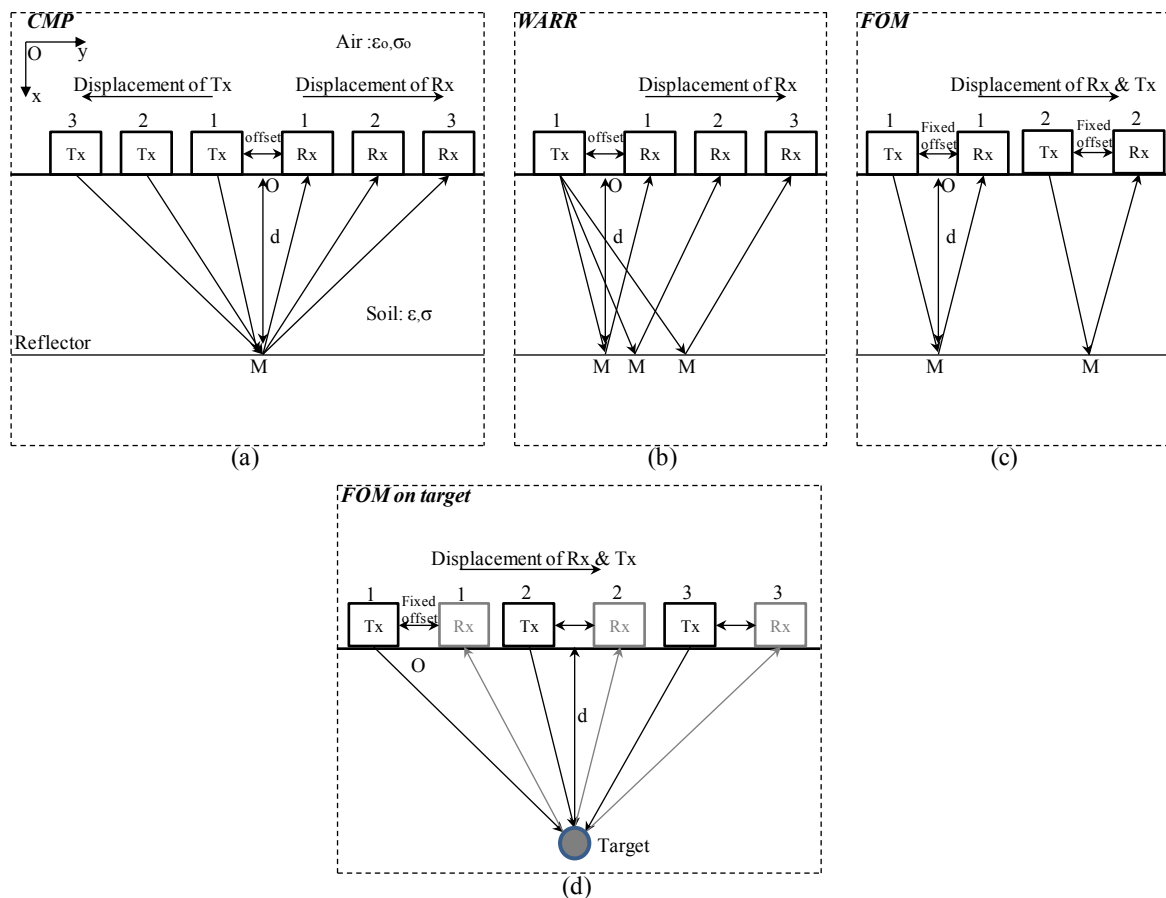


Figure 1.5: GPR survey types: a) CMP survey, b) WARR survey, c) FOM survey on horizontal reflector d) FOM survey on target.

III.1. Plane reflector

Plane reflectors are encountered in a multilayer structure with dielectric contrast between layers such as presented in Figure 1.6(a). The several wave curves are produced generally in a WARR survey when the antenna offset is increased such as reported in Figure 1.6 (b). The different layers can be observed on the experimental radargram of Figure 1.6 (c) in the case of a sand box filled with 48 cm depth of non compacted sand. The GPR system is a SFCW radar composed of a pair of bowtie slot antennas, and the spectrum of the first derivative of a Gaussian pulse (centered at 1 GHz) has been multiplied to the frequency data to obtain the radargram. We observe several multi-reflections.

The antenna lateral dimension (SR) with the small offset appears non-negligible compared to the depth d . The latter dimensions are given by $Y_c = \frac{offset+SR}{2}$ for later use in the calculation.

The Dix's equation [21] takes account of the Euclidean distance $d^2 + Y^2 = R^2$ and allows to express the relationship between the arrival time t , the reflector depth d and the velocity v (see Figure 1.6 (a)) such as:

$$\frac{t^2}{4d^2} - \frac{Y^2}{d^2} = 1 \quad (1-10)$$

The latter equation allows to analyze the radargram displayed of Figure 1.6(c) and particularly to estimate the velocity in the medium (sand).

In the case of a planar multilayered medium, the velocity within each layer can be calculated from the root mean square velocity (v_{rms}) using the velocity/time spectrum analysis [22] [23]. The mean square velocity estimated in layer n is given by:

$$v_{RMSn} = \sqrt{\frac{\sum_{i=1}^n v_i^2 \Delta t_i}{t_n}} \quad (1-11)$$

v_i is the instantaneous velocity at the i^{th} layer, t_n is the total cumulative propagation time and Δt_i is the propagation time within the i^{th} layer.

The instantaneous velocity v_n is then calculated in a recursive-iterative way according to the following equation:

$$v_n = \sqrt{\frac{v_{rms(n)}^2 t_n - v_{rms(n-1)}^2 t_{n-1}}{t_n - t_{n-1}}} \quad (1-12)$$

In the case of a single layer (see Figure 1.6 (a)), the time/velocity spectrum gives the results of Figure 1.6 (d)), where the velocity energy peaks can be visualized at each time interval. The analysis of those hyperbolas to extract velocity at each layer is a very hard task, because of the overlapping between echoes and because of the complexity of multi-reflections within a multilayered medium.

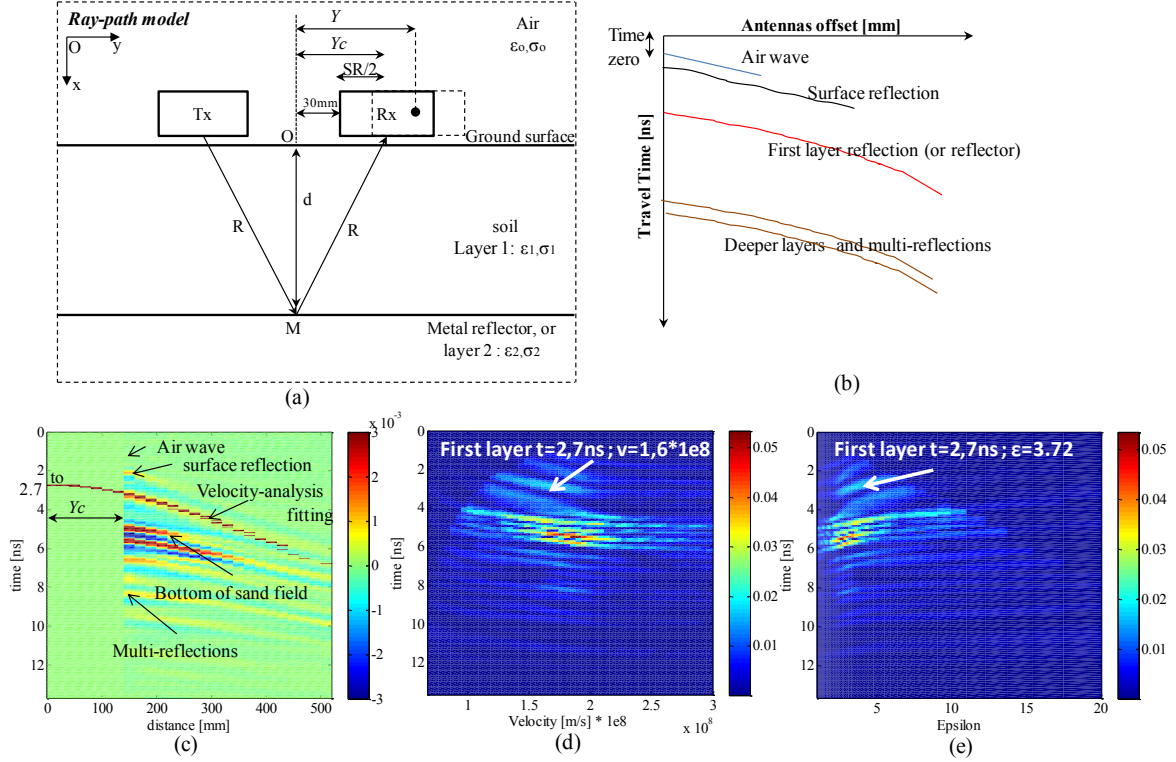


Figure 1.6: a) Ray-path model for a horizontal reflector in the WARR survey, b) Samples of waves curves obtained from a WARR/CMP survey, c) Experimental Bscan in the broadside configuration on a 48 cm thick sandy ground with d) Computed time-velocity spectrum and e) Computed time-epsilon spectrum.

III.2. Target reflection (Hyperbolic signature)

This section recalls the simplified modeling of the EM scattering by a canonical target which is buried in a soil at depth d . As a canonical target, we consider an infinite cylinder, with its axis along the z direction according to Figure 1.3. The resulting Bscan image using the FOM survey shows a hyperbolic signature.

An analytical model based on the ray-tracing hypothesis [24] allows to follow the wave path between the transmitter and the receiver. Using the Pythagorean theorem, the ray path shows a hyperbola shape (y_i, t_i) where the wave arrival time t_i is linked to the linear displacement y_i of the radar system (see figure 1.7 (a)). Considering the offset between the antennas and their lateral dimension, namely the parameter Yc defined in section III.1, the generalized hyperbola equation depends on five parameters (SR, y_0, d, R, v) such as:

$$\begin{cases} y_T = y_i - Yc \\ y_R = y_i + Yc \end{cases} \quad \text{and} \quad \begin{cases} L_{Tx2Target} = [(y_T - y_0)^2 + (d + R)^2]^{0.5} - R \\ L_{Rx2Target} = [(y_R - y_0)^2 + (d + R)^2]^{0.5} - R \end{cases} \quad (1-13)$$

$$t_i = (L_{Tx2Target} + L_{Rx2Target})/v \quad (1-14)$$

The top of the hyperbola, namely the apex, corresponds to the shortest distance and time delay between the target and the radar system (when the target is below the midpoint between both antennas). The apex time is calculated using the above equation when $L_{Tx2Target} = L_{Rx2Target}$. It must be underlined that in the ray path modeling, the reference time is taken where waves are emitted at the air-sol interface, thus a time zero correction has to be applied

in experimental and synthetic Bscans. This modeling will be used for hyperbola fitting using the least square criterion.

Figure 1.7 (b) shows the modeled hyperbola signatures of a metal cylinder probed with a bowtie slot antenna for different $Yc = (offset + SR)/2$ on the soil with relative permittivities 4 and 9. For this antenna, SR equals to 422 mm in the endfire configuration and to 291 mm in the broadside configuration. Generally, we observe that the slope of the hyperbola is higher when waves propagate in a lower velocity soil, i.e., higher real permittivity. And that larger distance SR implies delayed apex arrival time and flatter hyperbolas signatures.

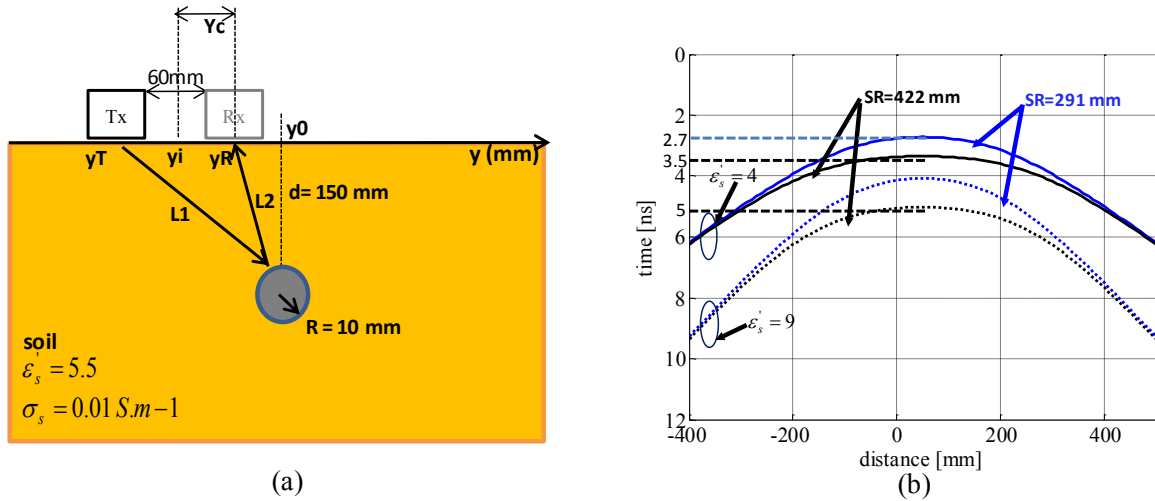


Figure 1.7: (a) Ray-tracing Pythagorean model associated with the (b) hyperbola signatures generated by the radar displacement.

IV. EM wave propagation in civil engineering materials

IV.1. Maxwell's equations

The electromagnetic signal detected by the receiving antenna is the result of propagation, reflection, diffraction and scattering phenomena that are governed by Maxwell's equations. A good understanding of the physics of high-frequency electromagnetic wave propagation and particularly in a lossy dielectric material is necessary. Civil engineering materials and soils can be considered as absorbing and dispersive (lossy) dielectric media, and they are generally non magnetic (permeability $\mu = \mu_0$). Maxwell's equations describe the wave propagation in such medium such as:

$$\begin{aligned} \text{rot } \vec{E} &= -\frac{\partial \vec{B}}{\partial t} \\ \text{rot } \vec{H} &= \vec{J} + \frac{\partial \vec{D}}{\partial t} \end{aligned} \quad (1-15)$$

Where E is the electric field strength (V/m), D the electric flux density, J the electric current density (A/m^2), B the magnetic flux density (Wb/m^2), and H the magnetic field strength (A/m).

When an electromagnetic wave propagates through a medium, the electric field causes electric charges to move. There exist conduction and displacement currents. The conduction currents are associated with the moving of free charges (i.e. electrons) in the medium that induces heat when collision occurs with stationary molecules. The displacement currents (i.e. polarization) occur when a charge can only move along a constrained distance.

In the frequency domain, both equations can be rewritten such as:

$$\begin{aligned} \vec{\nabla} \times \vec{E} &= -j \omega \mu \vec{H} \\ \vec{\nabla} \times \vec{H} &= (\sigma + j\omega\epsilon) \vec{E} \end{aligned} \quad (1-16)$$

Where σ and ϵ are associated with the electric conductivity and the dielectric permittivity. They are in general complex and frequency dependent parameters.

IV.2. Complex conductivity and permittivity

$\sigma = \sigma' - j\sigma''$: The complex conductivity includes an in-phase (real) component and an out-of-phase (imaginary) component. The conductivity describes generally the ability of a medium to conduct the electric current. The imaginary part is a measure of the polarization due to the surface density and the storage of electrical charge; it is usually negligible at radar frequencies and in dielectric grounds. The real part is a measure of how strongly a material supports the flow of an electrical current: it is considered as a frequency independent constant and can be divided into two parts, surface conductivity and fluid conductivity [25].

$\epsilon = \epsilon' - j\epsilon''$: The complex (relative) permittivity contains an in-phase (real) and an out-of-phase component. The real part of the permittivity describes the energy transfer by the current displacement and is the measure of the ability of the medium to be polarized under the incident field. At high frequency, the dipoles cannot follow the fast oscillation of the electric field, and the polarization will be out of phase, that causes a relaxation phenomenon. The imaginary part is directly related to the dispersion and losses of electric energy within the material due to polarization phenomenon and cannot be generally neglected at radar frequencies. It is directly proportional to the conductivity ($\epsilon'' \sim \frac{\sigma}{\omega}$) and may be negligible for lossless media, i.e. loss angle δ and conductivity σ are zero. In practice, a few dielectric media with low conductivity or low-losses, like air, sand and dry concrete, are considered as lossless materials at GPR frequency bandwidths. By contrast, the high conductivity of clay, wet concrete and salt water contribute to enhance the imaginary part of the permittivity and, and thus, to the attenuation of EM waves.

The complex effective permittivity expresses the total loss and energy storage effects within the material such as follows [26]:

$$\epsilon_e = \left(\epsilon' + \frac{\sigma''}{\omega} \right) - j \left(\epsilon'' + \frac{\sigma'}{\omega} \right) \quad (1-17)$$

The ratio of the imaginary part onto the real part of the complex permittivity is defined by the “loss tangent” as:

$$\tan \delta = \frac{\varepsilon''}{\varepsilon'} \approx \frac{\sigma'}{\omega \varepsilon'} \quad (1-18)$$

The influence of the imaginary part of the conductivity can be usually neglected with respect to the influence of the real part of the permittivity. Thus, the conductivity of the medium is reduced to the conductivity in the static case (DC):

$$\varepsilon' \gg \frac{\sigma''}{\omega} \quad (1-19)$$

The conductivity and the permittivity write now as follows:

$$\begin{cases} \varepsilon = \varepsilon' \\ \sigma = \sigma_{DC} + \omega \varepsilon'' \end{cases} \quad (1-20)$$

Earth materials are considered to be low-loss dielectric if the moisture content is not too high, thus having a small loss tangent such as:

$$(\tan \delta)^2 \ll 1 \quad (1-21)$$

IV.3. The wave propagation equation

The general solution of a harmonic plane wave that propagates in the x direction is:

$$\vec{E} = E_0 \exp(-jkx) \quad (1-22)$$

The complex wavenumber k of a plane wave propagating in the x direction can be separated into real and imaginary parts such as:

$$k = \beta - j\alpha \quad (1-23)$$

Thus, the plane wave can be written as:

$$\vec{E} = E_0 \exp(-\alpha x) \exp(-j\beta x) \quad (1-24)$$

The real part α (Np/m) contributes to the attenuation of the wave, and the imaginary part β (rad/m) is the phase shift (time delay). They are expressed in [26] respectively such as:

$$\alpha = \omega \left[\frac{\varepsilon\mu}{2} \left[\sqrt{1 + \left(\frac{\sigma}{\omega\varepsilon}\right)^2} - 1 \right] \right]^{\frac{1}{2}} \quad (1-25)$$

$$\beta = \omega \left[\frac{\varepsilon\mu}{2} \left[\sqrt{1 + \left(\frac{\sigma}{\omega\varepsilon}\right)^2} + 1 \right] \right]^{\frac{1}{2}} \approx \omega\sqrt{\varepsilon\mu} \text{ when } \sigma \ll \omega\varepsilon \quad (1-26)$$

The attenuation depends on the angular frequency, the conductivity and the permittivity. The attenuation α (Np/m) can be expressed in dB/m using the relation $\alpha' = 8.686 \alpha$ [27]. In Figure 1.8, the attenuation for several permittivities in an infinite medium is expressed as function of the depth at the frequency 1GHz.

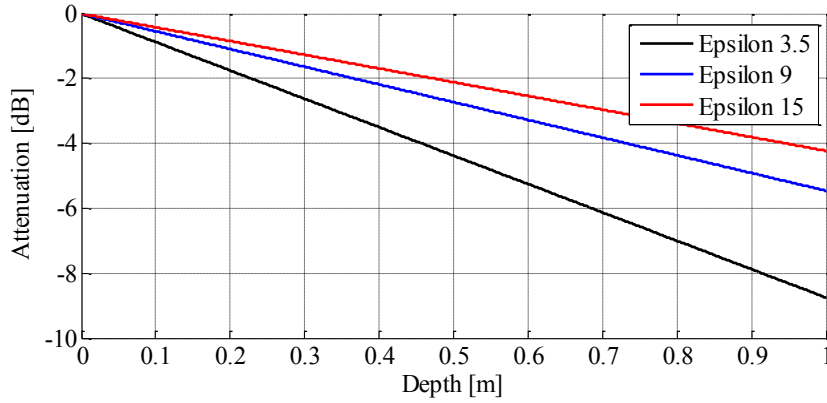


Figure 1.8: Variations of the attenuation $20 \log_{10}(\exp(-\alpha x))$ with regards to the depth within three different media with $\epsilon = 3.5; 9; \text{ and } 15; \sigma = 0.01 \text{ S/m}$ and $f=1 \text{ GHz}$.

IV.4. Dielectric characteristics of materials

Table 1.1 gives the dielectric permittivity and conductivity values for the different materials encountered in civil engineering structures [28]. They may have large range of variations within the GPR frequency bandwidth, mainly because of the presence of moisture. Asphalts [29] and the geographical origin of some constituents (granite, gravel) influence the dielectric permittivity values within a given frequency range; therefore it is impossible to have precise values for the dielectric parameters. Consequently, for each measurement site, the dielectric characteristics of the subsurface have to be estimated and compared to the tables in the literature before applying any signal processing algorithm. The values in table 1.1 have been collected from different references and help us to find a prospect for the range of material permittivities. Curtis, e.g., [27], has provided a lot of dielectric data on natural soils over a large frequency range.

It must be underlined that the medium where waves propagate acts as a low pass filter in such a way that it shifts the spectrum to lower frequencies and thus, modifies the shape of the transmitted radar impulse as a function of the medium's electromagnetic properties.

The volumetric water content plays a significant role in varying the dielectric permittivity of the soil made of several components (aggregates, voids, bound and free water). The presence of moisture in a soil increase its effective dielectric permittivity, because water shows a higher real permittivity (~ 80 at 20°C) than the permittivity of common minerals (from 3 to 7) that composes the soil. Hence, waves propagating through wet soils have a higher attenuation and dispersion (less depth penetration especially at high frequencies) and a higher dielectric permittivity (a decrease in wave's velocity) that induces a delayed time response.

The loss mechanism in a soil is highly dependent on water content: above frequency 0.5 GHz, the energy absorbed by the water present in soil pores rises with the frequency, and at 14.6 GHz (10°C), a maximum of absorption is reached [30]. Water is made of dipole molecules that polarize when excited by a high frequency electric field. Additional complexities are caused by bound water and temperature effects. Thus, in a soil, the effective complex permittivity is usually introduced by a frequency dependent model (Cole-Cole and Debye models).

Material type	Real part of the dielectric relative permittivity		Real part of the electric conductivity (S/m) at ~20°C	
	Value and	Frequency and reference	Value	reference
Air	~1	~	$8 \cdot 10^{-15}$	[31]
Sand/wet sand	3-6/10-30	100MHz [32]	$10^{-4} \rightarrow 10^{-1}$	[32], [27]
Clay/wet clay	2-6/15 \rightarrow 40	100MHz [33]	$2 \cdot 10^{-3} \rightarrow 2$	[17], [27]
Silt/wet silt	5-8/15 \rightarrow 30	100MHz [33]	$10^{-3} \rightarrow 10^{-1}$	[34]
Gravel	4 \rightarrow 7	0.4-1GHz [35]	$10^{-4} \rightarrow 10^{-2}$	[17]
Cement	4 \rightarrow 5	0.4-1GHz [35]	$10^{-4} \rightarrow 10^{-1}$	[17]
Concrete	8 \rightarrow 10	0.4-1GHz [35]	$10^{-3} \rightarrow 10^{-2}$	[32]
Asphalt	4 \rightarrow 8	0.4-1GHz [35]	$10^{-2} \rightarrow 10^{-1}$	[17]
Granite	5 \rightarrow 15	100MHz [32]	$10^{-5} \rightarrow 10^{-3}$	[32]
Teflon	1.8	10GHz [36]	$10^{-17} \rightarrow 10^{-15}$	[37]
Water	80	100MHz [33]	0.01 (drinkable water) \rightarrow 4.8 (sea water)	[38]
Wood	1.8 \rightarrow 26	2.45GHz [39]	10^{-14}	[40]
PVC	4-5	10MHz [41]	10^{-14}	[41]
Graphite (carbon)	5 \rightarrow 12	1MHz [42]	$2 \cdot 10^5$	[42]

Table 1.1: Dielectric characteristics of main materials encountered in civil engineering structures (ϵ' and σ).

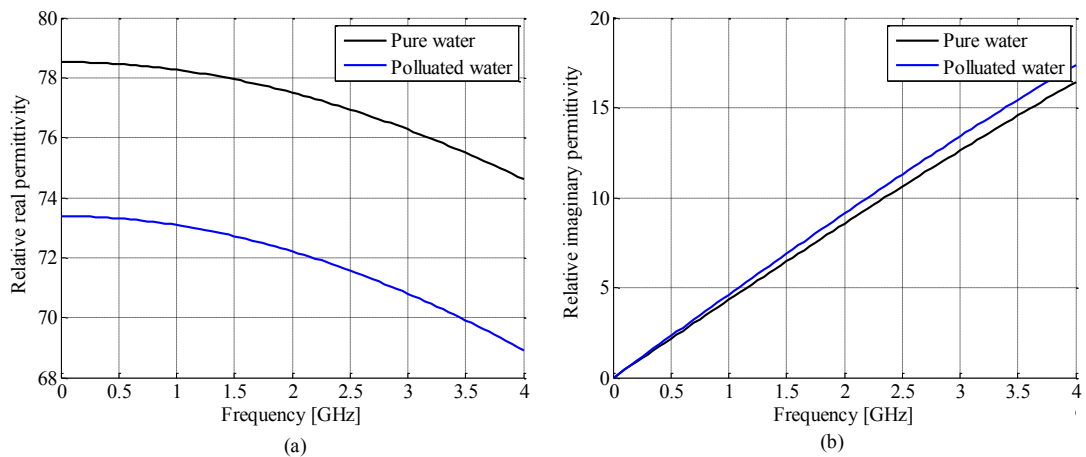


Figure 1.9: Relative complex permittivity of water according to the Debye's model, a) Real part (related to energy transfer) and b) Imaginary part (related to attenuation).

As an illustration, the frequency variations of the relative real and imaginary permittivities of a pure and polluted water have been plotted in Figure 1.9, using the Debye model with the following parameters: static permittivities [78.52; 73.38], high frequency

permittivities [5.43; 1.14] and relaxation times [9.45; 10.21] for pure and polluted water respectively (different parameters can be found in [30]). Thus, the behavior of waves in humid soils is very dependent on the wave frequency. Soil conductivity is also quite affected by water absorption that is dependent on the temperature and the frequency [43] [44].

IV.5. Polarization mechanisms of dielectric materials

The frequency dependence of the dielectric response of materials is tightly linked to the polarization mechanisms under the excitation of an electromagnetic wave. This polarization involves four basic mechanisms [45]:

The electronic or atomic polarization:

This polarization is due to changes in the electron cloud around the atomic center under the effect of an exterior electric field. Electrons cloud is distorted and deformed because of electrons low masses relatively to the frequency power; this distortion varies for different frequencies levels, and persists for frequencies between $10^{13}\sim 10^{15}$ Hz.

The ionic polarization:

This type of polarization involves the displacement process (a stretch or compression between negative and positive ions depending on the electric field direction) of atoms inside the same molecule under the effect of an exterior electric field. Atomic mass is much higher than electrons mass, therefore the resonant frequencies are between $10^9\sim 10^{12}$ Hz depending on materials.

The dipolar or orientation polarization:

Here, the polarization is at higher mass level and happens at frequencies below 10^9 Hz. It is mainly due to the orientation (moment) of molecular dipoles relatively to the electric field; the electric field rotates the molecular dipoles of materials. This type of polarization is influenced by the thermal variation. As a result of a thermal motion the molecular quantities are randomly arranged and the net sum of all molecular polarization becomes zero.

The interfacial of space charge polarization:

The interfacial polarization occurs when charge carriers migrate under the effect of external electric field and are restricted in their movements by local electrical potential (like metal electrodes in a capacitor, or like boundaries in heterogeneous mediums). This results in a distortion of the total electric field. These effects are very dependent on the materials and are important at relatively low frequencies ~ 1 kHz.

The GPR UWB signals with the bandwidth [0.1; 10] GHz, are mostly affected by both the ionic and the dipolar polarization mechanisms.

IV.6. Mixing models

There are number of empirical mixing models that provide the dielectric permittivity of soils made of several components (air, water, dielectrics...) [8] [46] [47].

Two main classes are distinguished here: models depending on volumetric contents of components, and frequency dependent models considering relaxation phenomena.

Non frequency dependent models:

- Topp's model (1980) is the simpler and an empirical model that describes the dielectric response of a quasi homogeneous soil in the presence of water. The model is inappropriate for clays and organic rich soils, but it agrees reasonably well for sandy and loamy soils over a wide range of water content (5-50%) in the frequency band [10 MHz; 1 GHz].
- The complex refractive index model (CRIM) is valid for a more wide variety of soils. It consists in linking the dielectric permittivity of the soil to the permittivities of the constituents and their volumetric fractions V in a restricted frequency bandwidth. A parameter a has been added to consider the wave orientation relative to the granular shapes (sphere, cylinder, spheroid) of the main constituents. The relation associated with the CRIM model is as follows:

$$\varepsilon^a = \sum_{i=1}^n V_i \varepsilon_i^a \quad \text{CRIM model: } a = \frac{1}{2} \quad (1-27)$$

- Effective medium theories (EMT) describe the macroscopic dielectric properties of composite materials by using a phenomenological mixing approach that gives a direct physical interpretation of the topology. These theories do not use the entire geometry of the soil, but a little piece of the studied sample or the induced field that constitutes a representative elementary volume. The different effective medium theories mainly differ by the way they account for the EM interactions between heterogeneities that do not exist explicitly in the elementary cell but are used for the modeling. Among them, the most well-known models are the Bruggeman-Hanai-Sen (1981) model and the Maxwell-Garnett model [48].

Frequency dependent models:

- The Debye model [49] associated with a uniform material describes its dielectric response as a function of the relaxation time τ and static parameters conductivity and real permittivities at frequency 0 and infinite (ε_s and ε_∞ respectively). The relation is expressed as follows:

$$\varepsilon^*(\omega) = \varepsilon' - j\varepsilon'' = \varepsilon_\infty + \frac{\varepsilon_s - \varepsilon_\infty}{1 + j\omega\tau} - j\frac{\sigma}{\omega} \quad (1-28)$$

Where the term $\frac{\sigma}{\omega}$ can be negligible for a low conductive media at high frequencies.

The Debye's model states that the relaxation time depends on both the molecular size and the viscosity of the liquid. Further modifications were introduced in the literature [50] like the Cole-Cole (1941) model [51], and the Davidson-Cole (1951) model.

- Jonscher model provides a general modeling of the multi-constituent material which respects the causality principle as for the Debye model. Compared to the others, Jonscher model requires a fewer parameters, and has been known to describe the propagation within absorbing and attenuating media, namely the Q-constant medium. It has been used to model the propagation of GPR pulse within soils mostly, e.g., Chahine et al. [9].

V. Waves polarization

The polarization of an electromagnetic wave is usually described in terms of the orientation of the electric field vector E . The antenna polarization is assumed to be constant within the main lobe of the radiation pattern. In common GPR systems, the antenna polarization is linear (the amplitude of E oscillates in a single direction), that has been assumed for the bowtie slot antenna used in the SFCW radar. In a GPR survey, the orientation of both transmitting and receiving antennas relatively to the direction of the radar displacement determines the mode of polarization TE or TM (details in chapter 5). Commercial GPR systems generally use wide band dipoles which are oriented such that the electric field is perpendicular to the survey line (TM mode). In GPR, two main depolarization phenomena are induced by dielectric discontinuities: planar interfaces, or buried objects. Concerning objects, the wave interaction (ray path approach) can be explicitly described by analytical formulas only in the case of canonical objects (infinite long cylinders, spheres...).

Depolarization by planar interfaces:

The basic geometry considers that the soil (medium) is modeled as the superposition of planar homogeneous layers (multilayered medium) and is excited by an incident plane wave. Studies mentioned in [52] highlights the fact that the planar interfaces induce depolarization effects in both modes TE and TM if only the incident field is not perfectly perpendicular to the planar surface (angle of incidence different from 0) and also when the planar surface is rough. Refraction and reflection phenomena on planar interfaces are analytically described by the Fresnel equations [53] [54] in Appendix A, and by the Snell-Descartes ray laws [55].

Scattering by canonical objects:

The detection and characterization of canonical targets, e.g., pipes modeled as infinite cylinders, is one of the main concerns of our work. The scattering by such objects at GPR frequencies has been developed analytically in [56] [17] and experimentally by many authors (chapter 5, section 2). The latter studies showed that the polarization of backscattered echoes is very dependent at first on the ratio between the target diameter and the wavelength, and secondly on the dielectric contrast between the target and the surrounding medium.

A parametric study of the scattering responses of dielectric and metallic targets has been made using a modified version of the implemented analytical model in the Matlab software done by [57] (Appendix B and chapter 5). The modified version includes an additional implementation of the polarization TE, and frequency dependence in the calculation.

VI. Processing GPR data

In GPR, the raw data can be easily displayed in real time on a computer. Basic processing is required for the initial data interpretation. Generally, a gain correction is performed as a function of the time to compensate for amplitude attenuation as a function of depth and to highlight deeper image features. However, the data interpretation may become difficult over a complex medium made of heterogeneous materials and several objects. Within this context, the data processing to be undertaken depends on the application under scope and the parameter to estimate. Nowadays, users are not only interested in object location and velocity analysis but also on estimating quantitative information (geometry, depth, dimensions, dielectric characteristics, and orientation) associated with targets. The processing usually performed for GPR raw data includes the following steps [32]:

Time-zero correction (static shift): in a GPR survey, the first waveform which arrives at the receiver is the air wave. In general, there is a delay in the time of arrival for the first waveform in air due to several reasons: generation of the time signal, delay introduced by the electronic unit, the antenna, delay of the cable connection, etc. Therefore, the time-zero must be associated with depth zero, and a time offset has to be removed from all traces. The time zero is calculated by subtracting the theoretical direct air wave time $t_{air.theoretical}$ from the simulated/measured time t_{air} in a CMP profile [58].

$$t_{zero} = t_{air} - t_{air.theoretical} \quad (1-29)$$

Background removal: the background signal is an unwanted signal that is repetitive and produces a coherent banding effect, parallel to the surface wave, and across the image. As illustrated in Fig. 1.1b, this includes the direct-air wave and the ground-bounce signal. For ground-coupled configuration, these signals may overlap with the target signal and thus disturbs the estimation of the parameters attached to the target. Some background removal techniques are tested in chapter 3.

Gain: gain correction is used to compensate for amplitude decay with depth in the GPR image; early signals have greater amplitude than the late signals because of smaller attenuation. Losses are caused by geometric spreading as well as intrinsic attenuation in the ground material. Various time-variable gain functions may be applied: linear, exponential, spherical, AGC (automatic gain control). The most commonly applied is AGC that is a time-varying gain that runs on a window of selected length along each trace, point by point, by finding the average amplitude over the length of the sliding window. A gain function is then applied such that the average at each point is made constant along the trace. However, we have remarked in practice that a simple linear time varying function (expressed in dB/m) is the best solution with experimental data.

Topographic correction: this pre-processing technique consists in applying a time shift to each individual trace to compensate for some elevation variations along the recorded GPR line.

Frequency filtering: it is a way of removing unwanted high and/or low frequencies in order to ease the data interpretation of GPR images. A combination of a low-pass and high-pass filtering can be achieved with a band-pass filter, where the filter retains all frequencies in the pass band, but removes the high and low frequencies outside the pass band.

Frequency apodisation: The SFCW provides data in the frequency domain, from which the time data can be reconstructed by IFFT. To reduce the level of side lobes in the time domain, the fall of the frequency bandwidth, i.e. the transition vs. frequency between the pass band and the stop band of the spectrum is smoothed by an apodisation window (Hanning window in general). This step is also combined with zero-padding technique to increase the time resolution at the IFFT step.

Migration: the goal is to reconstruct the geometrically radar reflectivity distribution of the subsurface in a radargram. Migration is a spatial deconvolution process aiming at the removal of the transmitter and receiver directionality to focalize the energy (association of the energy of wavelets) on the reflecting object. An estimation of the velocity of the underground structure is necessary before migration. The background velocity can also be adjusted iteratively to optimize the radargram. There exist different migration algorithms: reverse time migration, Kirchhoff migration, matched filter migration, eccentricity migration, F-K based migration.

F-K (Frequency-wavenumber) filters: FK can suppress specific artifacts related to slanted layered underground discontinuities, because different (right and left dips) dip angles are transformed into positive and negative wave-numbers, and therefore can be separated.

Wavelet transform (WT): WT is used to extract the instantaneous parameters (amplitude, phase and frequency) of the echoes contaminated by noise, by comparing time and frequency wavelet transformed responses, it acts as the Hilbert transform that compares real and imaginary part of signal. WT of time signal can also be linked to WT of frequency signal as function of the Hilbert transform. In [59], the estimated parameters are used to obtain more information about the noise and the attenuation.

In this work, the following data pre-processing techniques have been used to improve the quality of the Rx data and to contribute to ease the data interpretation at some extent: time-zero correction and filtering are applied directly in the frequency domain to Rx signals. Afterwards, the background removal techniques presented in chapter 3 have been performed in the temporal domain, using an inverse Fast Fourier transform (IFFT) and a frequency domain zero padding to increase the time resolution. The main signal processing techniques reported in chapter 3 consists in evaluating clutter removal techniques, such as PCA and ICA, for objects in the ground-coupled radar configuration.

VII. Applications of GPR surveys in civil engineering

Civil engineering structures are generally made of different materials including concrete, natural soils and bituminous materials. These materials are involved in a wide variety of civil engineering structures such as transportation infrastructures (i.e., road pavements, bridges, and railway tunnels), urban buildings, nuclear structures, hydraulic generation facilities, embankments, dams, breakwater, foundations, etc.

GPR surveys have been widely used in civil engineering to obtain either qualitative or quantitative information about the subsurface [60]. The information and the applications of GPR survey vary according to the material and the dimension of the object to probe. In geophysics, GPR survey is used to determine rock region limits, to detect voids, e.g., karsts, to perform vertical profiling and characterize soil materials [61] (including the determination of soil water content), ice profiling [62], water and minerals mapping. For pavement, GPR survey is mainly devoted to layer thickness estimation [63], the mapping of debonding areas [64], the estimation of the depth of visible cracks (superficial) and the location of embedded cracks [64]. For concrete [65], GPR surveys extend to the mapping and the location of reinforcement bars, i.e., metal elements in concretes structures, and eventually the corrosion of the latter [66], and the estimation of water content within the concrete [67].

For urban applications, GPR is used for the mapping of buried urban utilities (cables and pipes) [68] [64]. In particular, cables and pipes are always present in urban areas and their number and concentration increase dramatically in new structures. Thus, damages during digging can occur to those objects and there is a need to use accurate non-destructive techniques to locate urban utilities. GPR systems have been widely used in mining and numerous data processing have been developed that could be useful for civil engineering applications.

In practice, nor the position neither the direction of the cylinder are known before the survey. Therefore, a general survey is performed in two orthogonal directions. The size of buried objects investigated varies from a few to several tens of centimeters, and the depth from five centimeters to the range of one or two meters. Nevertheless, the range of the reachable depth by a GPR system depends on many factors such as the central frequency, the two-way travel path attenuation, the radar cross-section of the targets or discontinuities (which in turn depends on the size of the target and the dielectric contrast with the surrounding material) and the dielectric characteristics of the probed materials.

VIII. Challenges in the detection and characterization of utilities

The problems of urban utilities detection is treated internationally (largely in UK) [64] [69]. Much development and new methods are published continuously in Europe in this field within the COST Action Tu1208 [64] [70] and for concrete material characterization with the RILEM union [65]. In Europe, many utilities have been installed a few hundred years ago and they play an essential role in the development of urban life. Utilities are lines for telephones, natural gas, fiber optics, electric grids, traffic lights, waste water pipes... Actually, we do not dispose any mapping and characteristics of all buried utilities, i.e., location, geometry, type and function, because they are often been buried by different firms without consultations and

development plan. To prevent damage to them and the surrounding environment, the GPR technology appears a good candidate to insure the mapping. The performance of GPR technique has to be validated in this complex environment made of trenches, excavated soil, soil structure rebuilt, and buried objects of different dimensions and dielectric characteristics.

In this context, this work focuses on the detection of small urban utilities with dimensions less than ten centimeters. We considered targets (cylindrical and rectangular shapes) with very small dimensions compared to the wavelength (0.3λ to 1.5λ), and with different natures: metallic, PVC (plastic), air-filled (gases) PVC, and water-filled PVC (liquids). Small targets have less scattering signal amplitudes, and have a size comparable to the wavelength, which can result in a depolarization effect on the scattered waves.

Within this context, there are many challenging situations with hardly detectable cases. Among others, the challenge is the detection of shallow targets with regards to the material wavelength. This implies some challenging advancement in enhancing the target signals by either removing the background signal or/and by using the polarization diversity. It is then proposed to especially contribute to the following items to ease the detection and the characterization of targets:

- In chapter 3, some statistical background reduction techniques are proposed to overcome the effect of the overlapping between the clutter and the target signals, and also to contribute to mitigate the influence of both the heterogeneous nature of medium and the roughness of the ground surface for different dielectric contrasts.
- In chapter 4, the detection of target hyperbolas with a small lateral dimension and various dielectric contrasts with regards to the surrounding soil at several depths: a few image processing techniques have been evaluated and the template matching appears promising.
- In chapter 5, multi-polarization surveys are opposed to the depolarization effects of waves on small targets, like phase and amplitude inversions. Consequently polarization effects are described in details, and can be used in an advantageous way to obtain information about the buried targets by comparing multi-configurations responses.

The main advantage of using an UWB impulse system relies on the trade-off between time-space resolution and penetration depth to extract enough quantitative and accurate information about the buried targets. However such system has some drawbacks especially in image migration [71], in radar range characterization [72], and on the degree of the impulse side lobes generated by the antennas, because they can obscure target shallow response with the clutter and might degrade the resolution between two close targets, thus a window (rectangular i.e. Hanning [73] [7] or triangular i.e. Bartlett [74]) can be used before the IFFT to reduce the side lobes on the receiver side, nonetheless on the transmitter side they are very dependent on the antenna structure.

Varying dielectric characteristics and water content depending on the area in the structure and the time (weather and age of the structure) is one of the often encountered problems in civil engineering. Consequently, wave velocity inside the structure may change from one area to another although being made of the same material. A velocity estimation algorithm has to

be applied before any data processing, because the velocity is used in the calculation of all arrival times and in later processing for information extraction. Nevertheless, the velocity analysis leads to an estimated value in complex civil engineering structures and this latter step is essential for each survey.

The different data and image processing techniques have been applied on synthetic and experimental data. The synthetic data have been obtained from simulations relying on the modeling of the GPR system (the SFCW radar composed of the bowtie-slot antennas) using the Empire XPU commercial software. This tool is based on the 3D-FDTD approach to solve differential Maxwell's equations and provides fast simulations in dielectric materials as compared to other modeling tools; moreover, it provides more accurate results for curved structures (PGA Perfect Geometry Approximation algorithm).

A qualitative and quantitative technique for evaluating and comparing different images is one of the hardest challenges encountered in this work, because of the lack of reference signatures and prior knowledge of the subsurface ground composition.

At last, other challenges are encountered in GPR imaging such as: the design of the GPR equipments by means of studying the antennas limitations on the impedance adaptation, the field patterns, the operating bandwidth and the efficiency; the radio-system limitations on the pulses quality, calibration, sampling resolution, temperature variations and dynamic range; the near field effect that distorts responses of shallow object with an overlapping soil surface reflection; the time consumption for high spatial resolution and multi-polarization surveys; and real time processing of data.

IX. Conclusion

The chapter 1 has introduced GPR operating systems, GPR surveys and applications in civil engineering structures. The basics definitions and techniques that are required to the understanding of the different chapters in this work have been presented.

The scope in this work concerns the detection of small urban utilities using a new UWB ground-coupled radar system that is presented in chapter 2. This application is challenging because the aim is to detect shallow and small targets within a Bscan with a dominant overlapping clutter. Thus, a first step in this work is the elimination of the soil surface reflection using statistical techniques to enhance the target signals; three techniques have been selected and compared in chapter 3. Later, the locations of targets reflections, hyperbolas, have been performed using an extended template matching algorithm. Finally, the enhancement of target signal is extended to polarization diversity in chapter 5 throughout different simulations and test data.

Bibliography

- [1] X. Derobert, "Techniques radar appliquées au génie civil," *Habilitation à diriger des recherches, Université de Nantes*, p. 117, 2003.
- [2] X. Derobert, C. Fauchard, P. Cote and E. Guillanton, "Performances de radars d'auscultation des chaussées sur des sites tests," *Bulletin des laboratoires des ponts et chaussées, IFSTTAR*, no. 230, pp. 15-22, 2001.
- [3] D. Leparoux, D. Gibert and P. Cote, "Adaptation of prestack migration to multi-offset ground-penetrating radar (GPR) data," *Geophysical prospecting, Wiley Online Library*, vol. 49, no. 3, pp. 374-386, 2001.
- [4] F. Sagnard and F. Rejiba, "Géoradar - Principes et applications," *Techniques de l'ingénieur Applications radars, TE5228*, pp. 1-15, 2010.
- [5] J. M. Simonin, D. Lievre and J. C. Dargenton, "Structural roadway assessment with frequency response function," *Eighth International conference on the Bearing Capacity of Roads, Railways and Airfields*, pp. 459-466, 2009.
- [6] F. Liu, "Calibration of the mono-static stepped-frequency GPR with a Vivaldi UWB antenna," *International Conference on Microwave and Millimeter Wave Technology, IEEE. ICMWT 2008.*, vol. 4, pp. 1691-1694, 2008.
- [7] C. Le Bastard, "Apport de techniques de traitement du signal super et haute résolution à l'amélioration des performances du radar-chaussée," *PhD Thesis, University of Nantes*, 2007.
- [8] M. Adous, "Caractérisation électromagnétique des matériaux traités de génie civil dans la bande de fréquences 50 MHz – 13 GHz," *PhD Thesis, Université de Nantes*, 2006.
- [9] K. Chahine, A. Ihamouten, V. Baltazart, G. Villain and X. Dérobert, "On the variants of Jonscher's model for the electromagnetic characterization of concrete," *13th International Conference on Ground Penetrating Radar (GPR)*, pp. 1-6, 2010.
- [10] X. Xiao, A. Ihamouten, G. Villain and X. Dérobert, "Application of electromagnetic waves propagating in multi-layered waveguide to monitor chloride ingress into concrete," *Proceedings of Int. Symp. on NDT-CE*, pp. 1-8, 2015.
- [11] F. Sagnard, "Design of a Compact Ultra-Wide Band Bow-Tie Slot Antenna System for the Evaluation of Structural Changes in Civil Engineering Works," *Progress In Electromagnetics Research B*, pp. 181-191, 2014.
- [12] F. Sagnard and J.-p. Tarel, "Template matching based detection of hyperbolae in ground penetrating radargrams," *Internal IFSTTAR report, submitted to IOP*, 2015.
- [13] F. I. Rial, M. Pereira, H. Lorenzo, P. Arias and A. Novo, "Resolution of GPR bowtie

- antennas: An experimental approach," *Journal of Applied Geophysics, Elsevier*, vol. 67, no. 4, pp. 367-373, 2009.
- [14] C. Nguyen and J. Han, "Time-Domain Ultra-Wideband Radar, Sensor and Components: Theory, Analysis and Design," *Springer Science & Business Media*, 2014.
- [15] P. Adrian, "An Optimization of Gaussian UWB Pulses," *10th International Conference on development and application systems*, p. 50, 2010.
- [16] H. Sheng, P. Orlik, A. M. Haimovich, L. J. Cimini Jr and J. Zhang, "On the spectral and power requirements for ultra-wideband transmission," *IEEE International Conference on Communications, 2003. ICC'03*, vol. 1, pp. 738-742, 2003.
- [17] D. J. Daniels, "Ground penetrating radar," *Wiley Editor, second edition*, 2005.
- [18] N.-F. Cheng, H.-W. Conrad Tang and C.-T. Chan, "Identification and positioning of underground utilities using ground penetrating radar (GPR)," *Environ. Res.*, vol. 23, no. 2, pp. 141-152, 2013.
- [19] A. P. Annan, "Ground-penetrating Radar: Workshop Notes," Sensors and Software, Inc., Mississauga, Ontario, 1996. [Online]. Available: <http://www.kgs.ku.edu/Current/2001/martinez/martinez5.html>.
- [20] R. D. Luzitano, "Revealing the effects of subsurface structure on the antenna coupling of ground penetrating radar," *Master Thesis, University of British Columbia*, 1995.
- [21] E. Blias, "Stacking and interval velocities in a medium with laterally inhomogeneous layers," *73rd Annual International Meeting, SEG, Expanded Abstracts*, pp. 706-709, 2003.
- [22] C. M. Hogan and G. F. Margrave, "An interactive velocity modelling tool in MATLAB," *CREWES Research Report*, vol. 21, 2009.
- [23] Y. Ozdogan, "Velocity Analysis, Statics Corrections, and Stacking," *Society of Exploration Geophysicists in Seismic Data Processing, 9th ed, Tulsa*, pp. 155-228, 1999.
- [24] A. V. Ristic, D. Petrovacki and M. Govedarica, "A new method to simultaneously estimate the radius of a cylindrical object and the wave propagation velocity from GPR data," *Computers & Geosciences*, vol. 35, no. 8, pp. 1620-1630, 2009.
- [25] N. Kettridge, X. Comas, A. Baird, L. Slater, M. Strack, D. Thompson, H. Jol and A. Binley, "Ecohydrologically important subsurface structures in peatlands revealed by ground-penetrating radar and complex conductivity surveys," *Journal of Geophysical Research: Biogeosciences (2005--2012)*, vol. 113, no. G4, 2008.
- [26] G. S. Baker and H. M. Jol, "Stratigraphic analyses using GPR," *Geological Society of America*, vol. 432, p. 181, 2007.
- [27] J. O. Curtis, "Moisture effects on the dielectric properties of soils," *IEEE Transactions*

- on geoscience and remote sensing*, vol. 39, no. 1, pp. 125-128, 2001.
- [28] A. Ihamouten, "Caractérisation physique et hydrique de bétons d'ouvrage par propagation d'ondes électromagnétiques," *PhD Thesis, Université de Nantes*, 2011.
- [29] T. Saarenketo, "Measuring electromagnetic properties of asphalt for pavement quality control and defect mapping," *Saarenketo/Roadscanners 2001-13 P*, 2009.
- [30] H. T. Banks, M. Buksas and T. Lin, "Electromagnetic material interrogation using conductive interfaces and acoustic wavefronts," *SIAM*, vol. 21, 2000.
- [31] S. Pawar, P. Murugavel and D. Lal, "Effect of relative humidity and sea level pressure on electrical conductivity of air over Indian Ocean," *Wiley Library, Journal of Geophysical Research: Atmospheres*, vol. 114, no. D2, pp. 1-8, 2009.
- [32] H. M. Jol, "Ground penetrating radar theory and applications," *Elsevier, First edition*, 2008.
- [33] A. Martinez and A. P. Byrnes, "Modeling dielectric-constant values of geologic materials: An aid to ground-penetrating radar data collection and interpretation," *Kansas Geological Survey, University of Kansas*, 2001.
- [34] J. Lee, J. C. Santamarina and C. Ruppel, "Parametric study of the physical properties of hydrate-bearing sand, silt, and clay sediments: 1. Electromagnetic properties," *Journal of Geophysical Research: Solid Earth (1978--2012)*, vol. 115, no. B11, 2010.
- [35] T. Saarenketo, "Electrical properties of road materials and subgrade soils and the use of ground penetrating radar in traffic infrastructure surveys," *Universitatis Ouluensis*, no. 471, 2006.
- [36] O. Buyukozturk, T.-Y. Yu and J. A. Ortega, "A methodology for determining complex permittivity of construction materials based on transmission-only coherent, wide-bandwidth free-space measurements," *Cement and Concrete Composites*, vol. 28, no. 4, pp. 349-359, 2006.
- [37] Y. Nishi, S. Iizuka, M. C. Faudree and R. Oyama, "Electrical Conductivity Enhancement of PTFE (Teflon) Induced by Homogeneous Low Voltage Electron Beam Irradiation (HLEBI)," *Materials Transactions*, vol. 53, no. 5, pp. 940-945, 2012.
- [38] R. Jones, "Measurements of the electrical conductivity of water," *IEE Proceedings Science, Measurement and Technology*, vol. 149, no. 6, pp. 320-322, 2002.
- [39] G. Daian, A. Taube, A. Birnboim, M. Daian and Y. Shramkov, "Modeling the dielectric properties of wood," *Wood science and technology*, vol. 40, no. 3, pp. 237-246, 2006.
- [40] W. Simpson and A. TenWolde, "Physical properties and moisture relations of wood," *Chapter in Wood handbook- Wood as an engineering material, Forest Products Laboratory.*, p. 463, 1999.

- [41] Kaye and Laby, "Tables of Physical & Chemical Constants (16th edition 1995)," http://www.kayelaby.npl.co.uk/general_physics/2_6/2_6_5.html, Version 1.0 (2005).
- [42] H. O. Pierson, "Handbook of carbon, graphite, diamond, and fullerenes: properties, processing, and applications," *NY: William Andrew Publishing/Notes*, 1993.
- [43] R. W. P. King, G. S. Smith, M. Owens and T. T. Wu, "Antennas in matter: Fundamentals, theory, and applications," *NASA STI/Recon Technical Report A*, p. 880, 1981.
- [44] X. Derobert, G. Villain, R. Cortas and J.-I. Chazelas, "EM characterization of hydraulic concretes in the GPR frequency band using a quadratic experimental design," *Proceedings of the 7th International Symposium on Non-destructive Testing in Civil Engineering, Nantes, France, June 30th-July 3rd, 2009*.
- [45] L. Comparon, "Étude expérimentale des propriétés électriques et diélectriques des matériaux argileux consolidés," *PhD Thesis, Institut de physique du globe de Paris-IPGP*, 2005.
- [46] A. Paz, E. Thorin and C. Topp, "Dielectric mixing models for water content determination in woody biomass," *Wood science and technology*, vol. 45, no. 2, pp. 249-259, 2011.
- [47] A. P. Tran, M. Ardekani and S. Lambot, "Coupling of dielectric mixing models with full-wave ground-penetrating radar signal inversion for sandy-soil-moisture estimation," *Geophysics*, vol. 77, no. 3, pp. H33-H44, 2012.
- [48] T. C. Choy, "Effective medium theory: principles and applications," *Oxford University Press*, no. 102, 1999.
- [49] K. Prokopidis and T. Tsiboukis, "Modeling of ground-penetrating radar for detecting buried objects in dispersive soils," *Applied Computational Electromagnetics Society Journal*, vol. 22, no. 2, p. 287, 2007.
- [50] D. F. Kelley, T. J. Destan and R. J. Luebbers, "Debye function expansions of complex permittivity using a hybrid particle swarm-least squares optimization approach," *IEEE Transactions on Antennas and Propagation*, vol. 55, no. 7, pp. 1999-2005, 2007.
- [51] A. H. Abdelgwad, T. M. Said and A. M. Gody, "Developing of A Ground Penetrating Radar Antenna for Detecting Water Pollution in Underground Pipelines," *International Journal of Microwaves Applications*, vol. 4, no. 1, 2015.
- [52] P. Lutz, S. Garambois and H. Perroud, "Influence of antenna configurations for GPR survey: information from polarization and amplitude versus offset measurements," *Geological Society, London, Special Publications*, vol. 211, no. 1, pp. 299-313, 2003.
- [53] M. Gonzalez Huici, "Accurate ground penetrating radar numerical modeling for automatic detection and recognition of antipersonnel landmines," *PhD Thesis, Rheinische*

Friedrich-Wilhelms-University of Bonn, 2013.

- [54] J. M. Carcione, D. Gei, M. Botelho, A. Osella and M. del la Vega, "Fresnel reflection coefficients for GPR-AVA analysis and detection of seawater and NAPL contaminants," *Near Surface Geophysics*, vol. 71, pp. 253-263, 2006.
- [55] D. Huston, "Structural sensing, health monitoring, and performance evaluation," *CRC Press, First edition*, 2010.
- [56] C. A. Balanis, "Advanced engineering electromagnetics," *Wiley New York, Second edition*, 2012.
- [57] K. Z. Guangan, "<http://individual.utoronto.ca/kzhu/>," *Matlab Central, (code is placed under the open BSD license)*, 2011.
- [58] A. Ihamouten, X. Derobert and G. Villain, "The effect of coupling on the determination of time zero for radar antennae," *IEEE, 13th International Conference on Ground Penetrating Radar (GPR)*, pp. 1-6, 2010.
- [59] L. Liu and M. Oristaglio, "GPR signal analysis: instantaneous parameter estimation using the wavelet transform," *Proc. 7th International Conference on Ground Penetrating Radar*, 1998.
- [60] A. Benedetto and L. Pajewski, "Civil Engineering Applications of Ground Penetrating Radar," *Springer*, 2015.
- [61] S. Lambot, E. C. Slob, I. Van den Bosch, B. Stockbroeckx and M. Vanclooster, "Modeling of ground-penetrating radar for accurate characterization of subsurface electric properties," *Geoscience and Remote Sensing, IEEE Transactions on*, vol. 42, no. 11, pp. 2555-2568, 2004.
- [62] A. Saintenoy, J.-M. Friedt, A. D. Booth, F. Tolle, E. Bernard, D. Laffly, C. Marlin and M. Griselin, "Deriving ice thickness, glacier volume and bedrock morphology of the AustreLøvenbreen (Svalbard) using Ground-penetrating Radar," *Near Surface Geophysics*, vol. 11, no. 2, pp. 253-261, 2013.
- [63] K. Chahine, V. Baltazart, X. Dérobert and Y. Wang, "Blind Deconvolution via independent component analysis for thin-pavement thickness estimation using GPR," *International Radar Conference-Surveillance for a Safer World, 2009. RADAR.* , pp. 1-5, 2009.
- [64] C. Plati and X. Dérobert, "Inspection Procedures for Effective GPR Sensing and Mapping of Underground Utilities and Voids, with a Focus to Urban Areas," *Chapter in book: Civil Engineering Applications of Ground Penetrating Radar*, pp. 125-145, 2015.
- [65] RILEM, "<http://www.rilem.org/gene/main.php?base=500218>," *Proceedings published by RILEM (International union of laboratories and experts in construction materials, systems and structures)* .

- [66] S. S. Hubbard, J. Zhang, P. J. Monteiro, J. E. Peterson and Y. Rubin, "Experimental detection of reinforcing bar corrosion using nondestructive geophysical techniques," *ACI Materials Journal*, vol. 100, no. 6, pp. 501-510, 2003.
- [67] F. Tosti and E. Slob, "Determination, by Using GPR, of the Volumetric Water Content in Structures, Substructures, Foundations and Soil," *Chapter in book: Civil Engineering Applications of Ground Penetrating Radar*, pp. 163-194, 2015.
- [68] S. W. Wahab, "Assessing the condition of buried pipe using ground penetrating radar," *PhD Thesis, University of Birmingham*, 2014.
- [69] H. Chen and A. G. Cohn, "Buried utility pipeline mapping based on street survey and ground penetrating radar," *ECAI 2010-19th European Conference on Artificial Intelligence*, vol. 215, pp. 987-988, 2010.
- [70] Proceedings of the General Meeting of COST Action TU1208, "http://www.cost.eu/domains_actions/tud/Actions/TU1208," *Rome (IT)*, 22-24 July 2013.
- [71] R. Zetik and R. Thoma, "Imaging of distributed objects in UWB sensor networks," *Springer Book: Ultra-Wideband, Short Pulse Electromagnetics 9*, pp. 97-104, 2010.
- [72] B. Scheers, Y. Plasman, M. Piette, M. P. Acheroy and A. Vander Vorst, "Laboratory UWB GPR system for land mine detection," *8th International Conference on Ground Penetrating Radar*, pp. 747-752, 2000.
- [73] Y. He, H. Mitsumoto and Z. Ren, "Echo Extraction Method for a Ground Penetrating Radar," *PIERS Online*, vol. 3, no. 5, pp. 701-703, 2007.
- [74] F. Parrini, M. Fratini, M. Pieraccini, C. Atzeni, G. De Pasquale, P. Ruggiero, F. Soldovieri and A. Brancaccio, "ULTRA: Wideband ground penetrating radar," *Radar Conference, 2006. EuRAD 2006. 3rd European*, pp. 182-185, 2006.

List of figures and tables

Figure 1.1: GPR principles: a) Scheme of a ground-coupled GPR system on a soil including a buried metallic pipe at a 160 mm depth; b) Synthetic Bscan (FDTD simulations) corresponds to the buried metallic pipe.	20
Figure 1.2: GPR wavelet defined as the first derivative of Gaussian pulse in (Top) time domain, and in (Bottom), frequency domain.	23
Figure 1.3: Footprint of an elliptical illuminated surface as function of the depth x	24
Figure 1.4: Target geometry for the radar range problem in the bi-static configuration.	25
Figure 1.5: GPR survey types: a) CMP survey, b) WARR survey, c) FOM survey on horizontal reflector d) FOM survey on target.	26
Figure 1.6: a) Ray-path model for a horizontal reflector in the WARR survey, b) Samples of waves curves obtained from a WARR/CMP survey, c) Experimental Bscan in the broadside configuration on a 48 cm thick sandy ground with d) Computed time-velocity spectrum and e) Computed time-epsilon spectrum.	28
Figure 1.7: (a) Ray-tracing Pythagorean model associated with the (b) hyperbola signatures generated by the radar displacement.	29
Figure 1.8: Variations of the attenuation $20\log_{10}exp - \alpha x$ with regards to the depth within three different media with $\epsilon = 3.5; 9; \text{ and } 15; \sigma = 0.01 \text{ S/m}$ and $f=1 \text{ GHz}$	32
Figure 1.9: Relative complex permittivity of water according to the Debye's model, a) Real part (related to energy transfer) and b) Imaginary part (related to attenuation).....	33
Table 1.1: Dielectric characteristics of main materials encountered in civil engineering structures (ϵ' and σ).....	33

Chapter 2: Ground-coupled GPR system and experimental test sites

Résumé

Ce chapitre présente le matériel expérimental qui a été utilisé tout au long de cette thèse. Il intègre premièrement le système radar de sol, qui a été conçu et développé depuis environ cinq ans à l'IFSTTAR. Le radar est un système bi-statique composé de deux antennes papillon ultra large bande en émission et en réception. Selon le chapitre 1, la configuration de couplage au sol a été sélectionnée pour améliorer le rendement des antennes et renforcer la dynamique des signaux rétrodiffusés sur les cibles enfouies dans le sol. Les caractéristiques des antennes, leur géométrie et leur disposition géométrique sont brièvement présentées. Des études antérieures ont permis d'optimiser le blindage des antennes.

Le système d'acquisition des données est basé sur la technologie de génération d'ondes continue avec sauts de fréquences. Un analyseur de réseau vectoriel (VNA) permet de scanner la bande passante de 0.05 à 4 GHz. La transformée de Fourier inverse permet de synthétiser les données temporelles, qui sont comparées avec données simulées aux chapitres 3 et 5.

La deuxième partie de ce chapitre présente brièvement les sites-tests expérimentaux sur lesquels les données radar ont été recueillies. Il comprend deux bacs à sable sec (intérieur et extérieur), un remblai extérieur en terrain limoneux-calcaire, et un site d'essai urbain extérieur. Des essais préliminaires ont été effectués pour caractériser la permittivité diélectrique de chaque site de test. Ces caractéristiques sont ensuite utilisées comme paramètres d'entrée pour générer des données simulées et faciliter des comparaisons ultérieures entre données de simulation et données expérimentales.

Contents

Résumé	49
I. Introduction.....	51
II. GPR SFCW system	51
II.1. Overview.....	51
II.2. Antenna geometry and design.....	52
II.3. Parametric study.....	55
II.4. Tx and Rx Antenna configurations for GPR survey	55
II.5. Acquisition system.....	57
III. Test Sites	58
III.1. Sand boxes.....	58
III.2. Embankment near the IFSTTAR building.....	59
III.3. The urban test-site Sense-City.....	60
IV. Conclusion	62
Bibliography	63
List of figures and tables.....	64

I. Introduction

This chapter presents the experimental equipment which has been used throughout this thesis. First, the bi-static GPR system has been designed and developed for about five years at IFSTTAR. It is based on two UWB bow-tie slot antennas. According to chapter 1, the ground-coupled GPR system has been selected to improve the energy coupling with the ground and to enhance the scattered signals from embedded targets. At first, some characteristics of the antennas, geometry and design of the GPR system, are briefly presented. The shielding of the antennas has been optimized according to previous studies.

The data acquisition system is based on the step-frequency continuous wave technology (SFCW). A vector network analyzer (VNA) enables to scan the [0.05;4] GHz frequency bandwidth. An IFFT applied on the frequency data after preprocessing algorithms allows to synthesize the time data which can be further compared with the FDTD simulated dataset.

The second part of this chapter briefly presents the experimental test-sites where radar data have been collected. It includes an indoor sandy test-site, an outdoor sandy test-site, a silt outdoor test-site and an outdoor urban test-site in the sense-city mini-city. Preliminary measurements have been performed to characterize the dielectric permittivity of the soil in each test-site and to use it as an input parameter for generating the simulated data set.

II. GPR SFCW system

II.1. Overview

Antennas that are commonly used in commercial ground coupled GPRs are generally wide band planar antennas whose frequency band is centered at a frequency between 100 and 1500 MHz. Usually, the same antenna geometry is used in transmission and reception to form a bistatic system. The frequency band defined depends on the size of the target to be detected and on the soil attenuation. Radio frequencies, from 10 to 250 MHz [1], are best suited for applications requiring deep penetration capability (i.e. geological [2], geohydrological [3] and stratigraphic surveys, deep pipes and bedrock detection [4]). Microwave frequencies, i.e., 300 MHz up to 4GHz [5], are better suited for applications requiring refined time resolution and accurate spatial detection i.e. demining and civil engineering applications cited in chapter 1 (concrete inspection, locating rebar, road mapping, utility and void detection, bridge maintenance, and quality assessment of precast structures).

It is unlikely that a single antenna can cover a wide range of applications. That is why GPR manufacturers propose a range of antennas that can be used with a single control unit. The pair of antennas can be separate or not in a module and they are usually shielded; the offset between antennas are defined in order to obtain the overlap of the main radiating lobes of both transmitting and receiving antennas. The antennas are generally dipoles, bowties and horns. These antennas have usually a limited bandwidth, low directivity and a linear polarization. To enhance the bandwidth, resistive loading has been commonly used [6] (introduced by Wu and King 1965) although it decreases the antenna efficiency. Recently,

micro-strip patch antennas have allowed the design of many types of geometries with advantages such as low-cost, light weight, and ease of fabrication.

The measurements performed in this work have essentially been made with a SFCW GPR system made of a pair of bowtie slot antennas previously designed in our laboratory [7]. Thus, it appears important to present the characteristics of these antennas as in this case the GPR can be entirely modeled using the FDTD approach and the synthetic data will serve as a reference for comparison with experimental results performed on the several test sites.

II.2. Antenna geometry and design

The bowtie slot antenna designed in our laboratory and visualized in Figure 2.1(a) is dedicated to radiate very close (a few cm) to a soil surface in an UWB and at the lowest possible low frequencies. Thus, its overall dimensions have been defined to fit less than a A4 paper size ($W_s = 190.4 \text{ mm}$ and $L_s = 332.2 \text{ mm}$) using the planar technology based on a single-sided FR4 substrate ($h = 1.5 \text{ mm}$; $\epsilon_r' = 4.4$; $\tan\delta = 0.01$; $35 \mu\text{m}$ copper-clad). In air, the bandwidth which is defined by the return loss $S_{11dB}(f) \leq -10 \text{ dB}$, ranges from 460 MHz to beyond 4 GHz in air and on a standard soil material ($\epsilon_s' = 5.5$; $\sigma_s = 0.01 \text{ S.m}^{-1}$, elevation 1 cm). All the antenna design has been made using full-wave 3D FDTD simulations under the commercial software EMPIRE XPU with the aim of studying the radiating properties of the bowtie slot antenna in the presence of several soils.

The antenna is made of two rounded slot triangles ($W_1 = 86.59 \text{ mm}$ and $L_1 = 276.47 \text{ mm}$, radii r_1 and $r_2 = 20 \text{ mm}$) fed by a tapered CPW line with length $W_f = 67.02 \text{ mm}$. It is fed in port 1 from a SMA (subminiature version A) connector, which is connected to a 50Ω CPW (coplanar waveguide) line with $a = 0.4 \text{ mm}$ and $b = 2.8 \text{ mm}$. The antenna feed line is tapered for impedance matching with dimensions at the feed-point $a' = 1.84 \text{ mm}$ and $b' = 2.50 \text{ mm}$ [7]. To reduce significantly reflections from the upper environment and the coupling effect between the transmitting and the receiving units, a partial conductive shield included in a rectangular box ($362 \times 231 \text{ mm}^2$) is used, it is coated internally with a conductive sheet and filled with a layered absorbing material [7], as shown on Figure 2.2. In practice, the radar absorbing foam is a three thick-layered absorbing material (HPS 125 distributed by EUROMC) with a total height of 68 mm.

The surface current distribution j_{xy} on the antenna at 450 MHz is displayed in Figure 2.1(b); the main direction of the electric field appears parallel to the antenna shortest axis that explains the origin of the linear polarization of the antennas. Thus, two perpendicular planes of polarization TM and TE, represented in Figure 2.1(c) at 450 MHz, on a soil with $\epsilon' = 5.5$ and $\sigma = 0.01 \text{ S/m}$, will be used during the measurements to excite specific dielectric contrasts or targets in the subsurface. In the TE mode, nulls of radiation at the antenna mid-axis are observed. Moreover, we visualize the computed radiation patterns (E_θ and E_ϕ) in the far field zone and in the air are presented in Figure 2.3 for a shielded bowtie slot antenna at four frequencies 0.45, 0.8, 1 and 2 GHz in both planes TM ($\Phi = 0$) and TE ($\Phi = 90^\circ$). It must

be underlined that the backward radiation into the ground that corresponds to the bottom half plane of the antenna is situated in the range $[90^\circ:0^\circ:90^\circ]$ in Figure 2.3. In the E-plane (TM mode), the component E_θ appears dominant and consequently the component E_ϕ can be assumed negligible. In air, without shielding, the maximum gain reached is 5.4 dB at 0.8 GHz. In the H-plane (TE mode), a lower amplitude difference between both E-components is observed at frequencies 0.8 and 1 GHz within the angle ranges $[30^\circ;70^\circ]$ and $[110^\circ;150^\circ]$. In both planes a maximum gain close to 4.2 dB is observed at 0.8 and 1 GHz. In the direction 180° , it is noticed an attenuation above 20 dB for the main components in both planes.

Comparing to the literature, this bowtie-slot antenna shows the best compromise with bandwidth and size as compared to existing bowtie antennas. However, it shows limited gain factor and thus the overall radiated energy is lower compared to other GPR antennas. The low directivity of the antenna is partly mitigated by the influence of the ground, which acts as a lens to focus the radiation pattern downward.

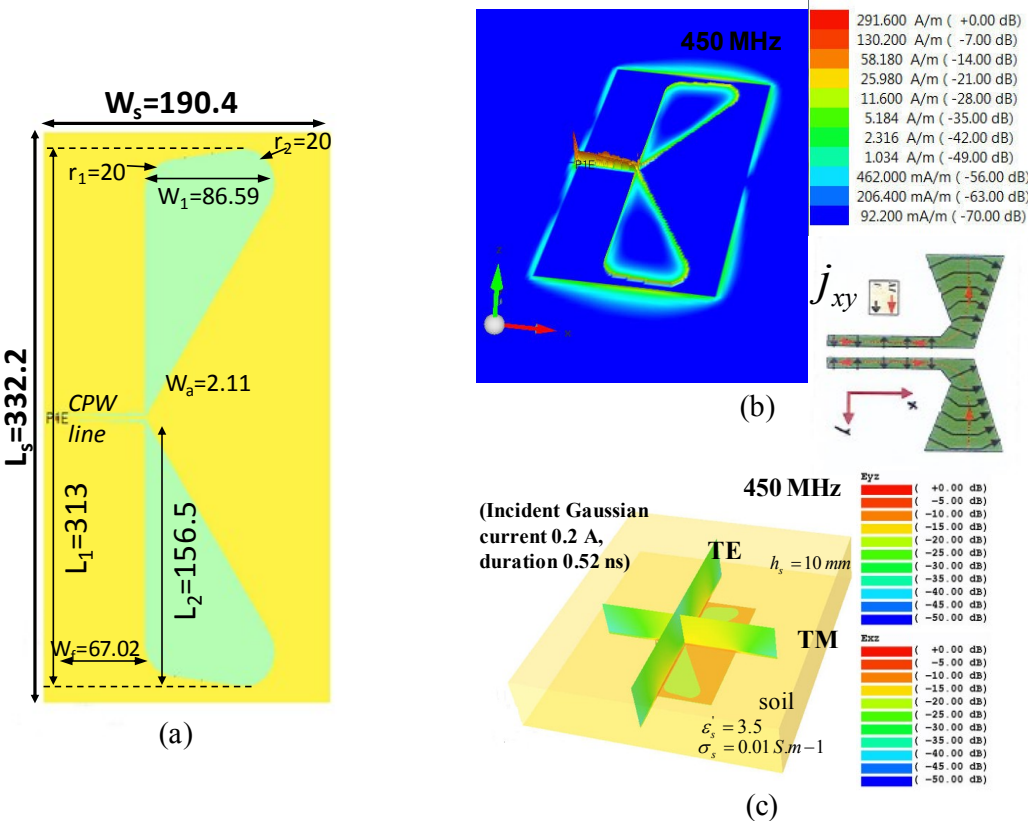


Figure 2.1: (a) Bowtie-slot Antenna dimensions (in mm), and (b) Surface current distribution and (c) radiation patterns in the TE and TM planes at 450 MHz (on the courtesy of F. Sagnard [7])

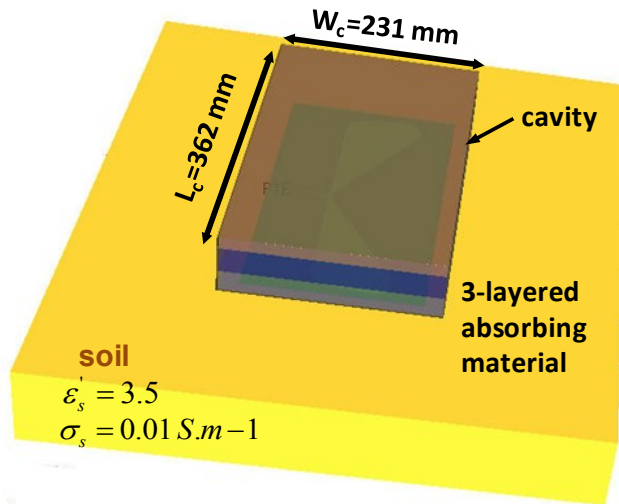


Figure 2.2: Cavity-backed shielded antenna.

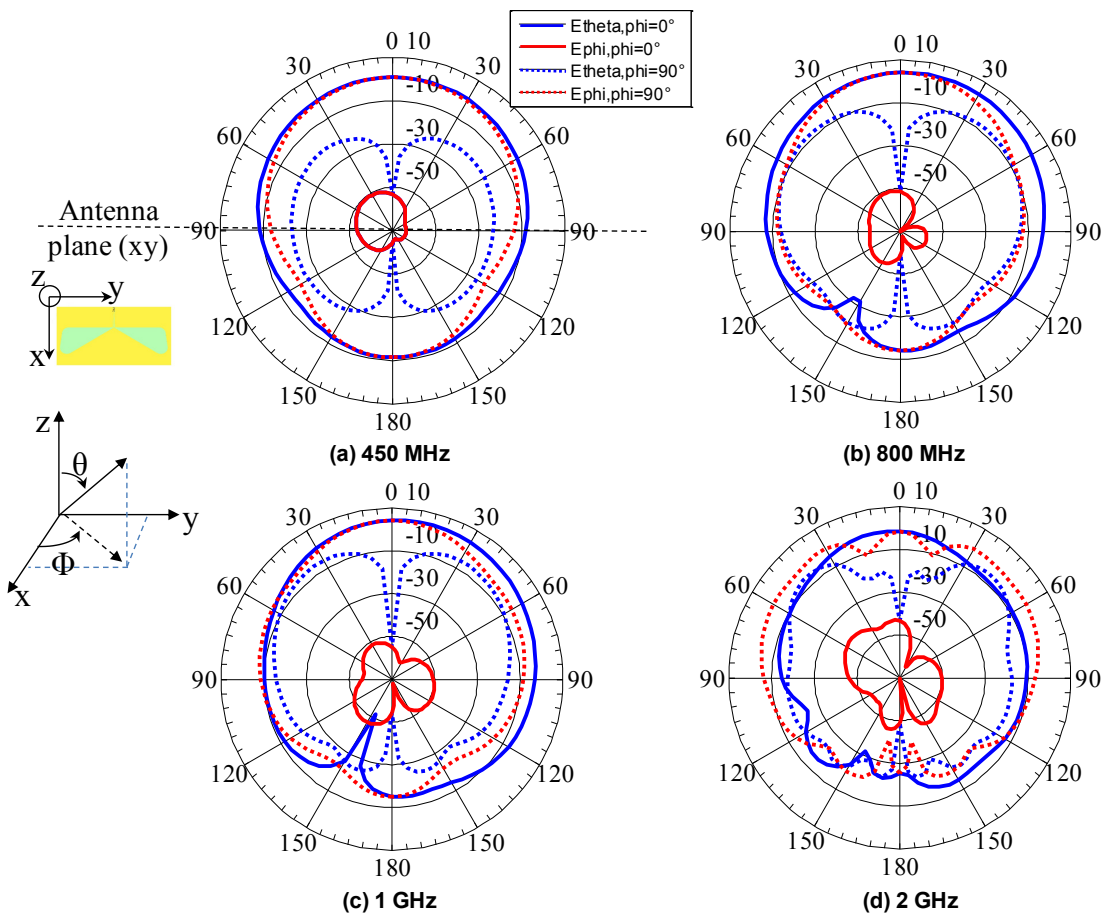


Figure 2.3: Theoretical logarithmic radiation patterns of the shielded bowtie slot antennas at frequencies 0.45, 0.8, 1 and 2 GHz (on the courtesy of F. Sagnard [7]).

II.3. Parametric study

The amplitude variation of the reflection coefficient $S_{11}(dB)$ as function of the frequency allows highlighting the bandwidth of the antenna; it is usually defined at -10 dB as shown on figure 2.4(a) [7]. Above a soil the response of the shielded antenna is shifted towards the lower frequencies; the first frequency associated with $S_{11}(dB) = -10$ dB is then shifted from 0.469 to 0.287 GHz. In general, we have observed that the shielding smoothes the S_{11} amplitude. In the presence of a conventional soil, the $S_{11}(dB)$ amplitude associated with the shielded antenna decreases significantly as compared to the case in air at frequencies higher than 0.840 GHz. Moreover, the first resonant peak remains almost at the same position. Thus, a satisfactory antenna matching with the soil has been obtained.

First experiments have been made on both dry sand and slightly wet pure sand originating from the Seine valley in France [7]. The dry sand has been deposited in a large box (height 740 mm, length 2 m, and width 1 m) inside our laboratory, and the slightly wet sand test-site (480 mm in depth) corresponds to the playground for children in the public garden Perichaux (Paris 15). Both sands have not been compacted. From Figure 2.4 (b), it has been observed that the lower frequency corresponding to $S_{11} = -10$ dB is estimated to 292 MHz; it appears identical for both sand materials. However, the outdoor sand introduces rapid fading to the return loss S_{11} within the frequency band 1.36 and 3.07 GHz as compared to the indoor sand.

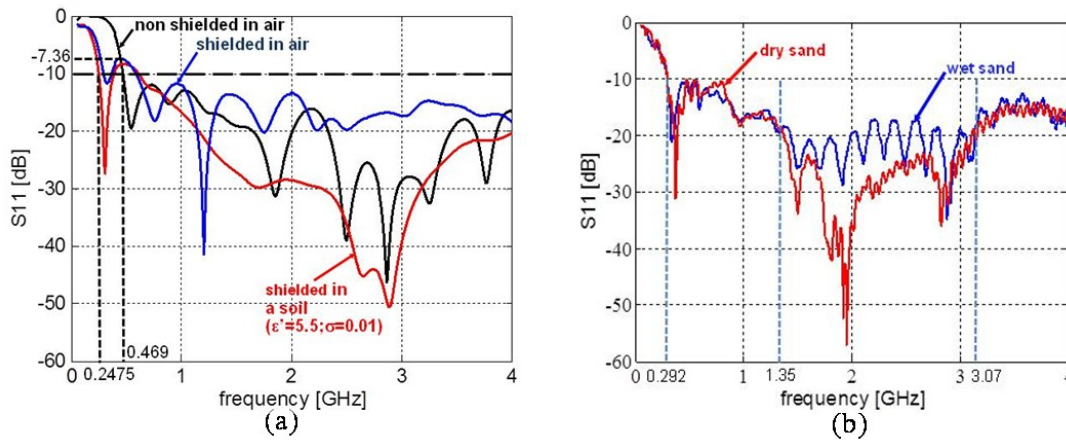


Figure 2.4: a) Simulated S_{11} for shielded and unshielded antenna, on soil and in air, b) S_{11} records over dry and wet uncompacted natural sand; see the test-sites in section III.1 (on the courtesy of F. Sagnard [7]).

II.4. Tx and Rx Antenna configurations for GPR survey

The radar system is made of a pair of transmitting (Tx) and receiving (Rx) shielded triangle bow-tie slot antennas that are positioned on the ground (the elevation is estimated to $h = 1$ cm in the simulations). The generating and recording polarizations depend on the antenna orientations that are not only based on their position relative to each other but also to their orientation relative to the survey line direction (and buried target orientation). Three main configurations can be considered: the endfire configuration (TM polarization, see Figure 2.5a) where the antennas are aligned along their larger dimension, the broadside configuration (TE polarization, see Figure 2.5b) where the antennas face each other symmetrically along

their larger dimension, and the cross-polarization configuration (see Figure 2.5c) where the antennas are oriented at 90° to each other with two orientation possibilities for the transmitting-receiving system. It must be underlined that TE and TM polarizations of the slot antennas are oriented perpendicularly as compared to the orientation of non slot dipole antennas (see details in chapter 5).

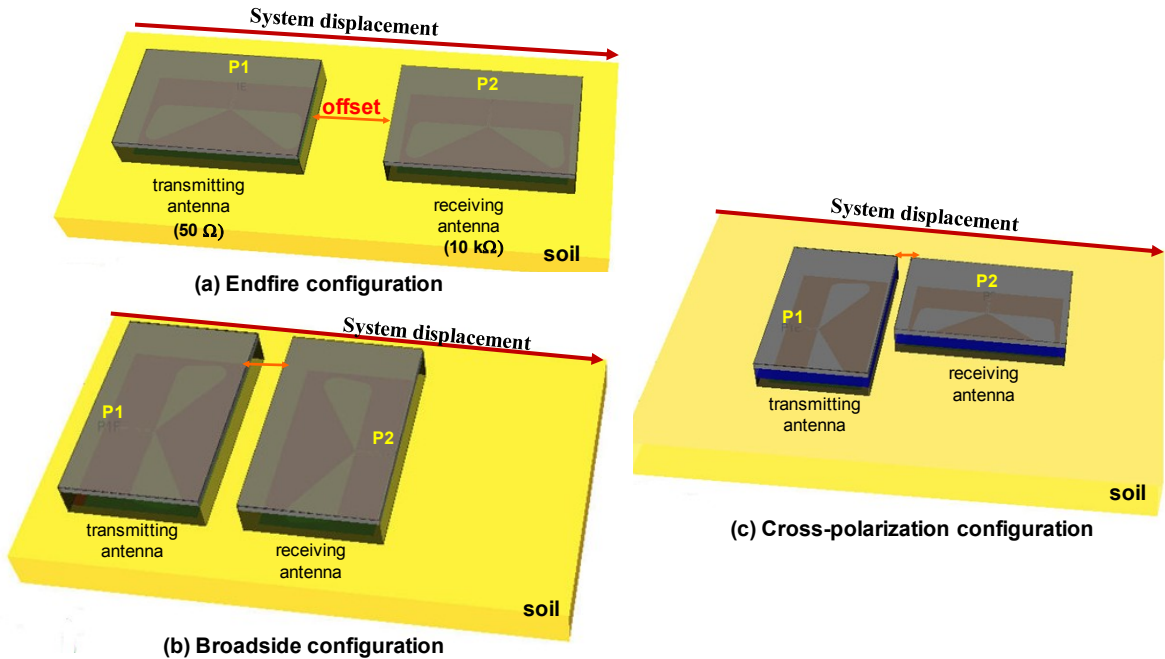


Figure 2.5: Tx and Rx antenna configurations (a) Endfire configuration (TM mode) (b) Broadside configuration (TE mode) and (c) Crossed antenna configuration.

In the end-fire and broadside antenna configurations, the offset value between antennas results from a trade-off between a low strength for the direct path signal and the best possible strength of the useful signal from either buried object or dielectric interface. Using FDTD simulations under EMPIRE, the offset has been varied in the range $[0; 160]$ mm to provide WARR profiles in both configurations on a soil with dielectric characteristics ($\epsilon' = 5.5$ and $\sigma = 0.01 S/m$), see figure 2.6 [7]. The frequency variations of $S_{21}(f)$ magnitude highlight the higher coupling effect between both antennas around 12 dB for frequencies below 1.5 GHz (figure 2.6). It appears that a higher coupling effect at a given offset particularly below 1 GHz is observed in the broadside configuration that can be explained by the lower lateral dimension of each antenna in this configuration. Thus, to obtain a compact system with a reduced coupling at lower frequencies, the antenna offset has been set to 60 mm.

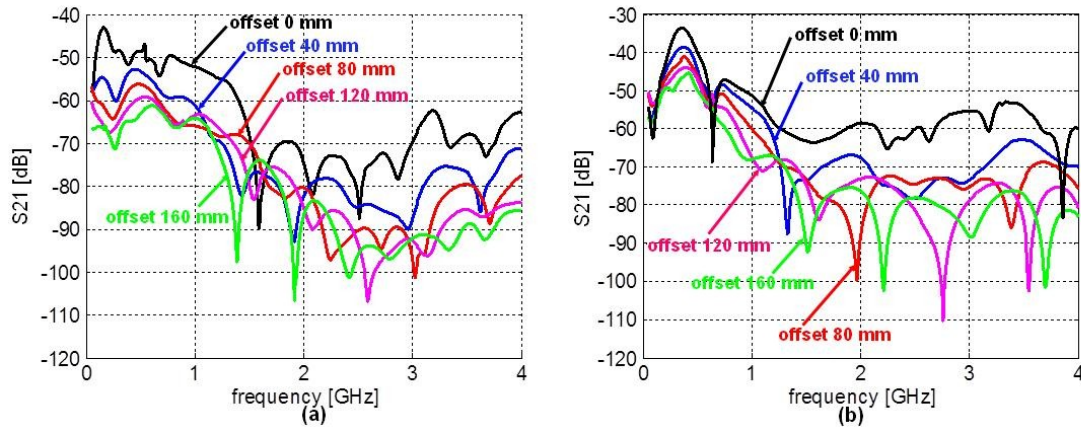


Figure 2.6: Simulated S_{21} versus frequency with variable antennas offsets [0; 160] mm in both configurations (on the courtesy of F. Sagnard [7]). a) endfire configuration, b) broadside configuration.

II.5. Acquisition system

a) Step-frequency radar system

Measurements with the pair of shielded bowtie slot antennas have been made in the frequency range [0.05;4] GHz with a portable VNA (Vector Network Analyzer) ANRITSU MS 2026B. The IF (Intermediate Filter) frequency filter defining the frequency resolution has been defined between 5 kHz and 10 kHz. The bandwidth is made of 1601 frequency samples. Each antenna acts as a module and has its own shield. A full two ports calibration has been made with two 2 m length radiofrequency cables. The offset between antennas has been maintained at 60 mm and the system has been moved manually along a survey line with a distance step of 40 mm. The complex transmission coefficients $\tilde{S}_{21}(f)$ measured in the frequency band [0.05; 4] GHz is recorded and will serve to obtain the radargram (Bscan).

A synthetic pulse used in the FDTD simulations under EMPIRE has been introduced in the experimental data to compare measurement and simulated data. The fundamental pulse used, that serves as a current excitation of the transmitting antenna in FDTD simulations, is the first derivative of the Gaussian function, with duration 0.5 ns corresponding to 98% of the total energy ($t_0=0.33$ ns). Thus, a frequency apodisation associated with each offset has been made to smoothly extend the signal bandwidth from 4 to 9 GHz with zero padding. The impulse signal is multiplied by the measured \tilde{S}_{21} , to further calculate the inverse Fourier transform (IFFT) and obtain time data (figure 2.7) [7]. The calibration of the time zero in the measurements has been made using the theoretical air wave time arrival (time reference at the soil surface to compare with ray path models).

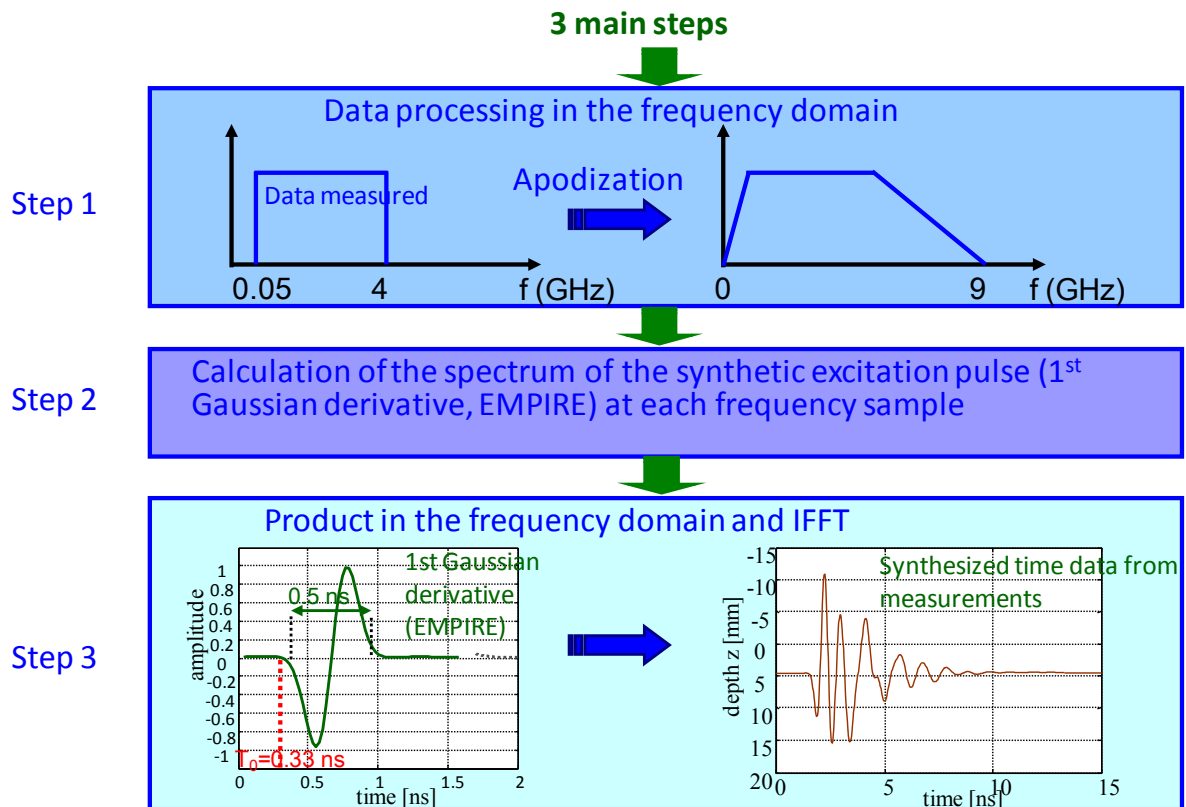


Figure 2.7: Three-steps process to synthesize the data in the time domain and to ease the comparison with the simulated data set (on the courtesy of F. Sagnard [7]).

b) Time domain GSSI systems

The laboratory GeoEND (Department GERS) at IFSTTAR-Nantes has been using for several years the GSSI radar equipments attached to the SIR 3000. The SIR 3000 can be equipped with three pairs of antennas with different size, which the central frequencies f_0 are: 500, 900 and 1600 MHz. The antenna module have the following dimensions: at 500 MHz $33 \times 37 \text{ cm}^2$, at 900 MHz $18 \times 33 \text{ cm}^2$ and at 1500 MHz $10 \times 15 \text{ cm}^2$. In these time domain GPRs, the bandwidth of the excitation signal roughly reaches the value of the central frequency f_0 .

III. Test Sites

The probing the subsurface using the SFCW GPR system has been performed on three test-sites in the open air. These test-sites are partially controlled environments as the layered subsurface structure is known within 60 cm depth, however their dielectric characteristics have been estimated during the measurements. These test-sites that include buried canonical objects, pipes and blades, have served to evaluate the experimental system and to compare field data to numerical data.

III.1. Sand boxes

The first two test-sites are made of pure sand from the Seine valley (France). The first test-site is indoor and consists in a box filled with dry and non compacted sand with

dimensions: depth 740 mm, length 2 m, and width 1 m. It has been first installed at Ifsttar-Paris in 2012. The sand box has served to characterize the bowtie slot antenna radiation properties in the frequency domain using a VNA (see Figure 2.8 (b)). The real permittivity of the sand has been estimated to 3.5.

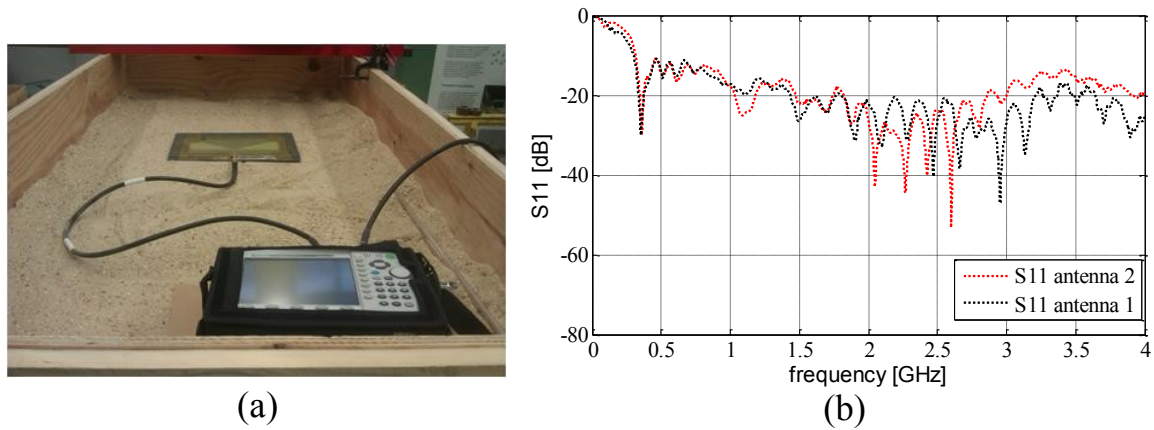


Figure 2.8: a) Indoor test-site made of dry sand within a box of dimension $2 \times 1 \times 0.74 \text{ m}^3$, b) S11 comparison between bowtie antennas (1 and 2).

The second test-site is an outdoor sand box (figure 2.9), which is located in the public children playground at a park of Paris 15th district. The sand with a thickness of 48 cm was not compacted and slightly humid; its real permittivity has been estimated close to 5.5 according to the WARR profile in figure 2.9b [8].

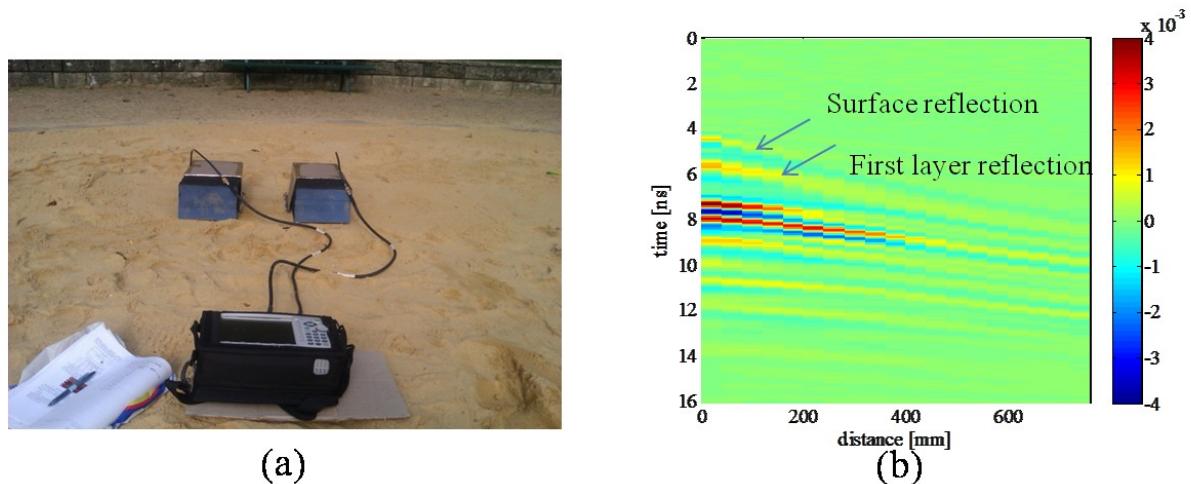


Figure 2.9: a) Outdoor test-site made of wet sand with layered subsurface structure, b) corresponding WARR profile for soil permittivity characterization in the broadside configuration.

Sand is the most common material on the earth’s surface; it is easy to handle and to bury objects.

III.2. Embankment near the IFSTTAR building

The outdoor embankment is situated near the IFSTTAR building in Marne-La-Vallée, along the “boulevard Newton”. The soil is wet after a rainy day and seems to contain compacted clay and silt materials. It includes small stones and debris that are at the origin of

heterogeneities. According to Figure 2.10b, the real permittivity has been measured with a cylindrical coaxial cell [9] filled with a small soil sample. The permittivity was found equal to 15 at the central frequency of 1 GHz on the first day and to 5 after a two-days sunny period of time.

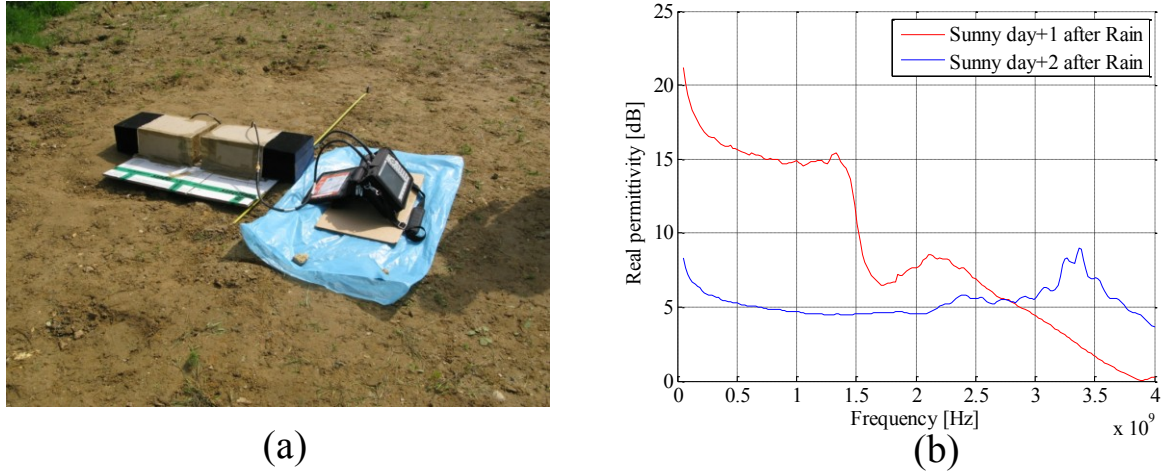


Figure 2.10: a) Outdoor clay/silt embankment near IFSTAR building, b) Clay/silt ground permittivity as function of the frequency.

III.3. The urban test-site Sense-City

The urban test-site takes part of the scale model Sense-City, which is an equipment of excellence for the future national investment program in the period 2015-2019 and is supported by University Paris-Est (Marne-La-Vallée, France) [10]. It is a realistic mini-city demonstrator in the open air that is made of urban innovations focused on instrumented habitat and intelligent road. A first preliminary version has been built in 2015 for test measurements such as visualized in Figure 2.11a, and a larger test-site will be built at the end of 2016 on a nearby area.

At present, the test-site includes some surface and subsurface urban facilities. For example, a part of the test site presented in Figure 2.11 is made of a circular stretch of road where ten aligned utilities (pipes and blades) dielectric or conductive have been buried at depths ranging from 14.5 to 64.5 cm and separated by 70 cm offset. The PVC pipes can be filled with a liquid to bring an additional dielectric parameter in the site. The multilayered structure of the soil has quite different values of real permittivities ranging from 4 to 35. The test-site Sense-City offers the opportunity to study, in a controlled environment, the capability of the GPR technology to display and detect underground urban facilities [11].

The WARR profile in Figure 2.12a has been measured with the bowtie slot antennas; it is found very complicated to analyze it, owing to the high density of adjacent curves, due to the superposition echoes from many shallow layers with low permittivity contrast.

The soil characterization has been performed using the Fixed Offset Method (FOM) in a single profile within a target-free area at the central frequency 900 MHz using the GSSI SIR 3000 GPR system. The raw radargram (without time zero correction and clutter removal) presented in Figure 2.12b shows a layered soil with four layers corresponding to asphalt (layer

1), aggregate cement (layer 2), a natural soil (layer 3), and a wetter natural soil (layer 4) below the geotextile. Within layer 3, an additional sub-layer, namely layer 3b on the Bscan in Fig 2.12b, is the result of the compaction of the natural soil. Providing a prior knowledge on the thickness h for each layer at the construction phase, the real permittivities for each layer can be estimated according to the arrival times.

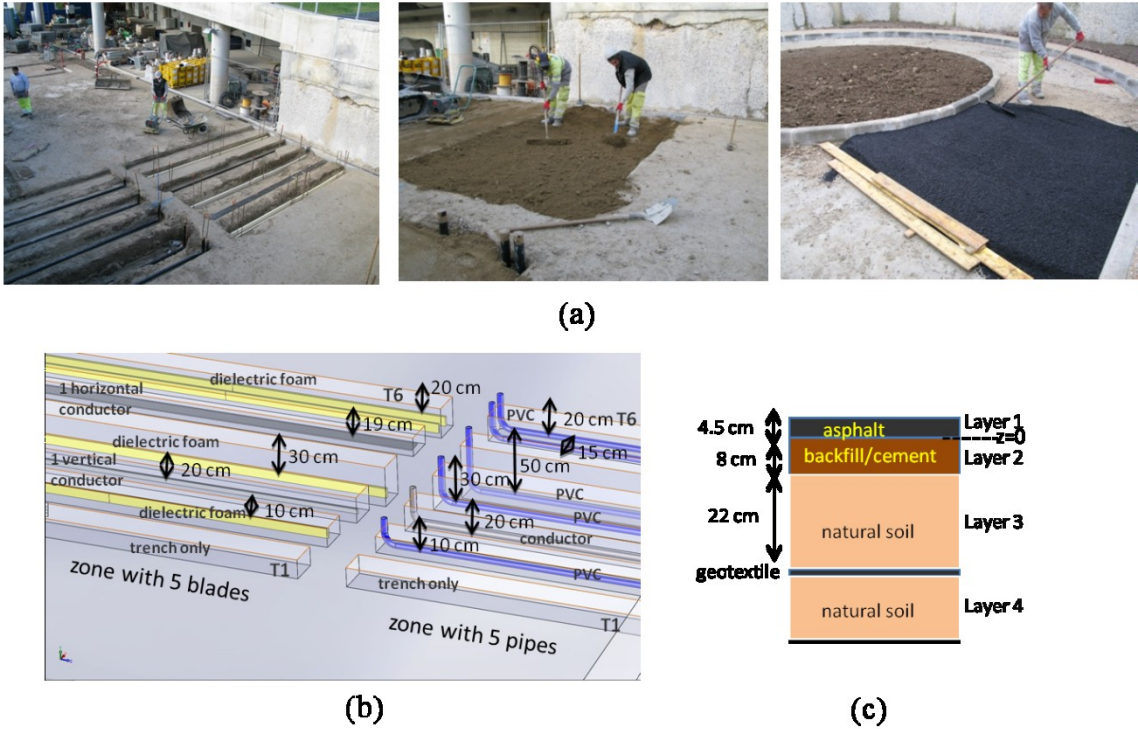


Figure 2.11: a) Urban test-site and the trenches where urban facilities were buried, b) structure of the pipe zone c) Layered structure depths of the urban test-site (on the courtesy of F. Sagnard [7]).

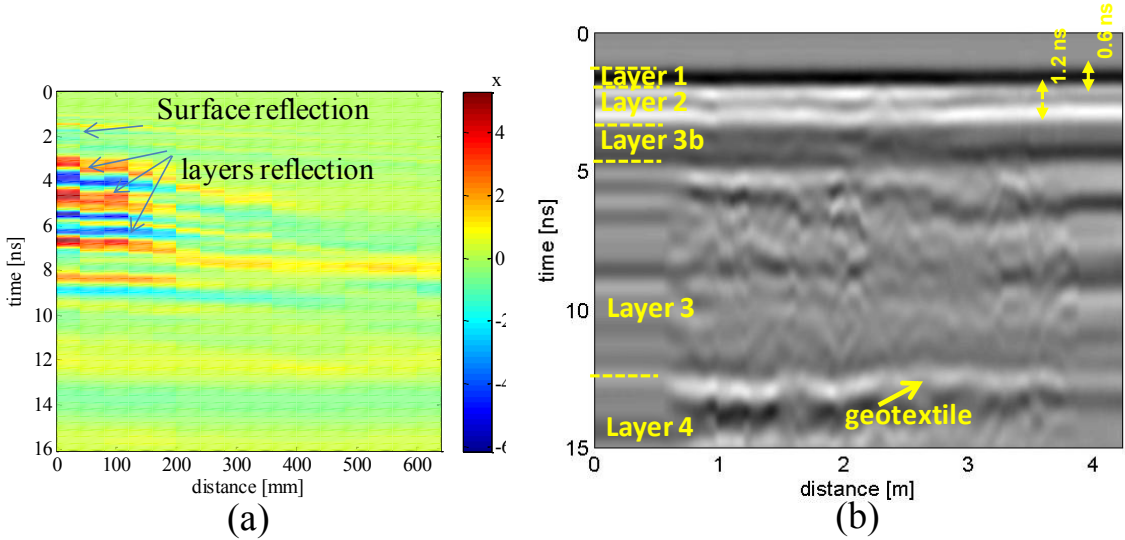


Figure 2.12: Experimental radargram over a target-free area of the urban test-site. a) WARR profile measured by the SFCW radar coupled with the bowtie antennas in the broadside configuration, b) FOM profile measured by the commercial SIR 3000 radar system (linear gain and low and high pass filters applied) at 900 MHz (F. Sagnard et al. [11]).

IV. Conclusion

This chapter presents the experimental equipments used in the several test sites. The laboratory made bi-static GPR system is based on two UWB bow-tie slot antennas with an A4 size. The ground-coupled radar configuration enables better energy coupling to the ground and larger SNR of the target signals.

The data acquisition system uses a VNA, which allows the scanning the [0.05;4] GHz frequency bandwidth with the step frequency technique. The performing of an IFFT along a frequency apodisation allows to synthesize experimental time data to be compared with the simulated data sets.

The field data have been collected over four experimental test-sites, one indoor test-site and three outdoor test-sites. Three test-sites are devoted to the probing of a quasi homogeneous soil, while the fourth one represents an urban test-site. Preliminary tests have been performed to characterize the dielectric permittivity on each test-site to use it as an input parameters for generating synthetic data sets under 3D FDTD simulations.

Bibliography

- [1] M. Slowik, "Influence of GPR measurement conditions on depth penetration and resolution of radar images illustrating lowland valley alluvial fill (field experiment)," *14th International Conference on Ground Penetrating Radar (GPR)*, pp. 707-712, 2012.
- [2] D. Eisenburger, Y. Krellmann, H. Lentz and G. Trilitzsch, "Stepped-frequency radar system in gating mode: an experiment as a new helicopter-borne GPR system for geological applications," *IEEE International Geoscience and Remote Sensing Symposium, IGARSS 2008.*, vol. 1, pp. I-153, 2008.
- [3] A. Saintenoy, J.-M. Friedt, A. D. Booth, F. Tolle, E. Bernard, D. Laffly, C. Marlin and M. Griselin, "Deriving ice thickness, glacier volume and bedrock morphology of the AustreLóvenbreen (Svalbard) using Ground-penetrating Radar," *Near Surface Geophysics*, vol. 11, no. 2, pp. 253--261, 2013.
- [4] J. L. Hager and M. Carnevale, "GPR as a Cost Effective Bedrock Mapping Tool for Large Areas," *14th EEGS Symposium on the Application of Geophysics to Engineering and Environmental Problems*, 2001.
- [5] F. I. Rial, M. Pereira, H. Lorenzo, P. Arias and A. Novo, "Resolution of gpr bowtie antennas: An experimental approach," *Journal of Applied Geophysics, Elsevier*, vol. 67, no. 4, pp. 367-373, 2009.
- [6] K. Kim and W. R. Scott, "Design and realization of a discretely loaded resistive vee dipole for ground-penetrating radars," *Radio science*, vol. 39, no. 4, pp. 1-9, 2004.
- [7] F. Sagnard, "Design of a Compact Ultra-Wide Band Bow-Tie Slot Antenna System for the Evaluation of Structural Changes in Civil Engineering Works," *Progress In Electromagnetics Research B*, pp. 181-191, 2014.
- [8] F. Sagnard, E. Tebchrany and V. Baltazart, "Evaluation of an UWB ground-coupled radar in the detection of discontinuities using polarization diversity: FDTD modeling and experiments," *7th International Workshop on Advanced Ground Penetrating Radar (IWAGPR)*, pp. 1-6, 2013.
- [9] M. Adous, "Caractérisation électromagnétique des matériaux traités de génie civil dans la bande de fréquences 50 MHz – 13 GHz," *PhD Thesis, Université de Nantes*, 2006.
- [10] "<http://sense-city.ifsttar.fr>," *last access on 24/11/2015*.
- [11] F. Sagnard and al., "Utility measurement and detection on the urban site Sense-City using ground-penetrating radar systems," *Internal IFSTTAR report, submitted to IOP Aug 2015*.

List of figures and tables

Figure 2.1: (a) Bowtie-slot Antenna dimensions (in mm), and (b) Surface current distribution and (c) radiation patterns in the TE and TM planes at 450 MHz (on the courtesy of F. Sagnard [7]).....	53
Figure 2.2: Cavity-backed shielded antenna.	54
Figure 2.3: Theoretical logarithmic radiation patterns of the shielded bowtie slot antennas at frequencies 0.45, 0.8, 1 and 2 GHz (on the courtesy of F. Sagnard [7]).....	54
Figure 2.4: a) Simulated S11 for shielded and unshielded antenna, on soil and in air, b) S11 records over dry and wet uncompacted natural sand; see the test-sites in section III.1 (on the courtesy of F. Sagnard [7]).....	55
Figure 2.5: Tx and Rx antenna configurations (a) Endfire configuration (TM mode) (b) Broadside configuration (TE mode) and (c) Crossed antenna configuration.....	56
Figure 2.6: Simulated S21 versus frequency with variable antennas offsets [0; 160] mm in both configurations (on the courtesy of F. Sagnard [7]). a) endfire configuration, b) broadside configuration.	57
Figure 2.7: Three-steps process to synthesize the data in the time domain and to ease the comparison with the simulated data set (on the courtesy of F. Sagnard [7]).	58
Figure 2.8: a) Indoor test-site made of dry sand within a box of dimension $2 \times 1 \times 0.74 \text{ m}^3$, b) S11Comparison between bowtie antennas (1 and 2).	59
Figure 2.9: a) Outdoor test-site made of wet sand with layered subsurface structure, b) corresponding WARR profile for soil permittivity characterization in the broadside configuration.	59
Figure 2.10: a) Outdoor clay/silt embankment near IFSTTAR building, b) Clay/silt ground permittivity as function of the frequency.	60
Figure 2.11: a) Urban test-site and the trenches where urban facilities were buried, b) structure of the pipe zone c) Layered structure depths of the urban test-site (on the courtesy of F. Sagnard [7]).....	61
Figure 2.12: Experimental radargram over a target-free area of the urban test-site. a) WARR profile measured by the SFCW radar coupled with the bowtie antennas in the broadside configuration, b) FOM profile measured by the commercial SIR 3000 radar system (linear gain and low and high pass filters applied) at 900 MHz (F. Sagnard et al. [11]).	61

Chapter 3: Evaluation of statistical-based clutter reduction techniques for the pre-processing of ground-coupled GPR images

Résumé

Ce chapitre définit le 'clutter' comme un signal parasite composé de la superposition du signal réfléchi à la surface du sol, du signal de couplage dans l'air et dans le sol entre les antennes et des signaux de réflexion/diffraction induits par les hétérogénéités présentes dans le sous-sol. Dans le cas du radar couplé au sol, le signal de clutter chevauche dans les domaines temporel et fréquentiel, les signaux utiles provenant des réflexions sur des objets enfouis dans le sous-sol. La suppression du clutter, sujet de ce chapitre, s'avère une première étape essentielle à l'interprétation qualitative et à l'exploitation des images en vue d'extraire des informations associées aux objets enfouis dans les ouvrages du génie civil.

Tout d'abord, une revue bibliographique des techniques de réduction du clutter utilisées dans la littérature pour diverses applications, (localisation de mines dans le sol, imagerie à travers les murs) a été conduite. Parmi les techniques répertoriées, les méthodes d'Analyse en Composantes Principales (ACP) et d'Analyse en Composantes Indépendantes (ACI) ont été sélectionnées, car leur principe de fonctionnement permet potentiellement une utilisation dans de nombreuses configurations radar et de profondeurs de cibles. Ces deux techniques sont détaillées ainsi que leur application spécifique au filtrage du clutter radar. Nous proposons en particulier une adaptation de la méthode ACP pour rendre cette méthode indépendante des variations de RCS (radar cross section) des cibles le long d'un profil Bscan.

Les performances des méthodes de filtrage du clutter radar sont ensuite évaluées sur des données de simulations FDTD et de mesures réalisées sur les sites test présentés au chapitre 2. Dans cette évaluation, la technique de soustraction de la moyenne ou de la médiane sert de méthode de référence car elle est largement utilisée par la communauté scientifique GPR.

Les performances des méthodes sont établies quantitativement à partir des courbes ROC (ces dernières permettent d'identifier les méthodes capables d'atteindre le meilleur compromis entre bonne détection et fausse alarme), et le rapport d'énergie SCNR (rapport signal sur clutter+bruit). L'analyse qualitative des résultats repose sur l'examen de l'image Bscan et d'un signal Ascan associé à l'apex d'une hyperbole.

Les résultats d'évaluation ont montré dans le cas de cibles peu profondes, la supériorité de la méthode ACP, et dans le cas de cibles dont la profondeur d'enfouissement est supérieure ou égale à une longueur d'onde, celle de la méthode ACI. Cependant, la technique de référence par soustraction de la moyenne ou médiane s'avère la technique la plus robuste lors de l'étude paramétrique associée aux géométries variées de sol et objets lors des simulations et des expérimentations.

Contents

Résumé	65
I. Introduction.....	67
II. Existing clutter reduction techniques.....	68
III. Principal Component Analysis (PCA)	77
III.1. Introduction	77
III.2. Algorithm	78
III.2.1. Matrix Decomposition	78
III.2.2. Clutter reduction using PCA.....	79
III.3. Improved clutter reduction technique using PCA.....	81
III.3.1. Problem overview	81
III.3.2. Principle and illustration for modified PCA	81
III.3.3. Application to the data.....	82
IV. Independent component Analysis (ICA).....	84
IV.1. Introduction	84
IV.2. Application strategies for ICA	84
IV.3. Algorithm	86
IV.3.1. Preprocessing.....	86
IV.3.2. The FastICA algorithm.....	87
IV.3.3. Independence estimation	88
IV.3.4. ICs selection	89
IV.4. ICA applied to GPR data.....	90
V. Performance assessment of the clutter reduction techniques	91
V.1. Introduction	91
V.2. Assessment criteria	92
V.2.1. Qualitative comparison	92
V.2.2. Signal to Clutter plus Noise Ratio (SCNR)	92
V.2.3. ROC curves.....	93
V.3. Results on the simulated data set	95
V.3.1. Data set	95
V.3.2. Results	97
V.4. Results on the field data set	108
V.4.1. Data set	108
V.4.2. Results	108
VI. Conclusion	114
Bibliography	116
List of figures and tables.....	121

I. Introduction

A GPR system delivers an electromagnetic wave that propagates into the ground. The measure of the reflected echoes allows detecting dielectric contrasts. The moving of the system along a linear scanning direction allows to image the sub-surface to form Bscan images. Dielectric targets with a small lateral extension induce defocusing hyperbolae that are noticeable. The problem of the detection and the classification of buried targets is important and challenging as targets are usually blurred by a set of unwanted signals (the clutter) which are uncorrelated to the target signals but overlap in time and frequency [1] [2]. The clutter leads to reduced detection possibilities in GPR images, as it appears difficult to distinguish between both signals and clutter without applying proper signal processing techniques, and particularly when the target is small, shallow, and low-contrasted with the surrounding soil. GPR performance highly depends on the ability to successfully differentiate the target signal from the clutter.

The clutter must be distinguished from noise $n(t,x)$, as noise is random in nature and generally differs spectrally from the target response. The noise is usually assumed to originate from electronics and as such, it is modeled by a zero-mean white additive gaussian signal (White Gaussian Noise, WGN).

The clutter in experimental GPR signals is usually made of three components (see Figure 3.1):

- The cross-talk or direct coupling (cross-coupling) between the transmitting and the receiving antennas $c(t,x)$ in air and in the soil (antenna ringing, cable reflections...)
- The reflection $b(t,x)$ from the air-ground interface (ground bounce)
- The scattered signals $sc(t,x)$ from other objects, discontinuities and inhomogeneities (tree roots, air gaps, stones...) within the soil.

The similarity between all these unwanted signals is that they may spread over the whole Bscan image and on the same time intervals, whereas target response exists on a limited image zone of the Bscan with varying time intervals.

The basic model of an Ascan signal $y(t,x)$ is made of the superposition of four components as follows:

$$y(t,x) = s(t,x) + c(t,x) + b(t,x) + sc(t,x) \quad (3-1)$$

Where $s(t,x)$ represents the target signal. Besides, the principle of superposition that sustains the latter data model assumes a weak electromagnetic interaction between the contributors. This latter assumption may fail for shallow-buried target, because the scattering process over the target may modify the clutter signal and vice versa.

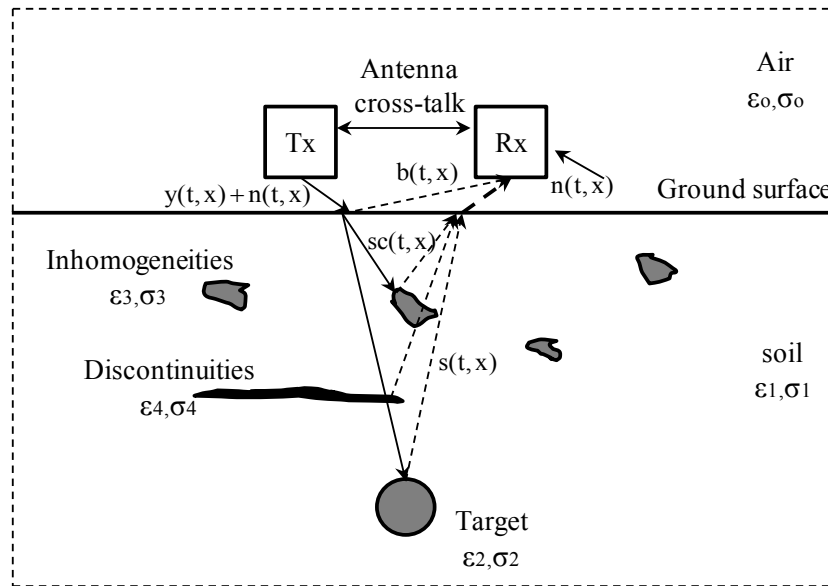


Figure 3.1: Typical GPR transmitter - receiver configuration model for target detection.

Generally, the direct coupling $c(t, x)$ between the antennas and the surface echoes $b(t, x)$, arises earlier than the other signals and appears much stronger than the reflecting signal induced by a buried dielectric target. Both components, generally quasi-stationary (in time and space along the Bscan) are easier to distinguish and eliminate. Signals $sc(t, x)$ resulting from inhomogeneities within the soil, give incoherent clutter that is a more difficult to eliminate.

Preprocessing techniques appear necessary to improve and ease the qualitative interpretation of GPR data. The main purposes of preprocessing techniques are signal conditioning and data correction before applying any further processing method [3] [4]. Clutter reduction is one of the most important preprocessing steps. Many clutter reduction techniques are proposed in the literature, and this is currently an active research topic because of the complex nature of the clutter.

This chapter describes briefly a few well-known clutter reduction techniques. The two statistical-based techniques, i.e., ICA (independent component analysis) and PCA (principal component analysis), have been assessed on simulated and experimental GPR data sets and have been compared with the well-known mean-subtraction technique.

II. Existing clutter reduction techniques

The main developments associated with clutter reduction have been made in the field of mine detection and identification using a GPR system [5] [6]. Clutter reduction techniques have been extended to the detection of damages and utilities in civil engineering structures, and to thru-the-wall imaging [7]. Actually, there exists a large variety of mines (dielectric or conductive), which are shallowly buried into the ground. A discontinuous subsurface distribution and a rough soil surface can lead to a non-stationary ground clutter. Nowadays, as mines encountered are often dielectric, shallow and small, their detection has required developing of a wide variety of signal processing techniques to extract information among unwanted signals.

This section proposes to present the existing clutter reduction techniques for civil engineering purposes into three main classes [8], and to give details relatively to their operating domains.

1. Background subtraction techniques

This family of techniques is the simplest one and is generally used in the time domain. It is assumed that the ground reflection is stationary along the scanning distance, and occurs earlier than the target reflection, i.e., it does not overlap with the target signal in the time domain. These techniques have to be used with cautious and are inappropriate when the targets are very shallow. They include early time gating, and mean (or median) subtraction technique (MST) [9]. Some authors use either predefined or reference background signatures for subtraction [10], [11], the scaling and the time shift of the reference signal can be tuned to Ascan signal. But prior information is not always available in civil engineering applications, and supposes a manual operation to this aim.

The mean subtraction technique is the most technique used. Here, the mean signal is supposed to estimate the clutter to be filtered out. This technique is suited for removing steady clutter and high frequency noise from data. It includes the following three approaches:

1. Mean subtraction calculated across all traces: The simplest process estimates the background signal as the average or median value across all N traces (B-scan). This approach assumes that the ground has steady dielectric permittivity and that the ground surface is constant along the scanning direction. Accordingly, it is adapted only to a tightly controlled, homogeneous environment with a smooth surface [12].
2. Mean subtraction with a reference background signal: the reference background is usually calculated either in the absence of a target [13] or over the part of the Bscan image which is assumed target-free. Then the reference signal is subtracted from a current A-scan. The window must be wide enough to make an accurate estimate, with a low variance, in a narrow window enough to avoid introducing effects from the nearest target response. This approach is better suited than the first one when the target is shallow, because in the first approach the calculated mean value is affected by objects reflection, leading to an artifact in the image after the subtraction.
3. Mean subtraction over a moving window: the background signal is estimated as the average of surrounding A-scans along a moving window [9]. However, the window must be wide enough to make an accurate estimate, with a low variance, while narrow window enough to avoid introducing effects from the changes in the local background characteristics. This approach is suited for deep targets and when slight variation occurs in the properties of the ground surface along the scanning direction that causes the clutter to be no longer uniform on the entire image. Two problems arise in this approach: the first relies on the selection of the appropriate window to obtain accurate results, and the second is related to a shallow object that disturbs the calculation of the mean value.

Consequently, we consider that the second approach is best suited to study both shallow and deep buried targets. Moreover, the median value subtraction technique can be used instead of the mean value technique. The median subtraction is better suited for spike removal and serves as a de-spiking or clean-up filter. However, both mean and median subtraction techniques are ineffective in the presence of spatially unsteady clutter (owing to rough surface and/or non homogeneous soil) because they are based on an estimation of a single value; used for the subtraction of an unsteady clutter. Inaccurate background estimation may affect the accuracy of any further target characterization.

2. Classification-based techniques

These techniques rely on clutter parameterization or statistics. As opposed to the background subtraction technique, the classification-based approaches rely on the form of the clutter model (unsteady form) as well as on the hypothesis that sustains its statistic features from Bscan measurements. These techniques are: Prony-based algorithms (linear combination of damped sinusoids) [14], the SVD (Singular Value Decomposition) related techniques [15] [16] [17], the information theoretic criterion [18], the adaptive Linear Prediction (LP) theory [19], the Sliding-Window Space-Frequency Matrices [20], the wavelet packet decomposition [21] [22], subspace decomposition techniques [23] [24], and compressive sensing (CS) methods [25].

- a. Model-based techniques: Prony method is among the signal processing methods that uses a parametric modeling of the target signal as a reference. The method relies on the decomposing the GPR traces in the frequency domain into the sum of damped exponentials. Firstly, it separates the clutter that it supposes to have high resonant energy poles, then it determines the damped function for the reference target signal plus a delay function, and it separates by iterations the measured target from clutter residuals, by estimating the corresponding complex parameters using the least square error (LSE) criterion. There are three major limitations: unknown number of resonant poles, the noise level, and the influence of non-resonant signals. TLS-Prony and LCTLS-Prony methods have been introduced later to improve the robustness against the noise. The method showed very good results in [14] on rough and heterogeneous grounds according to ROC curves.
- b. Statistical-based techniques [15] [16] [17]: These methods allow Blind Source Separation (BSS) between the clutter and the target signals. They include the SVD (Singular Value Decomposition), the Principal Component Analysis (PCA), and the Independent Component Analysis (ICA). These methods rely on different statistical properties sustained by the clutter and the target signals. They have been selected in sections III and IV of this chapter owing to their expected performance in estimating and detecting the clutter. PCA relies on the decorrelation and energy separation between the clutter and the target, while ICA only relies on the statistical independency between the latter signals.
- c. Other related works to SVD are the Information Theoretic Criterion (ITC) (it is used along with the SVD technique to improve the detection capabilities of the latter), the factor

analysis [26], and more recently the 2D-PCA [27]. The latter technique is based on the spatial averaging process over a number of Bscan images before applying 1D-PCA (or PCA by extension).

- d. The linear prediction technique assumes that the clutter signature can be predicted in the frequency domain as the parametric modeling of adjacent Ascans with a few coefficients. The estimation of the coefficients of the clutter model is made adaptive to the height variation of the antenna above the ground (a variable time shift) and to the movement along the scanning direction. The coefficients are calculated using the Maximum Likelihood (ML) method [19] then used for locating the target along the scanning direction. The processing is made in the frequency domain to gain further advantage of splitting the analysis into frequency subbands.
- e. Sliding-Window Space-Frequency Matrices in [20] decompose the Bscan in the time domain according to a sliding window along the scanning direction. Later, each sub-Bscan is processed using the matrix decomposition algorithm SVD in the frequency and time domains to separate the clutter from the target. The first windows of the Bscan contain only clutter information, therefore they are used to extract the clutter components, and these window are compared to other windows components to consider rough clutter variation and finally subtract them from the entire Bscan. It shows very effective results on rough clutter, on mid-depth embedded targets (partial overlapping) and in homogeneous ground.
- f. The Wavelet Packet Decomposition (WPD) in [21] [22] is a time-space segmentation. This technique allows the segmentation of the locations in the Bscan image with embedded anomalies (targets and discontinuities), and to separate them from the locations without anomalies, using a background signal model estimated from a homogeneous area. It applies the Translation Invariant Wavelet Decomposition (TIWPD) algorithm, based on the entropy in a moving window, to detect anomalies. It was tested on very shallow targets (0.5 cm to 4 cm) [21] [22], and showed better performance than the MST. As a counterpart, any soil heterogeneity can be detected as a potential target.
- g. Many subspace decomposition techniques are described in the literature [23] [24]. In most cases, they are combined to either a matched filter or to a polynomial estimation algorithm to obtain the full suppression of the non-stationary clutter.
- h. The Compressive Sensing (CS) technique in [25] is based on a reconstruction scheme in the frequency domain. It reconstructs a sparse signal from a few numbers of linear measures at each position, for different frequencies. It is assumed that the ground clutter signatures are similar at different frequencies while the target signatures are not. Therefore this similarity is used with the Maximum Likelihood (ML) criterion to estimate the time shift, and to obtain a clutter model at each position for later subtraction. It has shown good detection for shallow and deep targets in a homogeneous ground.

3. Filtering techniques

This class of techniques consists in using various filtering techniques in the frequency, the time or the space domain [28]. Lot of techniques and combinations of them exist in the literature; they cannot all be cited here. Among others, this section introduces the decorrelation and symmetry filtering algorithm [29], Digital filtering [30], Time-Frequency Separation technique (TFS) [31] [32] [33], and the Kalman filter [34] [12].

- a. The symmetric filtering (SF) algorithm [29] assumes that the clutter and anomalies are spatially asymmetric features while pipes and mines have symmetrical shapes along the scanning direction in the Bscan images; thus, the SF algorithm aims at filtering asymmetric spatial responses. It uses median and mean subtraction before applying SF to remove the smooth clutter. Then, it locates the symmetry points through the detection of the max (apex) for each target. The detection results were very efficient for shallow objects.
- b. Digital filtering (DF) in [30] operates in the frequency domain to deal with shallow targets, for which clutter and target signatures overlap in the time domain. As a matter of fact, it is only relevant for clutter and target whose spectra do not overlap to each other in the frequency domain. The technique requires to determine the cutoff frequency of both spectra (for clutter and target), in order to define the resulting frequency filter. This method is conditioned by the lateral extension of the target signature that must be small compared to Bscan width.
- c. Time Frequency Separation (TFS) transforms in [32] [33] are time-frequency analyses that allow separating clutter and target signals in the time-frequency plane. The clutter and the target signal are expected to not overlap simultaneously in the time and the frequency domains (they show slight different spectra and arrival times). For example in [31], they separate the hyperbola from the clutter reflection by using a Blind Source Separation (BSS) algorithm; it is based on the analysis of the correlation between observed Ascans in the Time-frequency plane. It calculates the cross Time-Frequency Distribution (TFD) function on the time-frequency plane, and interprets the obtained TFD to extract corresponding cutting edges. It is well adapted to the analysis of non-stationary data and showed very good suppression of rough clutter and shallow targets.
- d. Kalman filter is one of the most frequently used methods for filtering slowly non stationary signals in various applications. In [12], it is applied for removing the noise and the clutter. It decomposes the Bscan into non-overlapping horizontal bands with constant height (opposed to other techniques, vertical bands) before applying the Kalman filtering algorithm that tries to separate the two models: target-free model, and target-present model. The Kalman filter technique is computationally expensive and supposes that the target is contained in one band and that the noise have Gaussian distribution.
- e. Physical-based modeling: the work developed in [35] combined three techniques for clutter reduction: linear transfer function, the Green function and a phase shift migration. They show good performance on shallow targets.

4. Synthesis

This section proposes to synthesize the existing clutter reduction techniques, in order to help to select the best matched techniques to the scope of the given application. The two next tables collect the main characteristics of the existing methods and their conditions of assessment which can be deduced from the literature review.

The main conditions of assessments of the existing techniques are resumed in Table 3.1. Within the scope of the application of this thesis, we are looking for the methods which show performance to detect small and shallow buried targets. Besides, for the sake of the various tests on simulated and experimental data, the method is expected to detect with equivalent success rates the targets with various RCS (radar cross section) (strong RCS on metallic target, smaller RCS on dielectric target). The first is intended to provide a large modification of the antenna scattering at near field compared to dielectric target; then, the clutter may strongly change along the scanning direction, especially at the apex of the hyperbola. Thus, among different criteria, we put emphasis on the following considerations:

- The depth of the targets relatively to λ_{mat} , the wavelength within the embedded materials; the latter depends on the dielectric permittivity of the subsurface and on the center frequency of the radar pulse. The ratio in Table 3.1 is a rough average of many evaluated cases in each technique at different depths, different frequencies and different media. The ratio $depth/\lambda_{mat}$ gives an idea about the depth of the buried target.
- It is worth mentioning that, in case of multiple buried targets into the subsurface, the overlapping of echoes in time depends, not only on depth (arrival times), but also on the antennas beam pattern, and consequently on the dimensions and the types of the antennas used.
- The heterogeneous/homogeneous nature of the subsurface, the surface roughness of the ground (rough/smooth) and the RCS of the target may influence the stationnarity of the clutter along the scanning direction.

For the processing point of view, Table 3.2 gives the main features of the existing clutter removal techniques. The selected methods must cope with the case of overlapping echoes in either the frequency or in the time domain, and the case of slowly varying clutter along the scanning direction (equivalent to a non-stationary signal). The selected methods are intended to exploit relevant and realistic assumptions on the data, and to make the clutter removal processing semi-automatic or fully unsupervised (i.e., to minimize the manual operation as much as possible).

It is worth mentioning that this work is mostly devoted to the detection of small targets that implies the detection of the scattering hyperbola on 2D images. Another criterion will be required to deal with the applications for which the targets have larger spatial extension, like for example the detection of debonding areas within pavement structures.

Within this context, it is then proposed to further study the two statistical-based data decomposition techniques to remove the clutter from the data, namely the Principal Component Analysis (PCA) and the Independent Component Analysis (ICA). Both will be compared to the conventional mean subtraction technique MST (or background removal).

PCA and ICA are multivariable and statistical techniques aiming at reducing the data dimensionality.

Basically, PCA (resp. ICA) relies on the small correlation magnitude (resp. independency) between the clutter and the target signal. PCA uses the second order statistics to perform the correlation analysis, whereas ICA requires higher order statistics (fourth moment). As opposed to ICA, the conventional PCA is sensitive to the energy ratio between the clutter and the target signals along the scanning direction. Both techniques use limited prior information on the data. The statistical properties of both methods are expected to not be influenced by the overlapping between the two signals, i.e. the depth of the target, and by the likely variations of the clutter along the scanning direction.

Besides, PCA and ICA have been partially tested and compared for targets at various depths and for heterogeneous subsurface.

<i>Evaluated on:</i>	<i>Depth</i> λ_{mat}	Shallow/Deep targets	Surface roughness	Heterogeneous/Homogeneous subsurface
MST	All depths	Shallow+/Deep +	Rough-/smooth+	Heterogeneous-/Homogeneous+
Time gating	N.A.	Deep +	Rough+/smooth+	Heterogeneous-/Homogeneous+
Predefined background	0.93	Shallow-/Deep +	Rough-/smooth+	Homogeneous+
Prony methods	0.46	Shallow+/Deep +	Rough+/smooth+	Heterogeneous+/Homogeneous+
SVD/PCA literature	N.A.	Deep +	Rough-/smooth+	Homogeneous+
ICA literature	N.A.	Deep +	Rough+/smooth+	Homogeneous+
Evaluated PCA	0.43 →1.56	Shallow+/Deep +	Rough+/smooth+	Heterogeneous+/Homogeneous+
Evaluated ICA	0.43 →1.56	Shallow-/Deep +	Rough+/smooth+	Heterogeneous-/Homogeneous+
LP theory	N.A.	Shallow+	Rough+/smooth+	Heterogeneous+/Homogeneous+
Sliding-Window Space-Freq	0.5 →1.5	Shallow+/Deep +	Rough+/smooth+	Homogeneous+
WPD Space-Time	0.32 →0.67	Shallow+	smooth+	Homogeneous+
subspace decomposition	0.75 →3	Shallow+/Deep +	Rough+/smooth+	Homogeneous+
CS	0.31 →2.33	Shallow+/Deep +	Rough+/smooth+	Homogeneous+
SF	0.32	Shallow+/Deep +	Rough+/smooth+	Heterogeneous+/Homogeneous+
DF	0.31 →0.62	Shallow+	Rough+/smooth+	Homogeneous+
TFS	0.37 →1.87	Shallow+/Deep +	Rough+/smooth+	Homogeneous+
Kalman filter	N.A.	Deep +	Rough+/smooth+	Homogeneous+

Table 3.1: Conditions of assessment of the existing clutter removal methods. The colored methods are detailed in the two next sections; and the ones in purple are evaluated within the scope of our application in section 5. The ones in black are a complete state-of-the-art; the +/- symbols indicate if the methods reach good/bad performance on specified conditions (shallow or deeply buried target, strong or small surface roughness).

<u>Processing Characteristics:</u>	1D/2D²	Filtering	statistics	Supervised /Automatic	Prior Knowledge
MST	1D	-	+	A	No
Time gating	1D	+	-	S	No
Predefined background	1D	-	-	A	Yes
Prony methods	1D	-	+	A	Yes
SVD/PCA literature	1D	-	+	S	No
ICA literature	1D	-	+	A	No
Evaluated PCA	1D	-	+	S	No
Evaluated ICA	1D	-	+	A	No
Linear prediction theory	1D	+	+	A	Yes
Sliding-Window Space-Frequency	2D	+	+	S	No
WPD Space-Time	2D	+	+	A	Yes
subspace decomposition	1D	+	+	S	No
CS	2D	+	+	A	No
SF	1D	+	-	A	No
DF	2D	+	+	A	Yes
TFS	2D	+	+	S	No
Kalman filter	1D	+	+	A	No

Table 3.2: Main features and characteristics of the existing clutter removal techniques. The colored methods are detailed in the two next sections; and the ones in purple are evaluated within the scope of our application in section 5. The ones in black are a complete state-of-the-art.

² 1D: temporal, frequency or spatial method; 2D: time-frequency, time-space or frequency-space method

III. Principal Component Analysis (PCA)

III.1. Introduction

Principal component analysis (PCA) is a multivariate technique analysis based on the second-order statistics that analyzes a data set in which the data are described by several inter-correlated dependent variables [36]. PCA is a way of identifying patterns in data, and expressing the data in such a way as to highlight their similarities and differences.

The algorithm aims at decomposing the components of the input data on a set of orthogonal basis vectors, into uncorrelated components namely the Principal Components, PCs. PCs with the largest eigenvalues come first and contribute the most to the variations of the data set, as opposed to the smallest eigenvalues. As a result, PCA allows to express the original data set in another domain by means of linear transformation. However, it appears difficult to assign any physical meaning to the individual components (PCs). The PCs are decorrelated and represent a linear combination of dependent and independent variables from the original data set.

PCA applications mainly concern data compression, noise filtering, signal restoration, face recognition and other image processing [36] [37]. PCA has been used on GPR data for clutter reduction purposes.

Assuming that the radargram (Bscan) is made of N vectors $M \times I$ (Ascans) issued from the radar displacement along the scanning direction, forming the data matrix $X(M \times N)$ (where $N < M$), the PCA algorithm is given in the following linear transformation:

$$Y = SX \quad (3-2)$$

Where Y has the same dimension as X , but is formed from fewer components. The data contained in X represent the combination of the target signal, the clutter and the noise. It can represent the GPR data in either the time or the frequency domain. PCA (as in ICA later on) technique aims at transforming the matrix X containing the sum of responses, into a matrix Y containing only the desired target signal.

PCA (and ICA) is a technique of array processing and data analysis that will consider matrix X as the only input without any prior knowledge of the target and clutter signatures. PCA separates data based on correlation between adjacent Ascans (probably strongly correlated), this correlation measures the degree of similarity between two adjacent points, and thus a high correlation means that clutter is more likely in this region because it has less time variance between the Ascans. The final set of data Y ought to be mutually uncorrelated and gaussianly distributed.

As detailed in the next section, the PCA algorithm is composed of three steps: the decomposition of the data, the selection of the principal components using the selection criteria and finally, the back projection to the initial space (linear transformation) with the clutter removed and an improved SNR. Before performing PCA, the raw data in matrix X are normalized to zero mean along each Ascan as follows:

$$x_{ij} = x_{ij} - \frac{1}{M} \sum_{i=1}^M x_{ij} \quad (3-3)$$

Where x_{ij} denotes the i^{th} time sample in the j^{th} measurement (Ascan).

III.2. Algorithm

III.2.1. Matrix Decomposition

The PCA algorithm can be performed directly on the raw data, i.e., the rectangular $M \times N$ matrix X , or on the associated covariance $M \times M$ matrix. Thus, the two decomposition approaches are then the singular value decomposition (SVD) and the eigenvalue decomposition (EIG), respectively [27] [34].

a) Eigen value decomposition (EIG)

The covariance matrix C_X ($M \times M$) of the raw data X is defined as follows (case of real data):

$$C_X = \frac{1}{M-1} X^T X \quad (3-4)$$

It expresses the correlation characteristics between each pair of A-scans, i.e., the degree of statistical similarity; high magnitude value indicates a strong mutual correlation while a zero value indicates completely uncorrelated data.

Two cases emerge for the covariance matrix decomposition: the right covariance matrix $X^T X$ and the left covariance matrix XX^T . In this work we are interested in the right covariance matrix $X^T X$ that gives the correlation between different Ascans vectors and not the correlation between different time vectors. It must be underlined that the normalization $M-1$ is generally used (instead of the full number of samples M) to afford unbiased estimates of covariance.

The covariance matrix C_X is then decomposed [38] into its eigenvalues and eigenvectors as follows:

$$C_X = V D V^T \quad (3-5)$$

V is an orthogonal matrix ($V^T V = I$) with size $N \times N$ whose columns are the eigenvectors. D is the diagonal matrix with size $N \times N$ which contains N non negative eigenvalues λ_j . In practice, the eigenvalues and the corresponding eigenvectors are sorted afterwards in decreasing magnitude order.

b) Singular Value Decomposition (SVD)

The SVD decomposition [39] which is applied on the $M \times N$ dimensional raw matrix X matrix is known to be faster than the Eigen decomposition of the associated covariance matrix. Within this decomposition, the PCs are automatically ordered according to their magnitude. Then, the matrix X is decomposed into a product of three matrices as follows:

$$X = U S V^T \quad (3-6)$$

Where U is an orthogonal matrix of size $M \times N$ whose columns are the left eigenvectors of the covariance matrix XX^T , S is a diagonal matrix of size $N \times N$ containing the singular values of the matrix X (i.e., the square roots of the right eigenvalues of the covariance matrix $X^T X$)

and V is an orthogonal matrix of size $N \times N$ whose columns are the right eigenvectors of the covariance matrix $X^T X$.

Compared to the Eigen decomposition, it can be shown that $S^2 = D$, and the singular values are the square roots of the eigenvalues of the covariance matrix, i.e. C_X :

$$C_X = X^T X = V S U^T U S V^T = V S I S V^T = V S^2 V^T \quad \text{with } U^T U = I \quad (3-7)$$

However from equation (3-5) we have:

$$C_X = V D V^T \quad (3-8)$$

$$\text{Hence the result } D = S^2 \quad S_j = \sqrt{\lambda_j} \quad 1 \leq j \leq N \quad (3-9)$$

N.B: Contrarily to the Eigen decomposition, it must be underlined that the covariance matrix used in the SVD algorithm has not been normalized.

c) Data reconstruction using PCA

The final step in PCA algorithm consists in removing the components that contains the clutter signal. By considering the SVD approach, (Both decomposition approaches led us to the same final result) the selection process chooses a specific number of eigenvectors to construct the reduced matrix vectors \hat{U} (respectively \tilde{V} for the Eigen decomposition). Then project the data X on the new orthogonal matrix \hat{U} to obtain matrix Y containing the sum of the selected PCs:

$$Y = \hat{U}^T X \quad (3-10)$$

Next the algorithm projects the reduced data on the initial data base, using the inverse³ of \hat{U}^T .

$$X_o = \hat{U} Y \quad (3-11)$$

Where X_o represents the reconstructed data of the selected information (eigen images).

III.2.2. Clutter reduction using PCA

The amount of information contained in each eigenvector u_j of matrix U (respectively v_j of matrix V) is directly proportional to the corresponding singular value s_j from matrix S (respectively eigenvalue λ_j from matrix D). And the singular values can be sorted in descending order according to their magnitude and the corresponding eigenvectors in matrices U and V reordered in the same way (e.g., Figure 3.9i (top)).

The surface reflects most of the energy along the scanning direction and then contributes the most to the image components. Thus, the PCs selection process assumes that the clutter has the largest eigenvalues throughout the data, i.e., the obtained matrix X_o , is composed by the eigenvalues attached to the target signal and those of the noise, which are the smallest.

The indexes k_1 and k_2 allow to distinguish between the three categories of components (clutter, target and noise). Then, the data matrix X can be then re-formulated with the help of the matrix decomposition according to:

³ This equality is true because U is an orthogonal matrix, and it verifies: $U^T = U^{-1}$

$$X = \sum_{i=1}^N S_i u_i v_i^T = \sum_{i=1}^{k_1} S_i u_i v_i^T + \sum_{i=k_1+1}^{k_2} S_i u_i v_i^T + \sum_{i=k_2+1}^N S_i u_i v_i^T \quad (3-12)$$

$$X = X_{Clutter} + X_{target} + X_{noise} \quad (3-13)$$

k_1 and k_2 are usually fixed according to some heuristic rules:

1. After ordering, the last singular values within the rank $[k_2+1, N]$ are considered as noise and do not contribute to the information contained in the data. k_2 is usually fixed such that the sum over the singular values from 1 to k_2 reaches 90% (energy percentage) of the total sum of all the singular values (99% in [15]). As a result, the synthesized data is expressed with the two first terms in eq. (3-12) and show an improved SNR.
2. The clutter or non-target related signals are usually contained in the first k_1 singular vectors because of their high energy (as in [20]); k_1 is usually equal to one for a real signal and can be equal to two for some limited cases.

The clutter-free dataset is then synthesized by projecting the remainder of the main components (the interval $[k_1, k_2]$ of the indexed principal components) as follows:

$$X_o = \sum_{i=k_1+1}^{k_2} u_i s_i v_i^T \quad (3-14)$$

N.B: In the literature, some authors visualize the eigenimages individually, i.e., the matrix $u_i v_i^T$ for each PCs, and selected manually some of them [28]. To this aim, the line of U^T which represents the desired PC rank is multiplied by the matrix X . Every part of the original signal x_j in eq. (3-12) can be represented as a weighted superposition of eigenimages.

In Section V, the PCA technique is assessed for clutter removal on the entire Bscan. For example, Figures 3.12 to 3.14 feature the case for which the clutter has the highest energy throughout the image, and then most of the information corresponding to the clutter is contained in the first principal component. However for Figures 3.2 and 3.9, the hyperbola representing the target signal shows higher energy than the clutter. PCA is not efficient in that latter case because some parts of the clutter is still merged with the second PC containing the hyperbola response.

In the literature, most cases rely on the first scenario when the clutter shows the largest energy. Then, PCA allows to eliminate the clutter components and to reduce the noise by filtering out the components with the largest and smallest energy. The results in [28] for example, show that the clutter is removed without affecting the signature of the mines. In many articles as in [16] and [40], PCA was applied to GPR images for the detection of land mines and it has showed good results without deforming the data, the clutter was removed without affecting the signature of the mines.

III.3. Improved clutter reduction technique using PCA

III.3.1. Problem overview

Conventional PCA enables a simple and fast implementation for clutter reduction. But, as pointed out in the previous section, some shortcomings may arise when the clutter does not have the highest energy within the Bscan image.

This is especially sensitive when PCA is performed on a window where the target signal is stronger than the clutter, e.g., when the target depicts a strong RCS, (that means metallic target or high contrasted dielectric target, e.g., PVC pipe filled in with water). Another difficulty may arise when PCA is applied within highly scattering background. Multiple targets or multiple echoes (owing to many interfaces) make more difficult the interpretation of the eigenvalue distribution and the set of the ad hoc threshold, i.e., the index rank k_1 and k_2 in PCA algorithm. As a tip, it is then recommended to limit the time window to the two-first arrivals; this requires to manually tune the time gating by an operator.

To mitigate the latter shortcomings encountered in the case of low clutter magnitude, a modified version of PCA has been introduced in section III.3.2.

III.3.2. Principle and illustration for modified PCA

The proposed technique is applied on a Bscan with only a single embedded target; an illustration is shown on Figure 3.2 for the case of the metallic infinite pipe at a depth of 160 mm and a radius of 12 mm of section V.3. For the sake of the illustration, the Bscan is manually decomposed into three smaller parts along the scanning direction. i.e., the apex zone, the left and the right zones apart the apex. PCA is performed on each Bscan zones separately:

- In the apex region, the energy attached to the hyperbola, i.e., the target, is larger than the clutter energy; thus, the clutter signal is contained in the second PC, and the clutter-free signal is synthesized by discarding the second PC as follows:

$$X_o = \sum_{i=1}^{k_1} u_i s_i v_i^T + \sum_{i=k_1+2}^{k_2} u_i s_i v_i^T \quad (3-15)$$

- In the zones aside the apex, the clutter recovers the larger energy compared to the hyperbola amplitudes, as sustained by the conventional PCA technique; thus clutter energy is contained in the first PCs, and the following clutter-free signal is synthesized as expected:

$$X_o = \sum_{i=k_1+1}^{k_2} u_i s_i v_i^T \quad (3-16)$$

- The final Bscan is shown on Figure 3.2 by putting the three results side by side.

As shown on Figure 3.2, the reduction of the clutter along the scanning direction is improved. But some spatial discontinuities have been introduced at the cutting zones. This technique is then capable of improving the detection but must be used with caution for any further data analysis based on the signal amplitude.

In Figure 3.2, the application of the modified PCA requires a manual separation of the raw Bscan image into three different regions, for distinguishing between the apex and the two aside zones. In practice, parameters $n1$ and $n2$ determine the limits of the latter zones. They have been manually set in Figure 3.2.

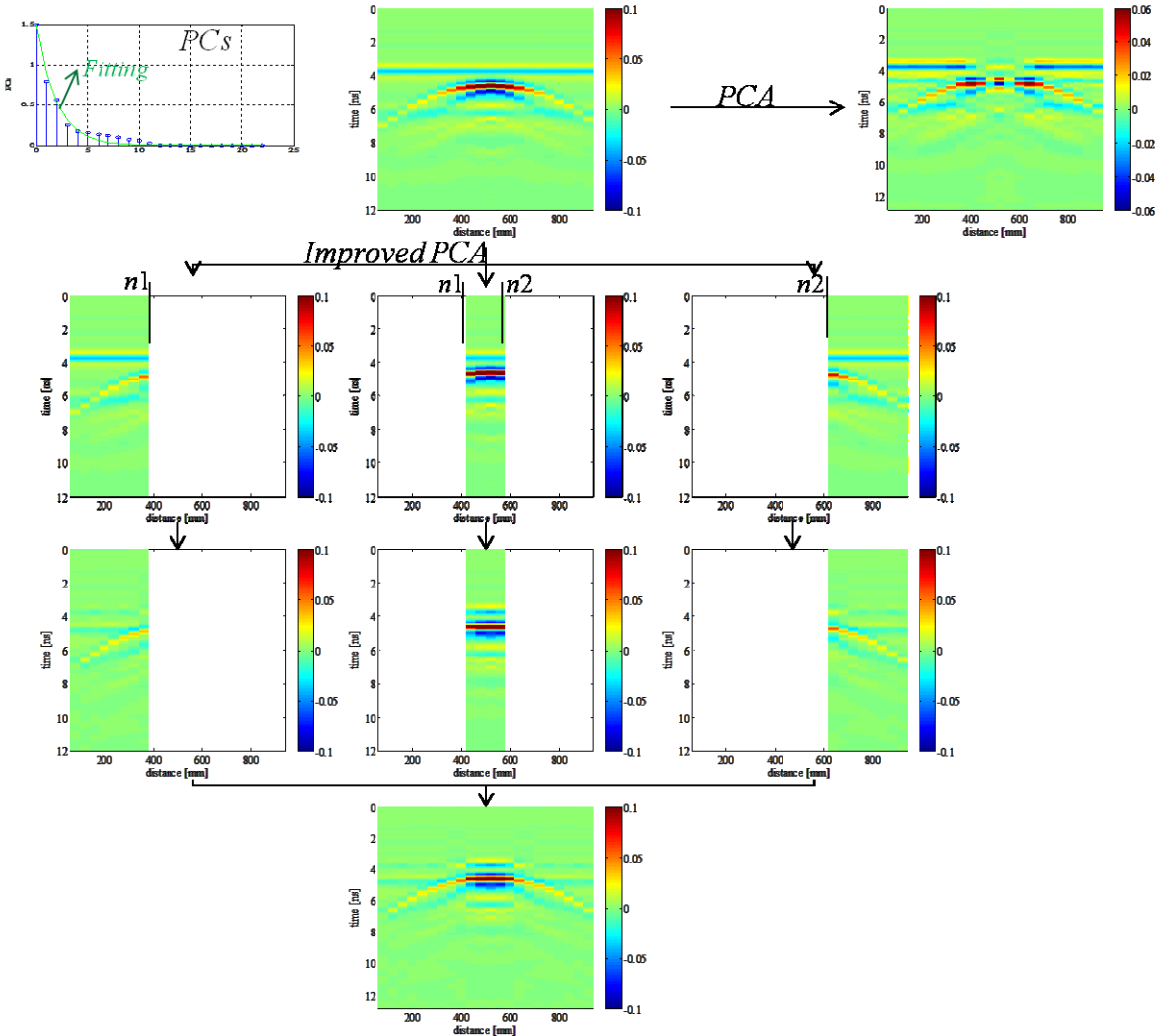


Figure 3.2: Illustration of the proposed modification for PCA. Top (from left to right): PCs distribution, raw Bscan, and the processed Bscan by the conventional PCA; middle top (from left to right): $n1$ first Ascans, apex zone from $n1+1$ to $n2$ Ascans, $N-n2+1$ last Ascans; middle bottom: the processed Ascans by the modified PCA; bottom: Bscan reconstruction.

III.3.3. Application to the data

The latter technique has been applied to numerical and experimental data sets in sections V. 3 and V.4 respectively. As in Figure 3.2, the parameters $n1$ and $n2$ have been manually selected for each Bscan to distinguish between the apex area and the two zones aside.

As a counterpart, the following algorithm has been proposed to automatically decide whether to apply the conventional PCA or the modified PCA on the raw image. Basically, it takes into account the following 2 criteria:

- Firstly, the clutter is assumed to always come first in the arrival time and before the target signal anyway. This latter characteristic is expected to remain steady along the scanning

direction within a certain variation time interval, which can be determined from the data. The algorithm compares which of the two following components comes first in time:

$$t1 = \arg \max_t \left(\sum_{i=1, j=n1}^{M, n2} x_{ij} \right)_{Apex_region} > \approx \arg \max_t \left(\sum_{i=1, j=1}^{M, n1} x_{ij} \right)_{Aside_region} = t2 \quad (3-17)$$

The function argmax mathematically represents the time picking process on the magnitude of the signals.

- Secondly, energy criterion enables to verify that the time picking has selected useful signals, namely the clutter or the target signals, and no signals issued from heterogeneities and having lower energy. To this aim, the sum of squared amplitudes of the picked times $t1$ and $t2$ along the Bscan are compared as follows:

$$E1 = \left(\sum_{i=t1, j=n1}^{i=t1, j=n2} x_{ij}^2 \right)_{Apex_region} > \approx \left(\sum_{i=t2, j=1}^{i=t2, j=n1} x_{ij}^2 \right)_{Aside_region} = E2 \quad (3-18)$$

The synoptic of the PCA algorithms is shown on Figure 3.3 The conventional PCA is applied whenever: $\{t1 \approx (t2 \pm \delta^4) \text{ and } E1 \approx (E2 \pm \Delta^5)\}$, or $\{t1 \approx (t2 \pm \delta) \text{ and } E1 \ll E2\}$, or $t1 < (t2 \pm \delta)$. The improved PCA is applied whenever $\{t1 \approx (t2 \pm \delta) \text{ and } E1 > E2\}$ or $t1 > t2$.

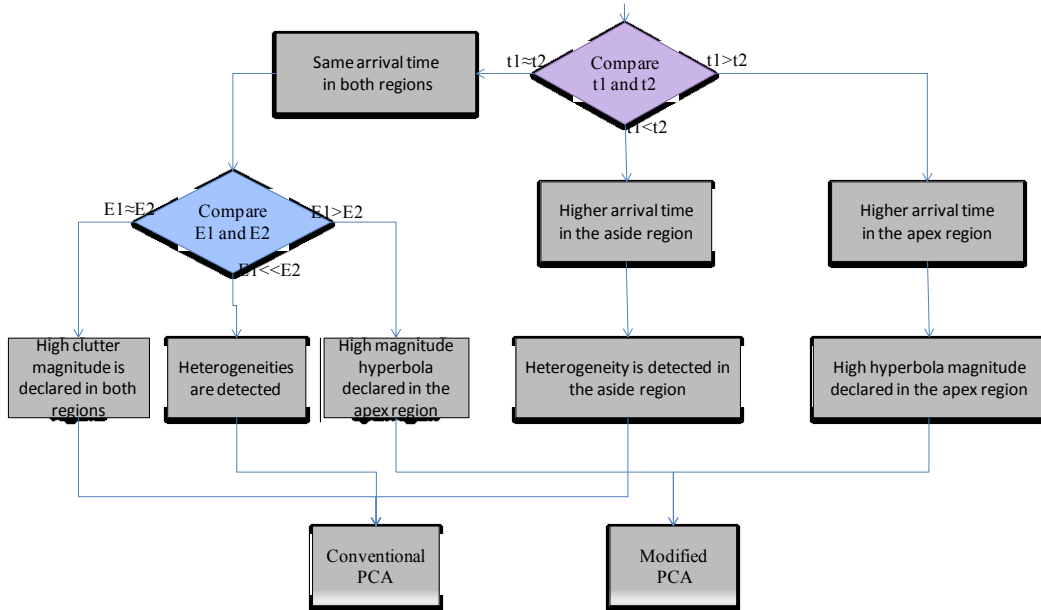


Figure 3.3: Synoptic for applying PCA and modified PCA on the data.

⁴ δ is defined around 0.4 ns proportionally to the clutter roughness (elevation).

⁵ Δ is proportional to the heterogeneities energy, it represents any energy less than 1% of the clutter energy.

IV. Independent component Analysis (ICA)

IV.1. Introduction

The previous section has shown that the PCA technique is based on the removal of the second order correlation between Ascans in the input data. Uncorrelatedness in itself can be not sufficient to separate the clutter from the target, especially if the gaussian assumption does not hold for the components of the data model. ICA is expected to mitigate the latter shortcomings by accounting for higher order statistical dependencies. This gives a wider usage for ICA and better performance are intended for clutter reduction. In addition, ICA divides original dataset into statistically independent components ICs, and assumes that the original sources are statistically independent.

Independent Component Analysis (ICA) is a method for finding the set of original data from their mixtures, without knowing the mixing process. Basically, it is assumed that the data matrix X is generated from the source matrix S through a linear process. The general mixing data model for ICA is then written as follows:

$$X = SA \quad (3-19)$$

Where $X = (x_1, x_2, \dots, x_N)$ is the same matrix as for PCA processing, $S = (s_1, s_2, \dots, s_{N_2})$ is the $M \times N_2$ source matrix ($N_2 \leq N$), and A is the $N_2 \times N$ mixing matrix. Each column x_i of the Bscan is a linear combination of the sources S .

The goal is to estimate the unknown matrices S and A from the data X with a few assumptions. Thus, ICA has been used as a blind source/signal separation (BSS) technique [41]. The term ‘blind’ stresses the fact that the mixing structure and the sources are both unknown. ICA has been used in many applications in a variety of fields: acoustical signal processing, biomedical signal processing like the Magneto encephalography (MEG) [17] and the electrocardiogram scan (ECG) [42], feature extraction and noise reduction in image processing [43], in telecommunication for separating mobile user signal from interfering of other users in CDMA (Code Division Multiple Access) [17], in face recognition [44], and for blind deconvolution to separate radar emitted wavelet from the reflectivity series [45].

Both techniques PCA and ICA attempt to project the data and identify the sources of interest and discarding the others, they both have been widely used in the literature for clutter reduction in GPR images without a deep comparison of their capabilities. The goal in using ICA on ground-coupled GPR data is to separate the sources into three classes, namely the clutter signal, the target signal which forms an hyperbola within the Bscan, and the additive noise, in order to provide a clutter-free Bscan image with reinforced signal-to-noise ratio.

IV.2. Application strategies for ICA

The three following schemes are reported in the literature for applying ICA to GPR data analysis. They depend on the scope of application, the prior information on the data model which is accounted for in the data processing and the assumptions that sustain the data structure.

1. Repetitive measurements for signal reinforcement: assuming the data model is composed of two components, i.e., the useful signal with additive noise, ICA is applied to repetitive

Ascans measurements at the same position. This induces a high redundancy in the data, which can be used to improve the separation between the signal and the noise. This strategy has been successfully applied to ECG (Electrocardiograms) scans. But, the data acquisition with such a measurement process is time consuming for GPR data collection since the measurements have to be repeated many times at each antennas position. Then, there is a great interest to find better ways to apply ICA to GPR data.

2. ICA with reference measurements: assuming prior information on the data model, i.e., the amount of components especially, specific experimental conditions enable the sequential measurements of some components (at least one) of the data model individually. This strategy is usually applied from the time domain in different ways. First, ICA is applied to a set of two Ascans (or Bscans), one containing only clutter with additive noise, and the other containing the target and the clutter information with additive noise. The two obtained ICs correspond to the two independent components. The selection of the ICs whose time of arrival comes at first allows selecting the clutter, while the second time of arrival signal corresponds to the target. In [15], the author used a clutter model from a target-free area, applied PCA as a whitening process to uncorrelate the matrices (clutter matrix and target matrix) and remove their noise, and finally suppressing the clutter from the signal observation by using ICA with the likelihood estimation. The author in [46] used a simulated clutter signal as a reference instead. In [47], X-T Li et al introduced another strategy to process air-coupled GPR data with ICA for estimating time delays of echoes and measuring the pavement thickness. This strategy requires the prior measurements of each component of the data model individually; the authors then record three different Ascans, one for the GPR data over the subsurface, another for the noise only (by directing the antenna to the sky) and the third one was the clutter with additive noise. The latter strategy implies strong assumption on the experimental conditions, which are hardly met in GPR radar configuration.
3. Data driven technique: this strategy consists in the direct application of ICA on data; the conventional mixing model for ICA is used as data model with no additive prior information on the amount of ICs. Within the scope of GPR application, ICA is then directly applied to the raw Bscan data by considering all Ascans at each position as the input matrix for the ICA algorithm, i.e., N vectors corresponding to the number of Ascans along the scanning direction. Each Ascan is a combination of N_2 sources, i.e., the target embedded into the ground. In [48], J. Liu et al presented a modified ICA-based method, which combined the selection of ICs with a Non-Homogeneous Detector (NHD). It is applied to the detection of non-metallic mines from Bscan data, and it showed better performance compared to PCA and the mean removal techniques. The authors in [7] selected the same number of ICs as for the number of Ascans, and compared to other processing techniques, i.e., Factor analysis FA, SVD, and PCA. They obtained the successful detection of metal and Teflon targets with ICA, while the other methods detected metal targets only. The authors in [49] selected a fixed amount of ICs from ICA, namely $N=12$. In [50], the latter techniques are successively applied on data: MST (Mean subtraction) algorithm is performed first and removed most of the ground bounce, PCA

and ICA are then applied to remove all residual of the clutter and the noise to improve the SNR.

4. Processing domains: it is worth mentioning that ICA can be performed on Ascan GPR data in either the frequency or the time domain. Both domains are corresponding to each other by dual transformation, i.e., Fourier transform, and then the data processing in both domains is expected to provide the same performance. Two dimensional Bscan data afford more possibilities and ask about the best domain to perform the data processing. For example, the authors in [51] provided a comparative study of frequency-domain and time-domain based ICA for clutter reduction and non-metallic landmine detection. The experimental results indicate very different extracted ICs and may depend on the family of ICA algorithm too. For example, the conventional Bscan is called time-time processing while the transpose Bscan matrix relies on time-spatial processing. The application of ICA to the two latter data structure sustains different assumptions on the sources vectors of the data model; this is time independence of time signals and spatial independence of time signals, respectively. According to [51], the first ICs which are obtained from the time-spatial data structure show strong landmine signatures. However, the authors do not give enough details on the use of ICA from complex frequency data.

In the following, the third solution, namely, the data driven strategy, has been preferred for practical consideration. This consists in processing the Bscans data directly without reference models; it uses only the data processed in the time domain as in [52].

ICA has been extended in [53] [54] to complex data. But this extension on complex data has never been used in a GPR application and it might be a good perspective for improving ICA. This is especially needed when performing ICA on the data in the frequency domain after the Fourier transform of time data. Then, some adaptation is required to measure the independency between complex data at each frequency.

IV.3. Algorithm

The ICA is performed firstly by formulating a contrast function which measures the gaussianity, and then maximizing the latter function with regards to some optimization algorithm. At first, to make the algorithm quickly converging, some preprocessing is required.

IV.3.1. Preprocessing

For applying ICA algorithm, it is worth mentioning that the data matrix $X(M \times N)$ is transposed ($X = X^T$) such as $X(N \times M)$ to adapt the software implementation. Thus, the data model can be written as:

$$X^T = A^T S^T \quad (3-20)$$

The preprocessing consists in the two following two steps:

1. Data centering: this step consists in subtracting the mean value 'm' from each Ascan measurement (vector) x_i in matrix X to obtain zero-mean variables. This implies that the estimated sources s_k of matrix S are zero-mean; therefore after estimating the mixing

matrix A with the centered data, the mean of S is estimated by applying $A^{-1} \times m$, and added back to the estimated data matrix S .

2. Whitening step: this step aims at removing the correlation between the components in the data matrix X , and normalizing the variance. The covariance matrix of the whitened data Y is equal to the identity matrix I as follows:

$$E\{YY^T\} = I \quad (3-21)$$

The whitening process represents a linear change of coordinate of the mixed data. Once the sources are found in this "whitened" coordinate frame by the ICA algorithm, the sources can be easily projected back into the original coordinate frame. Whitening process is done by applying a whitening matrix transformation B of size $M \times M$ to the data matrix X .

$$Y = BX \quad (3-22)$$

The conventional method for whitening a matrix consists in using the left eigenvalue decomposition of the covariance matrix X , such as U is an orthogonal matrix:

$$E\{XX^T\} = U\Lambda U^T \quad (3-23)$$

Whitening matrix B is expressed as a function of eigenvectors matrix and eigenvalue matrix:

$$Y = U\Lambda^{-1/2}U^T X \quad \text{Or} \quad Y = \Lambda^{-1/2}U^T X \quad (3-24)$$

And it is easy to verify that [Appendix C1]:

$$E\{YY^T\} = I \quad (3-25)$$

Thus, the whitening process can be seen as the transformation of the mixing matrix A into a new orthogonal one \tilde{A} :

$$\begin{aligned} Y &= U\Lambda^{-1/2}U^T AS \\ Y &= \tilde{A}S \end{aligned} \quad (3-26)$$

The whitening step is known to reduce the number of parameters to estimate and to improve the convergence of the ICA algorithm.

IV.3.2. The FastICA algorithm

In the data model defined in section IV.1, both the source matrix S and the mixing matrix A are unknown. The main computational issue in the ICA process is the estimation of the mixing matrix A , so that the ICs, i.e. the source matrix S can be obtained as follows:

$$S = XA^{-1} \quad (3-27)$$

Therefore, the ICA decomposition of matrix X can be obtained by finding a full rank separating linear transformation matrix $W=A^{-1}$ such that the output signal matrix can be defined by $\hat{S} = WX$ where \hat{S} is an estimation of the sources.

Matrix W must be chosen in a way to maximize the independency between the ICs. In the next section, we describe the measure of non-gaussianity and the associate contrast function. Many algorithms are proposed in the literature to maximize these contrast functions, e.g., FastICA algorithm or Fixed-Point ICA [55], RobustICA, information maximization (Infomax), temporal decorrelation source separation (TDSEP) and Joint Approximate Diagonalization of Eigen-matrices (JADE). Among others, the FastICA is an efficient and popular ICA algorithm introduced by Aapo Hyvärinen [56]. FastICA is based on the gradient-

descent scheme for finding a maximum of the non-gaussianity of $w^T x$ in [Appendix C3]. It can achieve faster learning and more reliability than the “neural on-line learning” method [57]. The two steps of the algorithm are described in [Appendix C3], namely the deflationary orthogonalization and the symmetric orthogonalization steps.

The measure of non-gaussianity is made according to several parameters described in the book by Hyvärinen [58]: kurtosis, negentropy, minimization of mutual information and maximum likelihood estimation. Among them, the kurtosis and negentropy have been selected.

IV.3.3. Independence estimation

This section introduces the relationship between non-gaussianity and independency, and the two most used criteria to measure the non gaussianity, namely kurtosis and negentropy. Mutual information and maximum likelihood information criteria have been used by others.

1. Relationships between non-gaussianity and independence

According to the data model, the ICA decomposition of matrix X consists in finding a full rank linear transformation W , such that the output signal matrix is an estimation of the source matrix $\hat{S} = WX$. The estimated matrix \hat{S} would correspond to the true source matrix S , if W is either the inverse or the Moore-Penrose pseudo inverse of the mixing matrix A . Otherwise, the output matrix is a linear combination of the sources, i.e., the weighted sum of the sources.

According to the central limit theorem, the sum of independent identically distributed random variables has a finite variance, and is approximately normally distributed, i.e. gaussian distribution. As a result, the statistical characteristic of the output matrix would be more gaussian than any of the sources.

Thus, the matrix W is calculated by converging the output matrix \hat{S} to be as independent as possible, i.e., maximizing the non-gaussianity between the ICs. As introduced later on, the contrast function G is required to measure the latter independency between components.

2. Kurtosis

Kurtosis is the simplest method to measure the non-gaussianity of a variable y_i , it is based on the calculation of the fourth-order moment y_i such as:

$$kurt(y_i) = E\{y_i^4\} - 3(E\{y_i^2\})^2 \quad (3-28)$$

In the case of a gaussian random variable, the kurtosis reduces to zero. For most non-gaussian random variables, the kurtosis can be either positive (super-gaussian, spiky form) or negative (sub-gaussian, flat form).

In practice, the estimation of kurtosis from data may be not a robust measure of non-gaussianity in some cases, e.g., when data include outlier, that means erroneous or irrelevant data which show large differences with the average trend [58]. The latter discrepancy may be solved by using the negentropy method.

3. Negentropy

In information theory, negentropy is based on the differential entropy, the more random or unpredictable the variable is, the larger is the entropy. A fundamental result of information theory is that a gaussian variable has the largest entropy among all random variables of equal variance. This means that entropy could be used as a measure of non-gaussianity, entropy is small for distributions that are concentrated on certain values.

Negentropy J for a data vector y of random values is defined as the difference between the entropy of gaussian variables (with the same covariance matrix as for the input data y) and the entropy of the input data y :

$$J = H_{y_{gauss}} - H_y \quad (3-29)$$

Negentropy is non-negative and higher for non-gaussian variables. The random variable y is assumed to be of zero mean (centered) and unit variance (whitened).

The advantage of using negentropy as a measure of non-gaussianity is that it is well justified by statistical theory. As a counterpart, negentropy is computationally difficult to calculate. Therefore, some approximations of negentropy have been introduced in the literature; the most used was defined by Hyvärinen [58] as follows:

$$J(y) = [E\{G(y)\} - E\{G(y_{gauss})\}]^2 \quad (3-30)$$

4. Contrast functions

In the latter relation, the contrast function G is some non-quadratic function that must help to optimize the performance of the ICA algorithm and to obtain a robust estimator for the independent components. The following contrast functions G are conventionally used in ICA algorithms:

$$G_1(y) = \frac{1}{a_1} \log \cosh(a_1 y) \quad g_1(y) = \tanh(a_1 y) \quad 1 \leq a_1 \leq 2 \quad (3-31)$$

$$G_2(y) = -\exp(-y^2/2) \quad g_2(y) = y \exp(-y^2/2) \quad (3-32)$$

$$G_3(y) = \frac{1}{4} y^4 \quad g_3(y) = y^3 \quad (3-33)$$

G_1 is a general purpose function, G_2 is used when the data are highly super-gaussian, and G_3 is similar to kurtosis and is used when data include sub-gaussian ICs; owing to its polynomial form, G_3 is preferred when fast and simple calculations are required [57].

IV.3.4. ICs selection

One of the main difficulties for ICA relies on the selection of ICs. Some authors [27] [49], select the ICs by visualizing each associated Bscan image; but this is not possible when we have more than 20 ICs. The most appropriate approach would require the automatic selection of ICS thanks to an ad hoc criterion.

According to the section IV.3.3, the automatic selection of ICs can be based on the measure of the gaussianity. The ICs with high non-gaussian characteristics carry the object information (super-gaussian structure) while the ICs with high gaussian characteristics carry

clutter information (sub-gaussian and gaussian structures) and non-target information (noise interferences) [51].

$$kurt(s_k) = E\{s_k^4\}/(E\{s_k^2\})^2 - 3 \quad (3-34)$$

In practice, selecting the ICs with the kurtosis beyond a certain threshold will provide the data that should contain the object information while the ICs with low values carry clutter information and noise [52] (see Figure 3.4).

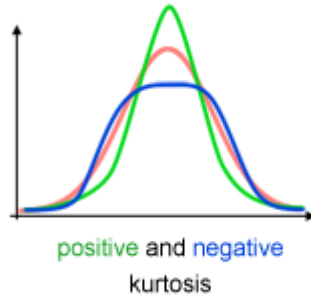


Figure 3.4: Influence of the kurtosis on the shape of PDF.

IV.4. ICA applied to GPR data

Preliminary tests have shown that only the third application scheme for ICA (as described in section IV.2) provides reliable performance in most cases, while the two others deliver versatile results. As a reminder, for the third scheme, ICA is applied directly to the real data matrix X forming the Bscan image. It is composed of N Ascans of $M \times I$ vector, each vector corresponding to a position of the antenna along the scanning direction and is presented as the function of time. For ICA, the number of Ascans must be at least equal to the number of sources (echoes) to be extracted, i.e., $N > N_2$. Each Ascans is then a combination of the N_2 sources; therefore FastICA will generate N_2 ICs without any prior knowledge on the clutter. Next step is to select the most non-Gaussian ICs, and reproject them using the calculated mixing matrix A to reconstruct the image. The obtained ICs with high non-gaussian structure carry the object information while the ICs with high gaussian structure carry clutter information. Using the normalized kurtosis, we select the ICs which kurtosis is higher than a certain positive threshold, and we provide the data which contain neither the clutter nor noise, (see Figure 3.9(i) (bottom)).

To illustrate the capability of ICA in separating sources, we consider a simulated ground-coupled GPR signal using GPRmax with one embedded target at 25 mm. Two Ascans responses are considered; the first one is for the clutter alone shown in Figure 3.5(a), by considering the measurement position far away from the target location, while the second Ascans corresponds to the location above the target, namely the apex. For the latter case, the target response is overlapping and masked by the high amplitude of the clutter signal as shown in Figure 3.5(b). The two sources which are identified by ICA are shown in Figures 3.5(c) and 3.5(d); they represent the clutter and the target responses, respectively. Thus ICA is able to separate the clutter from the overlapping target response; ICA is also able to recover

the true time location of the target and the initial amplitude of ~ 300 , *i.e.*, the target without any distortion.

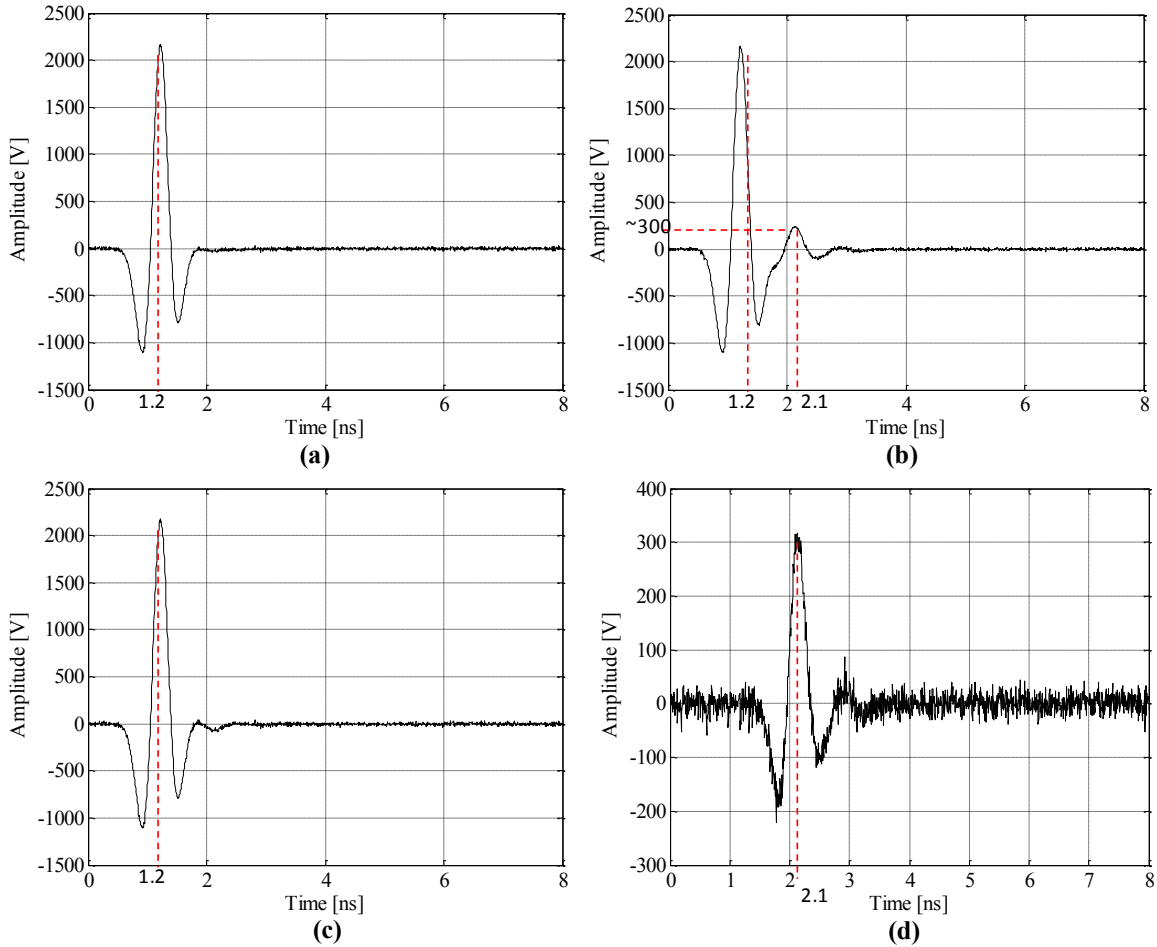


Figure 3.5: Simple ICA-BSS separation test on simulated Ascan with an SNR of 30 dB. a) target-free Ascan, b) simulated Ascan over the target (apex region), c) Extracted clutter response using ICA, d) Extracted target response using ICA.

V. Performance assessment of the clutter reduction techniques

V.1. Introduction

This section presents the methodology and the results to assess the performance of the clutter reduction techniques which are presented in this chapter, namely, PCA in section III, ICA in section IV and the mean subtraction technique (MST) in section II. The performance has been established on both simulation and measurement data sets, which are presented in section V.3 and V. 4, respectively.

The clutter signals can disturb the detection of the target signals. According to chapter 1, the level of disturbance depends on the following experimental factors: the depth of the target, the radar cross-section of the target (which also depends on the shape of the target and on the dielectric contrast between the target and the surrounding medium), and the antenna polarization. Within this scope, metallic and dielectric targets have been considered at

different depths for both data sets, and the two ground-coupled radar configurations have been used, namely broadside and endfire.

The methodology for the performance assessment includes qualitative comparison between Bscan images and also the quantitative evaluation using the criteria to be presented in section V.2, i.e., Signal to Clutter plus Noise Ratio and the Receiver operating characteristic (ROC) curves. Alternative criteria have been used by others, e.g., the mean structural similarity index in [38]. All the reduction techniques are processed on amplitude data in sections V.3 and V.4, i.e. real data.

V.2. Assessment criteria

V.2.1. Qualitative comparison

The visual comparison between the reconstructed clutter-free image and the raw image provides a first qualitative assessment of the clutter reduction techniques. In particular, the attention is paid to the spatial coherency of the main image features in the processed Bscan images along the scanning direction. The hyperbola of the target should be then clearly visible within the Bscan and the clutter may be greatly attenuated all along the scanning direction.

Within this scope, the most difficult situation for the clutter reduction technique relies on the Ascan data at the apex, for which the target and the clutter are the closest in time of arrival (they are likely to overlap), and may show the largest energy ratio. As for Figure 3.5 in section IV.4, the visual comparison between the raw Ascan and the processed Ascan serves as a benchmark test: the clutter should have been correctly attenuated while keeping the target signal unchanged in time location, in shape and in amplitude.

V.2.2. Signal to Clutter plus Noise Ratio (SCNR)

The first method to quantitatively compare the performance of the clutter reduction techniques is to calculate the SNR-like ratio (signal to noise ratio) from the processed Bscan images.

According to the literature, different terms exist for describing the same mathematical definition, namely SNR in [27], SCR (Signal to Clutter ratio) in [59], or SCNR (Signal to Clutter and Noise Ratio). The ratio is defined hereafter as the average energy of the reconstructed clutter-free image, namely ‘f’ which represents the expected target image, divided by the average energy contained in the “noise” image. The latter is obtained by subtracting the raw image, namely ‘g’, to the processed image, ‘f’.

$$SCNR_{dB} = 10 \log_{10} \left(\frac{P_{\text{target}}}{P_{\text{clutter+noise}}} \right) = 10 \log_{10} \left(\frac{\sum_{i=1,N} \sum_{j=1,M} |f_{i,j}|^2}{\sum_{i=1,N} \sum_{j=1,M} (|g_{i,j} - f_{i,j}|)^2} \right) \quad (3-35)$$

The “noise” image then includes the clutter and the additive noise. Then, it seems more suitable to use the term of SCR or SCNR, the first having a widespread use in the literature. In practice, the clutter reduction techniques do not provide a perfect target reconstruction image. As a result, ‘f’ does not represent a perfect clutter-and-noise-free image and the quantity ‘g-f’ a perfect target-free image neither.

The alternative solution in [7] uses the peak signal to clutter ratio (PSCR), which consists in considering the ratio between the maximum of the processed image (instead of the average energy as for SNR) and the power of the “noise”.

$$PSCNR_{dB} = 10 \log_{10} \left(\frac{NM \max(|f|)^2}{\sum_{i=1,N} \sum_{j=1,M} \left(|g_{i,j} - f_{i,j}| \right)^2} \right) \quad (3-36)$$

Both ratio values tend to infinity for identical images and provide small values for large difference between images. Besides, they depend on the efficiency of the clutter reduction techniques and also on the energy ratio between the target and the clutter. As a result, both ratio values are intended to afford a limited sensitivity and to be not accurate enough for the performance assessment of the clutter reduction algorithms. Therefore, the following ROC (receiver operating characteristics) measurement is introduced to overcome the latter shortcomings.

V.2.3. ROC curves

1. Background

The receiver operating characteristics (ROC) graph is introduced to quantitatively evaluate the clutter reduction techniques. ROC methodology has been introduced in the early 80's and has become a conventional technique for performance assessment within the image processing community [60] [61] and especially, for the evaluation of image segmentation. It has been used by many authors for evaluating the clutter reduction techniques in GPR images, e.g., [12] [14] [34].

ROC graphs are calculated by comparing pixel to pixel the two following binary images: the reference image, containing only the desired information to extract, and the assessment image, containing the binary transformation of the data processed by the method to be evaluated for a varying threshold S .

When comparing the two binary images with respect to the pixel, the following four categories of pixel appear: the True Positives pixels (TP) match in the reference image and the assessment image and point correct detection, the False Positive pixels (FP) are target pixels missing in the assessment image compared to the reference image, the False Negative pixels (FN) are detected in the assessment image but do not exist in the reference image and introduce false detection, and the True Negative pixels (TN) do not exist in both segmented images.

The ROC curves plot the TP rate with regards to the FP rate for different values of the threshold S which takes K values within the range $[0; \max(|g_{ij}|)]$. The variation of the threshold gives K points on the ROC curve.

Where:

- *TP rate*: is the number of true positive detection vs. the total number of positive in the reference image.

- *FP rate*: is the number of false negative detection vs. the total number of negative in the reference image.

2. Analysis of ROC curves

On the ROC curve, the best performance corresponds to the left top corner of the graph, which represents the highest *TP* rate and the lowest *FP* rate at the same time. In practice, four different situations may be obtained as shown on Figure 3.6 (a): ROC curve labeled *A* shows a low *FP rate* with a medium *TP rate*, *C* label reaches a high *TP rate* with a larger *FP rate* as before, *B* is the trade-off between the two latter cases *A* and *C*, and *D* represents the worst case among the three latter cases. It is also common to use the area under the ROC curve (AUC) that expresses the performance for the goodness of the ROC curve [60].

The construction of the two segmented images, namely the reference and the assessment images, is the backbone of this evaluation. Both are obtained by image segmentation. They have been established for each simulated and experimental Bscan images.

3. Reference image

Within the scope of the application, the reference image corresponds to the skeleton of the hyperbola, representing the signal scattered over the target to be detected along the scanning direction. To this aim, the user selects the pixels, from highest data amplitude, which are believed to belong to the hyperbola. The low signal to noise ratio makes difficult the pixel selection at the extremities of the hyperbola. This selection is harder when both the clutter and target signals overlap; therefore the time pointing can be executed on any of the clutter reduced images (for example Figure 3.12 (e)).

In fact, we have chosen to include in the reference image the first negative and the first positive half-cycles of the primary target signal amplitude. The reference image then appears with two successive hyperbolas, as shown in Figure 3.6(c), Late hyperbola signals due to multiple scattering (between the target and the soil surface for example) are ignored in the reference image.

4. Segmentation of the assessment image

The assessment image is the processed Bscan image. It is composed of the hyperbola, the residual clutter and some artifacts. As for the reference image, the positive and negative half-cycles of the hyperbola signal amplitude are recorded.

Within the scope of ROC curves, the assessment images are automatically segmented by setting a varying threshold S , which takes K values within the range $[0; \max(|g_{i,j}|)]$ (see Figure 3.6 (f, g, and h) for $k = \{40, 100 \text{ and } 250\}$ respectively) $S = \frac{\max(|g_{i,j}|)}{500}k$. In practice, the ROC curves are calculated from 500 different K values. For each point of the ROC curve, the segmented image is compared to the reference image.

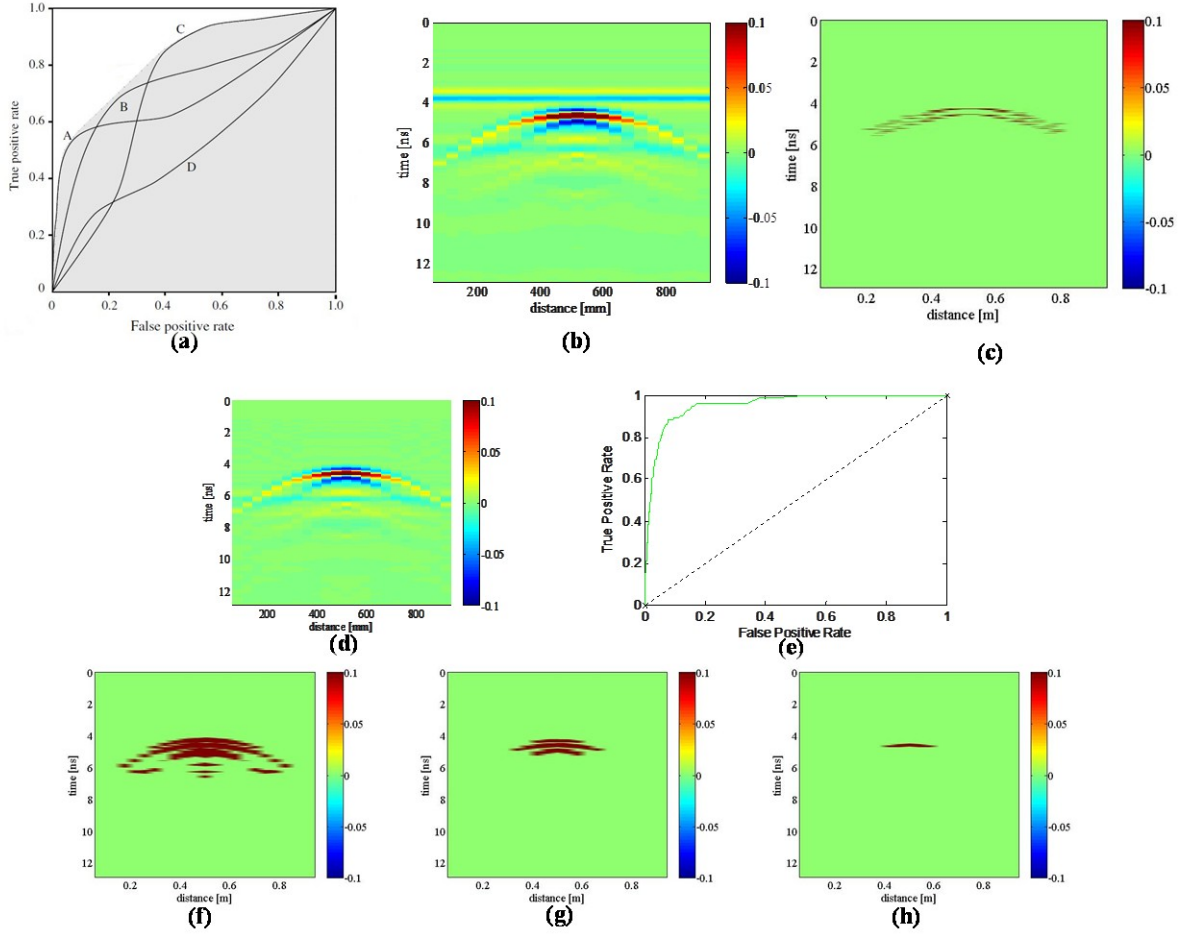


Figure 3.6: Theoretical and experimental ROC images: a) ROC curves, potentially optimal classifiers [60], b) Raw Bscan with a visual hyperbola fitting, c) Reference image obtained by inserting the fitted hyperbola in (b) into a null Bscan matrix having same dimensions as the raw image, d) Bscan treated with ICA technique, e) corresponding ROC curve for ICA, f) segmented ICA image with threshold $k=40$, TP rate = 0.7872 , FP rate = 0.0513, g) segmented ICA image with threshold $k=100$, TP rate = 0.4468, FP rate = 0.0165, h) segmented ICA image with threshold $k=250$, TP rate = 0.1489, FP rate = 0.0027.

V.3. Results on the simulated data set

V.3.1. Data set

Ground-coupled synthetic GPR data have been obtained from 3D full-wave FDTD simulations using the commercial software Empire, e.g., Figures 3.7 and 3.8.

According to chapter 2, the broadside (TE mode) and endfire (TM mode) antenna configurations have been considered for polarization diversity purpose to probe the medium with either a dielectric or a conductive pipe, respectively. For both polarization configurations, the center-to-center distances between antennas are $Y_c = 291$ mm and $Y_c = 422$ mm, respectively.

The target is a pipe with 12 mm radius; it is located at abscissa 500 mm and buried at different depths from the surface, namely, 60, 110, 160 and 240 mm. For the sake of generality, the latter depths are converted to wavelength assuming the soil permittivity $\epsilon' = 3.5$ at the central frequency 1 GHz: $0.37\lambda, 0.7\lambda, \lambda$ and 1.5λ , respectively. The target is buried in either a one-layer soil ($\epsilon' = 3.5$, and $\sigma = 0.01 S.m^{-1}$) as shown on Figure 3.7, or in a two-layer soil

($\epsilon'_1 = 5.5, \epsilon'_2 = 9$, and $\sigma_{1,2} = 0.01 S.m^{-1}$) with a 70 mm thick top layer, as depicted on Figure 3.8. The soil medium is homogeneous and includes some attenuation owing to the soil conductivity.

The simulated radar Ascans are calculated every 40 mm along the Oy axis in the range [0; 1000] mm. The soil surface is roughless. According to chap. 1, the excitation current has the shape of the first derivative of the Gaussian function with duration of 0.5 ns.

The reference time for measuring the propagation delay in the soil, namely the time zero as defined in chapter 1, is the sum of the excitation signal departure time (0.3ns) and the propagation delay between the transmitting and receiving antennas in air (estimated around 0.8ns), that results to a total time zero estimated to 1.1ns for the broadside configuration. It is obtained by subtracting the calculated direct wave arrival time from the measured time on the Bscan.

Two sets of simulated data have been performed and compared according to both the depth and the nature of the target: a first data set with shallow target implies overlapping time responses between the clutter and the echo from the target, and the second dataset with deeper target insures that the two latter echoes are resolved in time. For each simulation presented, the processed Bscan images resulted from each clutter reduction technique are showed, with the SCNR value, the associated ROC curve and the processed Ascans associated with the apex location. The color scale in the images was properly chosen to enhance the visual detection of targets before and after the processing.

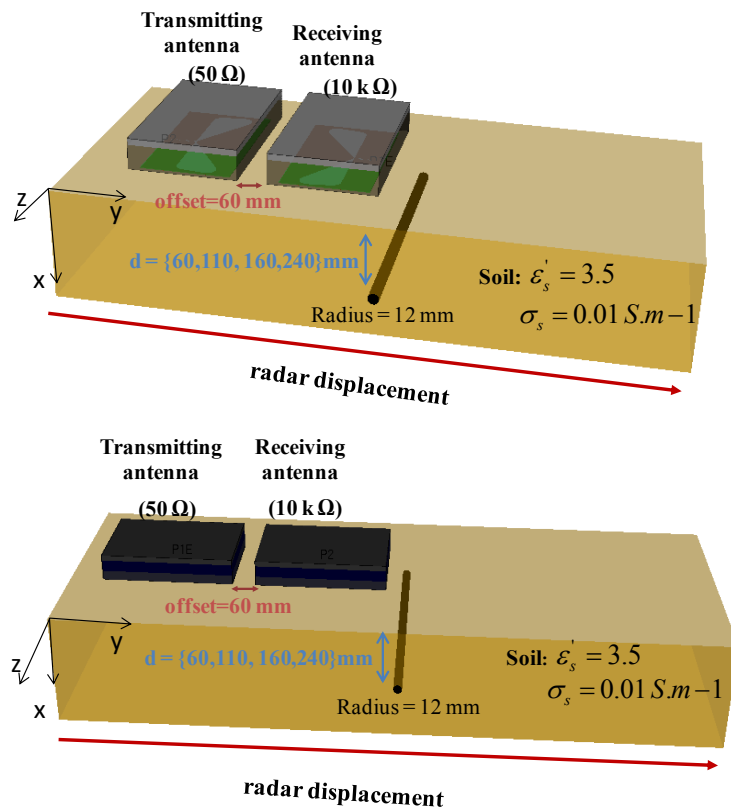


Figure 3.7: Experimental configuration for the FDTD simulations of GPR radar data with one layer soil model including a buried pipe; (top): broadside configuration (TE polarization); (bottom): endfire configuration (TM polarization).

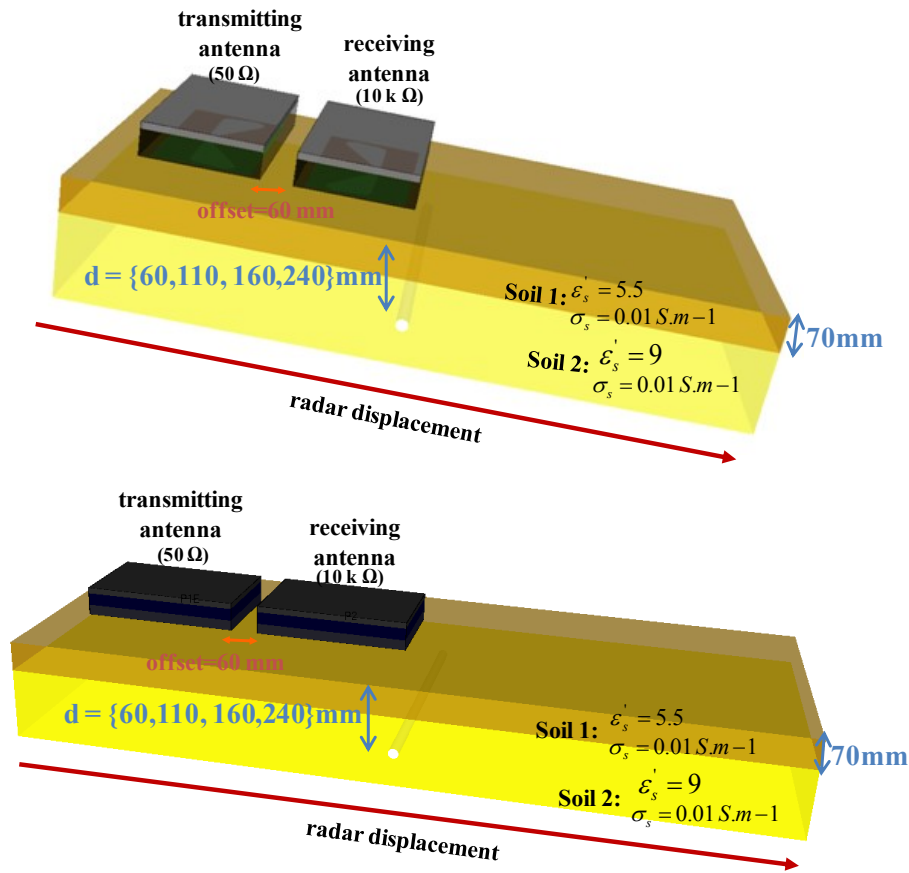


Figure 3.8: Experimental configuration for the FDTD simulations of GPR radar data with Two-layered soil model including a buried pipe; (top): broadside configuration (TE polarization); (bottom): endfire configuration (TM polarization).

V.3.2. Results

In this section, the clutter reduction techniques are performed on simulated data. Among others, three depths are selected (160, 110 et 60 mm) with the two polarization configurations. To ease the data interpretation, the results focus on the simulations with one-layer medium only.

1. Display format

The results shown on Figures 3.9 to 3.14 gather 8 Bscans. The first correspond to the raw data (a), and the seven next Bscans (b-h) represent the processed images by the different clutter reduction techniques: four MST-based techniques, two PCA-based techniques, and then the ICA-based technique. In frame (a), the reference image, i.e., the segmented hyperbola, has been superimposed on the raw Bscan. Raw Ascans and processed Ascans that correspond to the apex location of the target hyperbola are shown in the frame (j). It shows the time signatures delivered by each of the clutter reduction technique. It is expected to reproduce the target signal while attenuating the early signal containing the clutter.

The ROC curves are shown in frame (k). As a reminder, the ROC curve associated to the best clutter technique goes the closest to the top left corner. Qualitatively, any valuable technique should provide the ROC curve above the one obtained from the raw data. Below this limit, the processing would deteriorate the signal.

The top MST technique in frames (j-k) corresponds to the best performance MST-based technique among the three ones shown on the frames (b-d). Meanwhile, the frame (i) shows the distribution of the singular values from PCA (by descending order), and the selected strongest ICs from ICA.

For data interpretation, the Bscan data provide some basic information for qualitative comparison; in particular, they allow to point out the areas where the clutter reduction techniques do not work and to identify some artifacts, e.g., some horizontal signal throughout the Bscan.

SCNR and PSCNR ratios provide a global performance criterion: the highest value allows to select the best clutter reduction technique. Among the 7 Bscans, the ratios allow a coarse separation between the good clutter reduction technique and the others. But, among the satisfactory ones, the latter ratios are not sensitive enough to select the best one.

Finally, the data interpretation of the Ascans allows putting forward the technique which enables to accurately retrieve the target signal (with a few distortion, attenuation and time shift), while attenuating at the same time the leading part of the Ascan signal containing the clutter. The time which is indicated in the frame (j) corresponds to the amplitude peak of the first negative half-cycle target wavelet. However, the interpretations of the Ascan data are likely to be harder for shallower targets.

According to the assumptions applied on the medium (homogeneous soil and roughless surface), the simulations provide a uniform clutter, i.e., it does not change along the scanning direction. In this situation, the conventional subtraction techniques (mean or median subtraction techniques) are expected to provide the best performance for the deepest targets. The results on metallic and deepest targets are presented first.

2. Conductive pipe

Considering a conductive pipe probed in the end-fire configuration (TM mode as shown on Figure 3.7.b) at depth 160 mm (i.e., about one wavelength), the raw Bscan in Figure 3.9(a) shows that both the clutter and the hyperbola are separated in time. The clutter arrival time is 3.4 ns (positive half-cycle waveform) and the first hyperbola diffraction apex arrival time is estimated at 4.3 ns (negative half-cycle waveform). According to Figures 3.9 (b-h), the third MST technique (i.e., MST with clutter reference), the median subtraction technique and ICA succeed in suppressing the clutter all along the Bscan without any artifacts and any distortion on the hyperbola envelope. Four techniques, namely, the conventional and the moving MST, the conventional and the modified PCA techniques, introduce an horizontal artifact throughout the whole Bscan at different time locations. In addition, the conventional PCA shows unreliable results in the surrounding of the target location.

The good performance obtained by ICA and the third MST techniques is confirmed by the high SCNR values and on the ROC curves in figure 3.9(j), since the ROC curves is the closest to the top left corner. At the opposite, the conventional PCA depicts the worst performance: the corresponding ROC curve is located below the one obtained with raw data, and the SCNR value is negative.

In addition, the processed Ascans signals on Figure 3.9(j) corresponding to the apex of the hyperbola show that the conventional PCA provided an inverted, shifted and attenuated target signature compared to the raw data. The modified PCA preserved the target signal with a little change in amplitude only; but at the same time, it does not suppress the clutter within the time interval [3-4] ns. ICA provided a reliable target signature while lowering more significantly the clutter component in the range [3-4] ns.

As a summary, ICA affords better results than PCA in removing the clutter as stated by the higher SCNR/PSCNR, the ROC curves and the processed Ascans. Although this experimental configuration is close to the ideal situation, i.e., no overlapping between the clutter and the target time signatures, all the clutter reduction techniques are (surprisingly) far to provide similar performance. The MST with a reference target-free signal provides better performance than the two other MST, meaning that the clutter signature can be better estimated from a target-free Bscan region than by any averaging over the entire Bscan. Besides, the median filter is found more robust to the latter overlapping between clutter and target signatures than the conventional mean filter.

The conductive pipe has now been buried at the depth 110 mm, i.e. 3/4 of the wavelength within the soil material. As shown on the raw Bscan in Figure 3.10(a), the clutter and the target time signatures overlap to each other: the arrival times of the clutter and the target at the apex are 3.4 ns and 3.9 ns, respectively. According to Figures 3.10 (b-h), the modified PCA becomes more efficient in removing the clutter than ICA, the latter introducing a horizontal artifact with small amplitude. The MST with clutter-free reference and the median subtraction technique are still the best clutter reduction techniques.

The ROC curves in Figure 3.10(k) also lead to the same conclusion. The ROC curve associated with PCA is still below the one provided from the raw data. The largest SCNR and PSCNR levels are obtained by the third MST, the median-based MST, the modified PCA and ICA.

Ascans data in Figure 3.10(j) show that amplitudes are nearly recovered in all techniques with little variations, but there is a little shift in the hyperbola apex for the modified PCA technique. Only ICA, the median and the third MST strongly reduce the amplitude of the first positive half-cycle alternation of the clutter signal within the time interval [3 3.5] ns. As a partial conclusion, the modified PCA globally reaches close performance to the third MST in removing the clutter signal. But locally, especially in the apex region, ICA and the third MST remain the best technique.

For the last simulation, the metal pipe is buried at a very shallow depth of 60 mm, about one third of the wavelength. The result in Figure 3.11(a) shows that the clutter is strongly overlapping with the hyperbola time signature. As opposed to the two first simulations, PCA affords better result than both the modified PCA and the ICA techniques as shown on the ROC curves Figure 3.11(k). The conventional PCA reduces partially the clutter with some remaining distortion on the hyperbola shape as before. The conventional MST, PCA-based and ICA introduces an artifact as a horizontal band at various time.

ROC curves in figure 3.11(k) show that MST and median techniques afford the best performance, followed by PCA. However, this can be mitigated because the ROC curve associated with the raw data is partially above the one provided by PCA. According to the same criteria, the modified PCA and ICA are worthless in this situation.

Compared to the two first cases, the main observation is that the performance by ICA has degraded a lot and ICA only partially removes the clutter. As a potential explanation, the closeness of the target to the surface seems to challenge the statistical independency (between the clutter and the target signals) that relies on ICA.

Figure 3.11(j) shows the different processed Ascans at the apex of the hyperbola (i.e., $y = 500$). ICA is shown to be inefficient because the resulting signal unexpectedly looks like to the raw data. The amplitude peak on the PCA and the modified PCA techniques did not match to the one of the raw data. According to the location of the amplitude peak, the best result seems to be provided by the Top MST and the median technique; as a counterpart, both methods provide a larger amplitude than the raw data; it is believed that the lower amplitude of the raw data is the result of destructive interference between the clutter and the target signatures.

The broadside antenna configuration is considered in Figure 3.12 to obtain the TE mode. For this polarization, it has been shown in chapter 5 that the time clutter signature spreads over a larger time because of multiple reflections. To illustrate the influence of the polarization on the clutter reduction technique, we have selected the configuration with the same metallic pipe buried at a depth of 110 mm. As shown on Figure 3.12(a), the hyperbola is blurred by the overlapping of multiple clutter reflections. From the ROC curves and the different processed Bscans, the median and the third MST technique seem to give the best performance for reducing the clutter, followed by PCA; ICA provides the worst performance. The result on Ascans is made difficult to interpret because of multiple overlapping signals.

3. Dielectric cylinder

The influence of the dielectric characteristic of the target on the clutter reduction technique is illustrated on Figures 3.13 and 3.14, with the dielectric ($\epsilon_{pvc} = 3$) PVC pipe buried at 110 mm in depth and probed in the TM and TE polarizations, respectively. The raw Bscans are shown in Figures 3.13(a) and 3.14(a). The hyperbola associated with the target signal is masked by the strength of the clutter signal; the apex of the hyperbolas is located at 4.1 ns and 3.7 ns in TM and TE polarizations, respectively. The PVC pipe has a smaller radar-cross-section compared to the metallic pipe; as a result, the peak of the Ascan amplitude on the frame (j) is about ten times smaller than the one previously obtained on the metallic pipe. We observe that the third mean subtraction technique, the median subtraction technique and PCA succeed in reducing significantly the clutter. The conventional MST, PCA and ICA introduce a horizontal artifact. As opposed to the case with metallic pipe, PCA provides better performance than the modified PCA. It is worth noticing that raw data from the broadside configuration are harder to interpret, and the target signal is even more blurred by the clutter. Nevertheless, the clutter reduction techniques succeed in detecting the hyperbola with

different success rates. It seems that the less the hyperbola is visible on the Bscan data, the less ICA and the modified PCA enables to separate the hyperbola from the clutter and the more PCA enables to enhance the hyperbola. However, it appears from ROC curves plotted in Figures 3.13(k) and 3.14(k) that all the methods afford better performance than the one provided from the raw data. Among them, PCA and the MST afford the best performance in clutter removal. The Ascan in Figure 3.14(j) shows the large difference in amplitude between raw data and the processed data by the different clutter reduction techniques.

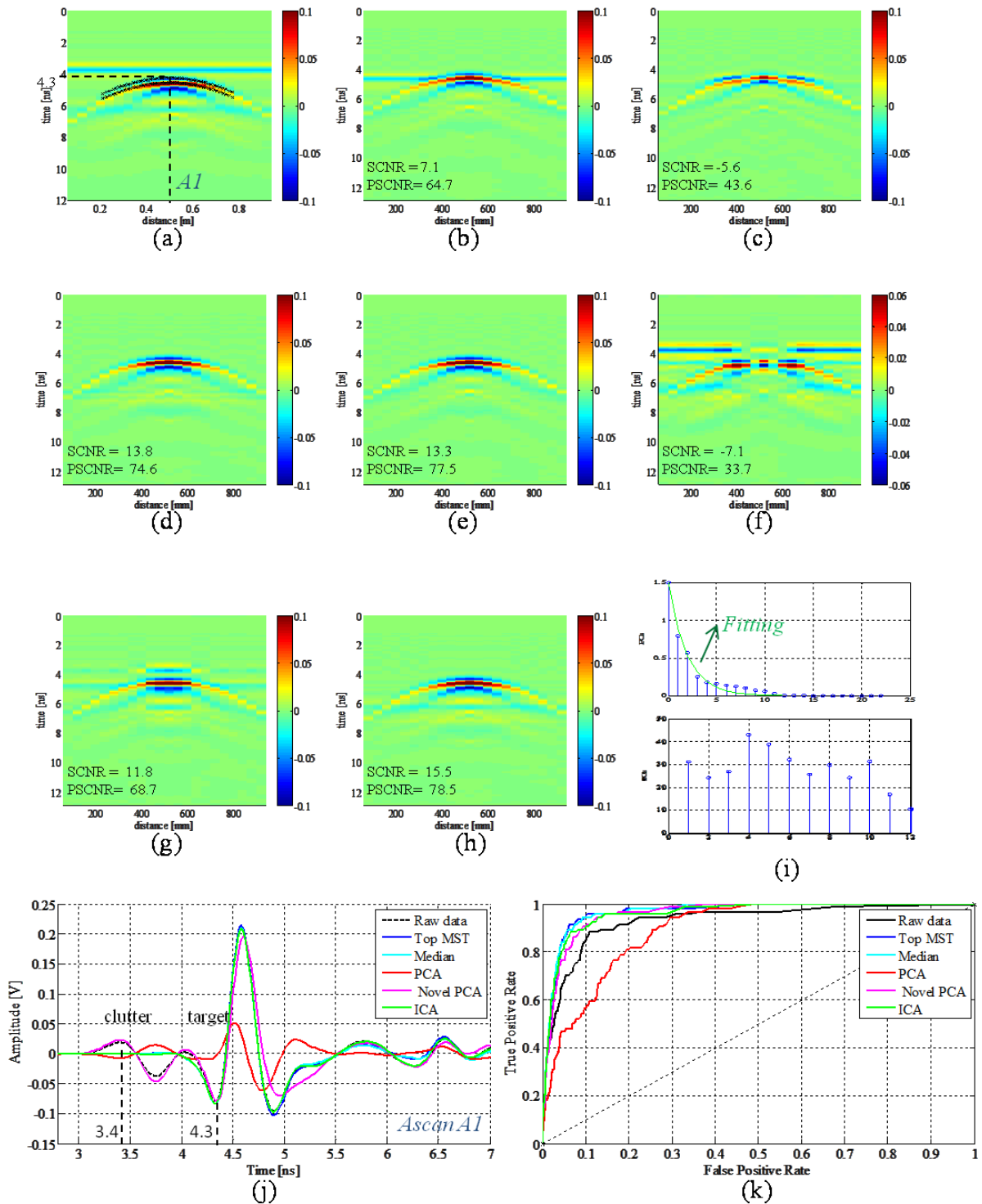


Figure 3.9: Simulated Bscans over a metal pipe buried at 160mm depth in a one-layer homogeneous medium, with antennas in the endfire configuration (TM). (a) Raw data (b) MST across all traces (c) Moving window MST (d) MST with target-free reference (e) Median MST (f) PCA (g) modified PCA (h) ICA (i) (Top) Eigenvalues amplitude against the order number plot, with best exponential fitting at $y=1.5*(\exp(-x/1.91))$ (i) (Bottom) kurtosis of ICs plot (j) Ascans (k) ROC, (top MST⁶ is (d)).

⁶ Top MST: represents the MST with the best performance for clutter reduction.

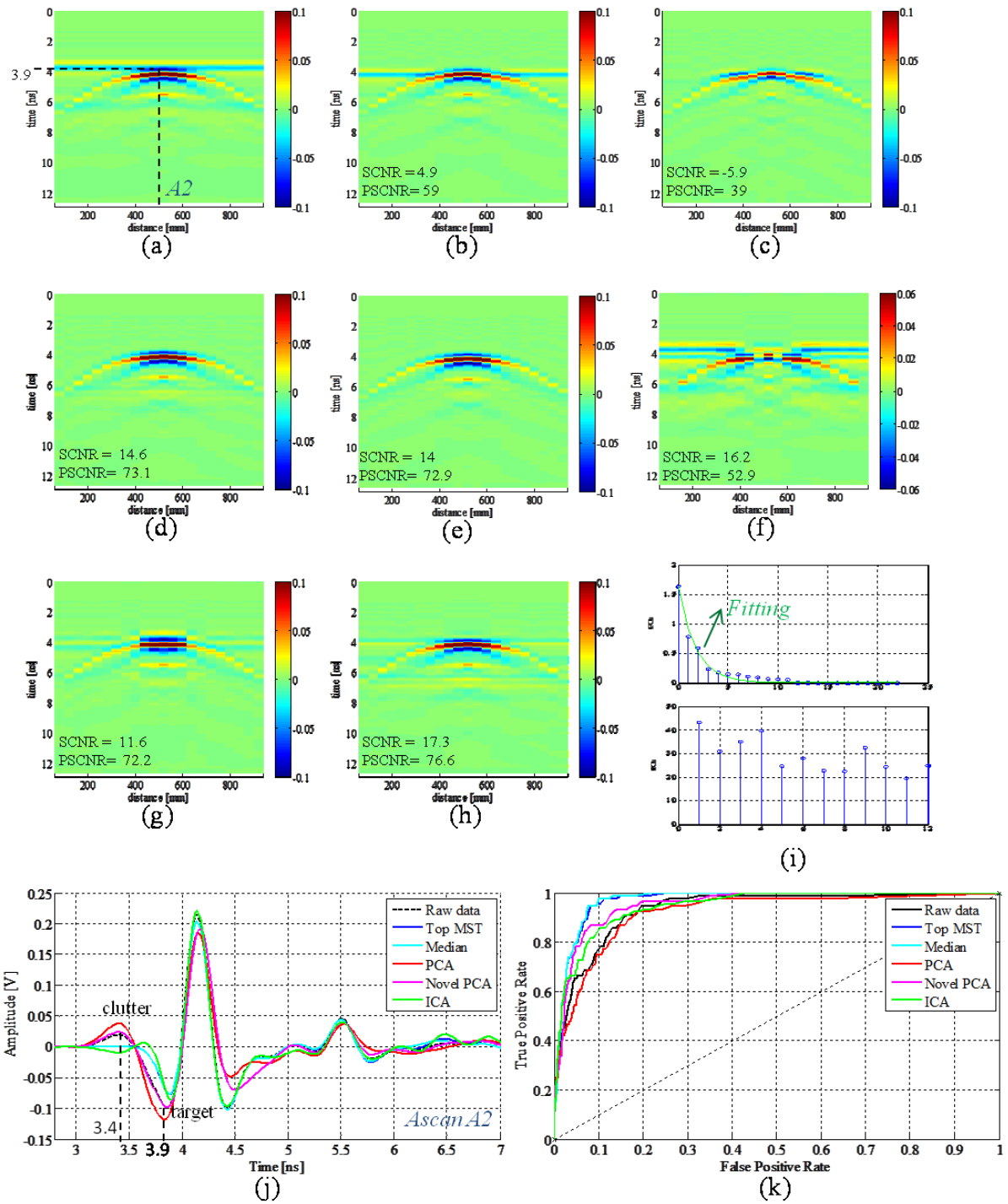


Figure 3.10: Simulated Bscans over a metal pipe buried at 110mm depth in a one-layer homogeneous medium, with antennas in the endfire configuration (TM). (a) Raw data (b) MST across all traces (c) Moving window MST (d) MST with target-free reference (e) Median MST (f) PCA (g) modified PCA (h) ICA (i) (Top) Eigenvalues amplitude against the order number plot, with best exponential fitting at $y = 1.64 * (\exp(-x/1.7))$ (i) (Bottom) kurtosis of ICs plot (j) Ascans (k) ROC, (top MST is (d)).

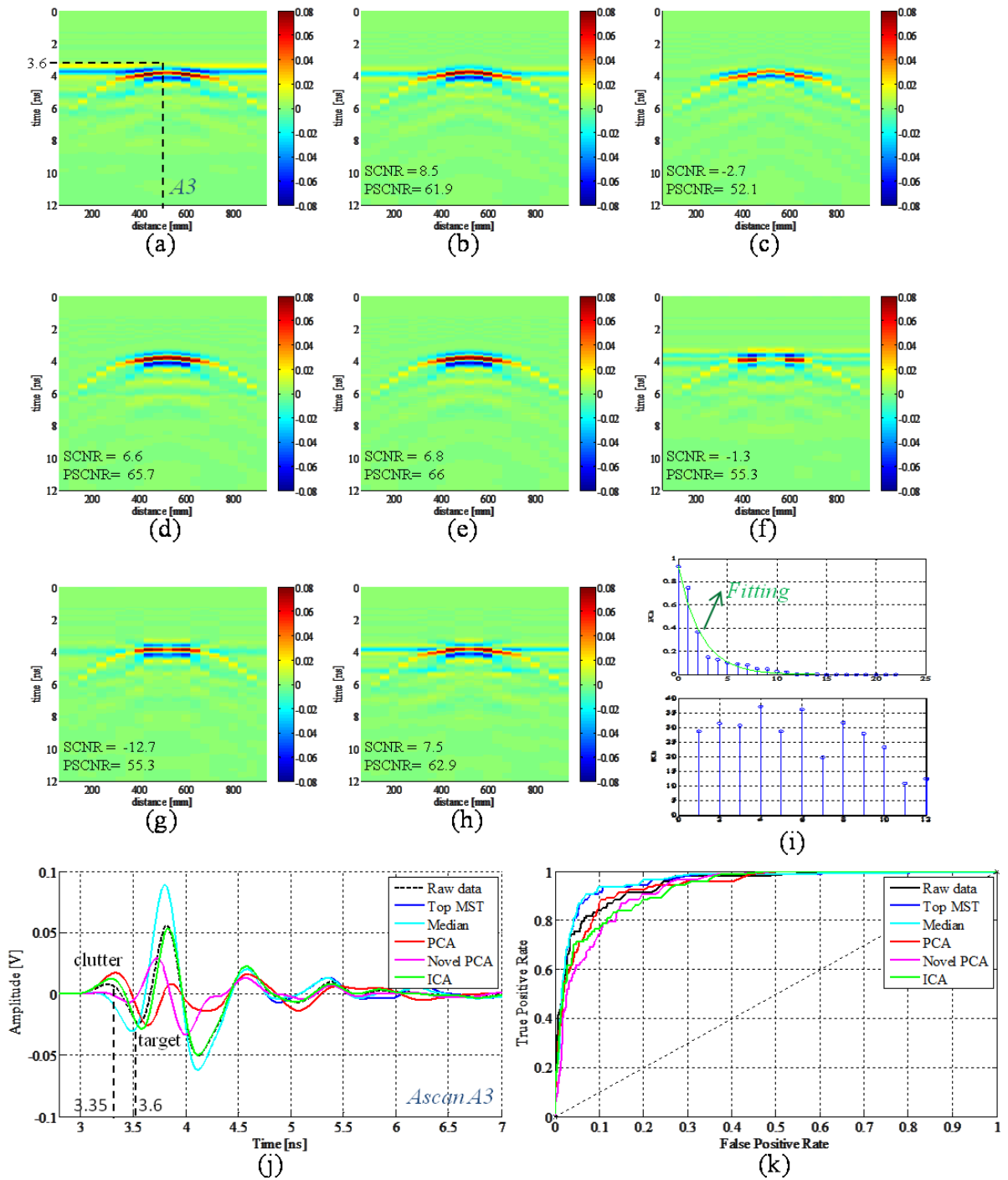


Figure 3.11: Simulated Bscans over a metal pipe buried at 60mm depth in a one-layer homogeneous medium, with antennas in the endfire configuration (TM). (a) Raw data (b) MST across all traces (c) Moving window MST (d) MST using target-free reference (e) Median MST (f) PCA (g) modified PCA (h) ICA (i) (Top) Eigenvalues amplitude against the order number plot, with best exponential fitting at $y = 0.93 * (\exp(-x/2.3))$ (i) (Bottom) kurtosis of ICs plot (j) Ascans (k) ROC, (top MST is (d)).

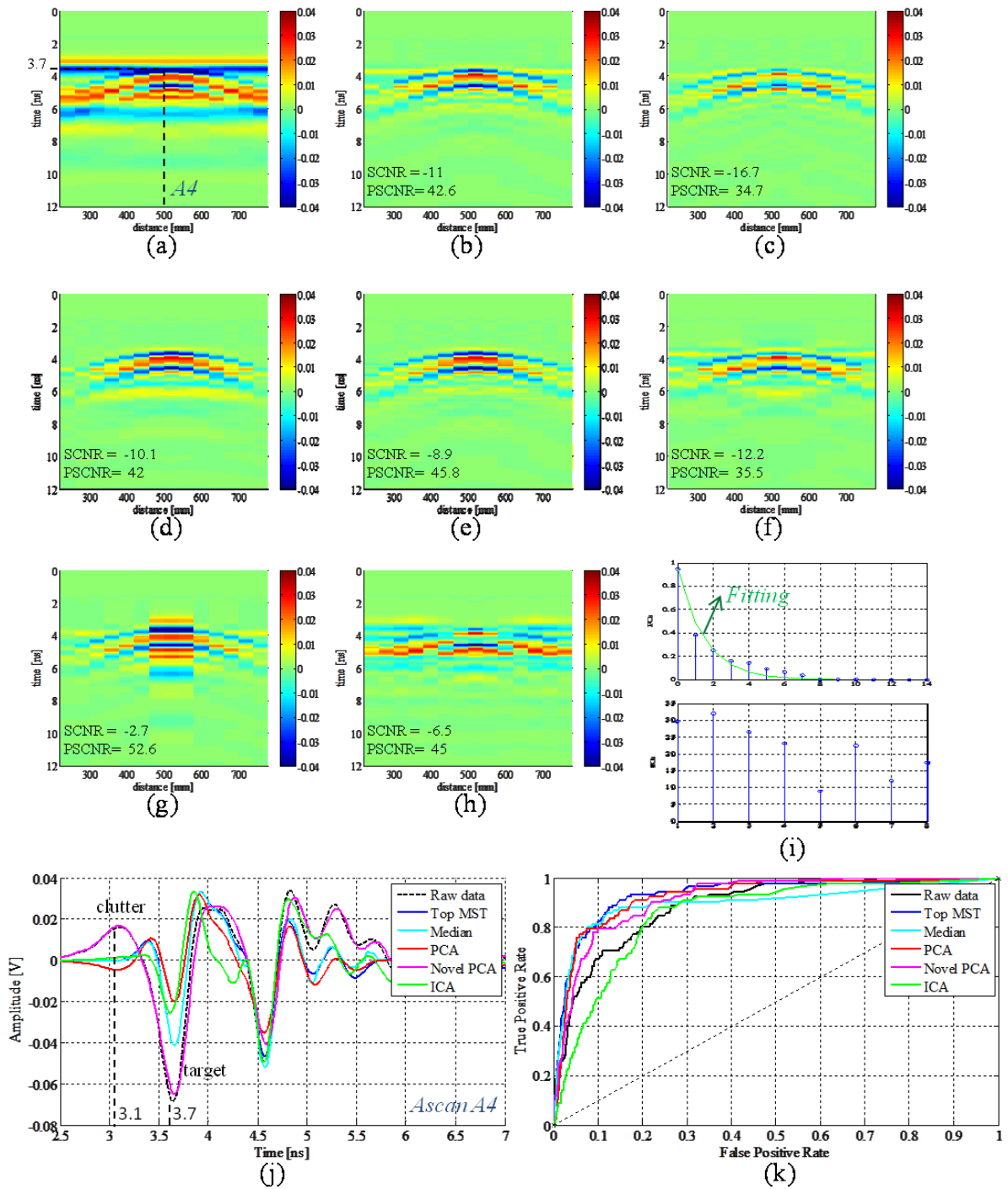


Figure 3.12: Simulated Bscans over a metal pipe buried at 110mm depth in a one-layer homogeneous medium, with antennas in the broadside configuration (TE). (a) Raw data (b) MST across all traces (c) Moving window MST (d) MST over target-free traces (e) Median MST (f) PCA (g) modified PCA (h) ICA (i) (Top) Eigenvalues amplitude against the order number plot, with best exponential fitting at $y = 0.94 * (\exp(-x/1.5))$ (i) (Bottom) kurtosis of ICs plot (j) Ascans (k) ROC, (top MST is (d)).

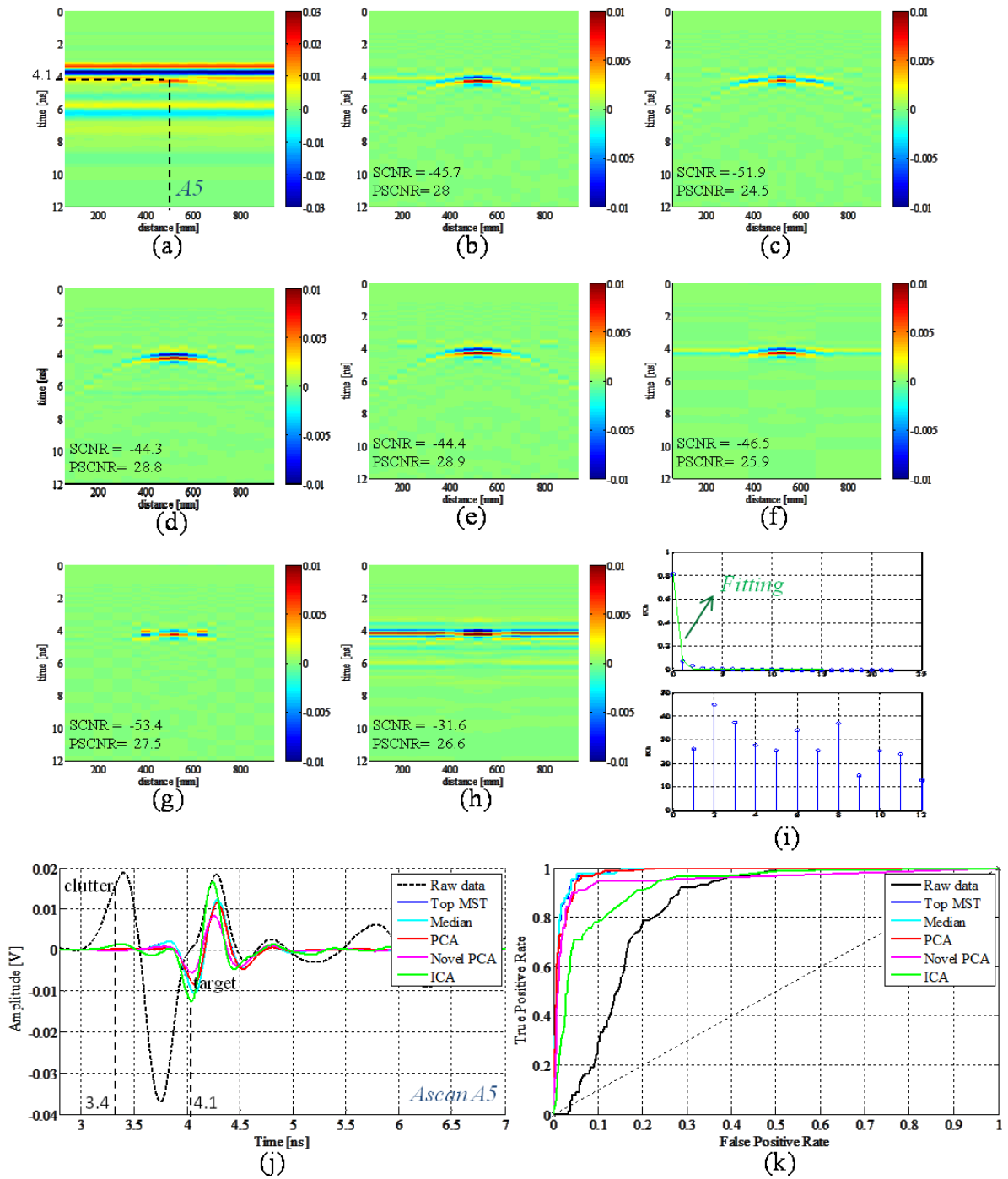


Figure 3.13: Simulated Bscans over a PVC pipe ($\epsilon=3$) buried at 110mm depth in a one-layer homogeneous medium, with antennas in the endfire configuration (TM). (a) Raw data (b) MST across all traces (c) Moving window MST (d) MST over target-free traces (e) Median MST (f) PCA (g) modified PCA (h) ICA (i) (Top) Eigenvalues amplitude against the order number plot, with best exponential fitting at $y=0.8*(\exp(-x/0.42))$ (i) (Bottom) kurtosis of ICs plot (j) Ascans (k) ROC, (top MST is (d)).

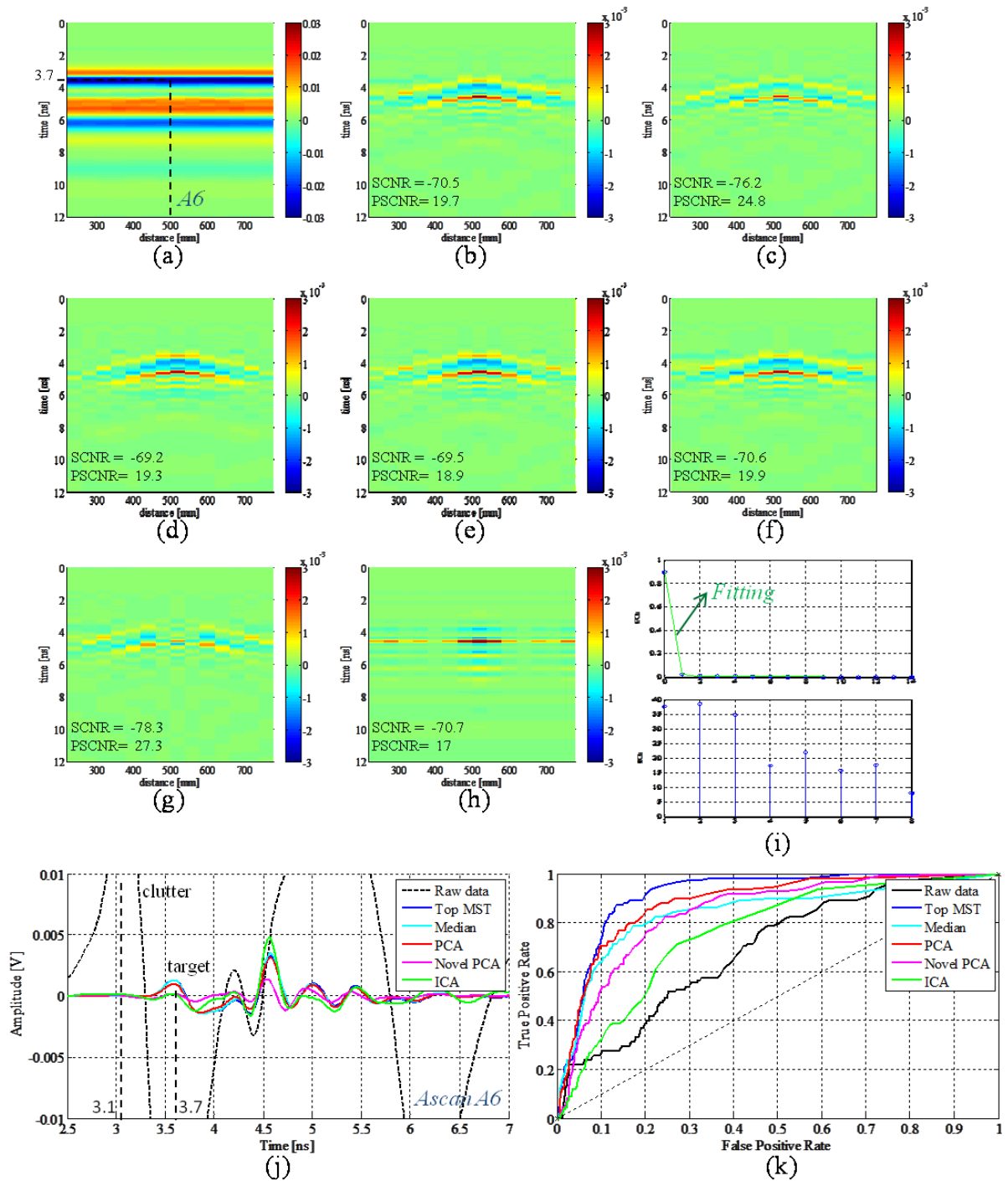


Figure 3.14: Simulated Bscans over a PVC pipe ($\epsilon=3$) buried at 110mm depth in a one-layer homogeneous medium, with antennas in the broadside configuration (TE). (a) Raw data (b) MST across all traces (c) Moving window MST (d) MST over target-free traces (e) Median MST (f) PCA (g) modified PCA (h) ICA (i) (Top) Eigenvalues amplitude against the order number plot, with best exponential fitting at $y=0.9*(\exp(-x/0.26))$ (i) (Bottom) kurtosis of ICs plot (j) Ascans (k) ROC, (top MST is (d)).

V.4. Results on the field data set

V.4.1. Data set

The field data set is composed of measurements performed with the UWB ground-coupled radar over the outdoor sandy box at the public garden Perichaux, Paris 15th district, as presented in chapter 2. The soil moisture was depending on the weather condition; we paid attention to collect the data under similar weather conditions. The soil heterogeneity was revealed a posteriori from the radar data. In fact, the sandy box is composed of different layers which provide several echoes on the Bscan images. The first layer (48 cm depth) is the thickest and its dielectric permittivity has been estimated to 3.5 according to work in [62]. The estimated arrival time is quoted on the latter figures and corresponds to the calculated arrival time in addition to the time zero of ~ 2.3 ns. Time zero has been estimated according to the travel time of the direct air-wave.

Most of the Bscan data were collected over two canonical objects, i.e. pipes with different radiuses, buried at a depth of ~ 160 mm and at two locations along the scanning direction., i.e., ~ 500 mm and ~ 1200 mm. The following pipes were successively considered: metal pipe, air-filled PVC pipe and water-filled PVC pipe.

Each Bscan is composed of 45 Ascans which were collected with a 40 mm uniform spatial sampling and covers the distance $[0; 1760]$ mm. In the processing, the Bscans are split into two images corresponding to the scanning distances $[0, 1000]$ mm and $[760, 1760]$ mm, respectively. Each reduced image in size contains a Bscan with a single target. Both polarizations TM and TE were recorded for each target.

Measurements have been qualitatively compared with simulations. The format of the results and the methodology for the data interpretation are the same as in the simulations in section V.3. Then, for each experimental configuration, the processed Bscan images resulting from each clutter reduction technique are showed, with the associated SCNR values, the associated ROC curves and the Ascans corresponding to the apex location. The color scale in the images was properly chosen to enhance the visual detection of targets before and after the processing.

V.4.2. Results

Experimental tests were conducted to verify the performance of the clutter reduction techniques on field data. Different radiuses have been used for each pipe. Owing to the soil heterogeneity, the data include some interference scattered all over the image. The processing results are evaluated firstly over the whole image and then over a limited time area in the image corresponding to the hyperbola response.

In the first measurement campaign, a 12 mm radius air-filled PVC pipe was buried within the sand at the depth 160 mm and has been probed with the ground-coupled GPR using the broadside configuration. The raw Bscan in Figure 3.15(a) shows the apex of the target hyperbola at the abscissa 500 mm. The slight vertical variations of the clutter signal along the scanning direction indicates the significant influence of the soil roughness. The echoes beyond 7 ns which are due to the layered structure of the sand material do not seem to overlap with the target signal. With a differential time shift of about 1 ns on the Ascan in Figure 3.15(j), the clutter and the target signals only slightly overlap on each other.

Owing to several features in the processed images, the best clutter reduction techniques can be hardly selected from the Bscans on Figures 3.15(b-h). Concerning the ROC curves on Figure 3.15(k), we remark that the FP rate does not reach zero because the hyperbola amplitude appears lower than the components not containing target information. Compared to the results on the simulated data in Figure 3.14, the clutter reduction techniques provide poorer performance in overall because the ROC curves are further from the top left corner. Only the median subtraction technique, PCA and the modified PCA provide better performance than the one obtained on the raw data. For ICA, more ICs have been considered compared to the simulated data set; but ICA depicts the worst performance. As a partial conclusion, PCA is recommended for clutter reduction in this case, as already observed for the similar simulated case in Figure 3.14.

The several echoes from deeper stratification of the medium are questioning and may disturb the performance of the clutter reduction techniques. The clutter reduction techniques have been then performed on Figure 3.16 on a reduced time window [4; 6.3] ns where the two useful signals are localized. It is observed that such a processing has not improved the performance by ICA. It is difficult once again to select the best other techniques with regards to the Bscans on Figure 3.16(b-h). The reduction of the time interval has improved the ROC curves time as shown on Figure 3.16(k), but has also provided closer performance between most of the techniques. In this situation, the median value subtraction shortly appears as the best candidate for clutter removal.

In the second measurement campaign, a 5 mm radius metal pipe has been buried at 160 mm in depth and approximately localized at abscissa 450 mm. It has been probed with the end-fire configuration instead. This result has to be compared with the simulations shown on Figure 3.9. From Figure 3.17(a), we remark that the clutter slightly overlaps with the hyperbola response. The hyperbola signature is characterized by higher amplitude as compared to other signals owing to the stronger RCS of the metal pipe.

According to the processed Bscans in Figures 3.17(b-h), ICA successfully reduces the clutter. Moreover, it is noticeable that ICA strongly removes most of the multiple reflections occurring at late time delays (beyond 6.5 ns), as opposed to the third MST and the modified PCA techniques. As a counterpart, ICA also removes some of the hyperbola edges. The two PCA-based clutter reduction techniques imperfectly reduce the clutter at the apex.

According to the ROC curves in Figure 3.17(k), the clutter reduction techniques afford better performance than the one provided from the raw data. Among others, ICA affords the best performance followed by the median subtraction technique. On the Ascans in Figure 3.17(j), it is worth noticing that ICA and the MST-based techniques reduce the amplitude of both the early signals (containing the clutter) and the late signals (containing multiple echoes)

By focusing the processing on the reduced time window [3.8; 6.5] ns on Figure 3.18, the superiority of ICA in removing the clutter is no longer lasting. The shortcomings of each technique are then more clearly visible on the processed Bscans. According to the ROC

curves, the median value subtraction and the first MST take over ICA and afford the best performance.

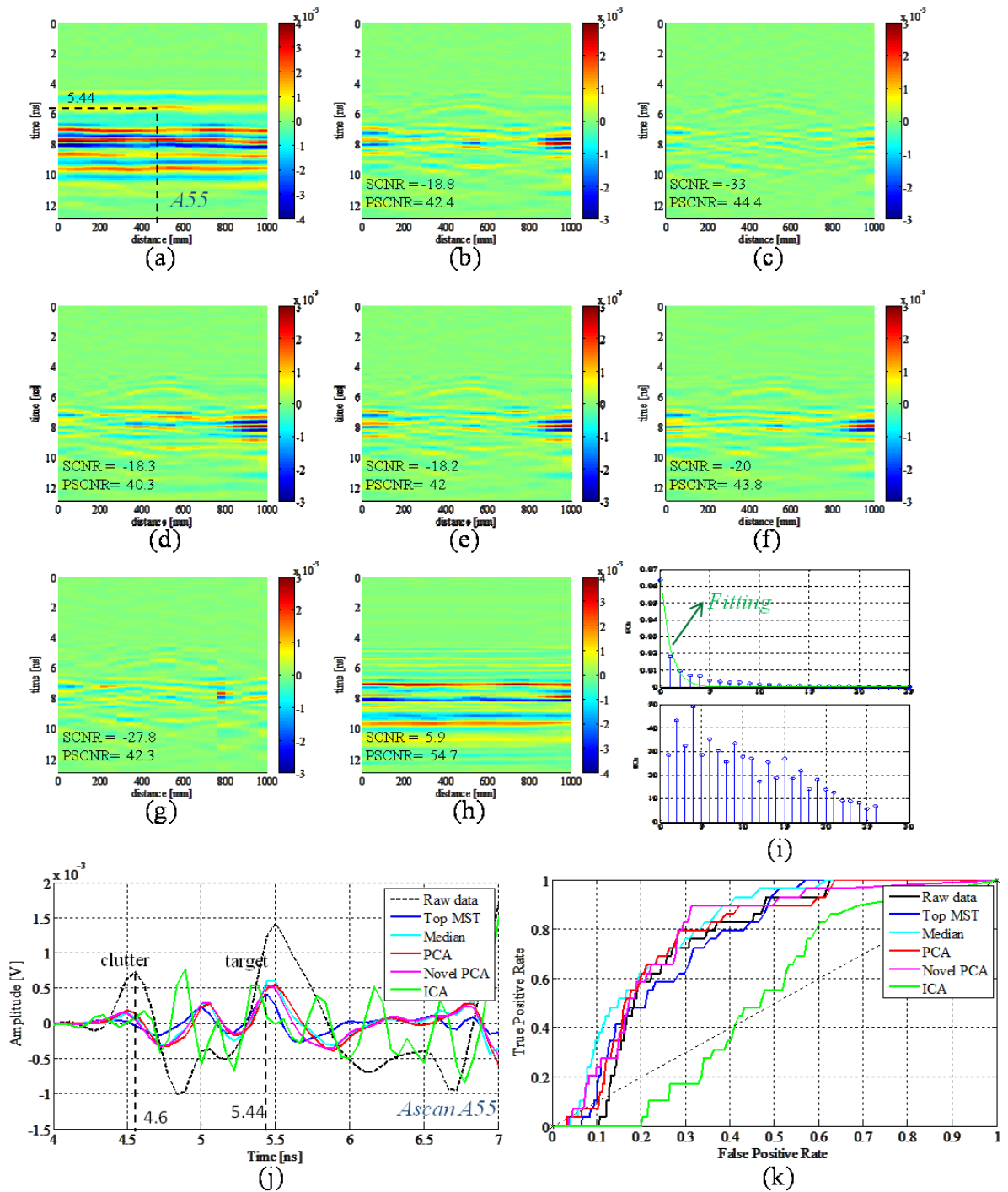


Figure 3.15: Experimental Bscans over a PVC pipe ($\epsilon=3$) buried at 160mm in depth within sand with the antennas in the broadside configuration (TE). (a) Raw data (b) MST across all traces (c) Moving window MST (d) MST over target-free traces (e) Median MST (f) PCA (g) modified PCA (h) ICA (i) (Top) Eigenvalues amplitude against the order number plot, with best exponential fitting at $y = 0.06 * (\exp(-x/0.9))$ (i) (Bottom) kurtosis of ICs plot (j) Ascans (k) ROC, (top MST is (c) based on ROC).

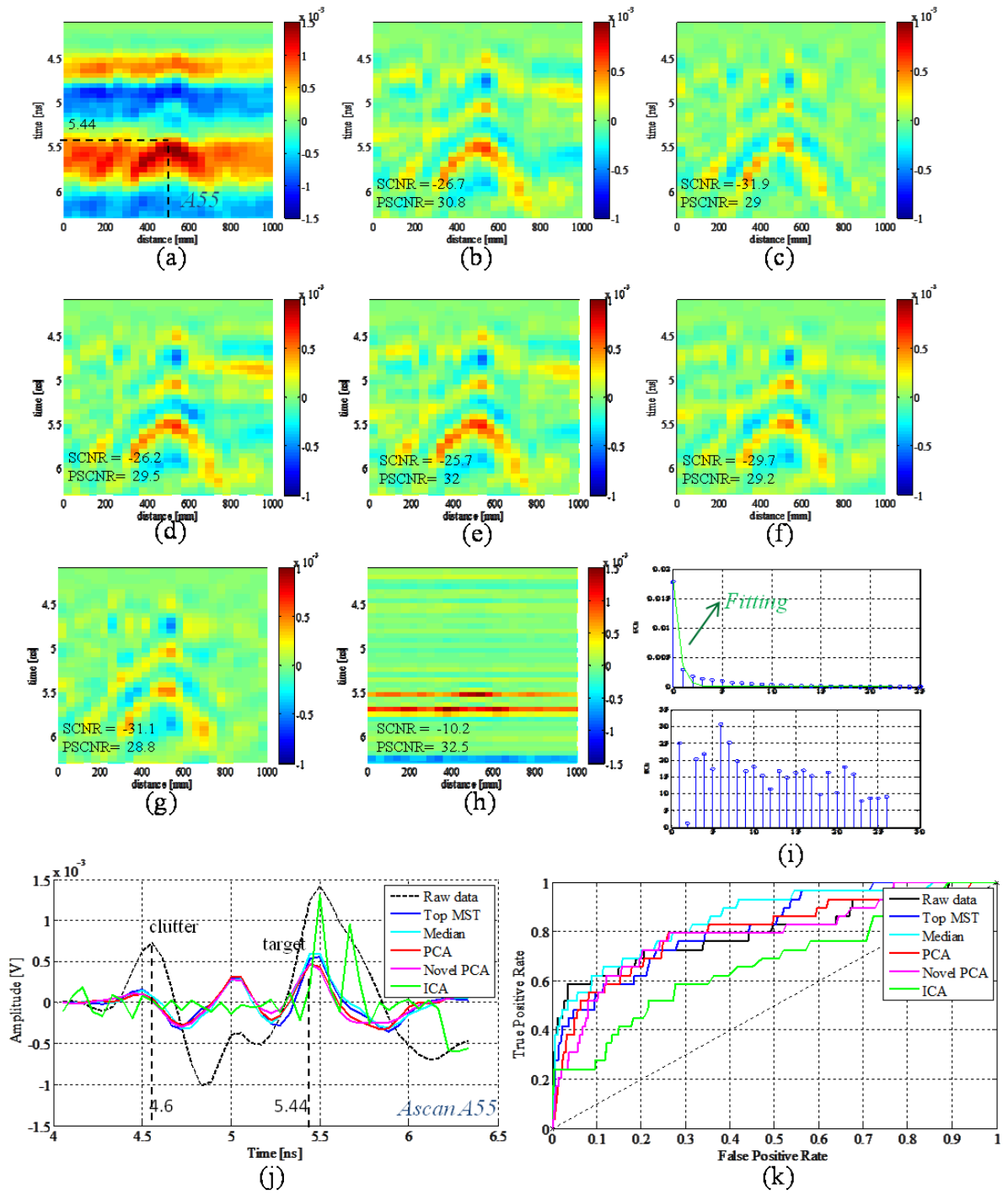


Figure 3.16: Processing results of the data on Fig. 3.15 over a reduced time window, [4; 6.3] ns. (a) Raw data (b) MST across all traces (c) Moving window MST (d) MST over target-free traces (e) Median MST (f) PCA (g) modified PCA (h) ICA (i) (Top) Eigenvalues amplitude against the order number, with best exponential fitting at $y=0.018*(exp(-x/0.61))$ (i) (Bottom) kurtosis of ICs plot (j) Ascans (k) ROC, (top MST is (d)).

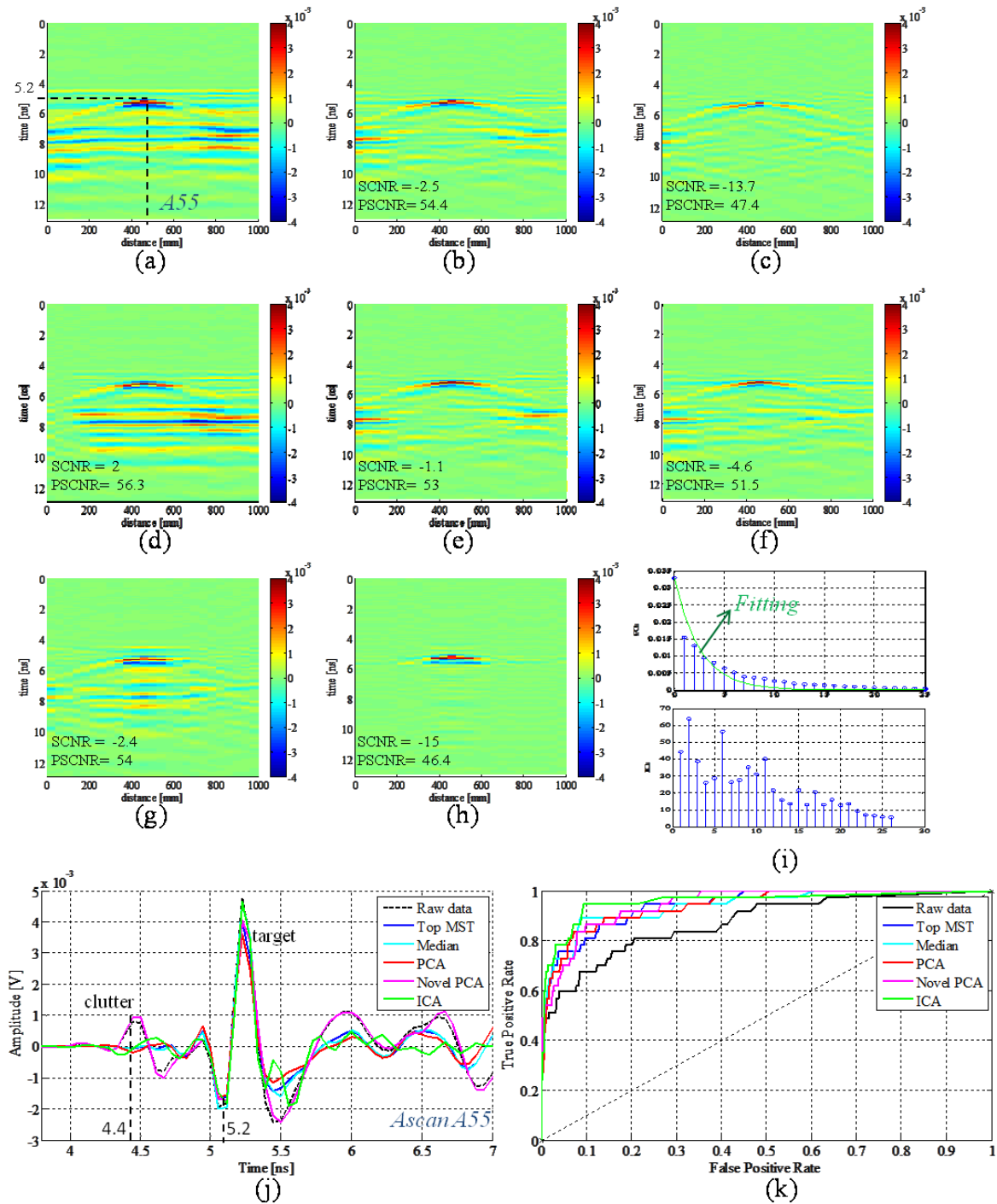


Figure 3.17: Experimental Bscans over a metal pipe buried at 160mm in depth within sand with the antennas in the endfire configuration (TM). (a) Raw data (b) MST across all traces (c) Moving window MST (d) MST over target-free traces (e) Median MST (f) PCA (g) modified PCA (h) ICA (i) (Top) Eigenvalues amplitude against the order number plot, with best exponential fitting at $y=0.03*(exp(-x/2.5))$ (i) (Bottom) kurtosis of ICs plot (j) Ascans (k) ROC, (top MST is (b)).

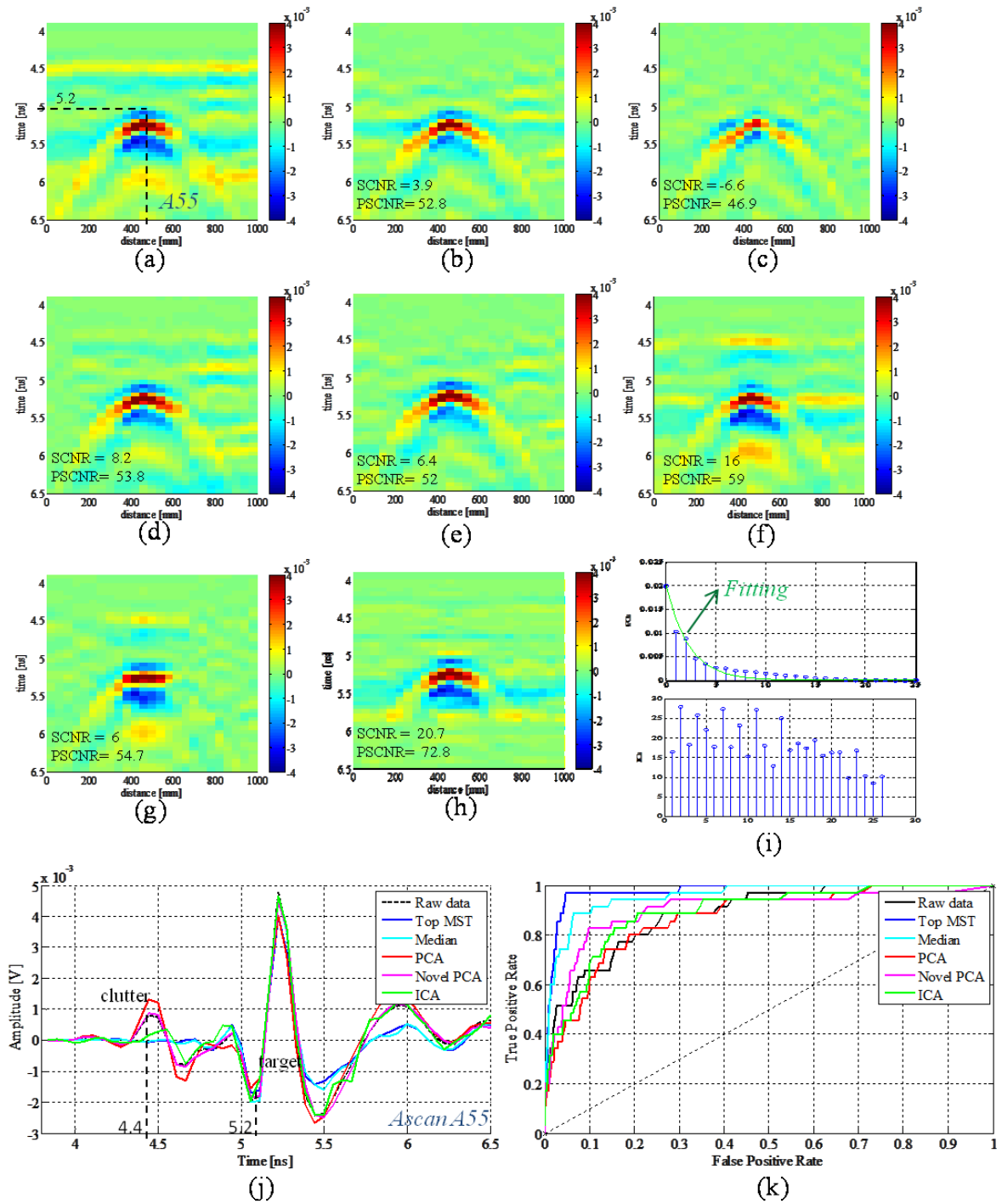


Figure 3.18: Processing results of the data on Fig. 3.17 over a reduced time window [3.8; 6.5] ns. (a) Raw data (b) MST across all traces (c) Moving window MST (d) MST over target-free traces (e) Median MST (f) PCA (g) modified PCA (h) ICA (i) (Top) Eigenvalues amplitude against the order number, with best exponential fitting at $y = 0.021 * (\exp(-x/2.28))$ (i) (Bottom) kurtosis of ICs plot (j) Ascans (k) ROC, (top MST is (b)).

VI. Conclusion

In this chapter, we have presented the application of some pre-processing techniques, namely PCA, ICA, mean and median subtraction techniques, for reducing the clutter and unwanted signals in ground-coupled GPR images. As a result, these techniques are expected to improve the detection of either dielectric or conductive targets embedded into the subsurface, including small defaults in civil engineering structures.

Firstly, simplified scenarios have been considered in the simulations and in the experimental test-site. The medium has been supposed to include a single pipe buried in either a two-layered or a one-layered media. The above selected results have been originated from the one-layer case, two-layered results are evaluated as well, but they are not showed here.

The performance of the clutter reduction techniques have been assessed from full-wave FDTD simulated data set and field data set on a specific test-site, using visual evaluation of the processed Ascans and Bscans, and also using some global quantitative criteria such as ROC curves, SCNR and PSCNR values. The widespread conventional background removal techniques, i.e., mean-based subtraction techniques, were used as a benchmark for assessing the performance of statistical-based techniques, namely, PCA and ICA.

The performance has been found different according to the depth of the target and to the polarization. Considering numerical and field data sets, we have noticed that in the case of shallow targets for which the depth is smaller than one wavelength (the clutter and the target time signatures overlap with each other), PCA appears to be more efficient than ICA. At the opposite, ICA appears to be more efficient than PCA for a deep target (the clutter and the target time signatures do not overlap with each other). In both cases however, the conventional background removal technique (MST) often overcome the performance of the statistical-based clutter reduction techniques. Among them, the third MST variant is the best but requires a reference target-free signal (from either the Bscan or a specific measurement). The median subtraction technique is shown to be quite robust to all experimental conditions.

The behavior of ICA is questioning because it is opposed to the performance evaluation which has been reported in the literature. Within the scope of the application, the ICA technique assumes that the clutter is statistically independent of the target signal, because the clutter signal exists whether the targets are present or not. However, for shallow targets, the EM wave interaction at near field makes the clutter signal becoming slightly dependent of the underlying targets. Therefore the ICA technique might not provide the correct ICs for shallow targets.

Another questioning limitation concerns the reliability of the performance assessment for shallow targets. It was assumed in section V.2.3 that the building of the reference image was not influenced by the depth of the target. This assumption can be hardly verified from data. Thus, it is recommended for shallow targets to only use a qualitative assessment of clutter reduction techniques. In particular, it is suggested to check the processed Bscans by a careful visual image analysis and to pay attention to the spatial coherency of the detected image features along the scanning direction. It is also suggested to check on the Ascan data that the

early part of the signal containing the clutter is effectively attenuated as expected by the clutter reduction technique.

Concerning the field data set, the limitation of the time window (i.e., the time horizon) would be worth to avoid the spurious signals due to multiple reflection and scattering on deep heterogeneities that make the data processing more difficult to handle. Mostly, the improvement has concerned the performance of the conventional background removal techniques, which then take over the statistical-based techniques. As a counterpart, such a time gating requires a manual intervention of the operator to adjust both the location and the duration of the time window to the useful signals.

Some improvement has been proposed for PCA to handle the varying clutter to target signal energy ratio along the scanning direction. The improvement consists in decomposing the entire Bscan into sub-Bscans based on the energy ratio. This makes PCA independent of the target RCS and to detect indifferently metal or dielectric targets. It seems also to give PCA the ability of separating deeper targets. Further improvement would concern the full automation of the modified PCA.

According to the evaluations in this chapter, PCA is then found better adapted than ICA for reducing the clutter in ground coupled GPR images as opposed to the literature review. Table 3.3 resumes the obtained results for each technique as function of the energy levels and the overlap between the clutter and the hyperbola. Working perspectives aim at testing the clutter reduction techniques for the identification of several targets in Bscan images. Moreover, it would be worth to extend the performance assessment to some of the clutter reduction techniques which have been reported in the literature review to achieve good performance on shallow targets. According to section II, it would concern among others the Time Frequency Separation technique, the Wavelet Packet Decomposition technique and the Compressive Sensing techniques. Finally, the influence of the polarization will be studied in next chapter in order to obtain the response of the target as a function of the polarization.

<i>Image holds:</i>	No-overlap $C \& H$ $E_C > E_H$	No-overlap $C \& H$ $E_C < E_H$	Overlap $C \& H$ $E_C > E_H$	Overlap $C \& H$ $E_C < E_H$
MST-Mean	+	+	+ -	+ -
MST-Median	++	++	++	++
PCA	+ -	--	++	+
Modified PCA	+	+	++	+
ICA	++	+ -	--	--

Table 3.3: Results-summary for the evaluated clutter reduction techniques. The techniques are resumed as function of the energy levels (E_C and E_H) and the overlap between the clutter, namely C , and the hyperbola, namely H . The +/- symbols indicate if the methods can/can't reduce the clutter (with different degree of reduction).

Bibliography

- [1] M. I. Skolnik, "Introduction to Radar Systems, Radar Handbook," *McGraw-Hill Professional, Third edition*, 2008.
- [2] U. Oguz and L. Gurel, "Frequency responses of ground-penetrating radars operating over highly lossy grounds," *IEEE Transactions on Geoscience and Remote Sensing*, vol. 40, no. 6, pp. 1385-1394, 2002.
- [3] Z. Zyada, T. Matsuno, Y. Hasegawa, S. Sato and T. Fukuda, "Advances in GPR-based landmine automatic detection," *Journal of the Franklin Institute*, vol. 384, no. 1, pp. 66-78, 2011.
- [4] R. Sakaguchi, "Image Processing Methods Applied to Landmine Detection in Ground Penetrating Radar," *PhD Thesis, Duke University*, 2013.
- [5] H.-S. Youn, "Development of unexploded ordnances (UXO) detection and classification system using ultra wide bandwidth fully polarimetric ground penetrating radar (GPR)," *PhD Thesis, The Ohio State University, USA*, 2007.
- [6] P. Millot, "Imagerie radar de subsurface à haute résolution: application à la detection de mines," *PhD Thesis, Ecole nationale supérieure de l'aéronautique et de l'espace, Toulouse*, 2002.
- [7] P. K. Verma, A. N. Gaikwad, D. Singh and M. Nigam, "Analysis of clutter reduction techniques for through wall imaging in UWB range," *Progress In Electromagnetics Research B*, vol. 17, pp. 29-48, 2009.
- [8] R. Solimene, A. Cuccaro, A. Dell'Aversano, I. Catapano and F. Soldovieri, "Ground Clutter Removal in GPR Surveys," *IEEE Journal of Selected Topics in Applied Earth Observations and Remote Sensing*, vol. 7, no. 3, pp. 792 - 798 , 2014.
- [9] G. T. Tesfamariam, D. Mali and A. M. Zoubir, "Clutter reduction techniques for GPR based buried landmine detection," *2011 International Conference on Signal Processing, Communication, Computing and Networking Technologies (ICSCCN)*, pp. 182-186, 2011.
- [10] J. W. Brooks, L. M. van Kempen and H. Sahli, "A Primary Study in Adaptive Clutter Reduction and Buried Minelike Target Enhancement From GPR Data," *AeroSense 2000*, pp. 1183-1192, 2000.
- [11] K. Chahine, V. Baltazart, Y. Wang and X. Dérobert, "Blind deconvolution via sparsity maximization applied to GPR data," *European Journal of Environmental and Civil Engineering*, vol. 15, no. 4, pp. 575-586, 2011.
- [12] A. M. Zoubir, I. J. Chant, C. L. Brown, B. Barkat and C. Abeynayake, "Signal

Processing Techniques for Landmine Detection Using Impulse Ground Penetrating Radar," *IEEE Sensors Journal*, vol. 2, no. 1, pp. 41-51, 2002.

- [13] Proceedings of the General Meeting of COST Action TU1208, "http://www.cost.eu/domains_actions/tud/Actions/TU1208," *Rome (IT)*, 22-24 July 2013.
- [14] A. Van Der Merwe and I. J. Gupta, "A novel signal processing technique for clutter reduction in GPR measurements of small, shallow land mines," *IEEE Transactions on Geoscience and Remote Sensing*, vol. 38, no. 6, pp. 2627-2637, 2000.
- [15] A. Morgenstjerne, B. Karlsen, J. Larsen, H. B. Sorensen and K. B. Jakobsen, "A comparative and combined study of EMIS and GPR detectors by the use of independent component analysis," *Defense and Security, International Society for Optics and Photonics*, pp. 988-999, 2005.
- [16] F. Abujarad and A. Omar, "GPR Data Processing Using the Component-Separation Methods PCA and ICA," *Proceedings of the 2006 IEEE International Workshop on Imaging Systems and Techniques, IST 2006*, pp. 60-64, 2006.
- [17] G. R. Naik and D. K. Kumar, "An overview of Independent Component Analysis and Its Applications," *Informatica: An International Journal of Computing and Informatics*, vol. 35, no. 1, pp. 63-81, 2011.
- [18] M. M. Riaz and A. Ghafoor, "Information theoretic criterion based clutter reduction for ground penetrating radar," *Progress In Electromagnetics Research B*, vol. 45, pp. 147-164, 2012.
- [19] K. Ho and P. D. Gader, "A linear prediction land mine detection algorithm for hand held ground penetrating radar," *IEEE Transactions on Geoscience and Remote Sensing*, vol. 40, no. 6, pp. 1374-1384, 2002.
- [20] M. E. Yavuz, A. E. Fouda and F. L. Teixeira, "GPR Signal Enhancement Using Sliding-Window Space-Frequency Matrices," *Progress In Electromagnetics Research*, vol. 145, pp. 1-10, 2014.
- [21] D. Carevic, "Clutter Reduction and Target Detection in Ground Penetrating Radar Data Using Wavelets," *Detection and Remediation Technologies for Mines and Minelike Targets IV*, vol. 3710, pp. 973-978, 1999.
- [22] L. M. van Kempen, H. Sahli, J. Brooks and J. P. Cornelis, "New results on clutter reduction and parameter estimation for land mine detection using GPR," *8th International Conference on Ground Penetrating Radar*, pp. 872-879, 2000.
- [23] A. Van der Merwe, I. J. Gupta and L. Peters Jr, "Clutter reduction technique for GPR data from minelike targets," *AeroSense'99, International Society for Optics and Photonics*, pp. 1094-1105, 1999.
- [24] A. H. Gunatilaka and B. A. Baertlein, "Subspace decomposition technique to improve GPR imaging of antipersonnel mines," *AeroSense 2000, International Society for Optics*

- and Photonics*, pp. 1008-1018, 2000.
- [25] M. A. C. Tuncer and A. C. Gurbuz, "Ground reflection removal in compressive sensing ground penetrating radars," *Geoscience and Remote Sensing Letters, IEEE*, vol. 9, no. 1, pp. 23-27, 2012.
- [26] F. Abujarad and S. Omar, "Factor and principle component analysis for automatic landmine detection based on ground penetrating radar," *German Microwave Conference. Karlsruhe (Germany)*, 2006.
- [27] N. Bostanudin, "Computational methods for processing ground penetrating radar data," *PhD Thesis, University of Portsmouth*, 2013.
- [28] D. Potin, "Traitement des signaux pour la détection de mines antipersonnel," *PhD Thesis, Ecole Centrale de Lille*, 2007.
- [29] G. Tesfamariam, D. Mali2 and A. M. Zoubir, "Symmetry filtering method of clutter reduction for GPR based buried landmine detection," *Elixir Elec. Engg.*, vol. 42, pp. 6365-6368, 2012.
- [30] D. Potin, E. Duflos and P. Vanheeghe, "Landmines ground-penetrating radar signal enhancement by digital filtering," *IEEE Transactions on Geoscience and Remote Sensing*, vol. 44, no. 9, pp. 2393-2406, 2006.
- [31] S. Ebihara, "Blind separation for estimation of near-surface interface by GPR with time-frequency distribution," *IEICE transactions on communications*, vol. 86, no. 10, pp. 3071-3081, 2003.
- [32] O. Lopera, N. Milisavljevic, D. Daniels and B. Macq, "Time-frequency domain signature analysis of GPR data for landmine identification," *4th International Workshop on Advanced Ground Penetrating Radar*, pp. 159-162, 2007.
- [33] T. G. Savelyev, L. Van Kempen, H. Sahli, J. Sachs and M. Sato, "Investigation of time--frequency features for GPR landmine discrimination," *IEEE Transactions on Geoscience and Remote Sensing*, vol. 45, no. 1, pp. 118-129, 2007.
- [34] G. T. Tesfamariam, "Signal Processing Techniques for Landmine Detection Using Impulse Ground Penetrating Radar," *PhD Thesis, TU Darmstadt*, 2013.
- [35] O. Lopera, E. C. Slob, N. Milisavljevic and S. Lambot, "Filtering soil surface and antenna effects from GPR data to enhance landmine detection," *IEEE Transactions on Geoscience and Remote Sensing*, vol. 45, no. 3, pp. 707-717, 2007.
- [36] I. Jolliffe, "Principal component analysis, Second Edition," *Wiley Library, Second edition*, 2005.
- [37] B. A. Draper, K. Baek, M. S. Bartlett and J. R. Beveridge, "Recognizing faces with PCA and ICA," *Computer vision and image understanding, Elsevier*, vol. 91, no. 1, pp. 115-137, 2003.

- [38] G. Coombe, "An Introduction to Principal Component Analysis and Online Singular Value Decomposition," *University of North Carolina, Chapel Hill, NC*, 2006.
- [39] K. Baker, "Singular value decomposition tutorial," *The Ohio State University*, 2005.
- [40] V. Kabourek, P. Cerny and M. Mazanek, "Clutter Reduction Based on Principal Component Analysis Technique for Hidden Objects Detection," *Radioengineering*, vol. 21, no. 1, pp. 464-470, 2012.
- [41] P. Comon and C. Jutten, "Handbook of Blind Source Separation," *Elsevier*, <http://www.sciencedirect.com/science/book/9780123747266>, 2010.
- [42] G. Clifford, "Singular Value Decomposition & Independent Component Analysis for Blind Source Separation," *Biomedical Signal and Image Processing Spring 2005*, 2005.
- [43] B. Matei, "A review of Independent Component Analysis Techniques," *Tutorial, Rutgers University, Piscataway, NJ, USA*.
- [44] Q. Gao, L. Zhang and D. Zhang, "Sequential row-column independent component analysis for face recognition," *Neurocomputing, Elsevier*, vol. 72, no. 4, pp. 1152-1159, 2009.
- [45] K. Chahine, V. Baltazart, X. Dérobert and Y. Wang, "Blind Deconvolution via independent component analysis for thin-pavement thickness estimation using GPR," *International Radar Conference-Surveillance for a Safer World, 2009. RADAR.*, pp. 1-5, 2009.
- [46] A. Zhao, Y. Jiang, W. Wang and X. Jiaotong, "Exploring independent component analysis for GPR signal processing," *PIERS Online*, vol. 1, no. 6, pp. 750-753, 2005.
- [47] X.-T. Li, X.-N. Zhang and D.-Y. Wang, "Measurement of a thin layer's thickness using independent component analysis of ground penetrating radar data," *Journal of Harbin Institute of Technology (New Series)*, vol. 15, no. 4, pp. 445-449, 2008.
- [48] J. Liu, R. Wu, T. Li and B. Zhang, "Novel Ground Bounce Removal Algorithms Based on Non-homogeneous Detector," *International Conference on Radar, 2006. CIE'06*, pp. 1-5, 2006.
- [49] B. Karlsen, H. B. Sorensen, J. Larsen and K. B. Jakobsen, "Independent component analysis for clutter reduction in ground penetrating radar data," *AeroSense 2002, International Society for Optics and Photonics*, pp. 378-389, 2002.
- [50] Q. Gao, T. Li and R. Wu, "A novel KICA method for ground bounce removal with GPR," *International Conference on Radar, 2006. CIE'06, IEEE*, pp. 1-4, 2006.
- [51] B. Karlsen, H. B. Sorensen, J. Larsen and K. B. Jakobsen, "GPR detection of buried symmetrically shaped minelike objects using selective independent component analysis," *AeroSense 2003, International Society for Optics and Photonics*, pp. 375-386, 2003.

- [52] S. Ozawa and M. Kotani, "A study of feature extraction and selection using independent component analysis," *Proc. of 7th Int. Conf. on Neural Info. Processing*, pp. 369-374, 2000.
- [53] M. Novey and T. Adali, "Complex ICA by negentropy maximization," *IEEE Transactions on Neural Networks*, vol. 19, no. 4, pp. 596-609, 2008.
- [54] J. Anemuller, T. J. Sejnowski and S. Makeig, "Complex independent component analysis of frequency-domain electroencephalographic data," *Neural Network*, vol. 16, no. 9, pp. 1311-1323, 2003.
- [55] "<http://research.ics.aalto.fi/ica/fastica/>," <http://perso.univ-rennes1.fr/laurent.albera/>.
- [56] A. Hyvärinen and E. Oja, "Independent component analysis: algorithms and applications," *Neural networks, Elsevier*, vol. 13, no. 4, pp. 411-430, 2000.
- [57] A. Hyvarinen, "Fast and robust fixed-point algorithms for independent component analysis," *IEEE Transactions on Neural Networks*, vol. 10, no. 3, pp. 626-634, 1999.
- [58] A. Hyvärinen, J. Karhunen and E. Oja, "Independent component analysis," *John Wiley & Sons*, vol. 46, 2004.
- [59] H. M. Jol, "Ground penetrating radar theory and applications," *Elsevier*, 2008.
- [60] T. Fawcett, "An introduction to ROC analysis," *Pattern recognition letters, Elsevier*, vol. 27, no. 8, pp. 861-874, 2006.
- [61] Y. Le Meur, J. Chanussot and J.-M. Vignolle, "Practical use of receiver operating characteristic analysis to assess the performances of defect detection algorithms," *Journal of Electronic Imaging*, vol. 17, no. 3, pp. 1-14, 2008.
- [62] F. Sagnard, E. Tebchrany and V. Baltazart, "Evaluation of an UWB ground-coupled radar in the detection of discontinuities using polarization diversity: FDTD modeling and experiments," *7th International Workshop on Advanced Ground Penetrating Radar (IWAGPR)*, pp. 1-6, 2013.

List of figures and tables

Figure 3.1: Typical GPR transmitter - receiver configuration model for target detection.....	68
Figure 3.2: Illustration of the proposed modification for PCA. Top (from left to right): PCs distribution, raw Bscan, and the processed Bscan by the conventional PCA; middle top (from left to right): n_1 first Ascans, apex zone from n_1+1 to n_2 Ascans, $N-n_2+1$ last Ascans; middle bottom: the processed Ascans by the modified PCA; bottom: Bscan reconstruction. .	82
Figure 3.3: Synoptic for applying PCA and modified PCA on the data.	83
Figure 3.4: Influence of the kurtosis on the shape of PDF.....	90
Figure 3.5: Simple ICA-BSS separation test on simulated Ascan with an SNR of 30 dB. a) target-free Ascan, b) simulated Ascan over the target (apex region), c) Extracted clutter response using ICA, d) Extracted target response using ICA.	91
Figure 3.6: Theoretical and experimental ROC images: a) ROC curves, potentially optimal classifiers [60], b) Raw Bscan with a visual hyperbola fitting, c) Reference image obtained by inserting the fitted hyperbola in (b) into a null Bscan matrix having same dimensions as the raw image, d) Bscan treated with ICA technique, e) corresponding ROC curve for ICA, f) segmented ICA image with threshold $k=40$, TP rate = 0.7872 , FP rate = 0.0513, g) segmented ICA image with threshold $k=100$, TP rate = 0.4468, FP rate = 0.0165, h) segmented ICA image with threshold $k=250$, TP rate = 0.1489, FP rate = 0.0027.	95
Figure 3.7: Experimental configuration for the FDTD simulations of GPR radar data with one layer soil model including a buried pipe; (top): broadside configuration (TE polarization); (bottom): endfire configuration (TM polarization).	96
Figure 3.8: Experimental configuration for the FDTD simulations of GPR radar data with Two-layered soil model including a buried pipe; (top): broadside configuration (TE polarization); (bottom): endfire configuration (TM polarization).....	97
Figure 3.9: Simulated Bscans over a metal pipe buried at 160mm depth in a one-layer homogeneous medium, with antennas in the endfire configuration (TM). (a) Raw data (b) MST across all traces (c) Moving window MST (d) MST with target-free reference (e) Median MST (f) PCA (g) modified PCA (h) ICA (i) (Top) Eigenvalues amplitude against the order number plot, with best exponential fitting at $y = 1.5 * (\exp(-x/1.91))$ (i) (Bottom) kurtosis of ICs plot (j) Ascans (k) ROC, (top MST is (d)).	102
Figure 3.10: Simulated Bscans over a metal pipe buried at 110mm depth in a one-layer homogeneous medium, with antennas in the endfire configuration (TM). (a) Raw data (b) MST across all traces (c) Moving window MST (d) MST with target-free reference (e) Median MST (f) PCA (g) modified PCA (h) ICA (i) (Top) Eigenvalues amplitude against the order number plot, with best exponential fitting at $y = 1.64 * (\exp(-x/1.7))$ (i) (Bottom) kurtosis of ICs plot (j) Ascans (k) ROC, (top MST is (d)).	103
Figure 3.11: Simulated Bscans over a metal pipe buried at 60mm depth in a one-layer homogeneous medium, with antennas in the endfire configuration (TM). (a) Raw data (b) MST across all traces (c) Moving window MST (d) MST using target-free reference (e) Median MST (f) PCA (g) modified PCA (h) ICA (i) (Top) Eigenvalues amplitude against the	

order number plot, with best exponential fitting at $y = 0.93 * (\exp(-x/2.3))$ (i) (Bottom) kurtosis of ICs plot (j) Ascans (k) ROC, (top MST is (d)).	104
Figure 3.12: Simulated Bscans over a metal pipe buried at 110mm depth in a one-layer homogeneous medium, with antennas in the broadside configuration (TE). (a) Raw data (b) MST across all traces (c) Moving window MST (d) MST over target-free traces (e) Median MST (f) PCA (g) modified PCA (h) ICA (i) (Top) Eigenvalues amplitude against the order number plot, with best exponential fitting at $y = 0.94 * (\exp(-x/1.5))$ (i) (Bottom) kurtosis of ICs plot (j) Ascans (k) ROC, (top MST is (d)).	105
Figure 3.13: Simulated Bscans over a PVC pipe ($\epsilon=3$) buried at 110mm depth in a one-layer homogeneous medium, with antennas in the endfire configuration (TM). (a) Raw data (b) MST across all traces (c) Moving window MST (d) MST over target-free traces (e) Median MST (f) PCA (g) modified PCA (h) ICA (i) (Top) Eigenvalues amplitude against the order number plot, with best exponential fitting at $y = 0.8 * (\exp(-x/0.42))$ (i) (Bottom) kurtosis of ICs plot (j) Ascans (k) ROC, (top MST is (d)).	106
Figure 3.14: Simulated Bscans over a PVC pipe ($\epsilon=3$) buried at 110mm depth in a one-layer homogeneous medium, with antennas in the broadside configuration (TE). (a) Raw data (b) MST across all traces (c) Moving window MST (d) MST over target-free traces (e) Median MST (f) PCA (g) modified PCA (h) ICA (i) (Top) Eigenvalues amplitude against the order number plot, with best exponential fitting at $y = 0.9 * (\exp(-x/0.26))$ (i) (Bottom) kurtosis of ICs plot (j) Ascans (k) ROC, (top MST is (d)).	107
Figure 3.15: Experimental Bscans over a PVC pipe ($\epsilon=3$) buried at 160mm in depth within sand with the antennas in the broadside configuration (TE). (a) Raw data (b) MST across all traces (c) Moving window MST (d) MST over target-free traces (e) Median MST (f) PCA (g) modified PCA (h) ICA (i) (Top) Eigenvalues amplitude against the order number plot, with best exponential fitting at $y = 0.06 * (\exp(-x/0.9))$ (i) (Bottom) kurtosis of ICs plot (j) Ascans (k) ROC, (top MST is (c) based on ROC).	110
Figure 3.16: Processing results of the data on Fig. 3.15 over a reduced time window, [4; 6.3] ns. (a) Raw data (b) MST across all traces (c) Moving window MST (d) MST over target-free traces (e) Median MST (f) PCA (g) modified PCA (h) ICA (i) (Top) Eigenvalues amplitude against the order number, with best exponential fitting at $y = 0.018 * (\exp(-x/0.61))$ (i) (Bottom) kurtosis of ICs plot (j) Ascans (k) ROC, (top MST is (d)).	111
Figure 3.17: Experimental Bscans over a metal pipe buried at 160mm in depth within sand with the antennas in the endfire configuration (TM). (a) Raw data (b) MST across all traces (c) Moving window MST (d) MST over target-free traces (e) Median MST (f) PCA (g) modified PCA (h) ICA (i) (Top) Eigenvalues amplitude against the order number plot, with best exponential fitting at $y = 0.03 * (\exp(-x/2.5))$ (i) (Bottom) kurtosis of ICs plot (j) Ascans (k) ROC, (top MST is (b)).	112
Figure 3.18: Processing results of the data on Fig. 3.17 over a reduced time window [3.8; 6.5] ns. (a) Raw data (b) MST across all traces (c) Moving window MST (d) MST over target-free traces (e) Median MST (f) PCA (g) modified PCA (h) ICA (i) (Top) Eigenvalues amplitude against the order number, with best exponential fitting at $y = 0.021 * (\exp(-x/2.28))$ (i) (Bottom) kurtosis of ICs plot (j) Ascans (k) ROC, (top MST is (b)).	113

Table 3.1: Conditions of assessment of the existing clutter removal methods. The colored methods are detailed in the two next sections; and the ones in purple are evaluated within the scope of our application in section 5. The ones in black are a complete state-of-the-art; the +/- symbols indicate if the methods reach good/bad performance on specified conditions (shallow or deeply buried target, strong or small surface roughness). 75

Table 3.2: Main features and characteristics of the existing clutter removal techniques. The colored methods are detailed in the two next sections; and the ones in purple are evaluated within the scope of our application in section 5. The ones in black are a complete state-of-the-art..... 76

Table 3.3: Results-summary for the evaluated clutter reduction techniques. The techniques are resumed as function of the energy levels (E_C and E_H) and the overlap between the clutter, namely C , and the hyperbola, namely H . The +/- symbols indicate if the methods can/can't reduce the clutter (with different degree of reduction)..... 115

Chapter 4: Hyperbola fitting and template matching for target detection within GPR Bscan images

Résumé

La détection automatique des signatures hyperboliques des objets enfouis permet de réduire les facteurs humains dans l'extraction des données quantitatives à partir des images Bscans. Un algorithme de détection "template matching" a été sélectionné pour être appliqué à la localisation des signatures de tuyaux cylindriques enfouis dans un sol. L'algorithme consiste à saisir une fenêtre sur une position (i,j) du Bscan et la superposer avec une image de référence (Template) afin de calculer une distance euclidienne ; l'amplitude de cette distance calculée détermine des minimums locaux (m,n) qui servent à définir la zone où existe une hyperbole dans le Bscan.

Une fois la position de l'hyperbole déterminée, les données relatives à cette région sont analysées pour extraire les paramètres d'un modèle analytique de l'hyperbole. Cette extraction s'effectue au moyen de la théorie des moindres carrés non-linéaires et concerne les caractéristiques du tuyau enfoui et du sol (position, profondeur, rayon et permittivité réelle).

L'algorithme a été mis en œuvre et évalué sur des données numériques puis sur des données expérimentales.

Contents

Résumé	125
I. Introduction.....	127
II. Ray-path model	127
III. Template matching.....	129
IV. Hyperbola extraction and fitting.....	130
V. Validation on numerical results	131
VI. Conclusion	133
Bibliography	134
List of figures and tables.....	136

I. Introduction

The reflection of EM waves on buried targets exhibits hyperbolic signatures on Bscan images, as showed in chapter 1. In this chapter, the analysis of hyperbola signatures is proposed in order to extract quantitative information about buried targets associated with their location, depth and dimension, and also the wave velocity of the subsurface. The estimation of such information has been performed using an analytical parameterized hyperbola model.

The analysis of a given hyperbola has been performed in two steps: hyperbola detection and hyperbola fitting. The detection/segmentation of hyperbolas can be performed by a wide range of techniques according to the literature: Hough transforms [1], cross-correlation [2], machine learning algorithms [3] [4], hyperbola flattening transform [5], template matching [6] and many others like neural networks classification, wavelet transform, and pattern recognition introduced in this thesis [7].

This chapter describes the technique developed in parallel to this work for hyperbola detection based on the template matching algorithm. This technique allows to further extract the hyperbola data for the fitting of the curve according to the least square criterion. The application of the template matching algorithm to Bscan images originates from [8] and the basics and applications of that technique in image processing are detailed in [9]. The algorithm uses a hyperbola template as the reference that is swept over the entire Bscan image to find the best location matching. The template matching has been successfully applied in different domains such as in the detection of road signs [10].

II. Ray-path model

The ray-path model describes the two-way travel time by the EM waves between an emitter and a receiver belonging to a ground-coupled GPR [11]. It is assumed that a cylindrical target is buried in a homogeneous soil as showed on Figure 4.1. The travel time t_i as function of the antenna position y_i (blue path) is expressed according to Pythagorean theorem, as follows:

$$\begin{cases} y_T = y_i - Y_C \\ y_R = y_i + Y_C \end{cases} \quad \text{and} \quad \begin{cases} L_{Tx2Target} = [(y_T - y_0)^2 + (d + R)^2]^{0.5} - R \\ L_{Rx2Target} = [(y_R - y_0)^2 + (d + R)^2]^{0.5} - R \end{cases} \quad (4-1)$$

Where y_0 , d and R are the unknown constants, and $Y_C = \frac{\text{offset} + SR}{2}$ is a known constant representing the center-to-center antenna distance. Equations in (4-1) expressed in chapter 1 (eq. 1-13), describe the reflected path which has traveled between the emitter Tx and the target and between the target and the receiver Rx. The total travel time for the i^{th} position y_i is the sum of both paths such as:

$$t_i = (L_{Tx2Target} + L_{Rx2Target})/v \quad (4-2)$$

$$\Rightarrow t_i = \frac{[(y_T - y_0)^2 + (d + R)^2]^{0.5} - R + [(y_R - y_0)^2 + (d + R)^2]^{0.5} - R}{v} \quad (4-3)$$

$$\Rightarrow t_i v + 2R = [(y_i - Y_c - y_0)^2 + (d + R)^2]^{0.5} + [(y_i + Y_c - y_0)^2 + (d + R)^2]^{0.5} \quad (4-4)$$

At the apex of the hyperbola, Tx and Rx are just above the target leading to the path in red (Figure 4.1) . When $L_{Tx2Target}' = L_{Rx2Target}'$ and $y_i = y_0$, the travel time is given by:

$$t_{apex} = (2L_{Tx2Target}')/v \quad (4-5)$$

$$\Rightarrow t_{apex} v = 2[(Y_c)^2 + (d)^2]^{0.5} \quad (4-6)$$

$$\Rightarrow d^2 = (t_{apex} v / 2)^2 - (Y_c)^2 \quad (4-7)$$

Considering that the velocity v is estimated according to the time/velocity spectrum analysis (chapter 1), and that the apex coordinate, position and arrival time (y_0 and t_{apex} respectively) are obtained from the detection algorithm in section III and IV; the corresponding depth value d is calculated according to Eq. (4-7).

Then, by substituting the expression of d in eq. (4-7) to eq. (4-4), and using the samples t_i and y_i from a first hyperbola analysis (section IV), the radius R can be numerically estimated according to eq. (4-4). The radius R can be solved with the Matlab 'solve' function.

Thus, the target parameters (position y_0 , depth d and radius R) are obtained by combining three techniques: detection, definition of a ray-path model, and a non linear and constraint fitting.

Particular approximations:

A usual approximation considers the case of a target located in the far-field zone of the pair of antennas [12], [13]. In such a case, the antennas are considered having a small lateral dimension (SR) and a small offset relatively to the depth d , meaning that $Y_c \approx 0$ (mono-static system $L1=L2$). Therefore Eq. (4-4) can be simplified in the following hyperbolic form:

$$t_i v + 2R = 2[(y_i - y_0)^2 + (d + R)^2]^{0.5} \quad (4-8)$$

$$\Rightarrow \frac{\left(t_i + \frac{2R}{v}\right)^2}{\left(t_{apex} + \frac{2R}{v}\right)^2} - \frac{(y_i - y_0)^2}{\left(\frac{t_{apex} v}{2} + R\right)^2} = 1 \quad (4-9)$$

-The term $b = \frac{t_{apex} v}{2} + R$ (respectively $a = t_{apex} + \frac{2R}{v}$): compared with the fitting expression (4-12) can serve to estimate the radius $R = \frac{b(a - t_{apex})}{a}$.

-The term $\frac{b}{a} = v/2$: can serve to calculate the velocity (if the velocity is not known).

When the aim is only the detection of the position and the depth of small targets [14], the cylinder is considered as a point in space with radius $R=0$, plus a negligible Y_c , eq. (4-9) can be simplified according to the following hyperbolic form:

$$\Rightarrow \frac{t_i^2}{t_{apex}^2} - \frac{(y_i - y_0)^2}{(t_{apex}v/2)^2} = 1 \quad (4-10)$$

It is worth noticing that the conventional approximations in the literature are not matched to a large lateral dimension of the antennas, and to shallow targets case, e.g., Y_c is larger than d , as shown on Figure 4.2. Then, nor the mono-static approximation (meaning $L1=L2$, and $Y_c \approx 0$ in the above equations), nor the point-like scatterer ($R = 0$ in the above equations) can be applied.

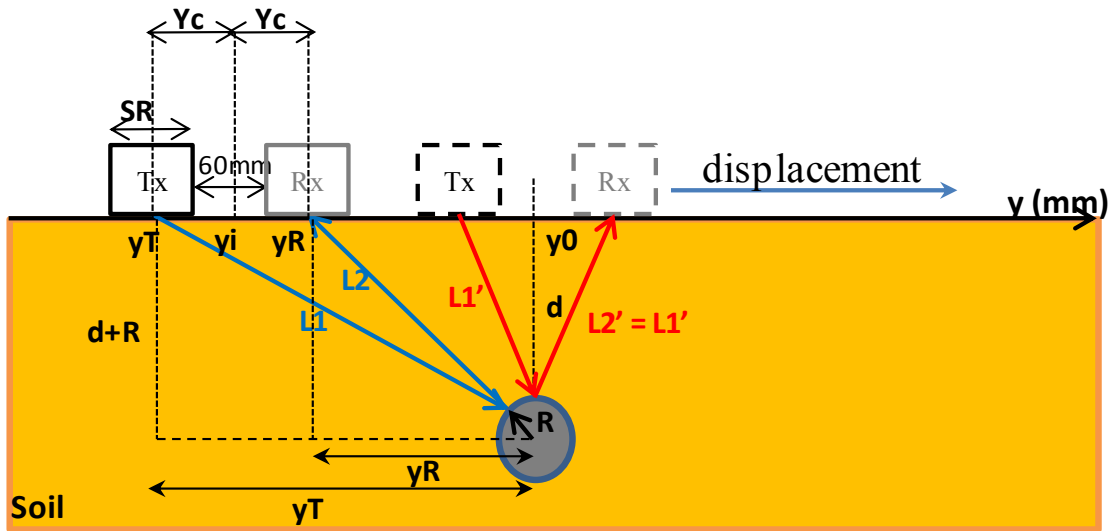


Figure 4.1: Geometry for the ray path model for a cylindrical target.

III. Template matching

This section reports the work in [8], which has been conducted by Ifsttar colleagues in parallel to this work. Main results are presented here.

The aim in the algorithm is the detection of the hyperbolas positions in a Bscan image for later extraction. Template matching algorithm is performed with 2 images: a template image used as a reference for the hyperbola shape and the Bscan Raw image.

The algorithm relies on the choice of the template image that must be chosen carefully. The template image (matrix t) is predefined according to the different hyperbola shapes observed in the Bscan. Therefore an interpretation on different types of target signatures is made before selecting the best candidate from the dataset to be used as a template. In general the conductive pipes show strongest reflection than dielectric pipes, thus such a signature has been used as a template.

Preprocessing algorithms (time zero correction, and noise filtering) have been preliminary applied on the raw Bscan image before applying the following algorithm; the clutter is removed using the suited technique according to chapter 3 to obtain a matrix g .

The template image has a smaller dimension than the raw Bscan, and its area is proportional to the area occupied by one hyperbola close to the apex. The template is translated on all possible pixels position (i, j) on the Bscan, and the corresponding Euclidian distance is calculated for each position (matrix E) defined as follows:

$$E(m, n) = \sqrt{\sum_i \sum_j (g(i, j) - t(i - m, j - n))^2} \quad (4-11)$$

For each position (m, n) of the Euclidian distance map, the calculated value represents the sum of all superposed pixels (i, j) of the translated template t on the Bscan image g ; the superposition is produced by the subtraction pixel to pixel the shifted template image from the entire Bscan.

The local minimums values of E (maximum of resemblance between g and t) correspond to positions $(m_1, n_1; m_2, n_2 \dots)$ on the Bscan; these positions serve in positioning the presence of the hyperbola in a precise region of the Bscan according to the template window size. In the next step, the latter region is used for extracting a hyperbola curve.

IV. Hyperbola extraction and fitting

This section is associated with the extraction and the fitting of the hyperbola curve in each location of the template inside the Bscan.

An interactive program [11] allows to select the hyperbola amplitude, on either the upper or the lower half zone inside the template position. The curve points associated with the first arrival times of a hyperbola can correspond to a maximum or a minimum amplitude. Because higher order reflections in a pattern may produce a stronger amplitude as compared to the amplitude of the first reflection, an interactive program is necessary to select the hyperbola curve either on the upper or the lower half zone of the template position. Thus, starting from the middle point, close points belonging to the hyperbola curve on the left and on the right legs are step by step extracted (pixel by pixel). The number of points to select on each hyperbola leg can be preliminary defined, usually 3 points have been considered.

The first time arrival in the selected window corresponding to the hyperbola apex is selected, coordinated as (y_0, t_{apex}) .

Afterwards, the hyperbola pixels are fitted by the following hyperbola equation:

$$\frac{(t_i - t_0)^2}{a^2} - \frac{(y_i - y_0)^2}{b^2} = 1 \quad (4-12)$$

The best fit with regards to the least-square criterion allows estimating the hyperbola coefficients $(a, b, y_0$ and $b)$ [15] [16]. The latter are compared to the ray model equations in

(4-4), (4-9) or (4-10) to extract information about the soil velocity and about the target depth and radius (y_0 represents the target position).

V. Validation on numerical results

Considering the end-fire configuration, Accordingly, the dataset (Figure 4.2(b)) is obtained by FDTD simulations over 3 buried pipes (conductor, dielectric with $\epsilon'=9$, and air-filled pipe) with different radiuses (32 mm, 22 mm, and 11 mm respectively) in a homogeneous soil ($\epsilon'_s = 3.5$ and $\sigma = 0.01 S.m^{-1}$) at several depths (168 mm, 79 mm and 148 mm respectively).

The modeled antennas are two blade printed dipoles antennas described in [17] as shown in Figure 4.2(a). The simulated Bscan includes the scattering from three targets visualized by three hyperbolas on Figure 4.2(c); the clutter has been removed with the median subtraction technique. The first two hyperbolas appear clearly; however the third one is overlapped and has a very small magnitude, and is thus hardly detectable.

The dataset matrix in Figure 4.2(c) is transformed into a pixel matrix as visualized on Figure 4.3(c). The resulted Bscan is processed with the template matching algorithm to extract visible hyperbola responses. The template image is chosen the same for the three pipes; it is associated with the conductor pipe response, because it has the largest magnitude. The template image has the dimension of 189×7 pixels as shown on Figure 4.3(a). According to the Euclidian distance map in Figure 4.3(b), two local minimums are present corresponding to the visible hyperbolas; with coordinates $(m_1 = 100, n_1 = 4.5; m_2 = 50, n_2 = 12)$. Two windows that well correspond to the hyperbolas positions in the Bscan image has been selected (Figure 4.3(c)).

In each window, the hyperbola coefficients (a , b , t_0 and y_0) are extracted (Figure 4.3 (d)) and used with the ray-path model for calculating the target parameters. The obtained parameters for each target are respectively: ($y_1 = -188$ mm, $d_1 = 157$ mm and $R_1 = 25$ mm to 35 mm) and ($y_2 = 113$ mm, $d_2 = 90$ mm and $R_2 = 25$ mm to 35 mm).

We observe in Table 4.1 that the pipe position and the depth estimations are very similar to the theoretical ones; however the radius estimation is very hard when the antenna dimensions are very large compared to the radius. A higher resolution extraction and fitting algorithm must be employed to obtain more accurate results and valid radius estimation.

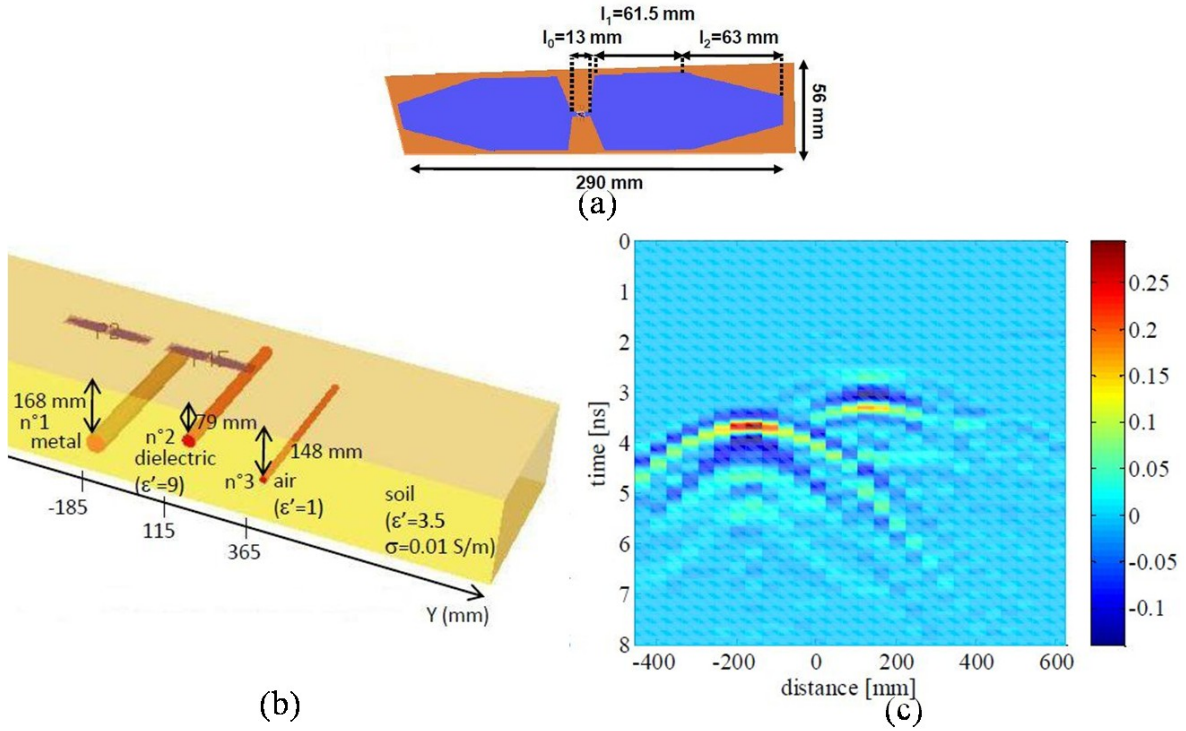


Figure 4.2: a) Blade dipole geometry, b) Geometry model used for simulation in the end-fire antenna configuration with 3 buried pipes, c) computed Bscan image after clutter removal by the median subtraction technique (on the courtesy of F. Sagnard [8]).

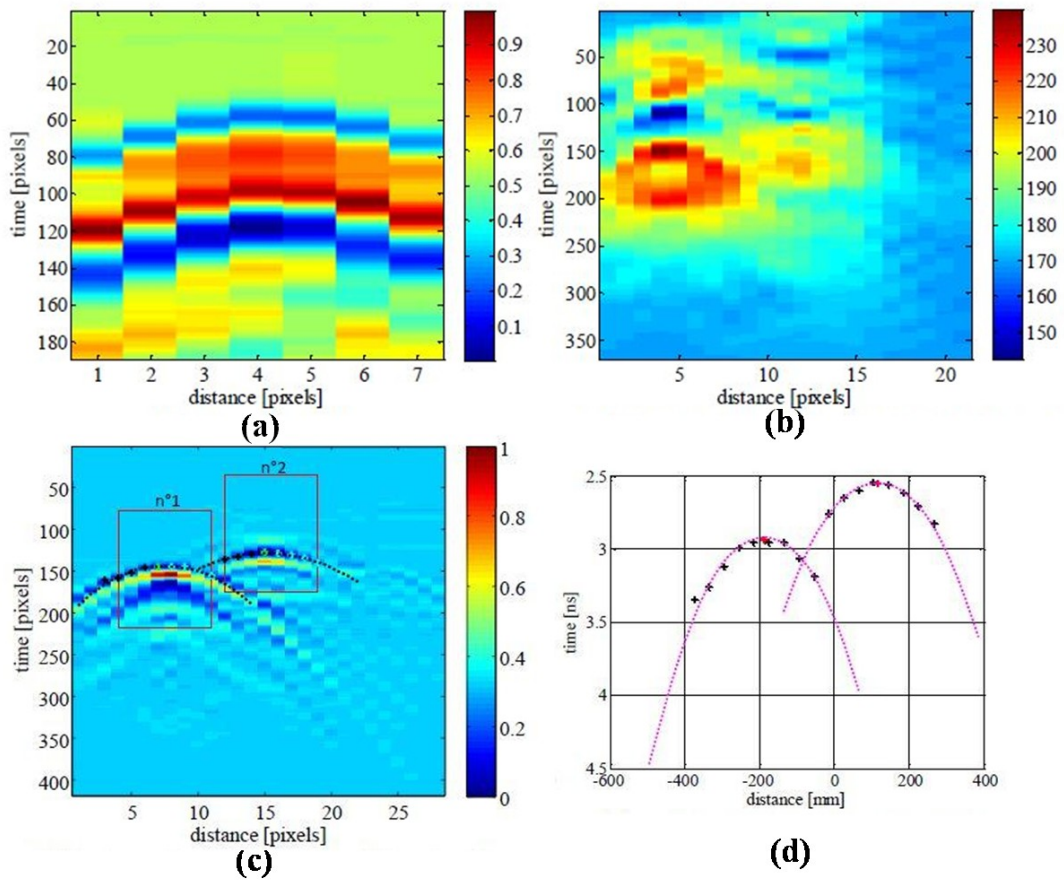


Figure 4.3: Illustration for template matching algorithm (on the courtesy of F. Sagnard [8]), a) template image, b) Euclidian distance map, c) Extracted hyperbola Positions using template matching, d) Fitting curves.

	t	d	y₀	ε'	R
Cylinder n°1 (1 st minimum)	2.94 ns	150 mm	-188.3 mm	3.93	30
Error %		10%	1.8%	12%	N.A
Cylinder n°2 (1 st minimum by extrapolation)	2.11 ns	80.6 mm	113.9 mm	2.99	30
Error %		2%	0.9%	14.6%	N.A

Table 4.1: Estimated target parameters and the corresponding uncertainty error, according to the ray-path model.

VI. Conclusion

This chapter introduced the use of the template matching technique to detect targets within Bscan images. The matching algorithm uses a predefined signature of targets to construct a matching instance image, later it detects the minimum of the Euclidian distance based on the instance image. Detected location is used to extract hyperbola points, which will be used to calculate the target parameters (position, depth and shape) according to the ray-path model.

The first evaluation of this technique was performed on cylindrical shaped targets buried within an homogeneous medium. The matching algorithm shows very good results for detecting non-overlapped target with large magnitude. However for target with small dielectric contrast with the ground, the hyperbola signature is very weak, and the matching algorithm cannot detect the signature. Further tests in [8] have been performed on field data with similar conclusion.

Much improvement can be proposed, especially for noisy images with low magnitude signatures, and in the detection of shallow targets.

Bibliography

- [1] C. G. Windsor, L. Capineri and P. Falorni, "A Data Pair-Labeled Generalized Hough Transform for Radar Location of Buried Objects," *Geoscience and Remote Sensing Letters, IEEE*, vol. 11, no. 1, pp. 124-127, 2014.
- [2] J. Wang and Y. Su, "Fast detection of GPR objects with cross correlation and Hough transform," *Progress In Electromagnetics Research C*, vol. 38, pp. 229-239, 2013.
- [3] X. Nunez-Nieto, M. Solla, P. Gomez-Pérez and H. Lorenzo, "GPR Signal Characterization for Automated Landmine and UXO Detection Based on Machine Learning Techniques," *Remote Sensing*, vol. 10, no. 6, pp. 9729-9748, 2014.
- [4] N. R. Syambas, "An Approach for Predicting the Shape and Size of a Buried Basic Object on Surface Ground Penetrating Radar System," *International Journal of Antennas and Propagation*, 2012.
- [5] J. A. Marble and A. E. Yagle, "The hyperbola-flattening transform," *Spie: Detection and Remediation Technologies for Mines and Minelike Targets IX*, vol. 5415, pp. 781-790, 2004.
- [6] Z. Zyada and T. Fukuda, "3D template based automatic landmine detection from GPR data," *SICE, 2007 Annual Conference*, pp. 1552-1557, 2007.
- [7] W. Al-Nuaimy, "Automatic feature detection and interpretation in ground-penetrating radar data," *PhD Thesis, University of Liverpool*, 1999.
- [8] F. Sagnard and J.-P. Tarel, "Template matching based detection of hyperbolae in ground penetrating radargrams," *Internal IFSTTAR report, submitted to IOP*.
- [9] R. Brunelli, "Template matching techniques in computer vision: theory and practice," *John Wiley & Sons*, 2009.
- [10] R. Belaroussi and J.-P. Tarel, "Détection des panneaux de signalisation routière par accumulation bivariée," *Traitement du signal*, vol. 27, no. 3, p. 265, 2010.
- [11] F. Sagnard and E. Tebchrany, "Using polarization diversity in the detection of small discontinuities by an ultra-wide band ground-penetrating radar," *Measurement, Elsevier*, vol. 61, pp. 129-141, 2015.
- [12] A. V. Ristic, D. Petrovacki and M. Govedarica, "A new method to simultaneously estimate the radius of a cylindrical object and the wave propagation velocity from GPR data," *Computers & Geosciences*, vol. 35, no. 8, pp. 1620-1630, 2009.
- [13] H. Chen and A. G. Cohn, "Probabilistic robust hyperbola mixture model for interpreting ground penetrating radar data," *The 2010 International Joint Conference on Neural*

Networks (IJCNN), pp. 1-8, 2010.

- [14] G. Borgioli, L. Capineri, P. Falorni, S. Matucci and C. G. Windsor, "The detection of buried pipes from time-of-flight radar data," *IEEE Transactions on Geoscience and Remote Sensing*, vol. 46, no. 8, pp. 2254-2266, 2008.
- [15] P. O'Leary and P. Zsombor-Murray, "Direct and specific least-square fitting of hyperbolae and ellipses," *Journal of Electronic Imaging*, vol. 13, no. 3, pp. 492-503, 2004.
- [16] S. J. Ahn, W. Rauh and H.-J. Warnecke, "Least-squares orthogonal distances fitting of circle, sphere, ellipse, hyperbola, and parabola," *Pattern Recognition*, vol. 34, no. 12, pp. 2283-2303, 2001.
- [17] F. Rejiba, F. Sagnard, C. Schamper, M. Froumentin and R. Guérin, "Zero-offset profiling using frequency cross-hole radar in a layered embankment test site: antenna design, simulation and experimental results," *Near Surface Geophysics*, vol. 9, no. 1, pp. 67-76, 2011.

List of figures and tables

Figure 4.1: Geometry for the ray path model for a cylindrical target.	129
Figure 4.2: a) Blade dipole geometry, b) Geometry model used for simulation in the end-fire antenna configuration with 3 buried pipes, c) computed Bscan image after clutter removal by the median subtraction technique (on the courtesy of F. Sagnard [8]).	132
Figure 4.3: Illustration for template matching algorithm (on the courtesy of F. Sagnard [8]), a) template image, b) Euclidian distance map, c) Extracted hyperbola Positions using template matching, d) Fitting curves.....	132
Table 4.1: Estimated target parameters and the corresponding uncertainty error, according to the ray-path model.....	133

Chapter 5: Contribution of polarization diversity to target detection

Résumé

Ce chapitre aborde l'influence de l'orientation des antennes (émettrice et réceptrice) sur les caractéristiques d'amplitude, de temps d'arrivée et de forme des échos radar sur des cibles enfouies. Il débute par une revue bibliographique sur l'effet de la diversité de polarisation sur la détection des cibles enfouies. Ensuite, nous étudions cet effet sur des cibles cylindriques de très faibles dimensions à travers une étude analytique et à partir des données simulées et expérimentales.

L'orientation des antennes l'une par rapport à l'autre et relativement à la cible permet de définir de nombreuses configurations de mesures possibles. Cependant, deux configurations sont prises en compte: "broadside" et "end-fire". Ce sont les deux configurations co-polarisées, car les champs électriques des deux antennes (Tx et Rx) sont parallèles entre eux. Les configurations de polarisation croisée demandent une étude approfondie.

Deux polarisations de base sont étudiées analytiquement: la première avec un champ électrique E perpendiculaire (mode TE) à l'orientation de l'axe du cylindre de la cible et la seconde avec le champ parallèle (mode TM) à l'axe du cylindre. La configuration des antennes définit une polarisation particulière qui peut être exprimée en fonction de ces deux polarisations de base. L'étude analytique utilisée est basée sur un modèle d'analyse via la méthode de Mie, en utilisant une onde incidente plane et les équations de Maxwell, Hankel et Bessel pour calculer la dispersion des ondes réfractées et réfléchies sur un cylindre infini. Des mesures GPR ont été réalisées sur des sites différents et en correspondance avec les données de simulation; elles ont servi à valider les résultats de l'étude analytique.

Les résultats finaux montrent que les cibles métalliques sont détectées dans les deux polarisations TE et TM; néanmoins la polarisation TM montre des échos d'amplitude plus élevée et des Bscans plus simples à interpréter. Toutefois, pour les cibles diélectriques nous remarquons deux cas: les cibles diélectriques avec une permittivité réelle plus élevée que la permittivité du sol, présentent plus de dispersion en polarisation TM, alors que les cibles de faible permittivité ont montré un comportement différent avec une préférence pour la polarisation TE. Ce comportement montre que le balayage du GPR en multi-polarisation peut être très utile pour détecter et qualifier la nature des tuyaux enterrés et le contenu des fractures dans un sol.

Contents

Résumé	137
I. Introduction.....	139
II. Previous studies	140
III. Multi-configuration for data acquisition	142
IV. Analytical scattering model for cylindrical targets.....	143
IV.1. Modeling Techniques	143
IV.2. Hypothesis	144
IV.3. Parametric study	145
IV.4. Scattering width (SW).....	148
V. FDTD simulation results.....	149
V.1. Geometries modeled	149
V.2. Results	151
VI. Experimental results.....	160
VII. Conclusion.....	165
Bibliography	167
List of figures and tables.....	170

I. Introduction

The polarization, which governs the vector nature of electromagnetic fields, is a fundamental property of propagation. It expresses the change of the field strength (E or H) in the plane perpendicular to the direction of the wave propagation, Balanis 1989 [1].

The interaction of electromagnetic waves with a target produces scattering and reflection that are at the origin of the depolarization effect that changes the amplitude and the phase of the excitation field. The depolarization effect can serve to discriminate several targets. A target made of a given medium properties and having a given orientation relative to the electric field direction has a specific scattering/reflection response in a polarization mode, that may improve its discrimination.

The data collection of multi-component, in particular the polarization diversity, allows to obtain the received EM field in different planes. The benefits are the visibility of the targets in some configuration more significantly than others, such as detailed in Roberts 1994 [2] and Daniels 1996 [3]. As a consequence, the polarization diversity is expected to improve the extraction of information, and within the scope of this work, to improve the capability to detect and to characterize shallow targets.

Conventional GPR systems are bistatic and use linearly polarized antennas. A few systems enable GPR surveys with a data collection of different polarizations simultaneously, [4]. Most of the GPR surveys are conducted with conventional systems, thus requiring a manual switching between the different antenna configurations to collect diversely polarized data. Within this scope, GPR surveys are usually carried out for convenience in a single polarization configuration, mainly the TM polarization.

The last difficulty is to handle the UWB characteristics of the GPR signal. We do not deal with pure and completely polarized waves as for monochromatic waves, but partially polarized waves (mostly because the propagation in the medium, the antennas and the target characteristics are not steady in both phase and amplitude over the whole bandwidth). Specific polarization features have been then introduced in the literature, e.g., coherency matrix, polarization degree. Nevertheless, the measured polarization is assumed to be dominated by the polarization characteristics of the wave at the central frequency of the GPR pulse (in the results presented $f_0=1$ GHz).

In GPR, a buried cylinder is an important model in civil engineering as it may represent a pipe, a cable or a bar. The model of a thin surface is also used as a canonical target to represent a fracture or a planar discontinuity. The present study is carried out to investigate the several effects induced by the interaction of a buried infinite cylinder in a medium to further facilitate target recognition or classification. Particularly, how the changes in antennas orientations may affect the amplitude, the arrival time and the shape of received signatures. In this chapter GPR polarization has been studied in several approaches:

- Analytically by using the Mie theory and the decomposition of a plane wave into cylindrical waves.

- Numerically by modeling and simulating the GPR system with a pair of antennas (bowtie slot and blade dipoles) using the 3D FDTD approach under the software EMPIRE.
- Experimentally by acquiring GPR profiles on the test-sites.

The results of these approaches have been qualitatively analyzed from plots and then compared to each other.

II. Previous studies

Polarization studies in GPR dating back to the 1970s, studied the response of buried cylinders. The scattering problem is solved using different methods that depend on the size of the target relative to the wavelength. The analytical scattering modeling of the electromagnetic scattering by canonical targets was an intensive research interest that has been treated in different fields such as remote sensing and light propagation [5]. This problem is considered since the beginning of the twentieth century. Analytical models that usually consider an excitation by a plane wave are chosen to provide more insight into the scattering interactions than numerical models. The main canonical objects are spheres, and cylinders [6]. In most electromagnetic scattering applications, the scattered field is generally measured in the far field. The basis of the Mie (1908) and cylinder theories is actually matched to the near field scattering, thus the far field solution is obtained by limiting value considerations of the near field formulas. However, the near field solution plays an important role for both ground-coupled GPR configuration and shallow buried targets as encountered in humanitarian demining, namely UXO [7], and civil engineering.

The solution of the scattering of electromagnetic waves by a sphere (Mie or Lorenz-Mie theory) and their extensions, e.g. the scattering by a layered sphere, the multiple scattering Mie solution (GMM) or the generalized Lorenz-Mie theory for an incident Gaussian beam (GLMT), are widely used for this purpose.

If the length of the cylindrical scattering structures is much larger than the diameter, the infinite cylinder approximation can be applied. The first exact solutions of Maxwell's equations were presented by Lord Rayleigh (1918). Analogous to the Mie solution, a various number of extensions exist for the infinite cylinder scattering theory [8], which include layered cylinder, multiple cylinders and Gaussian beam solutions [9].

Some studies extract a scattering matrix formed by the S parameters in different polarizations. Higgins et al. [10] used a full polarimetric system and swept each position in different polarizations for UXO (Unexploded Ordnance) mines-like object detection. They calculated two criteria, namely, ELF (Estimated Linearly Factor) and DEN (angle density), for the classification of UXO types. These criteria are expressed as function of all S parameters in 4 polarizations (two cross- and two co-polarizations). Also in [11], the authors propose an analysis of the scattering matrix for plastic anti-personal landmines with different orientations relatively to the antennas. The target features are then extracted from the eigenvalue of the scattering matrix as function of the frequency. And Villela et al. [12], studied the properties of the scattering matrix obtained from different polarizations to extract buried pipe properties.

For the application of GPR to civil engineering, the study of polarization effect on the detection of targets mainly concern cylinders and fractures. A synthesis of previous works is presented hereafter.

Concerning cylinders, a detailed parameter analysis (depth, permittivity of the background material, radius-to-wavelength ratio) has been proposed in the case of infinite length by Radzevicius et al. (2000) [13] using cylindrical wave decomposition based on Hankel and Bessel functions. The scattering properties have been studied in the far-field zone, in terms of the scattering width, and in both the TE and TM polarizations. The authors state that the TM polarization is preferred for the detection of a conductive cylinder, while the TE polarization is generally preferred for a dielectric cylinder. However, in the case of a dielectric pipe, this is the dielectric contrast between the soil and the pipe that governs the depolarization effect in the TE or TM polarization. The authors have observed that cross-polarized antennas appear more suitable for clutter reduction when a strong depolarization is induced by pipes. The work of Paulus et al. (2001) [14] deals with numerical results (Green's tensor) associated with the 2D distribution of the scattered field by a dielectric cylinder at optical frequencies in the presence of a stratified medium. It has been observed that in a homogeneous medium stationary waves are created in the backward direction in both polarizations (p-polarization=TE polarization, and s-polarization=TM polarization), but in the forward direction a maximum of magnitude can be observed inside the cylinder for the s-polarization and on the left and right sides of the cylinder for the p-polarization. The s-polarization appears to induce a greater scattering cross-section as well as in a 2 layered medium in the configuration proposed (real permittivity of the cylinder higher than in the medium). Capizzi et al. (2008) [15] have presented experimental polarized survey issued from buried conductive and dielectric pipes which are either thin or large compared to the minimum wavelength. The conclusion is that the TM polarization is preferred for a conductive pipe, and the TE polarization is best suited for a PVC pipe in a medium. Moreover, they have observed that a small cylinder diameter produces a higher depolarization effect. The authors have also studied azimuthal targets, and applied Alford's operator to estimate their strike direction. Roberts et al. (2009) [16] and Naser et al. (2010) [17] experimentally studied the detection of pipes with varying depth, diameter and filling for the two main polarizations on specific test sites. A full-resolution technique has been studied by Roberts and al. to improve the S/N ratio and improve the ability to distinguish pipes in crowded utility trenches. Böniger et al. (2012) [18] have demonstrated in a field test the potential of considering and analyzing polarization phenomena in 3D GPR data for pipes with different orientations (parallel and perpendicular to system displacement). They have introduced and used an attribute-based processing flow to enhance the structural and physical characteristics of targets. The attributes are calculated from dual-polarization data. Liu and al. (2014) [19] have designed a GPR system made of a pair of linear dual-polarization antennas (Vivaldi) at the reception and a circularly polarized antenna (spiral) at the transmission. The receiving antennas can work simultaneously. The GPR system acquires data in the frequency domain, using a VNA in the UWB [10 MHz; 4 GHz]. Finally, they evaluated the system on

small size metallic wires buried with different orientations. Moreover, polarization studies have been the topic of many PhD theses such as in [20] [21] [22].

Concerning fractures, Tsoflias et al. (2004) [23] evaluated polarization properties (E-pol and H-pol) on the detection of vertical fractures, they observed a phase lead when the E field is oriented orthogonal to the plane of the fracture, which allowed them to locate the fracture and extract its azimuth. Seren et al. (2012) [24] surveyed the test field in a direction perpendicular to the visible fractures on the ground surface by referencing Tsoflias work. Perll (2013) [25] studied the influence of cross-polarization in addition to the latter co-polarizations for the detection of fractured rocks and corresponding contaminants fluid flows, and used the summation of cross- and co-polarized components to increase the accuracy of the detection. In general oblique polarization relatively to the fractures leads to more accurate detection.

Most multi-polarization studies have shown an improved capability in target detection and classification (for pipes and cracks). And a polarization is declared preferential depending on the evaluated targets EM nature and orientation relatively to the electric field. However, by recording scattering in many polarizations with a smaller step size, more information and features about the target geometry and nature can be obtained: Roberts et al. [16] compare the benefits between high-resolution surveys and multi-polarizations surveys. High resolution is employed by sweeping more dense survey points, and two orthogonal polarizations are considered. The tests were evaluated on a ground containing pipes in different directions and dielectric natures. They found that applying a dense resolution is more benefit than using two polarizations, because not all pipes were visible in both polarizations and high resolution gives a more visible hyperbola queues, consequently better migration. The main drawbacks are time consumption in survey acquisition and in signal processing. In [26] Marchesini et al. also compared dense spatial sampling to polarization, but for cracks and ground fractures. They condition the capture of full resolution by having profile spacing at least equal to the quarter wavelength of the dominant center frequency. They observed that polarization alone gives some blurred and missed detections, and recommended to use the polarization in parallel with a high spatial sampling step size.

III. Multi-configuration for data acquisition

Supposing that both receiving and transmitting antennas are located in a separate box, measurements can be performed by manually switching the Tx and Rx antennas in different reciprocal orientations to each other. A configuration is ‘co-polarized’ when both antennas are oriented in the same direction (resp. their corresponding electric fields are parallel), whereas it is ‘cross-polarized’ when the antennas are perpendicular to each other (resp. their corresponding electric fields are orthogonal). i.e.: Feng et al. [4] and Liang et al. [27], described two sets of polarization: co-polarimetric and cross-polarimetric and each polarization is swept in two orthogonal directions.

Cross-polarized configurations are rarely used. For example, Li et al. [28], state that the cross polarization did not give any additional useful information for all pipe types, whereas Radzevicius et al. [13] observe that cross-polarized antennas appear more suitable for clutter reduction when strong depolarization is induced by pipes. Therefore cross-polarization can be useful in the rare cases where the depolarization well matches to the receiver antenna orientation.

A co-polarized configuration may be parallel, if the antennas are oriented parallel to the line of data collection; or perpendicular, if the antennas are perpendicular to the acquisition line. A co-polarized dipole configuration is called endfire when the two antennas are aligned along their larger dimension, whereas it is called broadside (or mirror) when they are parallel. In most cases, GPR surveys are made only in the broadside configurations.

Thus, there exist six possible configurations as visualized in Figure 5.1:

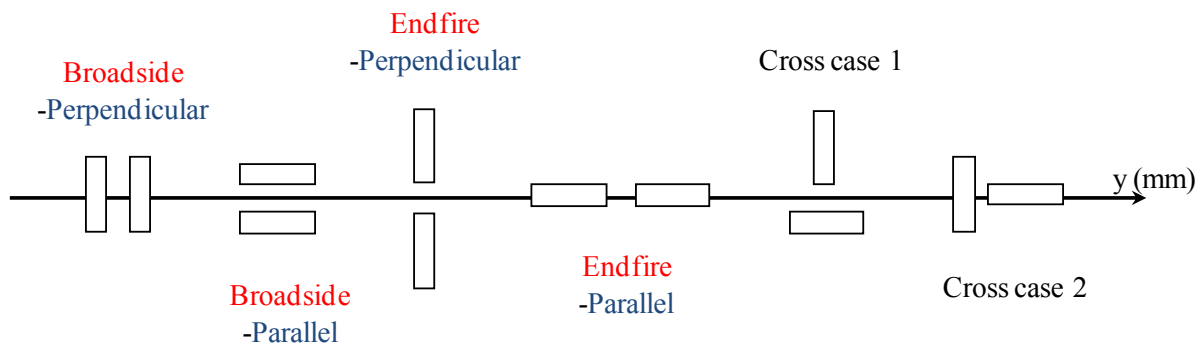


Figure 5.1: Antenna configurations for collecting GPR data with full polarization diversity; the four co-polarized (resp. two cross-polarized) antenna configurations are represented on the left (resp. on the right); because of antenna dimension, the offset can be different from one configuration to one another; in practice, GPR data collection are usually limited to the two co-polarized configurations: broadside-perpendicular and endfire-parallel.

N.B: This work considers three configurations: broadside-perpendicular (namely broadside), endfire-parallel (namely endfire) and cross case 2.

IV. Analytical scattering model for cylindrical targets

IV.1. Modeling Techniques

Cylindrical targets are part of the canonical objects in electromagnetism. They have motivated many authors in the past, e.g., Schuster [29] and Wait [30], to achieve analytical models for studying the scattering of planes waves from an infinite cylinder. Many methods exist in the literature to solve the corresponding EM scattering problem. Among others, the Geometrical Optics (GO) method (or Ray Optics), Geometrical Theory of Diffraction (GTD), and the Physical Theory of Diffraction (PTD) are used to achieve analytical modeling for the scattering of EM waves from both smooth surfaces and objects which diameter d is larger than the wavelength $d/\lambda \gg 1$. They are generally used for modeling the propagation of light [29].

At the opposite, the Rayleigh scattering (RS) theory is devoted to model the EM scattering from small particles compared to the wavelength $d/\lambda \ll 1$, like solids, gases and

liquids particles [5]. For small to large objects which dimensions are close to the wavelength $d/\lambda \approx 1$ and have canonical shapes like spheres or cylinders, the exact EM scattering solution can be found using the Mie scattering (MS) method; it solves Maxwell equations in cylindrical coordinate to calculate the electric and magnetic field inside and outside the corresponding object. Other different analytical studies for the scattering from cylinders can be found in [31] [32].

As opposed to the latter, the Finite-Difference Time-Domain (FDTD) method is a numerical method which is used to handle the scattering of EM waves over non canonical objects, heterogeneous media, rough surfaces and complex structures.

The ratio between the wavelength and the radius of the target is an important parameter to consider in polarization study. When radius size is much larger than the wavelength, the target will appear as a plane surface to the small wavelength and there will be no depolarization on a planar surface at normal incidence (Balanis book). In the opposite case, the scattered waves will have different properties from the incident waves (outside and inside the cylinder) and a strong depolarization may be expected.

In general for civil engineering structures, the cylindrical pipes have a fixed geometry and the size may be smaller or larger than the wavelength. This section deals with small radius cylindrical pipes, which have radius between 12 mm and 32 mm. Considering the central frequency of the radar pulse to be 1 GHz and the medium permittivity between 3.5 and 9, the pipe diameters range from $0.15\lambda_{mat}$ to $0.64\lambda_{mat}$, and the most appropriate analytical method to consider is the MS method. However one of the pipes used in experimental results has a radius of 5 mm, the diameter D is equal to $0.0625\lambda_{mat}$ and the Mie method may not be appropriate to calculate the corresponding scattering.

The EM scattering over embedded cracks is also considered. Cracks are modeled by planar surfaces like metallic strips (vertical cracks) or plates (horizontal cracks or debonding). Analytical studies are showed in Balanis [1] (Part 11.3) using the Physical Optics technique. The modeling is much more complex than for the cylindrical target because of the edge effects. Balanis showed large difference in the Scattering Width SW (to be defined in section IV.4) patterns between polarization TM and TE as function of the observation angle. Because of this complexity, the FDTD is usually more appropriate for simulating it through software tools. For example, Diamanti et al. [33] used FDTD to simulate the GPR signatures of opened vertical cracks within pavement.

IV.2. Hypothesis

The plane wave is one of the simplest mathematical forms to compute for EM waves, it can be considered when the target is in the far field region of the source. The following analysis is based on a simple case of plane incident wave to distinguish polarization effects, and it does not consider the radiation pattern of the antennas.

We aim at calculating the total and the scattered field in both modes TM and TE, for conductor and dielectric infinite cylindrical pipes. Scattering properties are described using Bessel and Hankel functions of the MS technique, the fields are calculated inside and outside

the cylinder. When working with cylindrical forms, it is most desirable to transform the rectilinear axis bases into cylindrical coordinates. And we assume that all fields are time-harmonic: oscillating with a single frequency that can be expressed by $e^{j\omega t} = e^{j2\pi ft}$.

We also consider an ideal homogenous lossless, non dispersive and isotropic medium. Let x be the vertical axis going in the ground, y the horizontal axis as the direction of the radar displacement and z the horizontal axis in the direction of the long axis of the pipe. The cylindrical pipes are, oriented along z axis, having an infinite length, and with radius $a < \lambda_{mat}$. We assume that the gap between the emitter and the receiver is small compared to the depth of the target, thus transmitter and receiver are approximated at the same position and the scattering is referred to backscattering with an angle of 180° , (normal incidence in the $+x$ direction) when the source is directly above the target. For the case of oblique incidence or for more details on the analytical model, readers are referred to Balanis Book [1].

Using the above hypothesis, the analytical model is presented in Appendix B. These equations (i.e. for TM mode see equations B-14, B-19, B-21 and B-25) confirm that the scattered field depends not only on the EM properties of the host medium and the cylinder, but also on the frequency (related to β) and on the radius a . In addition, the equations will be dependent on an angle of incidence θ if an oblique incidence is considered [1].

IV.3. Parametric study

The scattered field is evaluated in a homogeneous soil with different electric permittivities, different monochromatic frequencies and different pipes radii. For a medium with permittivity of 3.5, a pipe radius of 0.075λ (12 mm) and a frequency of 1GHz, the computed scattered fields inside and outside of the cylinder are shown on Figure 5.2 in both polarizations TM and TE.

The implemented model is a modified version of the Matlab implementation done by Guanran [34]; the modified version includes an extra implementation of the polarizations TE, a normalized E field and a frequency dependency in the equations. The field amplitudes values are given in dB ($20\log_{10}$). Poynting vector is showed in small black little arrows on the images. The following observations can be made:

- For metal targets both polarizations have high scattering, but the TM (E field parallel to the pipe axis) polarization got higher scattering in all directions (around -4 dB). Comparing TM and TE modes, Figure 5.2 shows low amplitudes (~nulls) of radiations in left and right directions of TE polarization and no nulls in TM mode.
- For dielectric targets, we can distinguish two different cases depending on the targets dielectric permittivity with regards to the one of the host medium (smaller or larger). For both polarizations, high permittivity dielectric pipes have more scattering and lower penetration waves, while low permittivity dielectric pipes have higher penetration and absorption, nevertheless:
 - 1) Dielectrics with low permittivity ($\epsilon'=1$) or high impedance relatively to the propagation medium, shows back-scattering magnitude less than -15dB in both

TE and TM mode; however, the scattering in TE mode appears more directive vertically. Both polarizations have low scattering for this type of pipe, therefore they might be better imaged in TE polarization (E field orthogonal to pipe axis), as it will be confirmed later in the experimental results.

- 2) Dielectrics with high permittivity ($\epsilon' = 9$) or low impedance relatively to the propagation medium, shows a back-scattering magnitude of -10 to -5 dB in TM mode and -15dB in TE mode; therefore, this confirms that dielectrics with a high permittivity are better imaged in TM polarization (E field parallel to pipe axis).

Same results as above are obtained for different frequencies ranging from 400MHz to 4GHz, and for radius lengths smaller than the wavelength (the targets considered are limited in size). The significant difference is seen when some changes in the materials properties happens on both the medium and the target.

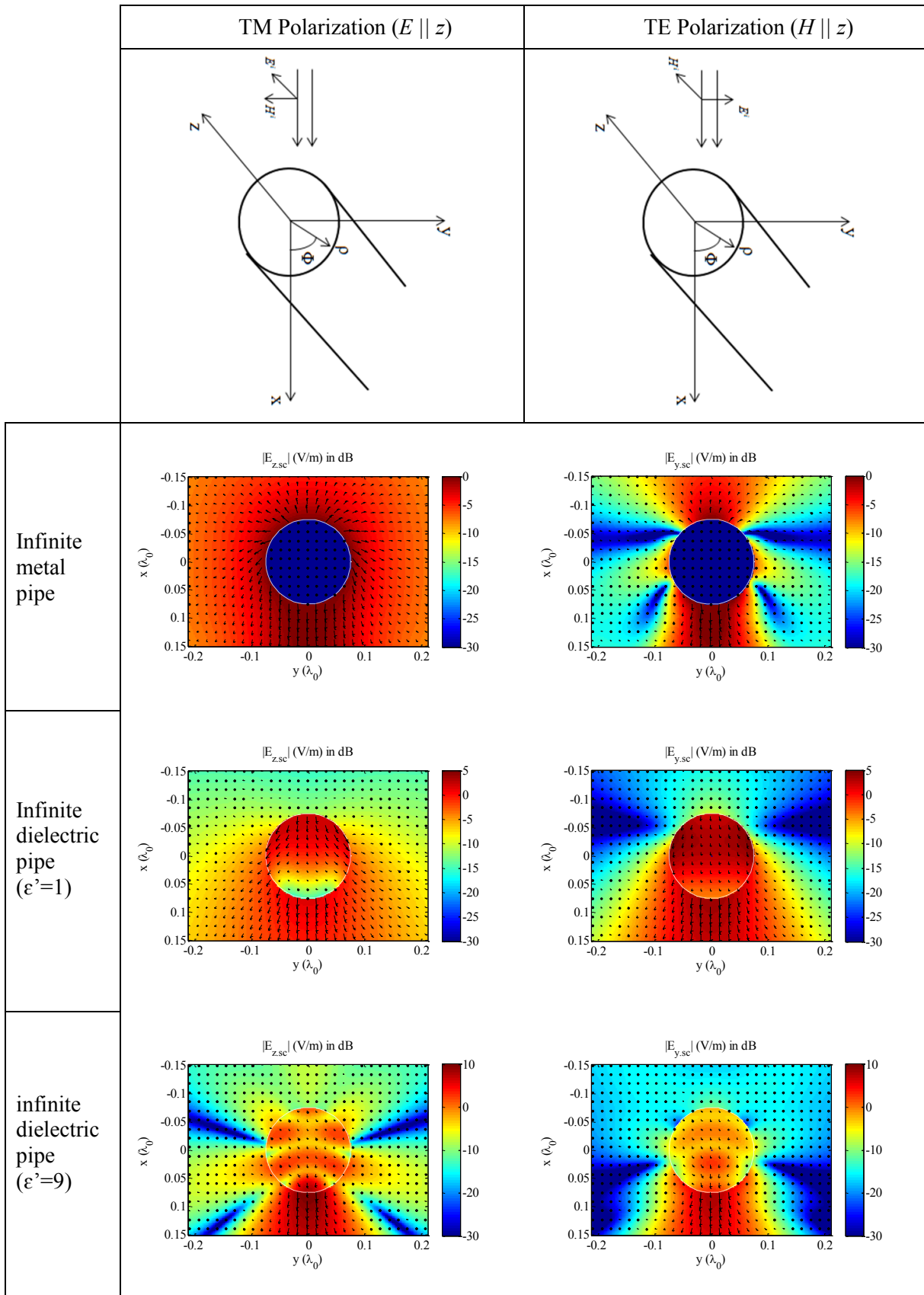


Figure 5.2: Computed TM and TE scattered field at 1GHz from infinite cylindrical pipe embedded within a soil with real permittivity of 3.5.

IV.4. Scattering width (SW)

The contrast in permittivity and the ratio between the size of the target and the wavelength contribute to enhance the radar cross section (RCS) of the target, and the magnitude of the target signature as a result (chapter 1). Therefore RCS is a very important parameter for characterizing scattering properties.

Scattering width is defined as the 2D adaptation of the radar cross-section (3D); it is used as a measure of the strength of the scattering waves from targets, and is only evaluated in the far field. It represents the equivalent area proportional to the apparent size of the target as seen by the electromagnetic field (based on the size, the orientation and the shape). Thus, if we consider the target in the far field region, the SW is proportional to the scattered field energy relatively to the incident field, as follows:

$$\sigma_{2D}(\varnothing) = \lim_{\rho \rightarrow \infty} \left(2\pi\rho \frac{|E^s|^2}{|E^i|^2} \right) = \lim_{\rho \rightarrow \infty} \left(2\pi\rho \frac{|H^s|^2}{|H^i|^2} \right)$$

Refereeing to Balanis book [1]:

$$\sigma_{2D}(\varnothing) = \frac{4}{\beta} \left| \sum_{-\infty}^{+\infty} a_n e^{jn\varnothing} \right|^2$$

Where a_n is calculated in Appendix B as the scattering field coefficient.

Fig. 5.3 shows the SW trend with regards to frequency ([0.2:2] GHz) for four increasing cylinder radii. Fig. 5.3 confirms that the TM polarization backscattering signal is larger than the TE mode for metallic and high real permittivity of cylinders. As opposed to the latter case, TE polarization is preferred for low permittivities of cylinders. For a conductive cylinder the SW oscillates in the TE polarization and not in the TM polarization, this is due to creeping waves that travel around the cylinder in TM polarization (creeping waves are very significant for cylindrical shapes), that are absent in the TE polarization (because field E is perpendicular to cylinder axis) [35] [36]. This phenomenon can be visualized in the field distribution on the surface of the cylinder on figure 5.2. Also, for increasing radius, the diameter become close to the wavelength, thus the SW frequency variations depict some fading for both polarizations with all pipe types.

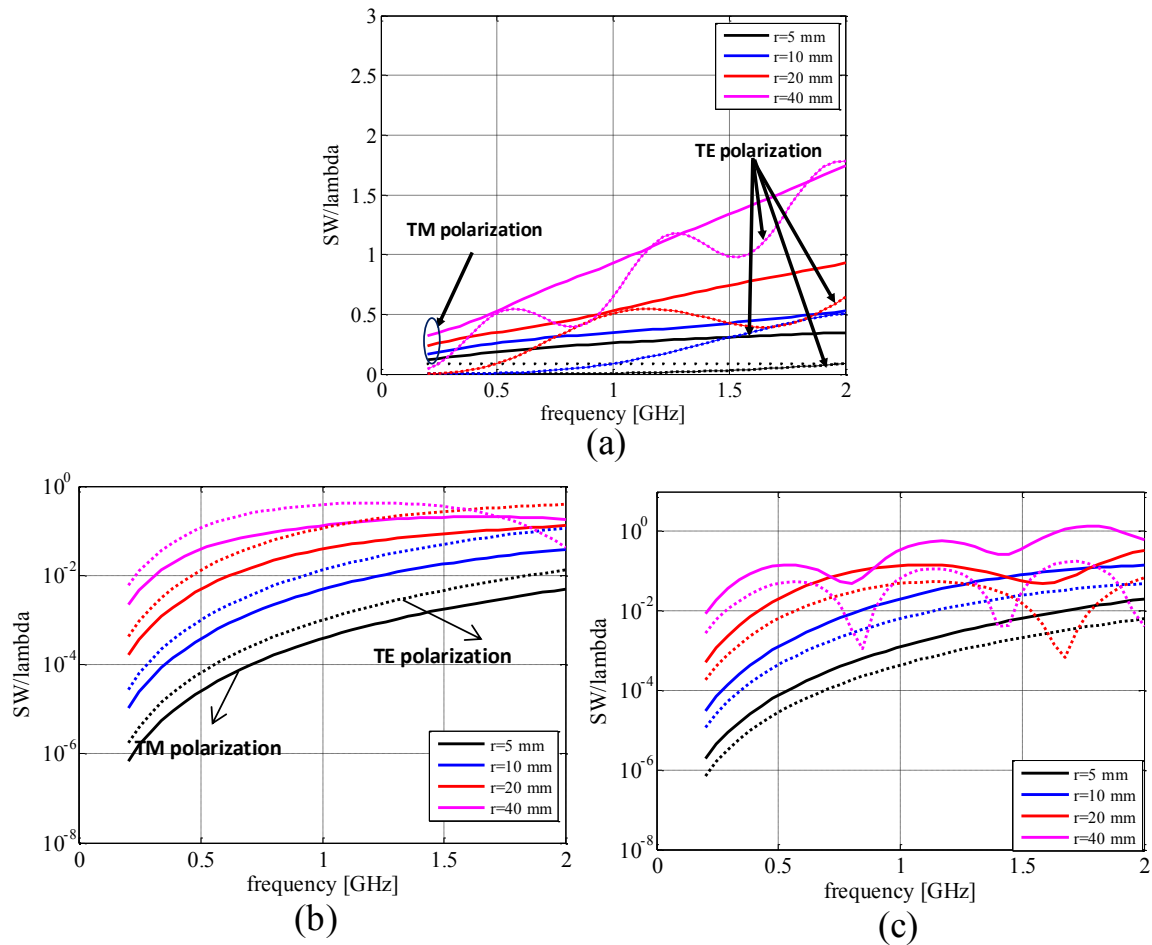


Figure 5.3: Scattering Width (SW) over a soil with real permittivity of 4 and in the case of: a) a conductive pipe, b) Low permittivity dielectric pipe ($\epsilon'=1$), c) High permittivity dielectric pipe ($\epsilon'=9$). TM polarization is drawn in filled lines; TE polarization in dashed lines [37].

V. FDTD simulation results

V.1. Geometries modeled

The SFCW GPR used is made of a pair of bowtie slot antennas (see chapter 2); the theoretical study of the radiation pattern of an antenna has highlighted that the electric field has a preferred direction in both TM and TE planes. Thus, it must be assumed that the radiated field is linearly polarized. This GPR system has been designed and optimized using a detailed description of the antennas under a numerical modeling based on the FDTD approach using the commercial software Empire. However, the computing time for such GPR simulations over a soil including buried objects appears prohibitive (around 2 weeks using a CPU i7-950 3.07 GHz).

Thus, we have replaced the pair of bowtie slot antennas by a pair of more simple non shielded planar blade dipoles designed on a FR4 substrate (see Figure 4.2a) with dimensions $290 \times 56 \text{ mm}^2$ that have been used in previous experiments [38]. The dipole antenna achieves much faster computational time (3 to 4 hours vs 3 to 4 days for a single pipe environment). It must be underlined that the polarization of the bowtie slot antenna and the blade antenna are perpendicular [39] [40] (figures 5.4 and 5.5). The offset between both types of antennas

remains equal to 60 mm, and the elevation above the soil has been fixed to 10 mm. the excitation current has the shape of the derivative of the Gaussian function with a time zero estimated to 0.3 ns and a duration (99% of the total energy) of 0.5 ns.

The simulated distribution of the electric field for each antenna type in both planes parallel and orthogonal (A and B respectively) to antennas long axis is visualized in Figure 5.4. In figures 5.4 (a) and (c), we observe the field E_{yx} (y direction for E) for both antennas bowtie and dipole respectively. In figures 5.4 (b) and (d), we observe the field E_{zx} (z direction for E) for both antennas bowtie and dipole respectively.

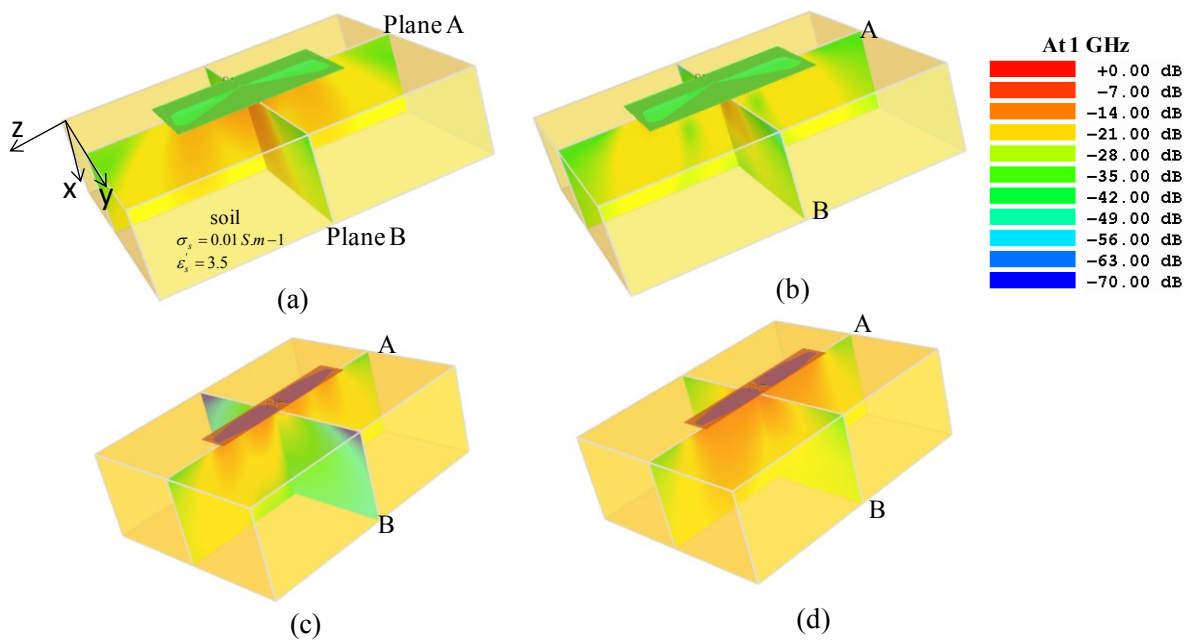


Figure 5.4: Distribution of the electric field in both planes parallel and orthogonal to antenna long axis. a) E_{yx} for the bowtie-slot antenna, b) E_{zx} for the bowtie-slot antenna, c) E_{yx} for the dipole antenna, d) E_{zx} for the dipole antenna.

The comparison of the distribution fields for the bowtie antenna shows higher amplitude in plane B for both E field components (E_{yx} and E_{zx}), which confirms that dominant E field is perpendicular to the long axis of the antenna. Therefore the bowtie-slot antennas in the end-fire configuration are considered equivalent to the TM mode and in the broadside configuration equivalent to the TE mode (Figure 5.5).

However, higher amplitude is observed for dipole antenna in plane A. Therefore the dipole-blade antennas in the end-fire configuration are considered to be equivalent to the TE mode; and in the broadside configuration, it is equivalent to the TM mode (Figure 5.5).

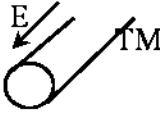
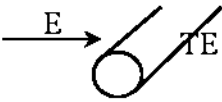

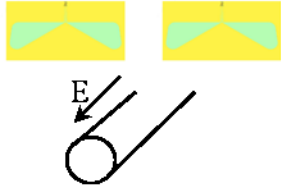
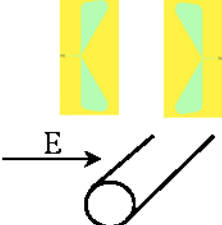
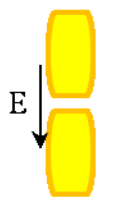
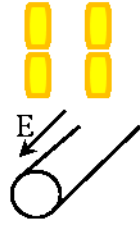
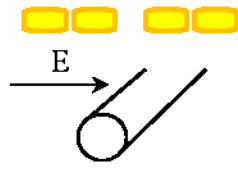
Polarization Antenna		
Bowtie-slot 	Endfire 	Broadside-mirror 
Dipole 	Broadside 	Endfire 

Figure 5.5: Antenna polarization configurations in case of bowtie-slot and dipole antennas.

V.2. Results

1. Simulation setup

FDTD simulations have been conducted using the different polarization configurations visualized in Figure 5.5 for the pair of bowtie-slot antennas and the dipoles respectively. The excitation is a first gaussian derivative pulse of duration 0.5 ns, with a 3 GHz the frequency bandwidth and a center frequency of 1 GHz. Simulation considers a dielectric homogeneous medium. The aim is to obtain some simple illustrative responses showing the effect of the polarization on target detection and thus, the gain to be expected by using polarization diversity. Three pipe dielectric characteristics have been considered to ease the comparison with the analytical model: a conductor and two dielectrics with $\epsilon'=1$ and 9; they are buried at a depth of 160 mm in a ground with real permittivity of 3.5 and conductivity of 0.01S/m. The Bscans are showed with and without clutter using the median subtraction technique (because the medium is homogeneously modeled) to enhance the hyperbolas signal feature.

2. Results with dipole antennas

The first comparison is performed using dipole antennas probing infinite pipes with radius of 32 mm (conductor, air-filled pipe and dielectric-filled pipe with $\epsilon'=9$). Thus, at the central frequency of the excitation pulse 1 GHz, the ratio $2R / \lambda_{mat}$ is 0.4.

Figures 5.6 and 5.7 show the data with and without the clutter respectively. They illustrate that with the broadside antenna configuration corresponding to a dominant TM mode, larger amplitudes are reached with a conductor pipe and with a dielectric pipe having permittivity $\epsilon' = 9$ (0.6 and 0.4 respectively) as compared to the endfire antenna configuration (0.3 and 0.15 respectively). However, in the case of a dielectric pipe with permittivity $\epsilon' = 1$ both configurations lead to the same maximum amplitude value evaluated to 0.1.

The results obtained are very close to the analytical model results, which state that the TM polarization is preferred for a metallic pipe and for a dielectric pipe with permittivity higher than the soil; in the case of a dielectric pipe with permittivity lower than the permittivity of the soil the TE and TM polarizations highlight similar amplitudes.

One cross-polarization configuration is shown on the third column of Figure 5.6 and 5.7. Compared to co-polarized configurations, much lower amplitudes are observed for hyperbolas and clutter responses whatever the pipe types. In addition to that, the hyperbola signature appears asymmetrical, because the propagation time on the emitter side is different from the propagation time on the receiver side (rectangular shape antenna, different width length $SR1 \neq SR2$).

3. Results with bowtie-slot antennas

Simulations have been performed using bowtie-slot antennas and smaller pipes of radius 12 mm (as for the field data set and the analytical model $2R / \lambda_{mat} = 0.15$) embedded within the same material as above. Bowtie-slot antennas dominant field polarization is orthogonal to dipole antennas as shown in previous section. Therefore corresponding dominant field TM and TE are inverted compared to the dipole antennas for the two configurations. Figures 5.9 and 5.10 show that in the endfire configuration, that corresponds to a dominant TM mode, larger amplitudes are observed with the metal pipe and the dielectric pipe having a real permittivity $\epsilon' = 9$ (0.17 and 0.06 respectively, at the apex) compared to the broadside configuration (0.05 and 0.02 respectively). However, in the case of a dielectric pipe with permittivity $\epsilon' = 1$ both configurations lead to the same maximum amplitude value of 0.02. These polarization preferences for each type of pipe are similar to the results obtained for dipole antenna and in the analytical model.

Figure 5.10 shows the Ascans at the apex position corresponding to the Bscan in Figure 5.8. In the TM configuration, the Ascans signals are shifted 0.3 ns to the left, to compensate for the larger antennas dimensions in the TM configuration, and to superpose clutter responses in both configurations.

4. Discussion

In the above simulations, the hyperbola signature seems very different from one configuration to one another. First, because antennas are rectangular shaped instead of a being squared, and then, the arrival time of echoes is affected by the relative antenna dimensions differences.

Another major difference is the presence of two echoes in the broadside configuration. Broadside configuration favors multiple reflections or signal called reverberation, and we suppose here that it is the result of noise produced from ‘ringing antennae’ when spaced too closely [41].

A change in the signal polarity of the echoes is observed from positive to negative (red and blue hyperbolas) or vice-versa according to the contrast in permittivity at the impact interface (figures 5.7 and 5.9). Positive polarity is observed for positive reflection coefficient, i.e.: meaning a lower velocity to higher velocity transition, e.g. air-filled pipe in the TE polarization. It can be inferred from Fresnel equations in Appendix A. Negative polarity occurs for negative reflection coefficient, as for water-filled pipe in the TE polarization. Another polarity change takes place at the interface air-soil and can be seen on the clutter response of dipole antenna (i.e. negative cycle before the positive figure 5.6). Also a polarity change may happen relatively to the reception antenna orientation. Consequently analyzing wave’s polarity at different interfaces may give useful information about the permittivity contrast.

Consequently, according to the analytical model and the numerical models with the bowtie and the dipole antennas, TM and TE polarizations enable to distinguish the metal and the high permittivity (relatively to the soil permittivity) dielectric targets from the low permittivity dielectric targets. Afterwards, the polarity changes within the observed echo allow distinguishing metallic from high permittivity dielectric targets.

Also the reversed results for both polarization between dipole antennas and bowtie antennas confirms the orthogonality of their dominant field directions studied in V.1.

We must also note that time zero was not corrected in the entire simulations and measurements setups presented in this chapter, because the interest in this chapter is only to visualize the hyperbolas without fitting.

5. Azimuthal pipe rotation

The pipe of radius 32 mm has now been shifted to the angle θ relatively to the z axis. The dipole antennas are chosen (because their modeling is faster) to observe the effect of the relative angle between the cylinder axis and antennas axis in both configurations (i.e. [13]). Figure 5.11 shows that for both configurations, the hyperbola gets more stretched and has an increased amplitude as the angle rises from zero to 75° because the pipe surface within the antenna pattern appears larger.

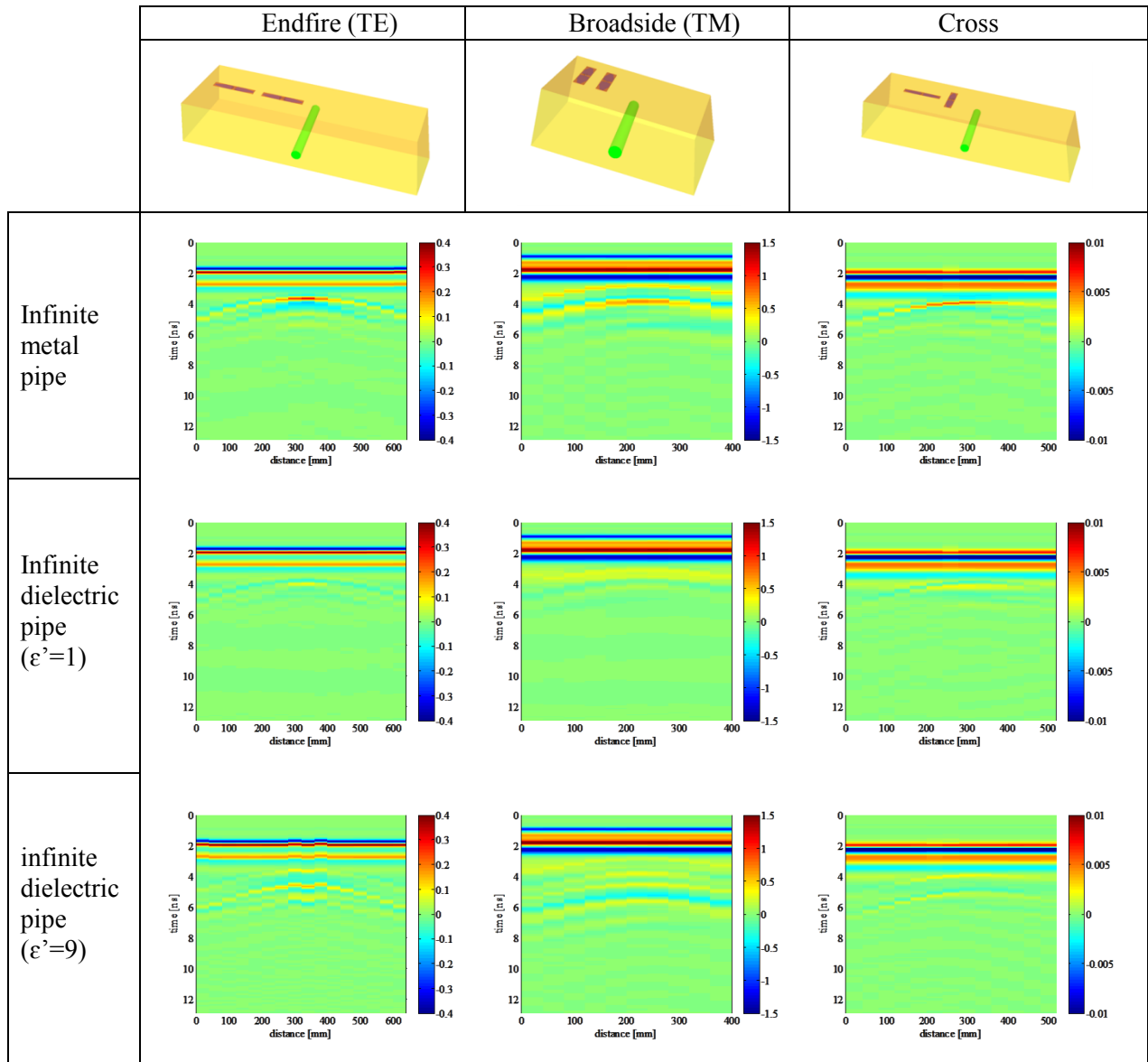


Figure 5.6: Computed raw Bscans with the dipole antennas over three types of infinite pipe.

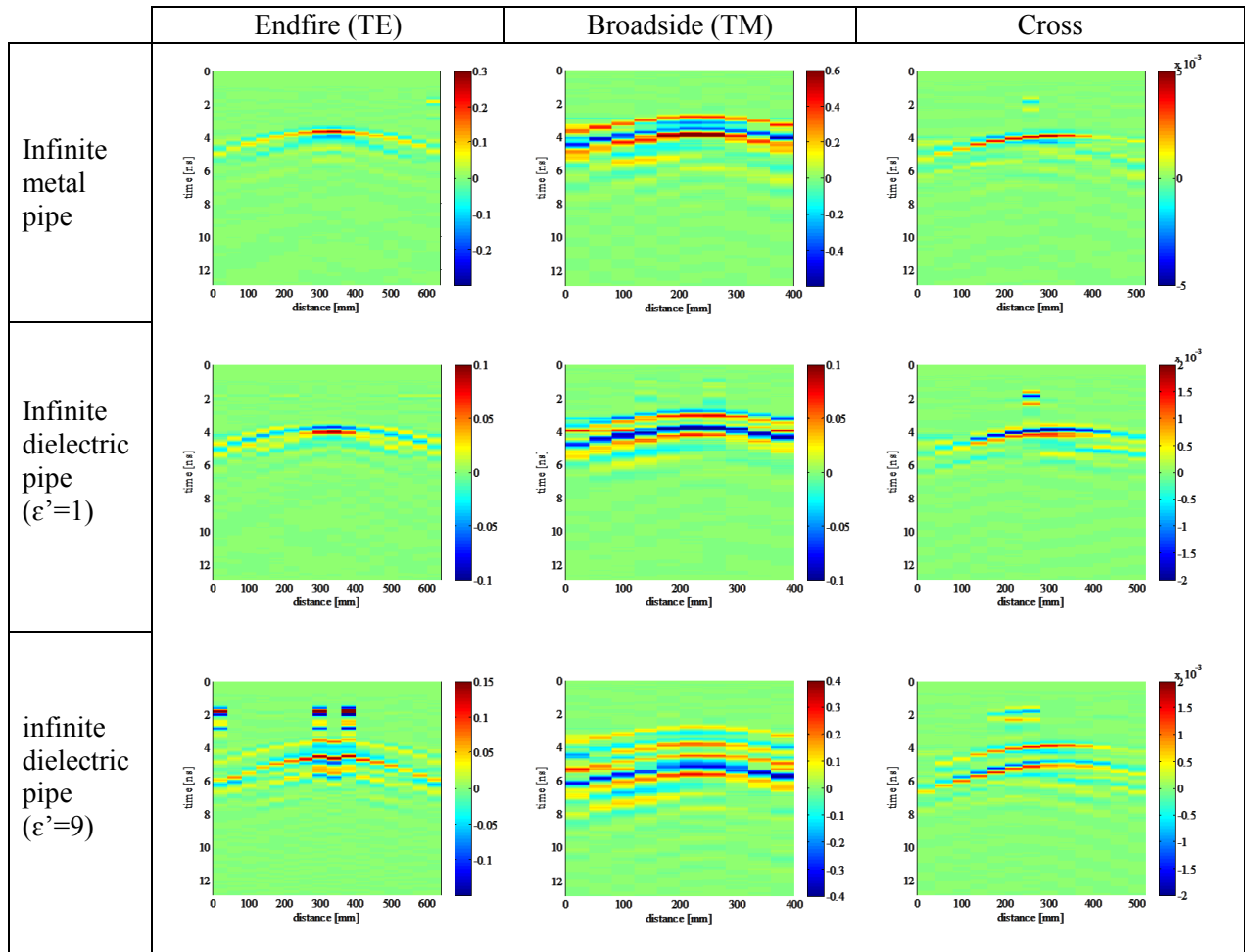


Figure 5.7: Computed Bscans with the dipole antennas over three types of infinite pipe, after clutter reduction with the median subtraction technique.

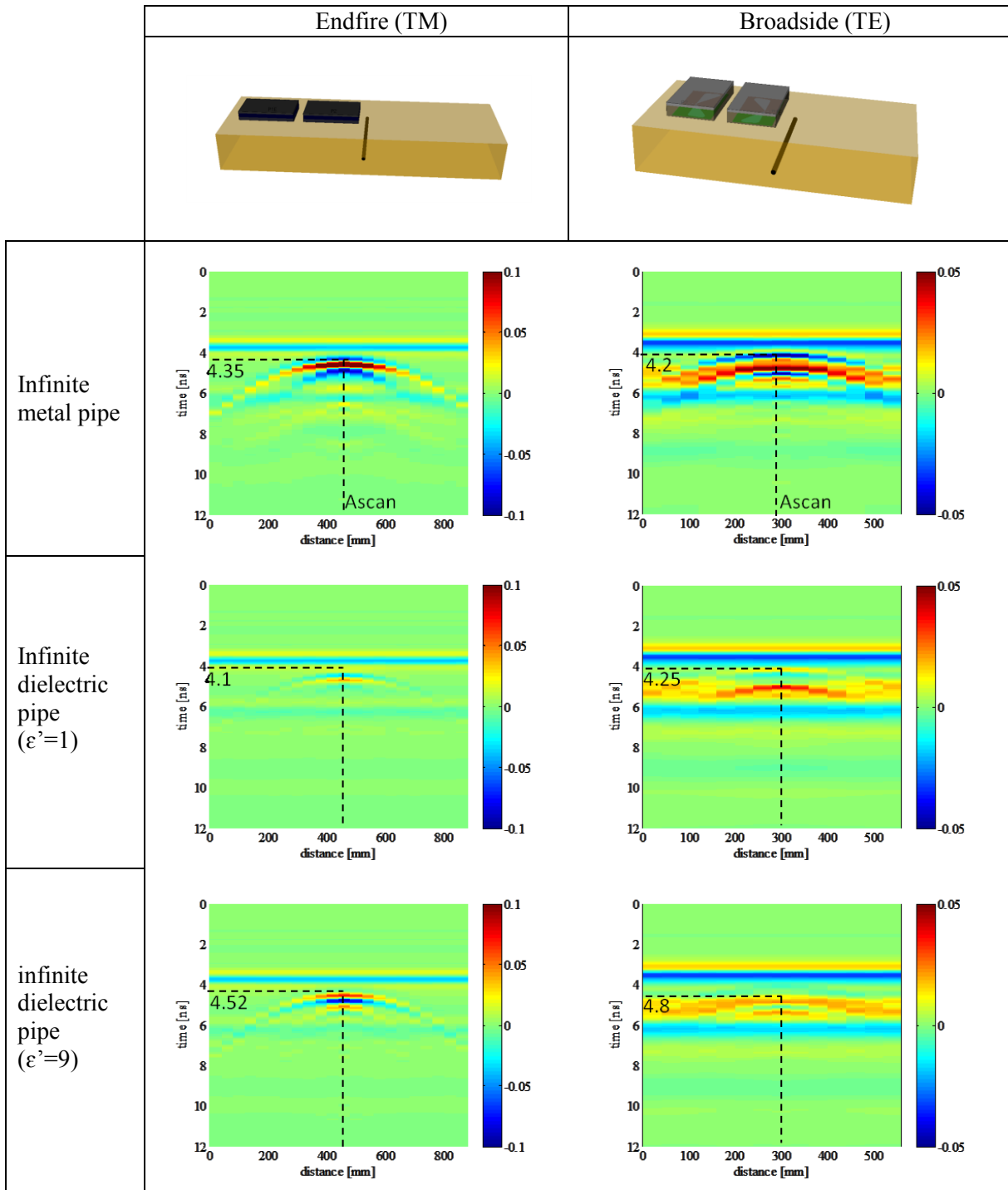


Figure 5.8: Computed raw Bscans with the bowtie-slot antennas over three kinds of infinite pipe.

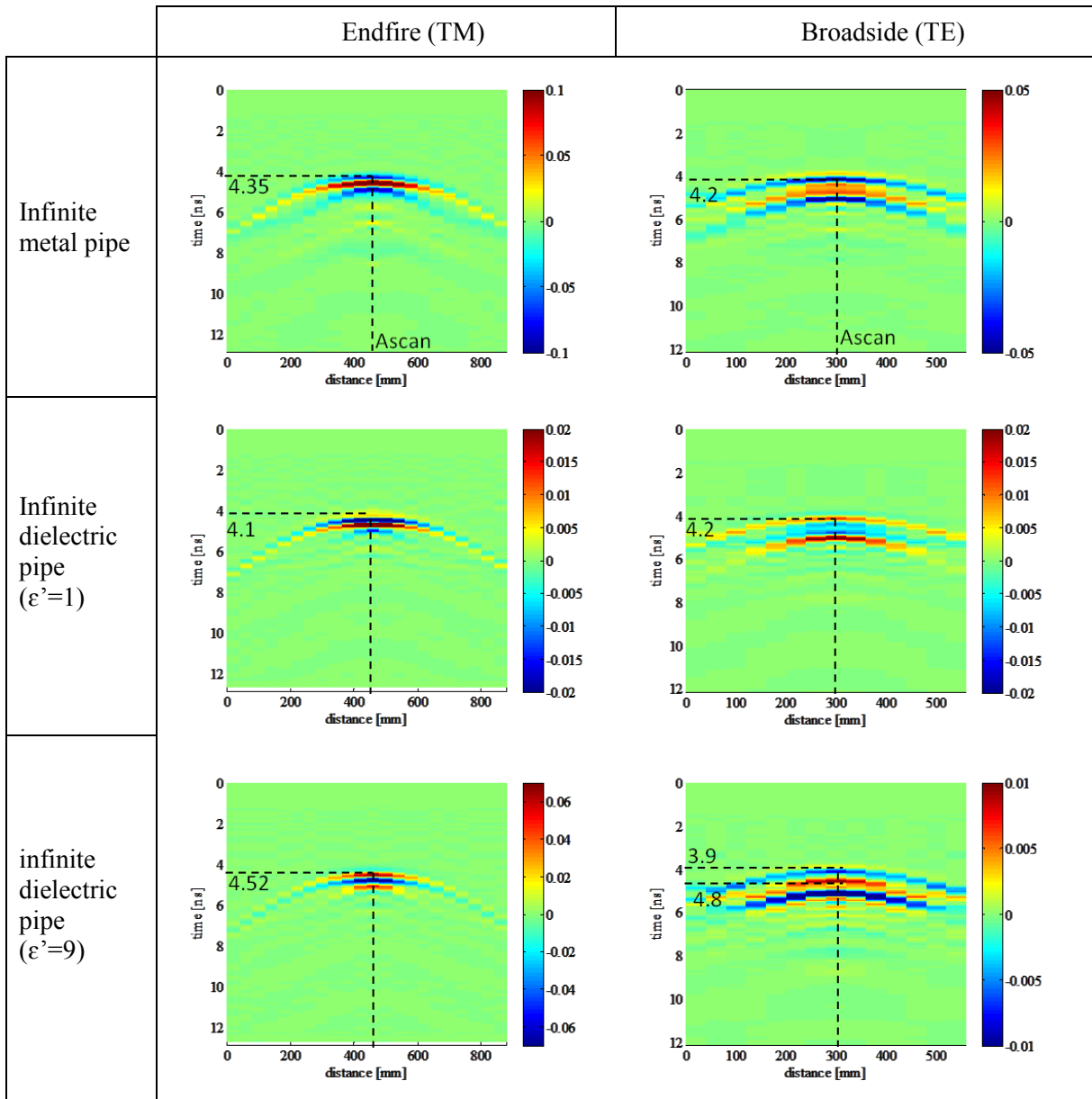


Figure 5.9: Computed Bscans with the bowtie-slot antennas over three kinds of infinite pipe after clutter reduction with the median subtraction technique.

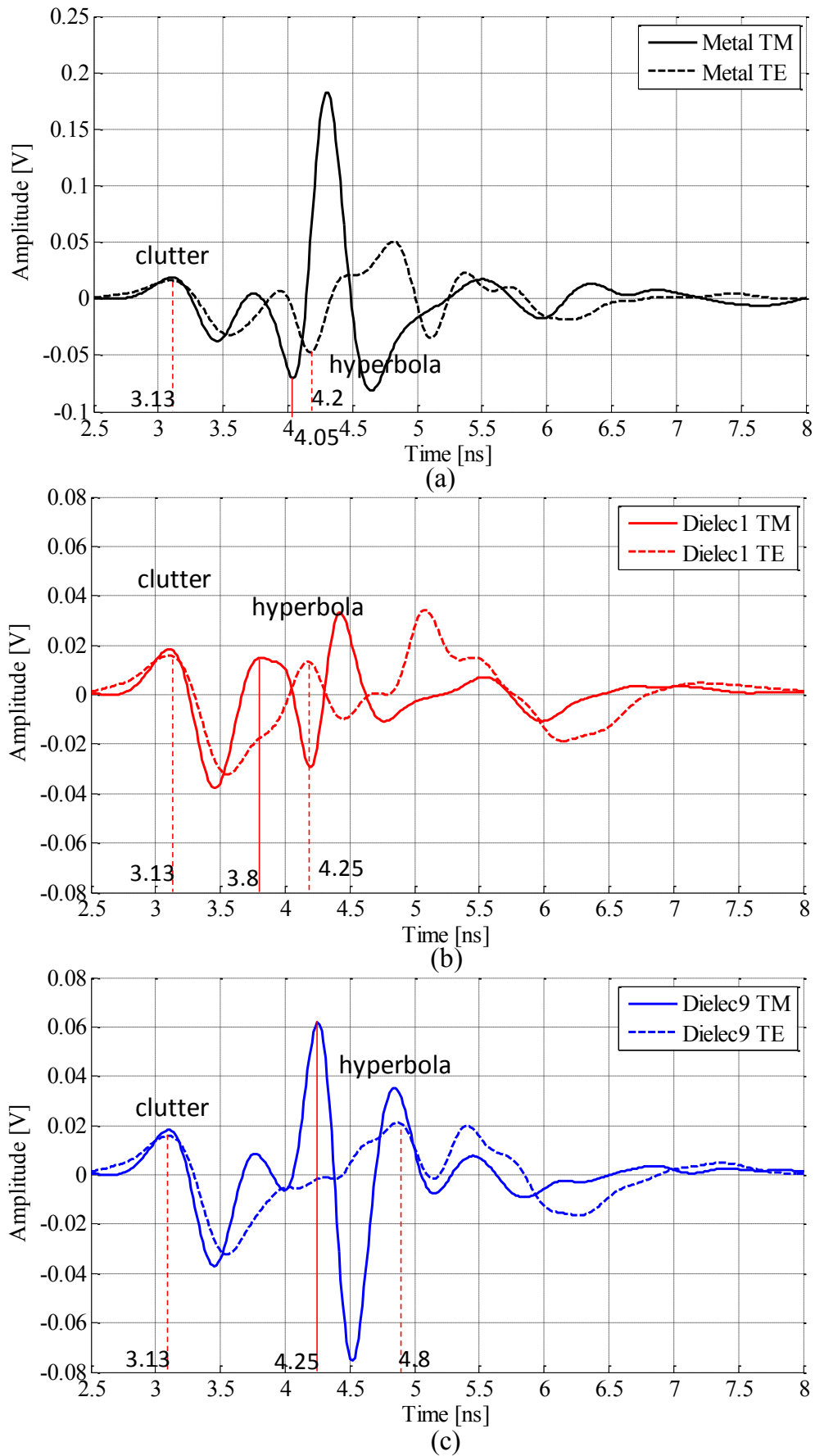


Figure 5.10: Extracted Ascans from the Bscans in figure 5.8 at the apex position.

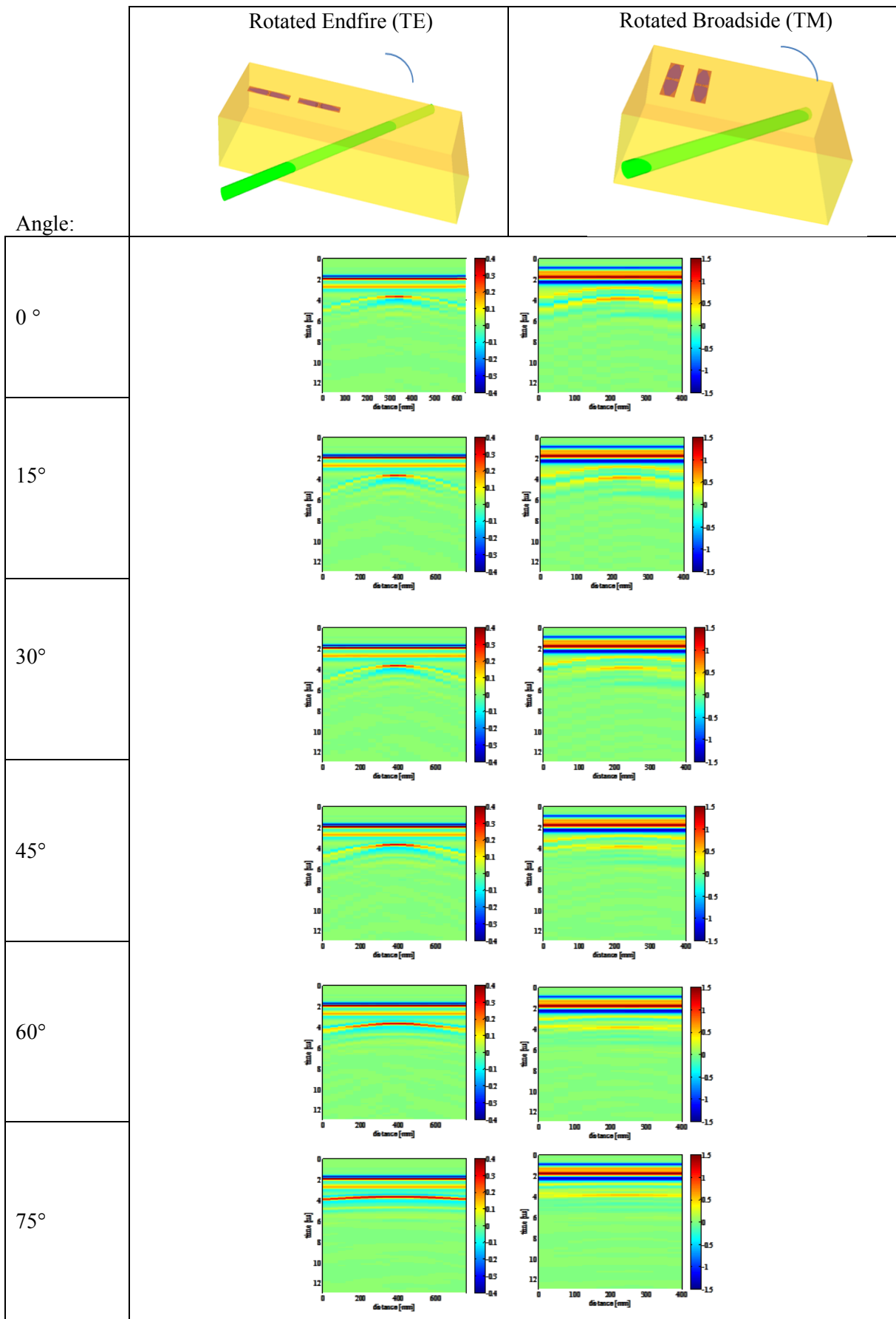


Figure 5.11: Computed raw Bscans with varying angle between the dipole antenna and the pipe axis.

VI. Experimental results

Field data are collected with the ground-coupled SFCW radar on two test-sites: the outdoor test-site in section and the urban test-site using the bowtie-slot antennas. The complex transmission coefficients S_{21} have been measured with the vector network analyzer configured as described in chapter 2. The radargrams are shown with and without clutter.

A. Outdoor sand box

In general, a couple of canonical dielectric or conductive objects (pipe or strip) have been studied in this survey. The objects, separated by a distance of 700 mm, have been buried at a depth close to 160 mm and at positions 500 and 1200 mm respectively. The position y_i corresponds to the center of the radar system in the direction of the survey.

Geometry 1

At first, an air-filled pipe with a 12 mm radius and a thin horizontal conductive strip (dimensions 2mm*10mm) buried at a depth of 160 mm (figure 5.12). According to chapter 2, the real permittivity of the sand has been estimated to 5.5. The Bscans in both polarization configurations and visualized in figure 5.13, highlight that the hyperbola associated with the metal strip appears visible in both polarizations; however, its amplitude appears more important in the endfire configuration (TM). The air-filled pipe is only detectable in the broadside configuration (TE).

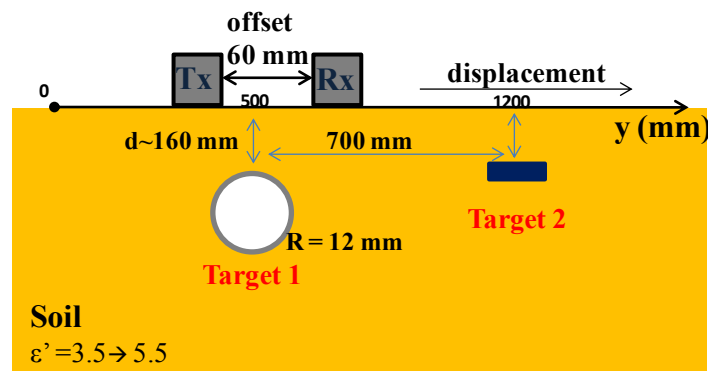


Figure 5.12: Measurement Setup corresponding to Figure 5.13.

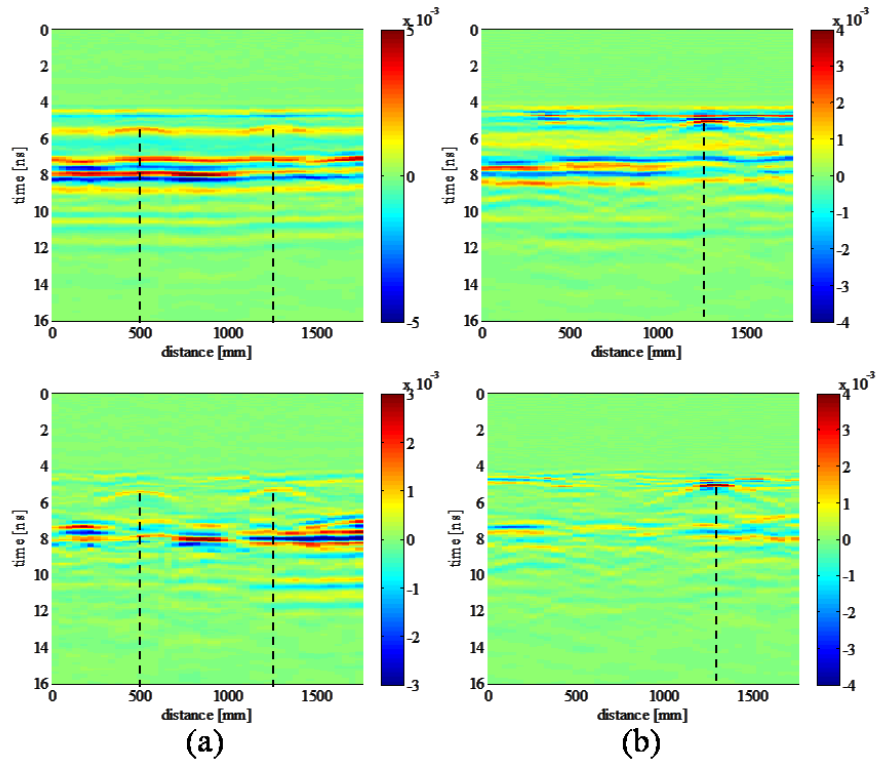


Figure 5.13: Experimental Bscan over an air-filled pipe and a horizontal metal strip within a sandy ground; a) Broadside configuration (TE), b) Endfire configuration(TM); top) Raw data, Bottom) clutter suppressed data.

Geometry 2

The air-filled PVC buried pipe (lower permittivity relatively to the soil) is now replaced by a water-filled pipe (higher permittivity relatively to the soil), and the metal strip is now oriented vertically. Figure 5.15 shows that the metal strip is no longer detected in the broadside configuration (TE), and the water filled PVC pipe is only detected in the endfire pipe configuration (TM).

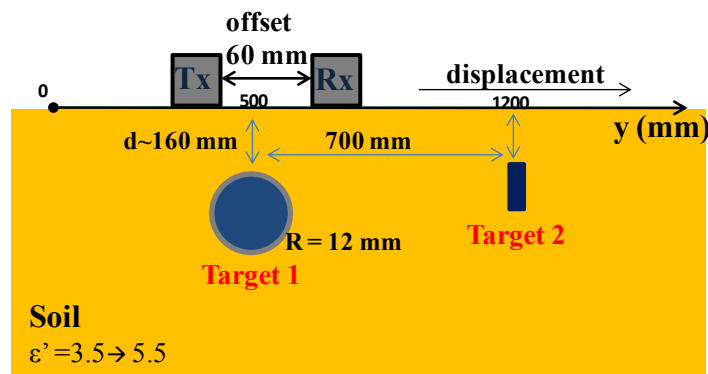


Figure 5.14: Measurement Setup corresponding to Figure 5.15.

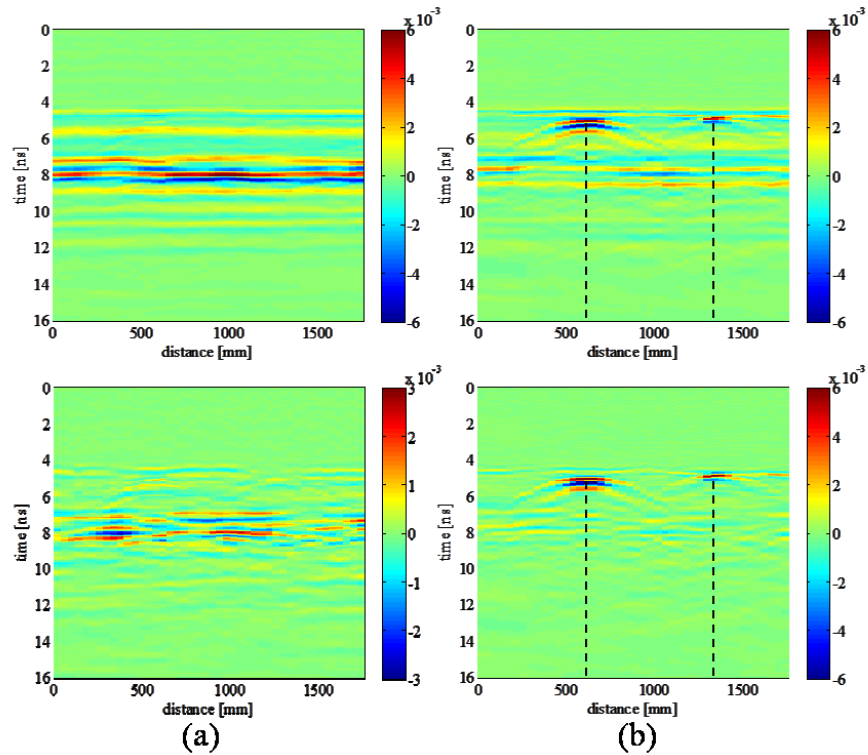


Figure 5.15: Experimental Bscan over a water-filled pipe and a vertical metal strip within a sandy ground; a) Broadside configuration(TE), b) Endfire configuration(TM); top) Raw data, Bottom) clutter suppressed data.

Geometry 3

The next shows the experimental Bscans over smaller targets, i.e., a 8 mm radius PVC pipe (with no gap) and a 5mm radius cylindrical metal pipe, they are buried at a depth of 160 mm. In Fig. 5.17, the PVC pipe is detected in the broadside configuration (TE), while the metal pipe is detected in the endfire configuration (TM) and hardly detectable in the broadside configuration (TE) (like the vertical metal strip in figure 5.15).

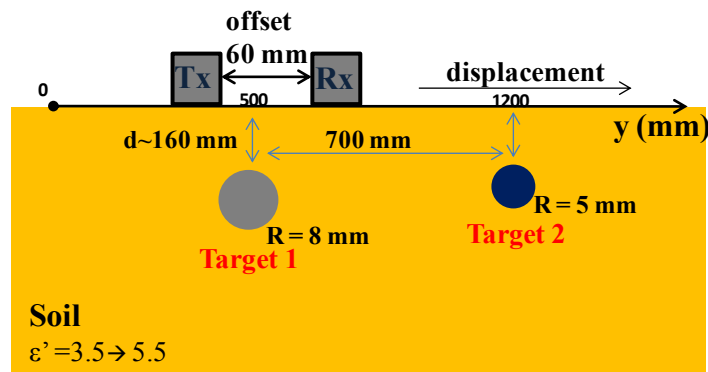


Figure 5.16: Measurement Setup corresponding to Figure 5.17.

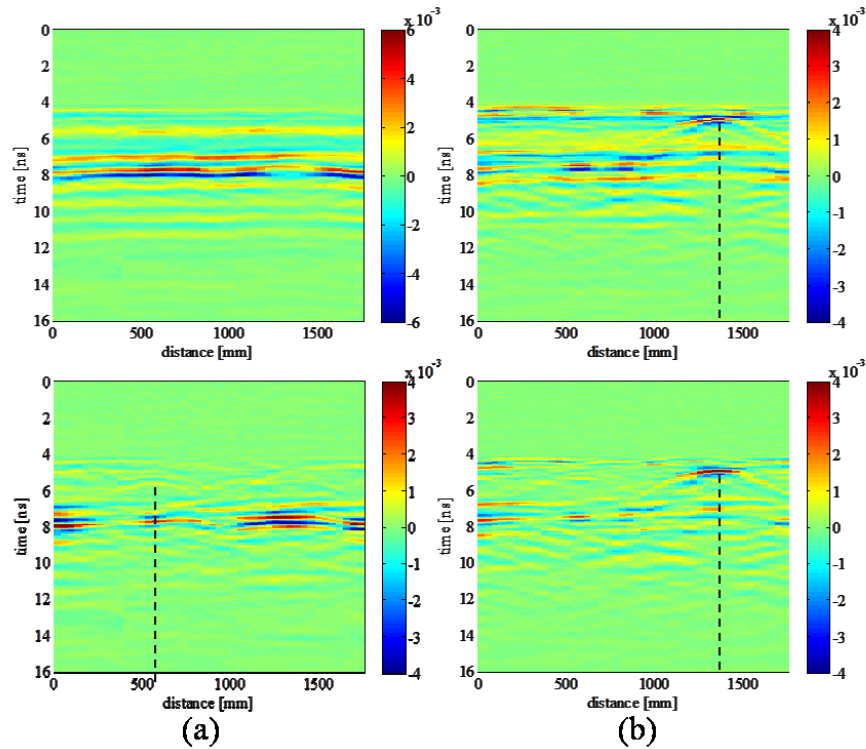


Figure 5.17: Experimental Bscan over a nylon pipe and a metal cylindrical pipe within a sandy ground; a) Broadside configuration(TE), b) Endfire configuration(TM); top) Raw data, Bottom) clutter suppressed data.

Discussion

Associated with the above three geometries, the results showed that metallic targets seem to be detected in both TE and TM configurations. Nevertheless, the TM polarization gives higher scattering magnitude. And when it comes to very tiny targets, below 5 mm (5 mm for the current GPR system, and in the sand ground environment), the TE polarization fails in detecting the buried target. We then found the same observation as for the simulations and for the analytical model: the metallic pipes show higher scattering magnitude in the TM configuration.

For dielectrics targets with higher permittivity than the soil, the behavior is close to the one for metallic targets and the same as it was observed in the FDTD simulations and the analytical model. For example, water content pipe are better detected in the TM polarization (because water conductivity is higher of other dielectric materials).

As opposed to previous cases, lower permittivity targets than the soil are better detected in the TE polarization, where the field E is orthogonal to pipe axis. This conclusion is not clearly seen in both analytical and simulation models, the models forecast similar amplitudes on both polarizations for low permittivity pipes.

B. Outdoor urban test-site (Sense-city)

The experimental profiles presented here concern the pipe zone of the test site Sense-City whose cross-section is visualized in Figure 5.18. All the dielectric pipes are air-filled. The

surveys have been acquired using the SFCW radar (bowtie antennas) system with a step distance of 40 mm in both configurations (broadside and endfire). A linear time gain has been applied to better visualize the hyperbola responses. The spectrum of a synthetic pulse (first Gaussian derivative) centered at the frequency 900 MHz has been multiplied to the frequency data in both polarizations to obtain the displayed time responses.

The radargrams on Figures 5.19 (bottom) and 5.20 (a) show that the air-filled pipes at depth 30 cm in T4 and at depth 10 cm in T2, have a detectable hyperbola signature in the broadside polarization only. However, the signature of trench T1 is not easily detectable, certainly because the distance step is not small enough.

Afterwards, measurements in the endfire configuration have been made in two sequences that induce a vertical discontinuity in the radargram. In general, we remark that all the hyperbolas appear strongly attenuated.

Thereafter, water has been put into the PVC pipe of trench T5, and a radar profile has been obtained using the SIR 3000 system at the frequency 900 MHz. From Figure 5.20(b) we observe that pipe in T5 appears visible. Thus it will be interesting to insert in the future a dielectric liquid in the PVC pipes to study its polarization as a function of the orientation of the main electric field on this complex site.

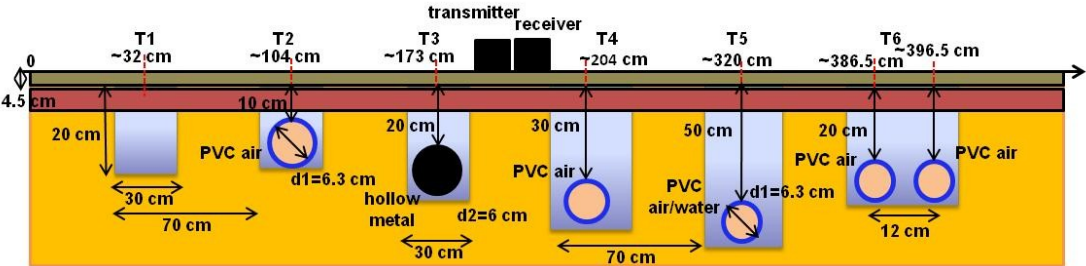


Figure 5.18: Cross-section of the pipe zone including the pipe positions and depths estimated during the site construction (on the courtesy of F. Sagnard [42])

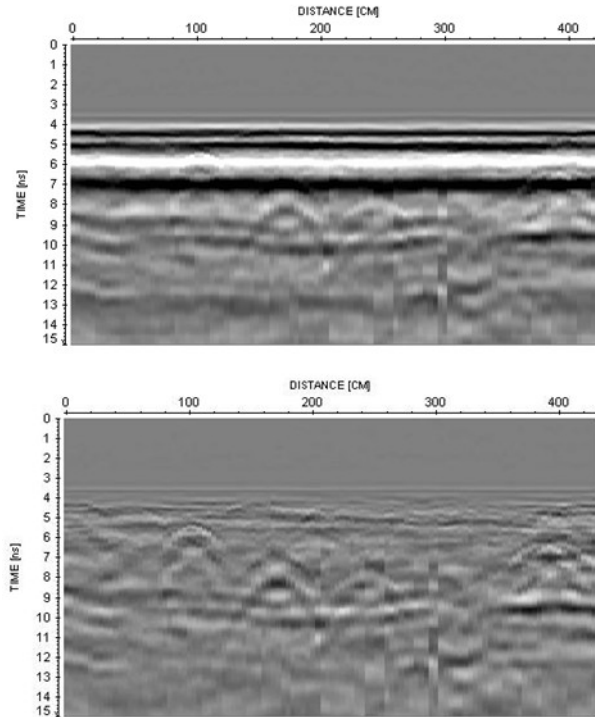


Figure 5.19: Bowtie antenna at 900 MHz in the broadside configuration, all pipes are air-filled. (top) raw data (Bottom) clutter suppressed data. (on the courtesy of F. Sagnard [42])

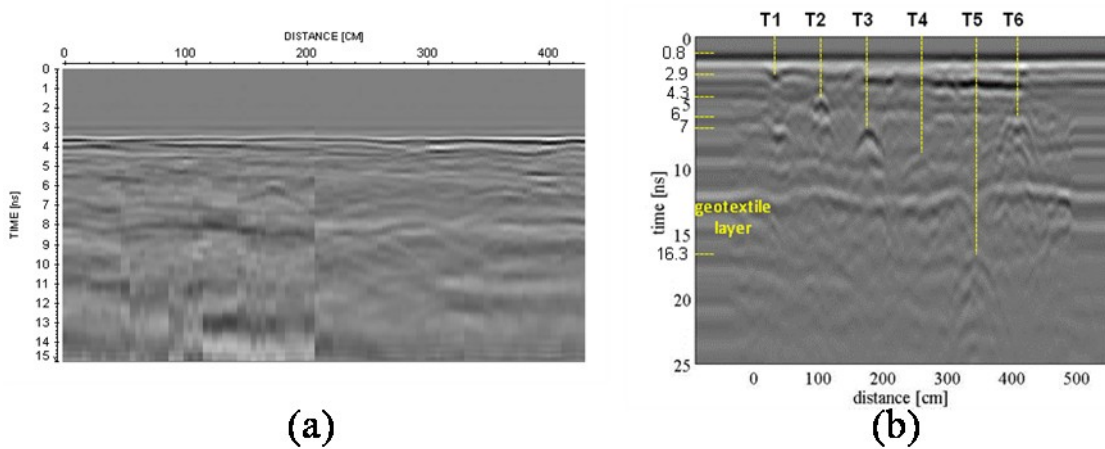


Figure 5.20: a) Clutter-free data with the bowtie antenna at 900 MHz in the endfire configuration, all pipes are air-filled, b) Raw data with the SIR3000 radar at 900 MHz, and pipes are air-filled except T5 water-filled. (on the courtesy of F. Sagnard [42])

VII. Conclusion

In this chapter, the interest in the use of polarization diversity in GPR has been presented. The polarization is based on the vector nature of electromagnetic waves. The influence of polarization has been shown theoretically and experimentally on canonical objects (pipes and strips). Multi-polarization survey is an opportunity for acquiring more information on the shape, orientation and nature of the embedded objects in the subsurface. The direction of measurement can strongly influence the resulting image, and in some cases buried objects can

be totally missed if the depolarization is not detected by the receiving antenna. According to the Stokes's matrix, a polarized component is presented with two orthogonal polarizations, which traditionally are expressed in terms of linearly polarized basis vectors. In GPR, the main problem in using the Stokes's matrix algorithm is the lateral dimensions of the antennas which have often dipole shape and thus not similar in the two main polarization directions. Thus, corrections and calibration have to be brought to calculate the degree of polarization.

The objects mainly studied in this work are dielectric and conductive pipes. We have observed that the most visible hyperbolas are formed by conductive pipes in the TM polarization. For dielectric pipes, if their real permittivity is higher than that of the soil, the same phenomenon occurs; if it is lower the TE polarization must be used (Summary in Table 5.1). Moreover, linear objects with the major axis in the direction of travel of the antenna produce linear features on a radar profile but do not produce hyperbolas, and we have noticed that other interception angles produce distorted hyperbolas.

A certain form of polarization diversity has been exploited, however full antennas configurations have not been exploited, thus three configurations out of six (section III) have been studied and compared to the literature. The results validate the literature conclusions and confirm the utility of multi-polarizations surveys for identifying the nature, the orientation and the content (liquids, gazes, solids ...) of the buried urban utilities; by using three configurations representing the possible polarizations (TM, TE and cross).

<i>Pipe type:</i>	TM polarization (Endfire configuration with the bowtie-slot antennas)	TE polarization (Broadside configuration with the bowtie-slot antennas)	Cross- polarization (or cross- configuration)
Metallc	++	+	+-
High dielectric ($\epsilon' > \epsilon'_{\text{medium}}$)	++	+-	+-
Low dielectric ($\epsilon' < \epsilon'_{\text{medium}}$)	+-	++	+-

Table 5.1: Summary for the detection quality over different buried pipe natures and under different electric field polarizations. The +/- symbols indicate the good/bad detection quality.

Bibliography

- [1] C. A. Balanis, "Advanced engineering electromagnetics," *Wiley New York, Second edition*, 2012.
- [2] R. L. Roberts, "Analysis and theoretical modeling of GPR polarization data," *PhD Thesis, The Ohio State University*, 1994.
- [3] D. J. Daniels, "Ground penetrating radar," *Wiley Library, Second edition*, 2005.
- [4] X. Feng, W. Liang, C. Liu, Q. Lu, Z. Zhou, Y. Zhang, L. Zou and H. Li, "Developing a novel full-polarimetric GPR technology," *IEEE International Geoscience and Remote Sensing Symposium (IGARSS)*, pp. 858-861, 2011.
- [5] C. F. Bohren and D. R. Huffman, "Absorption and scattering of light by small particles," *John Wiley & Sons*, 1983.
- [6] P. C. Pawliuk, "Evanescent field interactions in the scattering from cylinders with applications in super-resolution," *PhD Thesis, University of British Columbia*, 2013.
- [7] H.-S. Youn, "Development of unexploded ordnances (UXO) detection and classification system using ultra wide bandwidth fully polarimetric ground penetrating radar (GPR)," *PhD Thesis, The Ohio State University, USA*, 2007.
- [8] R. T. Wang, H. Van de Hulst and others, "Application of the exact solution for scattering by an infinite cylinder to the estimation of scattering by a finite cylinder," *Applied Optics*, vol. 34, no. 15, pp. 2811-2821, 1995.
- [9] S. Kozaki, "Scattering of a Gaussian beam by a homogeneous dielectric cylinder," *Journal of Applied Physics*, vol. 53, no. 11, pp. 7195-7200, 1982.
- [10] M. Higgins, C. Chen and K. O'Neill, "Data Processing Results for UXO Classification using UWB Full-Polarization GPR System," *Research project, US Army Corps of Engineers*, 2001.
- [11] P. Farinelli and F. Roth, "Frequency domain analysis of the polarimetric ground-penetrating radar response of landmines and minelike targets," *AeroSense 2003*, pp. 437-447, 2003.
- [12] A. Villela and J. M. Romo, "Invariant properties and rotation transformations of the GPR scattering matrix," *Journal of Applied Geophysics*, vol. 90, pp. 71-81, 2013.
- [13] S. J. Radzevicius and J. J. Daniels, "Ground penetrating radar polarization and scattering from cylinders," *Journal of Applied Geophysics*, vol. 45, no. 2, pp. 111-125, 2000.
- [14] M. Paulus and O. Martin, "Scattering experiments with a diving cylinder," *Optics express*, vol. 9, no. 6, pp. 303-311, 2001.

- [15] P. Capizzi and P. Cosentino, "GPR multi-component data analysis," *Near Surface Geophysics*, vol. 6, no. 2, pp. 87-95, 2008.
- [16] R. Roberts, D. Cist and A. Kathage, "Full-Resolution GPR imaging applied to utility surveying: insights from multi-polarization data obtained over a test pit," *IWAGPR 2009*, pp. 126-131, 2009.
- [17] M. Naser and A. Junge, "Influence of pipe filling, geometry and antenna polarisation on GPR measurements," *13th International Conference on Ground Penetrating Radar (GPR)*, pp. 1-6, 2010.
- [18] U. Boniger and J. Tronicke, "Subsurface utility extraction and characterization: Combining GPR symmetry and polarization attributes," *IEEE Transactions on Geoscience and Remote Sensing*, vol. 50, no. 3, pp. 736-746, 2012.
- [19] H. Liu, J. Zhao and M. Sato, "A hybrid dual-polarization GPR system for detection of linear objects," *Antennas and Wireless Propagation Letters*, vol. 14, pp. 317 - 320, 2014.
- [20] T. Khuut, "Application of Polarimetric GPR to detection of subsurface objects," *PhD Thesis, NIHON University*, 2009.
- [21] R. M. Al-Zayer, "Influence of the Host Medium on GPR Polarization Characteristics of a Cylinder," *Master Thesis, Colorado School of Mines*, 2005.
- [22] A. Langman, "The design of hardware and signal processing for a stepped frequency continuous wave ground penetrating radar," *PhD Thesis, University of Cape Town*, 2002.
- [23] G. P. Tsoflias, J.-P. Van Gestel, P. L. Stoffa, D. D. Blankenship and M. Sen, "Vertical fracture detection by exploiting the polarization properties of ground-penetrating radar signals," *Geophysics*, vol. 69, no. 3, pp. 803-810, 2004.
- [24] A. Seren and A. D. Acikgoz, "Imaging fractures in a massive limestone with ground penetrating radar, Haymana, Turkey," *Scientific Research and Essays*, vol. 40, no. 7, pp. 3368-3381, 2012.
- [25] C. Perll, "Evaluating GPR polarization effects for imaging fracture channeling and estimating fracture properties," *PhD Thesis, University of Kansas*, 2013.
- [26] P. Marchesini and M. Grasmueck, "Impact of spatial sampling and antenna polarization on 3D GPR fracture detection," *13th International Conference on Ground Penetrating Radar (GPR)*, pp. 1-6, 2010.
- [27] W. Liang, X. Feng, C. Liu, Q. Lu, Y. Yu, E. Nilot and Q. Ren, "Full polarimetric GPR system for underground targets measurements," *15th International Conference on Ground Penetrating Radar (GPR)*, pp. 803-806, 2014.
- [28] J. Li, Z.-F. Zeng, L. Huang and F. Liu, "GPR polarization simulation with 3D HO FDTD," *Session 3AP, China, Progress In Electromagnetics Research Symposium Proceedings*, 2010.

- [29] A. Schuster, "An introduction to the theory of optics," *GB: Edward Arnold*, 1909.
- [30] J. R. Wait, "Scattering of a plane wave from a circular dielectric cylinder at oblique incidence," *Canadian Journal of Physics*, vol. 33, no. 5, pp. 189-195, 1955.
- [31] S.-C. Lee, "Scattering by a radially stratified infinite cylinder buried in an absorbing half-space," *JOSA A, Optical Society of America*, vol. 30, no. 4, pp. 565-572, 2013.
- [32] D. E. Lawrence and K. Sarabandi, "Electromagnetic scattering from a dielectric cylinder buried beneath a slightly rough surface," *IEEE Transactions on Antennas and Propagation*, vol. 50, no. 10, pp. 1368-1376, 2002.
- [33] N. Diamanti and D. Redman, "Field observations and numerical models of GPR response from vertical pavement cracks," *Journal of Applied Geophysics, Elsevier*, vol. 81, pp. 106-116, 2012.
- [34] K. Z. Guanran, "<http://individual.utoronto.ca/kzhu/>," *Matlab Central, The code is placed under the open BSD license*, 2011.
- [35] J. Sun, C.-F. Wang, L.-W. Li and M.-S. Leong, "Creeping waves along a perfectly conducting cylinder with a lossy magnetic coating," *Antennas and Wireless Propagation Letters, IEEE*, vol. 2, no. 1, pp. 298-301, 2003.
- [36] T. Mavridis, L. Petrillo, J. Sarrazin, D. Lautru, A. Benlarbi-Delai and P. De Doncker, "Creeping wave model of diffraction of an obliquely incident plane wave by a circular cylinder at 60 GHz," *IEEE transactions on antennas and propagation*, vol. 62, no. 3, pp. 1372-1377, 2014.
- [37] F. Sagnard and E. Tebchrany, "Using polarization diversity in the detection of small discontinuities by an ultra-wide band ground-penetrating radar," *Measurement, Elsevier*, vol. 61, pp. 129-141, 2015.
- [38] F. Rejiba, F. Sagnard, C. Schamper, M. Froumentin and R. Guérin, "Zero-offset profiling using frequency cross-hole radar in a layered embankment test site: antenna design, simulation and experimental results," *Near Surface Geophysics*, vol. 9, no. 1, pp. 67-76, 2011.
- [39] C. A. Balanis, "Antenna theory: analysis and design," *John Wiley & Sons, Third edition*, 2005.
- [40] "<http://www.antenna-theory.com/antennas/main.php>," *Antenna Theory*, 2009.
- [41] L. Dojack, "Ground Penetrating Radar Theory, Data Collection, Processing, and Interpretation," *A Guide for Archaeologists, Report*, 2012.
- [42] F. Sagnard, "Utility measurement and detection on the urban site Sense-City using ground-penetrating radar systems," *Report IFSTTAR, submitted to IOP*. .

List of figures and tables

Figure 5.1: Antenna configurations for collecting GPR data with full polarization diversity; the four co-polarized (resp. two cross-polarized) antenna configurations are represented on the left (resp. on the right); because of antenna dimension, the offset can be different from one configuration to one another; in practice, GPR data collection are usually limited to the two co-polarized configurations: broadside-perpendicular and endfire-parallel.	143
Figure 5.2: Computed TM and TE scattered field at 1GHz from infinite cylindrical pipe embedded within a soil with real permittivity of 3.5.	147
Figure 5.3: Scattering Width (SW) over a soil with real permittivity of 4 and in the case of: a) a conductive pipe, b) Low permittivity dielectric pipe ($\epsilon'=1$), c) High permittivity dielectric pipe ($\epsilon'=9$). TM polarization is drawn in filled lines; TE polarization in dashed lines [37]..	149
Figure 5.4: Distribution of the electric field in both planes parallel and orthogonal to antenna long axis. a) E_{yx} for the bowtie-slot antenna, b) E_{zx} for the bowtie-slot antenna, c) E_{yx} for the dipole antenna, d) E_{zx} for the dipole antenna.....	150
Figure 5.5: Antenna polarization configurations in case of bowtie-slot and dipole antennas.	151
Figure 5.6: Computed raw Bscans with the dipole antennas over three types of infinite pipe.	154
Figure 5.7: Computed Bscans with the dipole antennas over three types of infinite pipe, after clutter reduction with the median subtraction technique.....	155
Figure 5.8: Computed raw Bscans with the bowtie-slot antennas over three kinds of infinite pipe.....	156
Figure 5.9: Computed Bscans with the bowtie-slot antennas over three kinds of infinite pipe after clutter reduction with the median subtraction technique.	157
Figure 5.10: Extracted Ascans from the Bscans in figure 5.8 at the apex position.....	158
Figure 5.11: Computed raw Bscans with varying angle between the dipole antenna and the pipe axis.....	159
Figure 5.12: Measurement Setup corresponding to Figure 5.13.	160
Figure 5.13: Experimental Bscan over an air-filled pipe and a horizontal metal strip within a sandy ground; a) Broadside configuration (TE), b) Endfire configuration(TM); top) Raw data, Bottom) clutter suppressed data.....	161
Figure 5.14: Measurement Setup corresponding to Figure 5.15.	161
Figure 5.15: Experimental Bscan over a water-filled pipe and a vertical metal strip within a sandy ground; a) Broadside configuration(TE), b) Endfire configuration(TM); top) Raw data, Bottom) clutter suppressed data.	162
Figure 5.16: Measurement Setup corresponding to Figure 5.17.	162
Figure 5.17: Experimental Bscan over a nylon pipe and a metal cylindrical pipe within a sandy ground; a) Broadside configuration(TE), b) Endfire configuration(TM); top) Raw data, Bottom) clutter suppressed data.	163
Figure 5.18: Cross-section of the pipe zone including the pipe positions and depths estimated during the site construction (on the courtesy of F. Sagnard [42]).....	164

Figure 5.19: Bowtie antenna at 900 MHz in the broadside configuration, all pipes are air-filled. (top) raw data (Bottom) clutter suppressed data. (on the courtesy of F. Sagnard [42])

..... 165

Figure 5.20: a) Clutter-free data with the bowtie antenna at 900 MHz in the endfire configuration, all pipes are air-filled, b) Raw data with the SIR3000 radar at 900 MHz, and pipes are air-filled except T5 water-filled. (on the courtesy of F. Sagnard [42])..... 165

Table 5.1: Summary for the detection quality over different buried pipe natures and under different electric field polarizations. The +/- symbols indicate the good/bad detection quality.

..... 166

Conclusion and perspectives

A. Conclusion

In this thesis, the general background on GPR systems and GPR survey operations was first presented in the introduction. Then, the work focused on the reduction of clutter and unwanted signals in GPR Bscan images using different statistical-based techniques. ROC curves enable to perform the qualitative assessment of the different clutter reduction techniques on simulated and experimental data with various conditions, i.e., deep and shallow targets, homogeneous and heterogeneous grounds. Next, the algorithm to detect target hyperbolas is presented and used in chapter 4. Finally, the polarization diversity is explored in the last chapter for the detection of buried targets. Throughout the work, the results are based on both simulated data and experimental Bscan data using two antennas (Blade-dipole and Bowtie-slot) operated in three antenna configurations (broadside, endfire and cross-polarization).

Two statistically-based clutter reduction techniques, namely, PCA and ICA, are studied in chapter 3. These techniques are mainly used for demining applications, and have never been rigorously compared on a large data base with various target depths, layered soils and different antenna configurations. They do not require prior knowledge about either the subsurface mapping or the targets and the clutter signatures. Then, they have been selected for clutter reduction in Bscan GPR images over civil engineering structures.

The latter clutter reduction techniques are evaluated qualitatively and compared to the conventional mean and median subtraction techniques (MST). The results showed that all techniques give versatile results, and the results were dependent on two criteria: the overlap of the target signature with the clutter and on the energy of the clutter compared to the target energy. Among them, the median subtraction technique gives the more reliable result in any condition.

For shallow buried targets, i.e., the clutter and the target signals overlap, the PCA suppressed the clutter while ICA introduces a distortion in the Bscan image. When the target is deeper buried and the target signal does not overlap with the clutter signal, the ICA mitigates the influence of the clutter as well as PCA without distorting the echoes. However, in most cases, PCA showed better performance over ICA, as opposed to the literature. The main limitation of PCA intervenes when the target echo has higher energy than the clutter; in this case, the principal components associated to the clutter echo are not well separated. Consequently, an improvement for PCA has been developed for high RCS targets. The modified PCA algorithm decomposes the Bscan into 3 sub-Bscans based on an energy ratio criterion between the clutter and the target signatures, then, it suppresses the clutter separately in each sub-Bscan. The proposed improvement showed very promising results. However, the decomposition into sub-Bscans in the PCA algorithm remains manually performed, and some automatization of the method has to be proposed as a working perspective.

Chapter 5 detailed the polarization mechanisms with the expectation to improve the detection of buried targets in raw Bscan images. The influence of polarization is illustrated on some examples of buried canonical targets with different EM properties and orientations. Assuming a plane wave with normal incidence to the ground surface, an analytical model is described for the case of buried cylindrical shaped objects under both TE and TM polarized electric fields. We compared the experimental and the simulated data with the analytical data to conclude about the utilities of multi-polarization GPR surveys for civil engineering applications. In practice, the used antennas show a dominant TM or TE mode, instead of a pure TE or TM mode as it is assumed for the analytical model.

Polarization is proved to be meaningful for extracting additional information about the nature (electrical properties) and the orientation of buried objects. The results show a preference for the TE polarization for the case of dielectric pipes with low permittivity contrast relatively to the soil permittivity; otherwise the TM polarization is preferred. Therefore, the multi-polarization appears very promising when dealing with dielectric targets.

Besides, we did not find that the cross-polarization was the best radar configurations for distinguishing between the target and the clutter as it is stated in the literature.

Finally, two main conclusions can be drawn in the presented work: the first deals with the clutter removal in GPR images, and the second one shows the importance of multi-polarization. After many experimental and numerical evaluations, the best clutter removal technique was found to be the median subtraction technique, and next comes the PCA technique. PCA seems better matched when it comes to rough surfaces and heterogeneous mediums. The multi-polarization GPR surveys was found meaningful for detecting small RCS buried targets, including both dielectric targets with low dielectric contrast compared to the surrounding ground and small metallic targets (~ 5 mm radius).

B. Perspectives

According to the application under scope and the difficulties encountered in this work, the following perspectives are proposed as a future work:

1-The work which was carried in this PhD was performed on canonical targets to model urban utilities. Thus, the first perspective to this work would be to extend the study to cracks and discontinuities with various shapes. A first experimental test on cracks is evaluated in the sand field (using the bowtie antenna) and modeled with rectangular objects. It has revealed the very low radar signatures for both polarizations. Therefore, for cracks, we propose to further explore the multi-polarization radar survey with a dense spatial radar data collection, namely, a small sampling step between Ascans.

2- The method proposed in section III.3.2 of chapter 3 may be further automatized by either scanning the Bscan image by a sliding window or by automatically selecting the width of the sub-Bscan window, namely, the parameters n_1 and n_2 of Figure 3.2. Besides, PCA will be tested on Bscan images with more than one target: the work can be extended to multi-target images, where multi-hyperbolas are observed and the extraction of different hyperbolas with different energy levels will surely require the use of the modified PCA. In this case the lateral resolution of GPR plays a very important role.

3- The determination of the reference image is one of the main difficulties encountered in this work for evaluating the clutter reduction techniques, because we have no prior knowledge about subsurface mapping and target signatures. In the near future, we then propose to study different construction methods to obtain a reliable reference image.

4- The work in chapter 5 has enlightened the need for some pre-processing to better exploit ground-coupled GPR data with polarization diversity. In fact, the lateral dimension of the GPR antennas implies some modifications when switching one polarization to one another. Some phase shifting is then required to compensate for different zero-offset between antennas configurations. An additional resampling is required on simulated data because the FDTD provides the data on different spatial grid mesh.

5-Future measurement campaigns may concern the future sense-city urban test-site which the construction is planned in 2016.

Appendix

Appendix A: Fresnel scattering equations

Considering an EM wave reaches at a dielectric interface, its energy will be decomposed into two parts, the transmitted part onto the next medium, and the reflected part in the same medium (figure A.1). Any EM wave can be expressed as a combination of the parallel and the normal vectors. For a given plan incident wave with incident angle θ^i Fresnel equations showed below describe waves behavior at the interface.

$$\tau_{\perp} = \frac{E_{0\perp}^t}{E_{0\perp}^i} = \frac{2\sqrt{\varepsilon_{eff}^1} \cos \theta^i}{\sqrt{\varepsilon_{eff}^1} \cos \theta^i + \sqrt{\varepsilon_{eff}^2} \cos \theta^t} \quad \text{and} \quad \tau_{\parallel} = \frac{E_{0\parallel}^t}{E_{0\parallel}^i} = \frac{2\sqrt{\varepsilon_{eff}^1} \cos \theta^i}{\sqrt{\varepsilon_{eff}^1} \cos \theta^t + \sqrt{\varepsilon_{eff}^2} \cos \theta^i}$$

$$\rho_{\perp} = \frac{E_{0\perp}^r}{E_{0\perp}^i} = \frac{\sqrt{\varepsilon_{eff}^1} \cos \theta^i - \sqrt{\varepsilon_{eff}^2} \cos \theta^t}{\sqrt{\varepsilon_{eff}^1} \cos \theta^i + \sqrt{\varepsilon_{eff}^2} \cos \theta^t} \quad \text{and} \quad \rho_{\parallel} = \frac{E_{0\parallel}^r}{E_{0\parallel}^i} = \frac{\sqrt{\varepsilon_{eff}^2} \cos \theta^i - \sqrt{\varepsilon_{eff}^1} \cos \theta^t}{\sqrt{\varepsilon_{eff}^1} \cos \theta^t + \sqrt{\varepsilon_{eff}^2} \cos \theta^i}$$

Where τ is the transmission coefficient, ρ is the reflection coefficient, \perp is the normal polarization (TE), \parallel is the parallel polarization (TM), E^t is the transmitted field, E^i is the incident field, E^r is the reflected field, θ^i is the incident angle, θ^t is the refraction angle, and ε_{eff}^1 and ε_{eff}^2 are the effective permittivity of mediums 1 and 2 respectively.

Fresnel coefficients are dependent the angle of incidence and on the materials dielectric properties on both sides of the surface, for a GPR application, the coefficients are not only dependent on the ground properties but also on the air varying conditions: humidity and temperature. Ground dielectric properties (parameter ε_{eff}) are variable in function of the frequency, consequently deferent frequencies produces different coefficient and refraction.

We must note that antennas does not emit plane waves, nevertheless plane waves are a preliminary study, and useful to extract a first conclusion on the behavior of EM waves. It is a simple modeling to understand the behavior of more complexes environments.

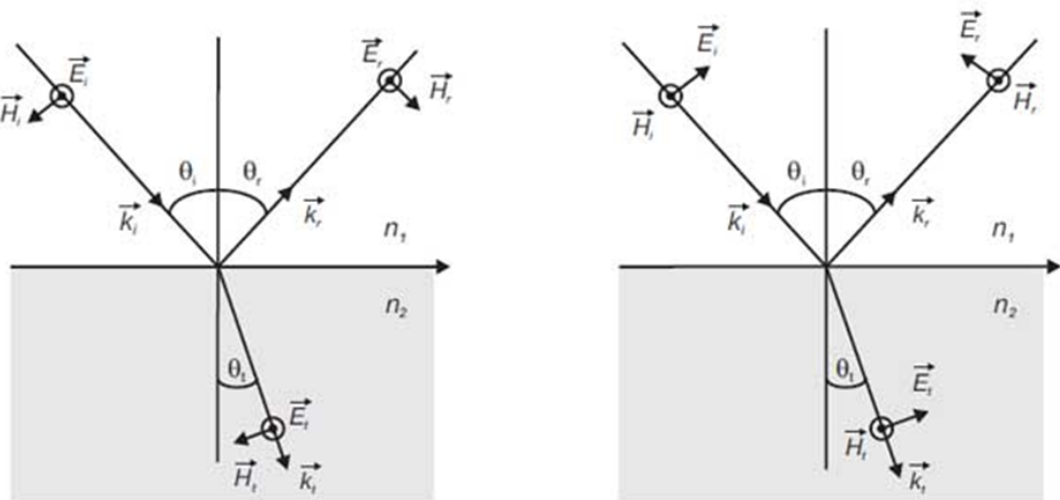


Figure A.1: EM wave breakdown on the impact with planar surface.

Appendix B: Scattering from a cylindrical infinite pipe

I. Case of a TM^Z polarization (E in z direction)

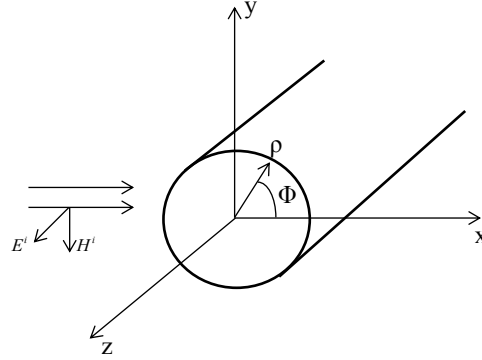


Figure B.1

The electric incident field can be written as:

$$\begin{aligned} E_z^i &= E_{z0} e^{-j\beta x} = E_{z0} e^{-j\beta\rho \cos\phi} \\ E_\rho^i &= 0 \\ E_\phi^i &= 0 \end{aligned} \quad (B-1)$$

And can also be expressed as an infinite sum of the Bessel function:

$$E_z^i = E_{z0} \sum_{n=-\infty}^{+\infty} j^{-n} J_n(\beta\rho) e^{jn\phi} \quad (B-2)$$

By using Maxwell's Faraday equation:

$$H^i = -\frac{1}{j\omega\mu} \nabla \times E^i \quad (B-3)$$

We obtain:

$$H_z^i = 0 \quad (B-4)$$

$$H_\rho^i = \frac{-E_{z0}}{j\omega\mu\rho} \sum_{n=-\infty}^{+\infty} n j^{-n+1} J_n(\beta\rho) e^{jn\phi} \quad (B-5)$$

$$H_\phi^i = \frac{-\beta E_{z0}}{j\omega\mu} \sum_{n=-\infty}^{+\infty} j^{-n} J_n'(\beta\rho) e^{jn\phi} \quad (B-6)$$

Incident wave impacts cylinder surface and creates scattering waves, therefore the total field E_z^t at each point of space is expressed as:

$$E_z^t = E_z^i + E_z^s \quad (B-7)$$

Where E_z^s is the scattered field, such as:

$$E_z^s = E_{z0} \sum_{n=-\infty}^{+\infty} j^{-n} a_n H_n^{(2)}(\beta\rho) e^{jn\phi} \quad (\text{B-8})$$

a_n represents an unknown coefficient, and $H_n^{(2)}(\beta\rho)$ represents the Hankel function of the second kind of order n .

$$E_z^t = E_{z0} \sum_{n=-\infty}^{+\infty} j^{-n} \left(J_n(\beta\rho) + a_n H_n^{(2)}(\beta\rho) \right) e^{jn\phi} \quad (\text{B-9})$$

I.1. Case of a perfectly conductive cylinder

For a perfectly conductive cylinder with $\sigma = \infty$, and by applying boundary condition for the total field we calculate the unknown coefficient a_n . Inside the cylinder the total field is zero:

$$E_z^t(\rho < a, 0 \leq \phi \leq 2\pi, z) = 0 \quad (\text{B-10})$$

At boundary the tangential fields are continuous in space and time, thus the tangential component z of the total electric field is zero on the cylinder surface is:

$$E_z^t(\rho = a, 0 \leq \phi \leq 2\pi, z) = 0 \quad (\text{B-11})$$

$$J_n(\beta a) + a_n H_n^{(2)}(\beta a) = 0 \quad (\text{B-12})$$

$$a_n = -\frac{J_n(\beta a)}{H_n^{(2)}(\beta a)} \quad (\text{B-13})$$

Thus,

$$E_z^s = -E_{z0} \sum_{n=-\infty}^{+\infty} j^{-n} \frac{J_n(\beta a)}{H_n^{(2)}(\beta a)} H_n^{(2)}(\beta\rho) e^{jn\phi} \quad (\text{B-14})$$

$$E_z^t = E_{z0} \sum_{n=-\infty}^{+\infty} j^{-n} \left(J_n(\beta\rho) - \frac{J_n(\beta a)}{H_n^{(2)}(\beta a)} H_n^{(2)}(\beta\rho) \right) e^{jn\phi} \quad (\text{B-15})$$

And H^t can be calculated as H^i through Maxwell's Faraday equation:

$$H^t = -\frac{1}{j\omega\mu} \nabla \times E^t \quad (\text{B-16})$$

I.2. Case of a dielectric cylinder

For a dielectric cylinder with an electric relative permittivity ϵ_d and relative permeability $\mu_d = 1$, one part of the incident electromagnetic field will refract through the cylinder, and the other part will reflect at the surface of the cylinder. The continuity of the tangential fields E_z^t and H_ϕ^t at the cylinder boundary gives:

$$E_z^t(\rho = a^+, 0 \leq \phi \leq 2\pi, z) = E_z^t(\rho = a^-, 0 \leq \phi \leq 2\pi, z) \quad (\text{B-17})$$

$$H_{\phi}^t(\rho = a^+, 0 \leq \phi \leq 2\pi, z) = H_{\phi}^t(\rho = a^-, 0 \leq \phi \leq 2\pi, z) \quad (\text{B-18})$$

Where fields E and H scattered inside the cylinder ($\rho < a$) are:

$$E_z^{t+} = E_z^{s+} = E_{z0} \sum_{n=-\infty}^{+\infty} j^{-n} c_n J_n(\beta_d \rho) e^{jn\phi} \quad (\text{B-19})$$

$$H_{\phi}^{t+} = H_{\phi}^{s+} = -\frac{\beta_d E_{z0}}{j\omega \mu_0} \sum_{n=-\infty}^{+\infty} j^{-n} c_n J_n'(\beta_d \rho) e^{jn\phi} \quad (\text{B-20})$$

with $\beta_d = w\sqrt{\varepsilon_d \varepsilon_0 \mu_0} = 2\pi f \sqrt{\varepsilon_d \varepsilon_0 \mu_0}$ phase cte

And fields E and H scattered outside the cylinder ($\rho > a$) are:

$$E_z^{s-} = E_{z0} \sum_{n=-\infty}^{+\infty} j^{-n} a_n H_n^{(2)}(\beta \rho) e^{jn\phi} \quad (\text{B-21})$$

$$E_z^{t-} = E_{z0} \sum_{n=-\infty}^{+\infty} j^{-n} \left(J_n(\beta \rho) + a_n H_n^{(2)}(\beta \rho) \right) e^{jn\phi} \quad (\text{B-22})$$

$$H_{\phi}^{s-} = -\frac{\beta E_{z0}}{j\omega \mu} \sum_{n=-\infty}^{+\infty} j^{-n} a_n H_n'^{(2)}(\beta \rho) e^{jn\phi} \quad (\text{B-23})$$

$$H_{\phi}^{t-} = -\frac{\beta E_{z0}}{j\omega \mu} \sum_{n=-\infty}^{+\infty} j^{-n} \left(J_n'(\beta \rho) + a_n H_n'^{(2)}(\beta \rho) \right) e^{jn\phi} \quad (\text{B-24})$$

a_n and c_n represent unknown coefficients, by replacing (B-19) and (B-22) in equation (B-17); and (B-20) and (B-24) in (B-18), we obtain two equations for calculating the two unknown coefficients:

$$c_n J_n(\beta_d a) = J_n(\beta a) + a_n H_n^{(2)}(\beta a) \quad (\text{B-25})$$

$$\frac{\beta_d}{\mu_0} c_n J_n'(\beta_d a) = \frac{\beta}{\mu} \left(J_n'(\beta a) + a_n H_n'^{(2)}(\beta a) \right) \quad (\text{B-26})$$

or $\frac{\beta}{\mu} = \frac{w\sqrt{\varepsilon\mu}}{\mu} = w \sqrt{\frac{\varepsilon}{\mu}} = w \cdot \frac{1}{\eta}$ where η is wave impedance for a dielectric material

η : Medium impedance

η_d : Cylinder impedance

We obtain:

$$a_n = \frac{\eta J_n'(\beta_d a) J_n(\beta a) - \eta_d J_n'(\beta a) J_n(\beta_d a)}{\eta_d J_n(\beta_d a) H_n'^{(2)}(\beta a) - \eta J_n'(\beta a) H_n^{(2)}(\beta a)} \quad (\text{B-25})$$

$$c_n = \eta_d \frac{J_n(\beta a) H_n'^{(2)}(\beta a) - J_n'(\beta a) H_n^{(2)}(\beta a)}{\eta_d J_n(\beta_d a) H_n'^{(2)}(\beta a) - \eta J_n'(\beta_d a) H_n^{(2)}(\beta a)} \quad (\text{B-26})$$

II. Case of a TE^Z polarization (H in z direction)

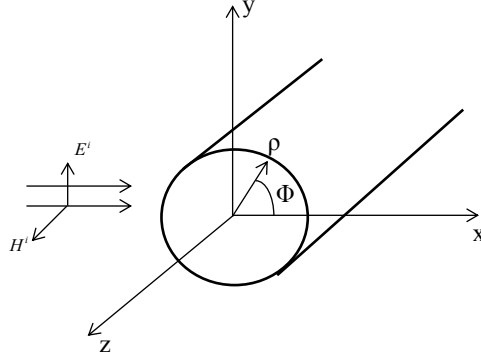


Figure B.2

For TE^Z polarization, the magnetic field H is in z direction, such as:

$$H_z^i = H_{z0} e^{-j\beta x} = H_{z0} e^{-j\beta\rho \cos\phi} = H_{z0} \sum_{n=-\infty}^{+\infty} j^{-n} J_n(\beta\rho) e^{jn\phi}$$

$$H_\rho^i = 0$$

$$H_\phi^i = 0$$
(B-27)

By using Maxwell's Faraday equation:

$$E^i = \frac{1}{j\omega\epsilon} \nabla \times H^i$$
(B-28)

We obtain:

$$E_z^i = 0$$
(B-29)

$$E_\rho^i = \frac{H_{z0}}{j\omega\epsilon\rho} \sum_{n=-\infty}^{+\infty} nj^{-n+1} J_n(\beta\rho) e^{jn\phi}$$
(B-30)

$$E_\phi^i = -\frac{\beta H_{z0}}{j\omega\epsilon} \sum_{n=-\infty}^{+\infty} j^{-n} J'_n(\beta\rho) e^{jn\phi}$$
(B-31)

Incident wave impacts cylinder surface and creates scattering waves, therefore the total fields E_z^t and H_z^t at each point of space are expressed as:

$$H_z^t = H_z^i + H_z^s$$
(B-32)

$$E_z^t = E_z^i + E_z^s$$
(B-33)

With the scattered fields:

$$H_z^s = H_{z0} \sum_{n=-\infty}^{+\infty} j^{-n} a_n H_n^{(2)}(\beta\rho) e^{jn\phi}$$
(B-34)

$$E_\rho^s = \frac{H_{z0}}{j\omega\epsilon\rho} \sum_{n=-\infty}^{+\infty} nj^{-n+1} a_n H_n^{(2)}(\beta\rho) e^{jn\phi}$$
(B-35)

$$E_\phi^s = -\frac{\beta H_{z0}}{j\omega\epsilon} \sum_{n=-\infty}^{+\infty} j^{-n} a_n H_n'^{(2)}(\beta\rho) e^{jn\phi}$$
(B-36)

And the total fields:

$$H_z^t = H_{z0} \sum_{n=-\infty}^{+\infty} j^{-n} \left(J_n(\beta\rho) + a_n H_n^{(2)}(\beta\rho) \right) e^{jn\phi} \quad (\text{B-37})$$

$$E_\rho^t = \frac{H_{z0}}{j\omega\epsilon\rho} \sum_{n=-\infty}^{+\infty} nj^{-n+1} \left(J_n(\beta\rho) + a_n H_n^{(2)}(\beta\rho) \right) e^{jn\phi} \quad (\text{B-38})$$

$$E_\phi^t = -\frac{\beta H_{z0}}{j\omega\epsilon} \sum_{n=-\infty}^{+\infty} j^{-n} \left(J_n'(\beta\rho) + a_n H_n'^{(2)}(\beta\rho) \right) e^{jn\phi} \quad (\text{B-39})$$

II.1. Case of a perfectly conductive cylinder

For a perfectly conductive cylinder with, and by applying boundary condition for the total field we calculate the unknown coefficient a_n . Inside the cylinder the total field is zero:

$$E_\phi^t(\rho < a, 0 \leq \phi \leq 2\pi, z) = 0 \quad (\text{B-40})$$

At boundary the field is continuous, thus the tangential component E_ϕ^t of the total field is zero on the cylinder surface:

$$E_\phi^t(\rho = a, 0 \leq \phi \leq 2\pi, z) = 0 \quad (\text{B-41})$$

$$J_n'(\beta a) + a_n H_n'^{(2)}(\beta a) = 0 \quad (\text{B-42})$$

$$a_n = -\frac{J_n'(\beta a)}{H_n'^{(2)}(\beta a)} \quad (\text{B-43})$$

Thus,

$$E_\phi^s = \frac{\beta H_{z0}}{j\omega\epsilon} \sum_{n=-\infty}^{+\infty} j^{-n} \frac{J_n'(\beta a)}{H_n'^{(2)}(\beta a)} H_n'^{(2)}(\beta\rho) e^{jn\phi} \quad (\text{B-44})$$

$$E_\phi^t = -\frac{\beta H_{z0}}{j\omega\epsilon} \sum_{n=-\infty}^{+\infty} j^{-n} \left(J_n'(\beta\rho) - \frac{J_n'(\beta a)}{H_n'^{(2)}(\beta a)} H_n'^{(2)}(\beta\rho) \right) e^{jn\phi} \quad (\text{B-45})$$

II.2. Case of a dielectric cylinder

For a dielectric cylinder with an electric relative permittivity ϵ_d and a relative permeability $\mu_d = 1$. The continuity of the tangential fields E_ϕ^t and H_z^t at the cylinder boundary gives:

$$E_\phi^t(\rho = a^+, 0 \leq \phi \leq 2\pi, z) = E_\phi^t(\rho = a^-, 0 \leq \phi \leq 2\pi, z) \quad (\text{B-46})$$

$$H_z^t(\rho = a^+, 0 \leq \phi \leq 2\pi, z) = H_z^t(\rho = a^-, 0 \leq \phi \leq 2\pi, z) \quad (\text{B-47})$$

Where tangential fields E and H scattered inside the cylinder ($\rho < a$) are:

$$H_z^+ = H_z^{s+} = H_{z0} \sum_{n=-\infty}^{+\infty} j^{-n} c_n J_n(\beta_d \rho) e^{jn\phi} \quad (\text{B-48})$$

$$E_\phi^+ = E_\phi^{s+} = -\frac{\beta_d H_{z0}}{j\omega \varepsilon_d \varepsilon_0} \sum_{n=-\infty}^{+\infty} j^{-n} c_n J'_n(\beta_d \rho) e^{jn\phi} \quad (\text{B-49})$$

with $\beta_d = \omega \sqrt{\varepsilon_d \varepsilon_0 \mu_0}$ phase cte

And fields E and H scattered outside the cylinder ($\rho > a$) are:

$$H_z^- = H_{z0} \sum_{n=-\infty}^{+\infty} j^{-n} a_n H_n^{(2)}(\beta \rho) e^{jn\phi} \quad (\text{B-50})$$

$$H_z^- = H_{z0} \sum_{n=-\infty}^{+\infty} j^{-n} \left(J_n(\beta \rho) + a_n H_n^{(2)}(\beta \rho) \right) e^{jn\phi} \quad (\text{B-51})$$

$$E_\phi^- = -\frac{\beta H_{z0}}{j\omega \varepsilon} \sum_{n=-\infty}^{+\infty} j^{-n} a_n H_n'^{(2)}(\beta \rho) e^{jn\phi} \quad (\text{B-52})$$

$$E_\phi^- = -\frac{\beta H_{z0}}{j\omega \varepsilon} \sum_{n=-\infty}^{+\infty} j^{-n} \left(J_n'(\beta \rho) + a_n H_n'^{(2)}(\beta \rho) \right) e^{jn\phi} \quad (\text{B-53})$$

a_n and c_n represent unknown coefficients, by replacing (B-48) and (B-51) in equation (B-47); and (B-49) and (B-53) in (B-46), we obtain two equations for calculating the two unknown coefficients:

$$c_n J_n(\beta_d a) = J_n(\beta a) + a_n H_n^{(2)}(\beta a) \quad (\text{B-54})$$

$$\frac{\beta_d}{\varepsilon_d \varepsilon_0} c_n J_n'(\beta_d a) = \frac{\beta}{\varepsilon} \left(J_n'(\beta a) + a_n H_n'^{(2)}(\beta a) \right) \quad (\text{B-55})$$

or $\frac{\beta}{\varepsilon} = \frac{\omega \sqrt{\varepsilon \mu}}{\varepsilon} = \omega \sqrt{\frac{\mu}{\varepsilon}} = w \cdot \eta$ where η is wave impedance for a dielectric material

η : Medium impedance

η_d : Cylinder impedance

We obtain:

$$a_n = \frac{\eta_d J_n'(\beta_d a) J_n(\beta a) - \eta J_n'(\beta a) J_n(\beta_d a)}{\eta J_n(\beta_d a) H_n'^{(2)}(\beta a) - \eta_d J_n'(\beta_d a) H_n^{(2)}(\beta a)} \quad (\text{B-56})$$

$$c_n = \eta \frac{J_n(\beta a) H_n'^{(2)}(\beta a) - J_n'(\beta a) H_n^{(2)}(\beta a)}{\eta J_n(\beta_d a) H_n'^{(2)}(\beta a) - \eta_d J_n'(\beta_d a) H_n^{(2)}(\beta a)} \quad (\text{B-57})$$

Appendix C: ICA algorithm

C1. Whitening proof

Let:

$$Y = \Lambda^{-1/2} U^T X \quad (\text{C-1})$$

We have:

$$E\{YY^T\} = \Lambda^{-1/2} U^T E\{XX^T\} U \Lambda^{-1/2} \quad (\text{C-2})$$

$$E\{YY^T\} = \Lambda^{-1/2} U^T U \Lambda U^T U \Lambda^{-1/2} \quad (\text{C-3})$$

$$E\{YY^T\} = \Lambda^{-1/2} \Lambda \Lambda^{-1/2} \quad \text{with } U^T U = U U^T = I \quad (\text{C-4})$$

$$E\{YY^T\} = I \quad \text{with } \Lambda^{-1/2} = \text{diag}\left(\frac{1}{\sqrt{\Lambda_{ii}}}\right) \quad (\text{C-5})$$

C2. Gaussianity and independence

1. According to the ICA data model, in order to estimate the independent components, a vector y defined by $y = Wx_i$ is introduced, where W is a matrix to be determined. If W is the inverse of A (or Moore-Penrose pseudo inverse of A if y and x_i do not have the same dimension), then y would actually equal to s_i .

$$\text{Or we have } y_i = W_i^T x_i = W_i^T A s_i$$

To obtain independent original sources we have to find W such that $y_i(t)$ is “least” Gaussian. Means that x_i is the sum of many y_i , thus x_i is more gaussian than any of y_i . Maximizing the non-gaussianity of $y_i = W_i^T x_i$ will produce an estimation of the independent component: $\hat{s}_i = y_i$

N.B: We can't say the inverse, that y_i is the sum of many x_i , so y_i is more gaussian than any of x_i because the x_i are not independent.

2. Note that there is a condition for ICA algorithm to work, that the gaussian variables are forbidden for the ICs, meaning we must have no gaussian sources in order to be able to estimate the ICs, because the transformation of any gaussian variable by the orthogonal mixing matrix A , will result into exactly the same gaussian variable, so as if we did no transformation. (Actually, if only one IC is gaussian the ICA algorithm will be able to estimate the ICs)

C3. FastICA algorithm

1. The one-unit algorithm

By unit we refer to one vector of the weight matrix W . The FastICA finds the unit vector w such that the projection $w^T x$ maximizes nongaussianity, by measure of the approximated negentropy $J(w^T x)$. The variance of $w^T x$ must be of unity, but since the data X are whitened this mean constraining the norm of w to be unity.

The basic form of the one-unit FastICA algorithm is shown as follows:

1. Choose an initial random weight vector w (with unity variance).
2. Let $w^+ = E\{xg(w^T x)\} - E\{g'(w^T x)\}w$
3. Let $w = \frac{w^+}{\|w^+\|}$
4. If not converged, go back to 2.

The algorithm above estimates just one of the independent components (ICs), by estimating one corresponding weight vector from the weight matrix, so it is called one-unit algorithm. Next we will see how to estimate all ICs or all sources in our signal.

Note that:

convergence means that the old and new values of w (w and w^+) points in the same direction, i.e. their dot-product are almost equal to 1, w and $-w$ are considered the same cause ICA cannot determine the sign of the vector. In step three we normalize to keep the variance of the projection $w^T x$ equal to unity. The optimization (minimization or maximization) of any contrast function in step 2 (we used G_I) enables the estimation of the mixing matrix. Afterwards, the sources can be estimated, and the equality in step two comes from calculation the maxima of the approximation of the Negentropy of $w^T x$ are obtained at certain optimum of $E\{G(w^T x)\}$.

Equality 2 approximation:

According to the Kuhn-Tucker conditions (Luenberger, 1969), the optima of $E\{G(w^T x)\}$ under the constraint $E\{(w^T x)^2\} = \|w\|^2 = 1$ are obtained at points where:

$$E\{xg(w^T x)\} - \beta w = 0 \quad (\text{C-6})$$

We solve this equation by Newton's method. Denoting the function on the left-hand side of the eq. above by F , we obtain its Jacobian matrix $JF(w)$ as:

$$JF(w) = E\{xx^T g'(w^T x)\} - \beta w \quad (\text{C-7})$$

To simplify the inversion of this matrix, we decide to approximate the first term, since the data is sphered, a reasonable approximation seems to be:

$$E\{xx^T g'(w^T x)\} \cong E\{xx^T\}E\{g'(w^T x)\} = E\{g'(w^T x)\}I \quad (\text{C-8})$$

Thus the Jacobian matrix becomes diagonal, and can easily be inverted. Thus we obtain the following approximative Newton iteration:

$$w^+ = w - [E\{xg(w^T x)\} - \beta w] / [E\{g'(w^T x)\} - \beta] \quad (\text{C-9})$$

This algorithm can be further simplified by multiplying both sides by $\beta - E\{g'(w^T x)\}$. This gives, after algebraic simplification, the second FastICA iteration.

2. Several units algorithms: Deflationary orthogonalization and Symmetric orthogonalization

To estimate all the ICs or all N sources, we need to run the one-unit algorithm using several units to estimate the N weighting vectors w_1, w_2, \dots, w_N (N is the number of ICs to estimate). But since w is chosen randomly, to prevent different vectors w_i to converge for the same maxima, we must decorrelate the outputs $w_i^T x$ after every iteration, a simple way is orthogonalization. Here comes the choice between two versions of algorithms to estimate the remaining ICs: Deflationary orthogonalization and Symmetric orthogonalization.

In deflationary orthogonalization, we have to estimate p ICs, such that one IC is estimated at a time. When the estimation of the weighted vector w_p is obtained, the vector is then orthogonalized with all previously estimated weight vectors w_j ($1 \leq j < p$), by calculating the projections $w_p^T w_j w_j$ and subtracting them from the current vector $w_p = w_p - \sum_{j=1}^{p-1} (w_p^T w_j) w_j$, and then normalize $w_p = w_p / \sqrt{w_p^T w_p}$. The basic algorithm is shown as below:

1. Center the data to make its mean zero and whiten the data to give X .
2. Choose the number of ICs to estimate: N .
3. Choose vector w_p randomly of length M .
4. Let $w_j = E\{xg(w_j^T x)\} - E\{g'(w_j^T x)\}w_j$
5. Do the orthogonalization $w_p = w_p - \sum_{j=1}^{p-1} (w_p^T w_j) w_j$
6. Let $w_p = w_p / \|w_p\|$
7. If w_p has not converged, go back to 4
8. Set $p = p+1$, If $p \leq N$ go back to 3

Differently, in symmetric orthogonalization, all sources are recovered simultaneously. It treats all vectors as a matrix and orthogonalizes them at once so no sources are privileged over others. Each weight vector w_p is estimated independently and then the resulting matrix $W = (w_1, \dots, w_N)^T$ is orthogonalized by using the matrix square root $W = (WW^T)^{-1/2}W$. The basic algorithm is shown as below:

1. Center the data to make its mean zero and whiten the data to give X .

2. Choose the number of ICs to estimate: N
3. Choose N initial values of unit norm for w_1, w_2, \dots, w_N
4. Orthogonalize the matrix as $W = (WW^T)^{-1/2}W$ and normalize it $W = W/\sqrt{WW^T}$
5. Let $w_j = E\{xg(w_j^T x)\} - E\{g'(w_j^T x)\}w_j$ for every $j=1,2,\dots,N$.
6. Do a symmetric orthogonalization of the matrix W by $W = (WW^T)^{-1/2}W$
7. Check the convergence: $WW_{old}^T \cong I$ If not, go back to 5

In step 4 we can replace $W = (WW^T)^{-1/2}W$ by $W = \frac{3}{2}W - \frac{1}{2}WW^TW$ to simplify calculations. And W is normalized to keep the variance of the projection $w^T x$ equal to unity since the whitened data X is of variance unity.

N.B: $w^T x$ is replaced by $w^H x$ for complex data.

We must note also that two ambiguities result from ICA algorithm. First ambiguity is that we cannot find out the variance value of each IC, because both S and A are unknown, any scalar multiplier in one of the sources could always be cancelled by dividing the corresponding column of the mixing matrix A , so the best solution for this ambiguity is to assume that each IC is of unity variance. Second ambiguity is after retrieving the ICs, we cannot know in which order the sources were (in the measured signal) so a rotation matrix must be introduced, but this ambiguity does not affect our application in clutter removing, because we are not interested in the order, we only want to eliminate some sources and then reconstruct the signal by projecting the chosen sources back on the mixing matrix.